
Artificial Metalloenzymes based on Copper Heteroscorpionate
Complexes for C-H Functionalization Catalysis

Inauguraldissertation

zur

Erlangung der Würde eines Doktors der Philosophie

vorgelegt der

Philosophisch-Naturwissenschaftlichen Fakultät

der Universität Basel

von

Corentin Rumo

Basel, 2023

Originaldokument gespeichert auf dem Dokumentenserver der Universität Basel

edoc.unibas.ch

Genehmigt von der Philosophisch-Naturwissenschaftlichen Fakultät
auf Antrag von

Prof. Dr. Thomas R. Ward

Prof. Dr. Olivier Baudoin

Prof. Dr. Pedro J. Pérez Romero

Basel, den 18. Oktober 2022

Prof. Dr. Marcel Mayor

Dekan

Acknowledgement

First and foremost, I would like to address my deepest gratitude to my supervisor Prof. Thomas R. Ward for the opportunity he gave me, the respect he demonstrated, and the precious support he has shown during difficult times. His wise words, applicable to more than chemistry, will resonate within my memory for the many years to come.

I also would like to thank my second supervisor Prof. Olivier Baudoin for his valuable input and his support. Also, a big thank you to Prof. Pedro J. Pérez for accepting to be my external expert and being the main source of inspiration of this work.

Thank you to all the researchers, without whom this thesis would not have been possible: Alina Stein, Alessandro Prescimone, Prof. Daniel Häussinger, Joan Serrano, Johannes G. Rebelein, Juliane Klehr, Maxime Barnet, Ryan Peterson and Ryo Tachibana.

From the bottom of my heart I would like to thank all the members of the DrEAM team. My fellow PhD colleagues: Alain Baiyoumy, Alina Stein, Boris Lozhkin, Dongping Chen, Elinor Morris, Fadri Christoffel, Iori Morita, Jaicy Vallapurackal, Jonas Schätti, Kun Yu, Nico Igareta, Snizhana Zaitseva, Valérie Waser and Valerio Sabatino. My Postdoc colleagues: Alexandria Liang, Daniel Brodbeck, Holly Davis, Isabel Alt, Joan Serrano, Johannes Rebelein, Manjistha Mukherjee, Robin Vinck, Ryo Tachibana, Simon Burgener, Sophie Basler, Xiang Zhang, Yasunori Okamoto, Yoann Cotelle and Zhi Zhou. The staff: Claudia Stadelmann, Esther Stalder, Jonas Zurflüh, Juliane Klehr, Michael Pfeffer, Valentin Köhler and Xiaochun Blatter.

Thank you as well to the analytical service of the university, the Werkstatt team and the administration for the top services.

A very special thank you goes to Alain, Alina, Dongping, Eli, Eva, Fadri, Kun, Manjistha, Nico and Xiang. This journey would not have been the same without every single one of you.

Finalement, j'aimerais remercier ma famille et mes proches, qui m'ont soutenu, du début à la fin. Merci infiniment.

"One must never forget when misfortunes come that it is quite possible they are saving one from something much worse; or that when you make some great mistake, it may very easily serve you better than the best-advised decision."

Winston Churchill, My early life, 1930

Abstract

This thesis capitalizes on the efforts of the Ward lab to develop artificial metalloenzymes based on earth-abundant transition metals for C-H functionalization chemistry.

Herein, a novel approach for the design of heteroscorpionate complexes was developed using pyrazole metathesis. This strategy enabled the access to an unprecedented tris(pyrazolyl)borate ligand chiral at the boron and to biotinylated copper heteroscorpionate complexes. Following supramolecular assembly with streptavidin, the resulting artificial metalloenzymes were characterized by spectroscopic and computational methods. Chemical optimization and single point mutation of these hybrid catalysts displayed high activity for intramolecular C-H insertion reactions. A protein expression/purification platform in 96-well plates was developed for the genetic optimization of the artificial metalloenzymes. Identification of superior mutants enabled the regio- and enantioselective functionalization of unactivated C-H bonds with high turnover numbers.

Additionally, an artificial metalloenzyme based on an iron(III) tetraamido macrocyclic ligand (Fe(TAML)) and the streptavidin technology was developed. Point mutations allowed to perform enantioselective intermolecular hydroxylation of benzylic C-H bonds using hydrogen peroxide. Kinetic studies revealed a kinetic resolution effect within the catalytic pocket. Finally, an enzymatic cascade relying on glucose oxidase enabled to use molecular oxygen as terminal oxidant.

Artificial metalloenzymes based on earth-abundant transition metals and C-H functionalization catalysis currently stand at the forefront of chemical research. We believe that this work opens promising avenues for the development of more efficient and sustainable chemical processes.

Table of Contents

ACKNOWLEDGEMENT	I
ABSTRACT.....	III
TABLE OF CONTENTS	IV
1. GENERAL INTRODUCTION.....	1
1.1 ARTIFICIAL METALLOENZYMES AND THE BIOTIN-STREPTAVIDIN TECHNOLOGY.....	1
1.2 C–H FUNCTIONALIZATION	2
1.3 REFERENCES	3
2. SUMMARY OF INDIVIDUAL CHAPTERS	7
2.1 CHAPTER 3. DESIGN OF BIOTINYLATED TP LIGANDS FOR ARTIFICIAL METALLOENZYMES AND INITIAL REACTIVITY STUDIES.....	7
2.2 CHAPTER 4. AN ARTIFICIAL METALLOENZYME BASED ON A COPPER HETEROSCORPIONATE ENABLES sp^3 C–H FUNCTIONALIZATION VIA INTRAMOLECULAR CARBENE INSERTION	7
2.3 CHAPTER 5. ENANTIOSELECTIVE HYDROXYLATION OF BENZYLIC C(sp^3)–H BONDS BY AN ARTIFICIAL IRON HYDROXYLASE BASED ON THE BIOTIN–STREPTAVIDIN TECHNOLOGY	7
3. DESIGN OF BIOTINYLATED TP LIGANDS FOR ARTIFICIAL METALLOENZYMES AND INITIAL REACTIVITY STUDIES.....	9
3.1 CONTRIBUTIONS TO THIS WORK.....	9
3.2 INTRODUCTION.....	9
3.3 RESULTS AND DISCUSSION	11
3.4 CONCLUSION.....	21
3.5 SUPPORTING INFORMATION	22
3.5.1 <i>General methods</i>	22
3.5.2 <i>Experimental</i>	23
3.5.3 <i>NMR and MS Spectra</i>	27
3.5.4 <i>X-ray reports</i>	38
3.6 REFERENCES.....	40
4. AN ARTIFICIAL METALLOENZYME BASED ON A COPPER HETEROSCORPIONATE ENABLES SP^3 C–H FUNCTIONALIZATION VIA INTRAMOLECULAR CARBENE INSERTION	45
4.1 CONTRIBUTIONS TO THIS WORK.....	45
4.2 INTRODUCTION.....	45
4.3 RESULTS AND DISCUSSION	46
4.4 CONCLUSION.....	56
4.5 SUPPORTING INFORMATION	56
4.5.1 <i>General methods</i>	56
4.5.2 <i>Carbene Insertion</i>	58

4.5.3 Cofactor synthesis.....	58
4.5.4 NMR experiments on the cofactor.....	62
4.5.5 CD titration and determination of the binding constant.....	65
4.5.6 QM/MM calculations	67
4.5.7 Substrates and catalysis products	67
4.5.8 Directed evolution	71
4.5.9 Catalysis.....	75
4.5.10 NMR and HRMS spectra	87
4.5.11 Protein HRMS	121
4.5.12 Calibration curves and chromatograms	125
4.5.13 Quantitative NMR	139
4.5.14 VCD Spectrum.....	140
4.5.15 X-ray reports.....	141
4.6 REFERENCES.....	145
5. ENANTIOSELECTIVE HYDROXYLATION OF BENZYLIC C(SP ³)-H BONDS BY AN ARTIFICIAL IRON HYDROXYLASE BASED ON THE BIOTIN-STREPTAVIDIN TECHNOLOGY.....	153
5.1 CONTRIBUTIONS TO THIS WORK.....	153
5.2 INTRODUCTION.....	153
5.3 RESULTS AND DISCUSSION	154
5.4 CONCLUSION.....	161
5.5 SUPPORTING INFORMATION	162
5.5.1 Synthesis of the ligand.....	162
5.5.2 Typical catalysis procedure.....	163
5.5.3 Supplementary plots.....	163
5.5.4 Oxidation of hydrocarbons: enzymatic cascade.....	166
5.6 REFERENCES.....	167
6. FINAL CONCLUSION AND OUTLOOK	173

1. General Introduction

1.1 Artificial Metalloenzymes and the Biotin-Streptavidin Technology

Artificial metalloenzymes (ArMs) are hybrid catalysts resulting from the incorporation of a non-natural cofactor within a protein scaffold. They combine the attractive features of enzymes with the versatility of homogeneous catalysts.¹ While the choice of the first coordination sphere of homogeneous catalysts is only limited by the imagination of the synthetic chemist, the molecular components that are not tightly bound to the metal center remain challenging to control. This challenge can be alleviated by providing the metal complex with a well-defined and genetically-evolvable second coordination sphere in the instance of a protein scaffold. The resulting hybrid catalyst can enable living organisms to access new-to-nature reactions as well as to develop more selective and more sustainable processes for the chemical industry.²⁻⁵

An artificial cofactor can be localized inside a protein scaffold according to the following anchoring strategies: covalent, supramolecular, dative or metal substitution. Supramolecular anchoring constitutes a particularly attractive approach and relies on the high affinity of a protein for a particular inhibitor, cofactor or substrate. Strategic modification of such high affinity tag with a synthetic, catalytic unit allows its incorporation into the desired protein.⁶ Relevant examples of proteins used for ArM assembly according to this strategy include: Avidin,^{7,8} Streptavidin,⁹ Carbonic anhydrase,¹⁰ Lactococcal Multidrug Resistance Regulator,¹¹ Papain proteases,¹² Serum albumins,¹³ D-Ala-D-Ala dipeptides,¹⁴ Ribonuclease S,¹⁵ nickel-binding protein,¹⁶ monoclonal antibodies,¹⁷ Heme oxygenase,¹⁸ Bovine β -lactoglobulin,¹⁹ and Neocarzinostatin.²⁰

A key factor for the reliable localization of the cofactor in the protein scaffold is a high affinity constant. The biotin-streptavidin interaction is one of the strongest found in nature ($K_d \approx 10^{14}$ M) and therefore represents a natural choice for ArM assembly. Additionally, this cofactor-protein complex demonstrates exceptional resilience against a broad range of extreme conditions such as pH, temperature, organic solvents and denaturing agents.^{21,22} Several groups have capitalized on this exquisite tool for the assembly of ArMs. These ArMs catalyzed various non-natural reactions including hydrogenation, cross-coupling, C-H activation or metathesis, etc.^{7,8,23-27} Their performances can be optimized chemically and genetically by introducing point mutations but also with directed evolution. However, some considerable challenges for the directed evolution of such ArMs include: developing a catalytic moiety that is compatible with cellular metabolites and achieving high activity at low ArM

concentration. Circumventing these limitations is of paramount importance for the development of more selective, efficient, and practical biocatalysts.

In addition to the design new types of ArMs, the following chapters aim at providing insights into the strategies that can be used to fulfill the above-mentioned requirements for the directed evolution of such hybrid catalysts.

1.2 C–H Functionalization

C–H activation, and more generally C–H functionalization, refers to chemical reactions where an inert C–H bond is cleaved and the hydrogen atom replaced with another element. Over the last decades, this strategy has attracted increasing attention due to its high step- and atom economy.²⁸ It gives access to shorter synthetic routes by preventing the interconversion of functional groups as well as innovative bond-forming strategies.²⁹ Saturated hydrocarbons, still mainly used as fuels, could hence become an abundant and inexpensive source of raw materials for the chemical industry. Indeed, a considerable obstacle towards their valorization is that they are only composed of inert C–H and C–C bonds, which are very difficult to functionalize, especially in a selective fashion.³⁰ The development of such methodologies is therefore highly desirable from an economic and environmental perspective.³¹

Similarly to the more established cross-coupling reactions, C–H activation methodologies still vastly rely on the use of precious metals such as palladium, ruthenium, rhodium or iridium.^{32–36} In addition to being cost-intensive, these metals are also toxic and environmentally hazardous from their extraction to their disposal.^{31,37} In comparison, 3d transition metals represent a particularly attractive alternative. Their natural abundance translates to significantly increased cost-efficiency as well as a reduced toxicity.³⁸ Consequently, an increasing number of new C–H functionalization methodologies based on earth-abundant transition metals have been reported.³⁹

Building on the current knowledge of 3d transition metal catalysis for C–H functionalization, the following chapters aim at demonstrating the great potential of ArMs based on earth abundant transition metals for the development of more efficient, selective and sustainable catalysts.

1.3 References

- (1) Hartwig, J. F.; Ward, T. R. New “Cats” in the House: Chemistry Meets Biology in Artificial Metalloenzymes and Repurposed Metalloenzymes. *Acc. Chem. Res.* **2019**, *52* (5), 1145–1145. <https://doi.org/10.1021/acs.accounts.9b00154>.
- (2) Burk, M. J.; Van Dien, S. Biotechnology for Chemical Production: Challenges and Opportunities. *Trends Biotechnol.* **2016**, *34* (3), 187–190. <https://doi.org/10.1016/j.tibtech.2015.10.007>.
- (3) Jeschek, M.; Panke, S.; Ward, T. R. Artificial Metalloenzymes on the Verge of New-to-Nature Metabolism. *Trends Biotechnol.* **2018**, *36* (1), 60–72. <https://doi.org/10.1016/j.tibtech.2017.10.003>.
- (4) Davis, H. J.; Ward, T. R. Artificial Metalloenzymes: Challenges and Opportunities. *ACS Cent. Sci.* **2019**, *5* (7), 1120–1136. <https://doi.org/10.1021/acscentsci.9b00397>.
- (5) Wittwer, M.; Markel, U.; Schiffels, J.; Okuda, J.; Sauer, D. F.; Schwaneberg, U. Engineering and Emerging Applications of Artificial Metalloenzymes with Whole Cells. *Nat. Catal.* **2021**, *4* (10), 814–827. <https://doi.org/10.1038/s41929-021-00673-3>.
- (6) Schwizer, F.; Okamoto, Y.; Heinisch, T.; Gu, Y.; Pellizzoni, M. M.; Lebrun, V.; Reuter, R.; Köhler, V.; Lewis, J. C.; Ward, T. R. Artificial Metalloenzymes: Reaction Scope and Optimization Strategies. *Chem. Rev.* **2018**, *118* (1), 142–231. <https://doi.org/10.1021/acs.chemrev.7b00014>.
- (7) Wilson, M. E.; Whitesides, G. M. Conversion of a Protein to a Homogeneous Asymmetric Hydrogenation Catalyst by Site-Specific Modification with a Diphosphinerhodium(I) Moiety. *J. Am. Chem. Soc.* **1978**, *100* (1), 306–307. <https://doi.org/10.1021/ja00469a064>.
- (8) Reetz, M. T. Directed Evolution of Artificial Metalloenzymes: A Universal Means to Tune the Selectivity of Transition Metal Catalysts? *Acc. Chem. Res.* **2019**, *52* (2), 336–344. <https://doi.org/10.1021/acs.accounts.8b00582>.
- (9) Liang, A. D.; Serrano-Plana, J.; Peterson, R. L.; Ward, T. R. Artificial Metalloenzymes Based on the Biotin–Streptavidin Technology: Enzymatic Cascades and Directed Evolution. *Acc. Chem. Res.* **2019**, *52* (3), 585–595. <https://doi.org/10.1021/acs.accounts.8b00618>.
- (10) Monnard, F. W.; Nogueira, E. S.; Heinisch, T.; Schirmer, T.; Ward, T. R. Human Carbonic Anhydrase II as Host Protein for the Creation of Artificial Metalloenzymes: The Asymmetric Transfer Hydrogenation of Imines. *Chem. Sci.* **2013**, *4* (8), 3269–3274. <https://doi.org/10.1039/C3SC51065D>.
- (11) Roelfes, G. LmrR: A Privileged Scaffold for Artificial Metalloenzymes. *Acc. Chem. Res.* **2019**, *52* (3), 545–556. <https://doi.org/10.1021/acs.accounts.9b00004>.

- (12) Reiner, T.; Jantke, D.; Marziale, A. N.; Raba, A.; Eppinger, J. Metal-Conjugated Affinity Labels: A New Concept to Create Enantioselective Artificial Metalloenzymes. *ChemistryOpen* **2013**, *2* (2), 50–54. <https://doi.org/10.1002/open.201200044>.
- (13) Mahammed, A.; Gross, Z. Albumin-Conjugated Corrole Metal Complexes: Extremely Simple Yet Very Efficient Biomimetic Oxidation Systems. *J. Am. Chem. Soc.* **2005**, *127* (9), 2883–2887. <https://doi.org/10.1021/ja045372c>.
- (14) Facchetti, G.; Bucci, R.; Fusè, M.; Erba, E.; Gandolfi, R.; Pellegrino, S.; Rimoldi, I. Alternative Strategy to Obtain Artificial Imine Reductase by Exploiting Vancomycin/D-Ala-D-Ala Interactions with an Iridium Metal Complex. *Inorg. Chem.* **2021**, *60* (5), 2976–2982. <https://doi.org/10.1021/acs.inorgchem.0c02969>.
- (15) Genz, M.; Köhler, V.; Krauss, M.; Singer, D.; Hoffmann, R.; Ward, T. R.; Sträter, N. An Artificial Imine Reductase Based on the Ribonuclease S Scaffold. *ChemCatChem* **2014**, *6* (3), 736–740. <https://doi.org/10.1002/cctc.201300995>.
- (16) Esmieu, C.; Cherrier, M. V.; Amara, P.; Girgenti, E.; Marchi-Delapierre, C.; Odon, F.; Iannello, M.; Jorge-Robin, A.; Cavazza, C.; Ménage, S. An Artificial Oxygenase Built from Scratch: Substrate Binding Site Identified Using a Docking Approach. *Angew. Chem. Int. Ed.* **2013**, *52* (14), 3922–3925. <https://doi.org/10.1002/anie.201209021>.
- (17) Kobayashi, Y.; Murata, K.; Harada, A.; Yamaguchi, H. A Palladium-Catalyst Stabilized in the Chiral Environment of a Monoclonal Antibody in Water. *Chem. Commun.* **2020**, *56* (10), 1605–1607. <https://doi.org/10.1039/C9CC08756G>.
- (18) Bacchi, M.; Veinberg, E.; Field, M. J.; Niklas, J.; Matsui, T.; Tiede, D. M.; Poluektov, O. G.; Ikeda-Saito, M.; Fontecave, M.; Artero, V. Artificial Hydrogenases Based on Cobaloximes and Heme Oxygenase. *ChemPlusChem* **2016**, *81* (10), 1083–1089. <https://doi.org/10.1002/cplu.201600218>.
- (19) Chevalley, A.; Cherrier, M. V.; Fontecilla-Camps, J. C.; Ghasemi, M.; Salmain, M. Artificial Metalloenzymes Derived from Bovine β -Lactoglobulin for the Asymmetric Transfer Hydrogenation of an Aryl Ketone – Synthesis, Characterization and Catalytic Activity. *Dalton Trans.* **2014**, *43* (14), 5482–5489. <https://doi.org/10.1039/C3DT53253D>.
- (20) Ghattas, W.; Cotchico-Alonso, L.; Maréchal, J.-D.; Urvoas, A.; Rousseau, M.; Mahy, J.-P.; Ricoux, R. Artificial Metalloenzymes with the Neocarzinostatin Scaffold: Toward a Biocatalyst for the Diels–Alder Reaction. *ChemBioChem* **2016**, *17* (5), 433–440. <https://doi.org/10.1002/cbic.201500445>.
- (21) González, M.; Argaraña, C. E.; Fidelio, G. D. Extremely High Thermal Stability of Streptavidin and Avidin upon Biotin Binding. *Biomol. Eng.* **1999**, *16* (1–4), 67–72. [https://doi.org/10.1016/S1050-3862\(99\)00041-8](https://doi.org/10.1016/S1050-3862(99)00041-8).
- (22) Määttä, J. A. E.; Eisenberg-Domovich, Y.; Nordlund, H. R.; Hayouka, R.; Kulomaa, M. S.; Livnah, O.; Hytönen, V. P. Chimeric Avidin Shows Stability against Harsh Chemical

- Conditions—Biochemical Analysis and 3D Structure. *Biotechnol. Bioeng.* **2011**, *108* (3), 481–490. <https://doi.org/10.1002/bit.22962>.
- (23) Hyster, T. K.; Knörr, L.; Ward, T. R.; Rovis, T. Biotinylated Rh(III) Complexes in Engineered Streptavidin for Accelerated Asymmetric C–H Activation. *Science* **2012**, *338* (6106), 500–503. <https://doi.org/10.1126/science.1226132>.
- (24) Hassan, I. S.; Ta, A. N.; Danneman, M. W.; Semakul, N.; Burns, M.; Basch, C. H.; Dippon, V. N.; McNaughton, B. R.; Rovis, T. Asymmetric δ -Lactam Synthesis with a Monomeric Streptavidin Artificial Metalloenzyme. *J. Am. Chem. Soc.* **2019**, *141* (12), 4815–4819. <https://doi.org/10.1021/jacs.9b01596>.
- (25) Facchetti, G.; Rimoldi, I. 8-Amino-5,6,7,8-Tetrahydroquinoline in Iridium(III) Biotinylated Cp* Complex as Artificial Imine Reductase. *New J. Chem.* **2018**, *42* (23), 18773–18776. <https://doi.org/10.1039/C8NJ04558E>.
- (26) Lewis, J. C. Beyond the Second Coordination Sphere: Engineering Dirhodium Artificial Metalloenzymes To Enable Protein Control of Transition Metal Catalysis. *Acc. Chem. Res.* **2019**, *52* (3), 576–584. <https://doi.org/10.1021/acs.accounts.8b00625>.
- (27) Lin, C.-C.; Lin, C.-W.; Chan, A. S. C. Catalytic Hydrogenation of Itaconic Acid in a Biotinylated Pyrphos–Rhodium(I) System in a Protein Cavity. *Tetrahedron: Asymmetry* **1999**, *10* (10), 1887–1893. [https://doi.org/10.1016/S0957-4166\(99\)00193-7](https://doi.org/10.1016/S0957-4166(99)00193-7).
- (28) Yi, H.; Zhang, G.; Wang, H.; Huang, Z.; Wang, J.; Singh, A. K.; Lei, A. Recent Advances in Radical C–H Activation/Radical Cross-Coupling. *Chem. Rev.* **2017**, *117* (13), 9016–9085. <https://doi.org/10.1021/acs.chemrev.6b00620>.
- (29) Lam, N. Y. S.; Wu, K.; Yu, J.-Q. Advancing the Logic of Chemical Synthesis: C–H Activation as Strategic and Tactical Disconnections for C–C Bond Construction. *Angew. Chem. Int. Ed.* **2021**, *60* (29), 15767–15790. <https://doi.org/10.1002/anie.202011901>.
- (30) Bergman, R. G. C–H Activation. *Nature* **2007**, *446* (7134), 391–393. <https://doi.org/10.1038/446391a>.
- (31) Dalton, T.; Faber, T.; Glorius, F. C–H Activation: Toward Sustainability and Applications. *ACS Cent. Sci.* **2021**, *7* (2), 245–261. <https://doi.org/10.1021/acscentsci.0c01413>.
- (32) Zheng, C.; You, S.-L. Recent Development of Direct Asymmetric Functionalization of Inert C–H Bonds. *RSC Adv.* **2014**, *4* (12), 6173–6214. <https://doi.org/10.1039/C3RA46996D>.
- (33) He, J.; Wasa, M.; Chan, K. S. L.; Shao, Q.; Yu, J.-Q. Palladium-Catalyzed Transformations of Alkyl C–H Bonds. *Chem. Rev.* **2017**, *117* (13), 8754–8786. <https://doi.org/10.1021/acs.chemrev.6b00622>.
- (34) Newton, C. G.; Wang, S.-G.; Oliveira, C. C.; Cramer, N. Catalytic Enantioselective Transformations Involving C–H Bond Cleavage by Transition-Metal Complexes. *Chem. Rev.* **2017**, *117* (13), 8908–8976. <https://doi.org/10.1021/acs.chemrev.6b00692>.

- (35) Kim, D.-S.; Park, W.-J.; Jun, C.-H. Metal–Organic Cooperative Catalysis in C–H and C–C Bond Activation. *Chem. Rev.* **2017**, *117* (13), 8977–9015. <https://doi.org/10.1021/acs.chemrev.6b00554>.
- (36) Arockiam, P. B.; Bruneau, C.; Dixneuf, P. H. Ruthenium(II)-Catalyzed C–H Bond Activation and Functionalization. *Chem. Rev.* **2012**, *112* (11), 5879–5918. <https://doi.org/10.1021/cr300153j>.
- (37) Ysart, G.; Miller, P.; Crews, H.; Robb, P.; Baxter, M.; L'Argy, C. D.; Lofthouse, S.; Sargent, C.; Harrison, N. Dietary Exposure Estimates of 30 Elements from the UK Total Diet Study. *Food Addit. Contam.* **1999**, *16* (9), 391–403. <https://doi.org/10.1080/026520399283876>.
- (38) Halka, H.; Nordstrom, B. *Transition Metals*, 2nd ed.; Facts on File, 2019.
- (39) Gandeepan, P.; Müller, T.; Zell, D.; Cera, G.; Warratz, S.; Ackermann, L. 3d Transition Metals for C–H Activation. *Chem. Rev.* **2019**, *119* (4), 2192–2452. <https://doi.org/10.1021/acs.chemrev.8b00507>.

2. Summary of individual Chapters

2.1 Chapter 3. Design of Biotinylated Tp ligands for Artificial Metalloenzymes and Initial Reactivity Studies

Several approaches for the synthesis of biotinylated Tp complexes were investigated. A new strategy based on pyrazole metathesis of a sterically-bulky Tp ligand was developed and gave a straightforward access to copper heteroscorpionates. The subsequent installation of a biotin derivative enabled the incorporation of the corresponding Tp's in streptavidin. The resulting artificial metalloenzyme was tested for intramolecular carbene insertion reactions into C–H bonds and displayed promising activity.

Building on the novel pyrazole metathesis procedure, the first Tp ligand chiral at the boron was synthesized as well. Chiral resolution of the compound enabled its characterization by X-ray crystallography.

2.2 Chapter 4. An artificial metalloenzyme based on a copper heteroscorpionate enables sp^3 C–H functionalization *via* intramolecular carbene insertion

An ArM based on a copper(I) heteroscorpionate and the biotin-streptavidin technology was engineered and tested for intramolecular carbene insertion reactions into C–H bonds. Following single mutant screening at position K121, the double saturation mutagenesis comprising 400 double mutants at position K121 and S112 was tested. Analysis of the data allowed to highlight correlations between the performance of the mutants and the nature of the amino acid residues. Directed evolution at position L124 enabled us to identify triple mutants displaying improved regio- and enantioselectivity. The best mutants for the model substrate were then evaluated with various substrates.

2.3 Chapter 5. Enantioselective Hydroxylation of Benzylic C(sp^3)–H Bonds by an Artificial Iron Hydroxylase Based on the Biotin–Streptavidin Technology

An ArM based on an iron(III) tetraamido macrocyclic ligand (Fe(TAML)) catalyzing C–H bond hydroxylation was engineered. The initial reactivity studies were performed with ethyl benzene as substrate and hydrogen peroxide as oxidant. A selection of single and double mutants at position K121 and S112 were tested. X-ray crystal structures could be obtained from the best

performing mutants. The substrate scope highlighted that up to >99 % enantiomeric excess could be obtained in the case of tetralin. Kinetic studies on this substrate revealed an underlying kinetic resolution effect. Finally, an enzymatic cascade starting from glucose oxidase highlighted that molecular oxygen could be used as terminal oxidant.

3. Design of Biotinylated Tp ligands for Artificial Metalloenzymes and Initial Reactivity Studies

3.1 Contributions to this Work

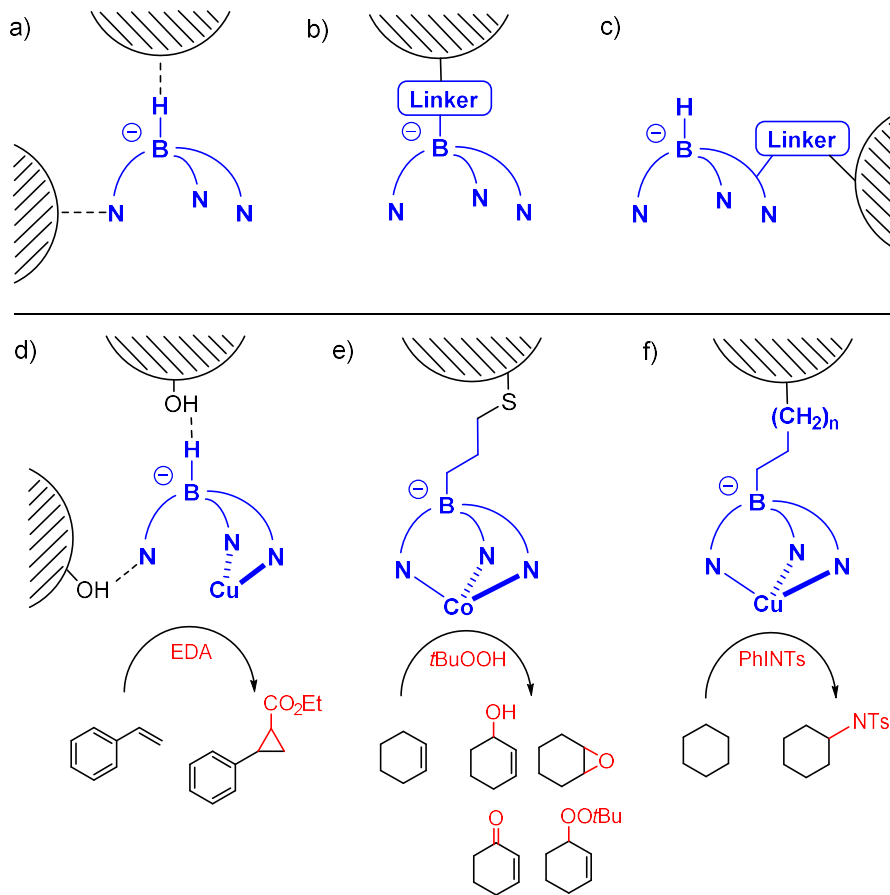
TRW supervised the project. CR carried out the entire project.

3.2 Introduction

Since their introduction in the 1960's by S. Trofimenko, poly(pyrazolyl)borate ligands, and more importantly Tp (tris(pyrazolyl)borate, sometimes referred as homoscorpionate) ligands have undoubtedly been among the most studied chelating N-ligands in coordination chemistry.¹⁻³ Their structural properties were often compared to those of Cp ligands. Indeed, both ligands donate six electrons to the metal center, carry a negative charge and occupy three facial coordination sites. However, despite of those structural similarities, the difference in electronic and steric properties discouraged any further attempts to relate the two ligands.⁴

An attractive feature of the Tp ligand resides in the high modularity of its pyrazole rings. Tp ligands prepared from pyrazole and dimethylpyrazole (Tp and Tp* respectively) are often considered as the first generation of homoscorpionate ligands. The introduction of various functional groups on the pyrazole rings in the so-called second generation Tp's allowed a more precise tuning of the steric and electron-donating properties of the Tp.^{5,6} This enabled the access to hundreds of new metal complexes.^{2,3} Initially limited, an increasing number of catalytic reactions mediated by transition metal Tp complexes were being reported. Relevant examples include: olefin polymerization,⁷ hydrogenation,⁸ arene trifluoromethylation,⁹ carbene insertion into X-H bonds,¹⁰⁻¹³ carbene insertion into C-Cl bonds,^{14,15} C-H bond oxidation,^{16,17} nitrene insertion in X-H bonds,¹⁸⁻²⁰ alkene functionalization,^{14,21-23} and atom transfer radical reactions.²⁴⁻²⁶ Considerable advances in the field of bioinorganic chemistry and enzyme mimics could also be made following the pioneering work of J.S. Lippard on the synthetic model of Hemerythrin.²⁷⁻³³

Scheme 1. Anchoring strategies of Tp complexes: a) non-covalent; b) covalent by installation of a fourth substituent; c) covalent *via* one pyrazole substituent. Reported examples of anchored and catalytically active Tp complexes: d) cyclopropanation catalyzed by a TpCu immobilized on silica gel; e) oxidation catalyzed by a TpCo immobilized on functionalized mesoporous silica; f) C-H amination catalyzed by a TpCu immobilized on polynorbornenes.



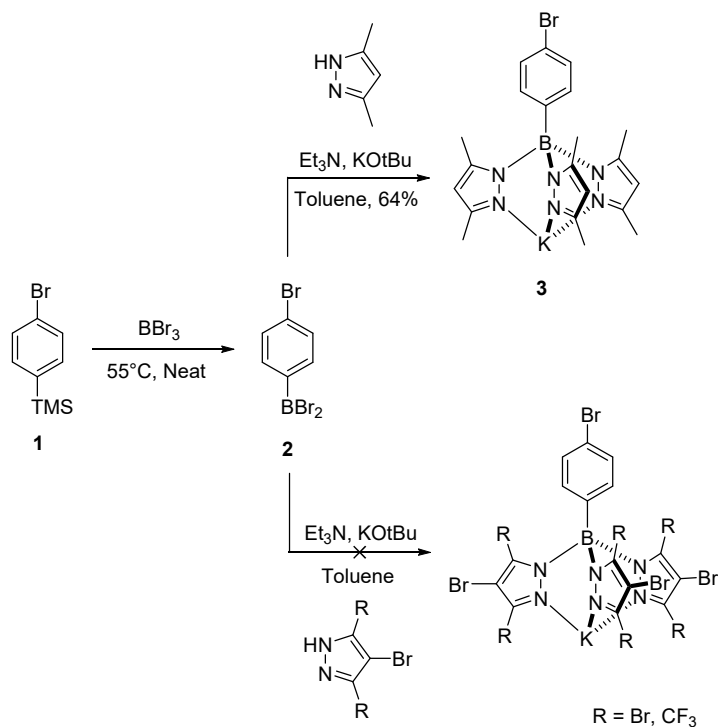
However, catalytically active Tp complexes are mostly limited to homogeneous systems. A likely reason could be the considerable synthetic challenge to functionalize the Tp ligand. Reported strategies include non-covalent interactions and covalent anchoring *via* the installation of a fourth substituent instead of the hydride or less commonly, *via* modification of one of the pyrazole arms, Scheme 1a-c. Among all the reported examples of anchored Tp complexes, only few displayed catalytic activity, Scheme 1d-e.³⁴⁻³⁶ To the best of our knowledge, there are no reports of bioconjugated Tp complexes that could also perform catalysis. This chapter summarizes our initial efforts in developing a straightforward strategy for the synthesis of functionalized Tp complexes that could be used for the engineering of artificial metalloenzymes.

3.3 Results and Discussion

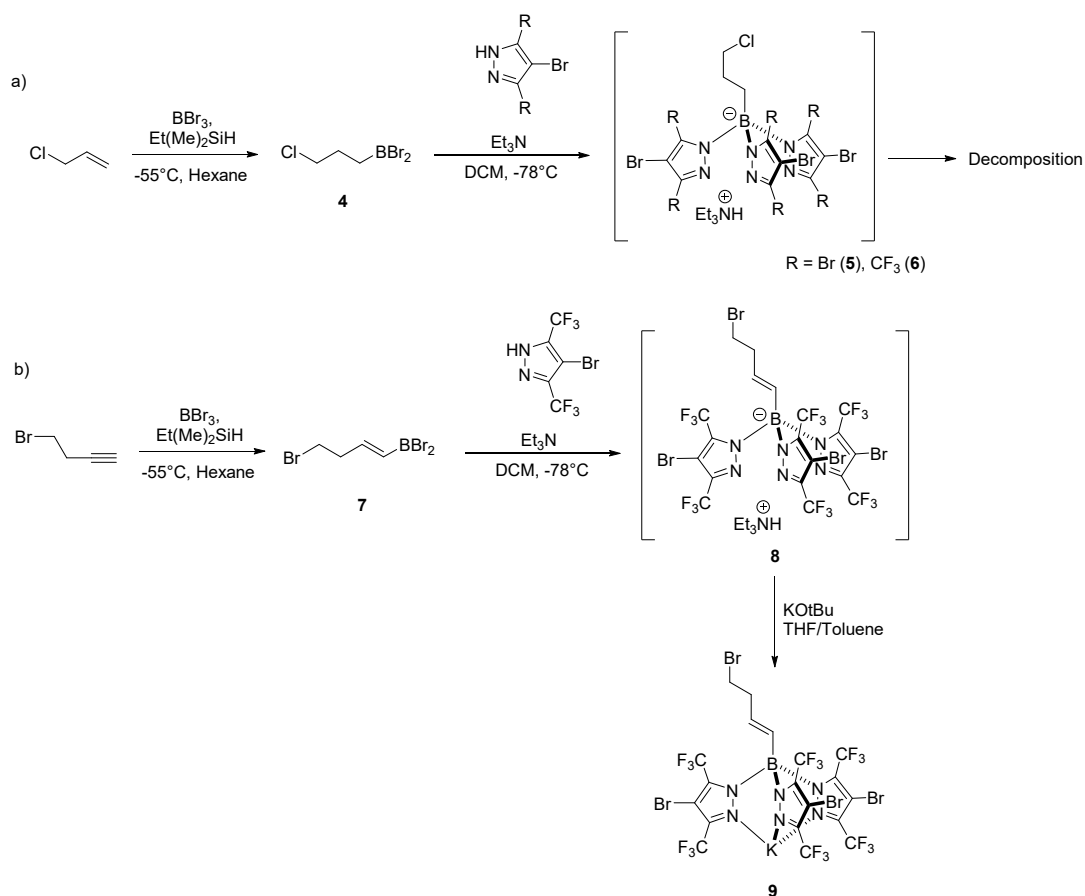
Our initial attempts to synthesize a Tp-based cofactor were inspired by a report from Zagerman and coworkers.^{37,38} The strategy relied on the installation of a bromophenyl substituent on the boron center by reaction of the TMS-bearing precursor **1** with boron tribromide. The resulting dibromoborane **2** would then be derivatised to the corresponding Tp ligand **3** in presence of dimethylpyrazole, Scheme 2. After reproducing the literature report, subsequent attempts to adapt the procedure to more electron-deficient pyrazole remained unsuccessful.

The use of a shorter and less sterically-demanding substituent on the boron center was also considered. A procedure based on a Matteson hydroboration of allyl chloride was developed to produce aliphatic dibromoboranes bearing a terminal halogen atom, Scheme 3a. Such substituent could have been used to install a high affinity tag such as biotinamine *via* S_N2 reaction or in a covalent anchoring to HaloTag if a longer hydrocarbon chain was used.³⁹ When the dibromoborane **5** was reacted with an electron-deficient pyrazole, the corresponding Tp **5** and **6** could be shortly observed by ESI-MS in the negative mode before slow degradation. Further attempts suggested that the stability of the substituted Tp was improved when the boron center was bound to a *sp*² hybridized carbon such as for the dibromoborane **7**, Scheme 3b. The corresponding potassium salt **9** could be made by reaction of the triethylammonium

Scheme 2. Initial attempts to design an electron-deficient Tp bearing a bromophenyl substituent based on the report of Zagerman and coworkers.



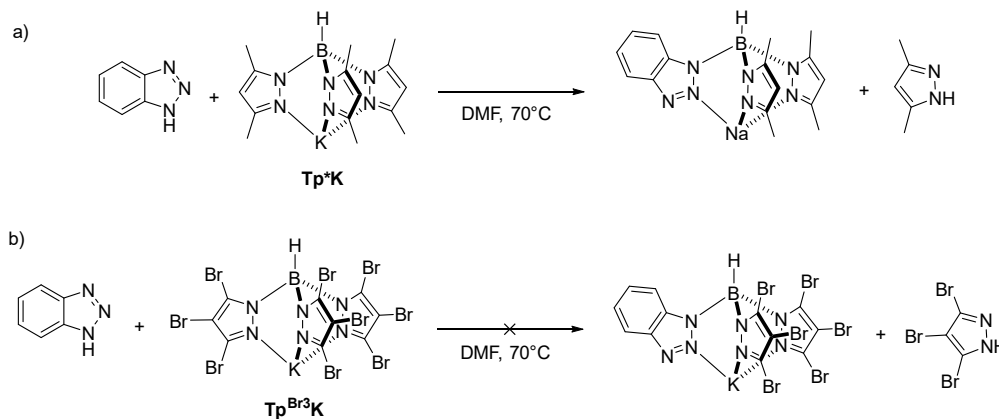
Scheme 3. Further strategies investigated for the synthesis of tetra-substituted and electron-deficient Tp complexes: a) Installation of a fourth substituent *via* a sp^3 -hybridized carbon; b) Installation of a fourth substituent *via* a sp^2 -hybridized carbon.



salt **8** with potassium *tert*-butoxide. However, although the Tp **9** displayed improved stability in solution, attempts to purify and isolate it remained unsuccessful. The crude product appeared as an oil that could not be crystallized or distilled and would readily decompose on silica. Critical evaluation of the present strategy led us to reconsider our synthetic approach towards a Tp cofactor.

While electron-deficient Tp's bearing a fourth substituent showed limited stability in our hands, more conventional analogues bearing a hydride moiety were significantly more robust. Desrochers and coworkers reported that one of the dimethylpyrazole arms of **Tp*K** could be substituted by benzotriazole, Scheme 4a.⁴⁰ However, no reaction was observed when the same procedure was attempted with **Tp^{Br3}K**, Scheme 4b.

Scheme 4. Pyrazole metathesis experiments: a) Displacement of a pyrazole arm of **Tp**K*** by benzotriazole (reported by Desroschers and coworkers); b) Same experiment carried out with **Tp^{Br3}*K***.

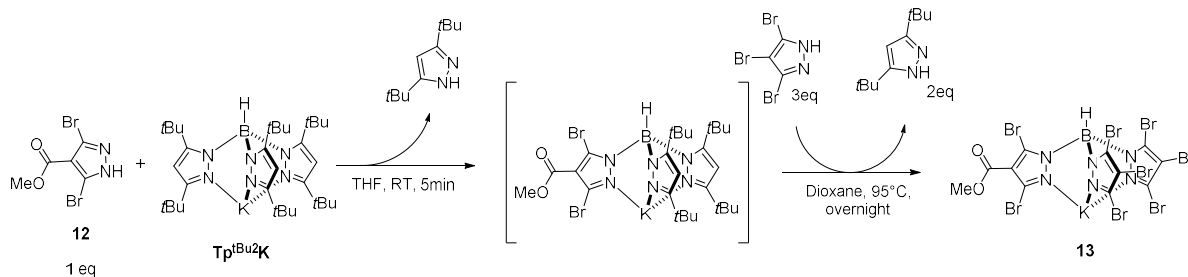


Further attempts revealed that perbromopyrazole had a similar ability to substitute one of the dimethylpyrazole arms of **Tp**K***, Scheme 5. The first substitution could be performed at 50 °C in DMF within a few hours, affording the monosubstituted Tp **10**. Although challenging, a second substitution was possible at elevated temperatures, affording the disubstituted Tp **11**. However, to our disappointment, the third dimethylpyrazole arm could not be exchanged.

Experimental evidence suggested that the stability of the B–N bond in Tp derivatives resulted from a combination of steric and electronic effects. Hence, we surmised that electron-rich and bulky substituents could facilitate the pyrazole metathesis. To our delight, the pronounced steric bulk of the **Tp^{(tBu)2}*K*** allowed a facile sequential substitution of the three *tert*-butylpyrazole Scheme 5. One pot pyrazole metathesis with excess of tribromopyrazole and **Tp**K***. The two first displacements leading to **10** ($m/z = 504.85$) and **11** ($m/z = 714.40$) were confirmed by ESI-MS in the negative mode.

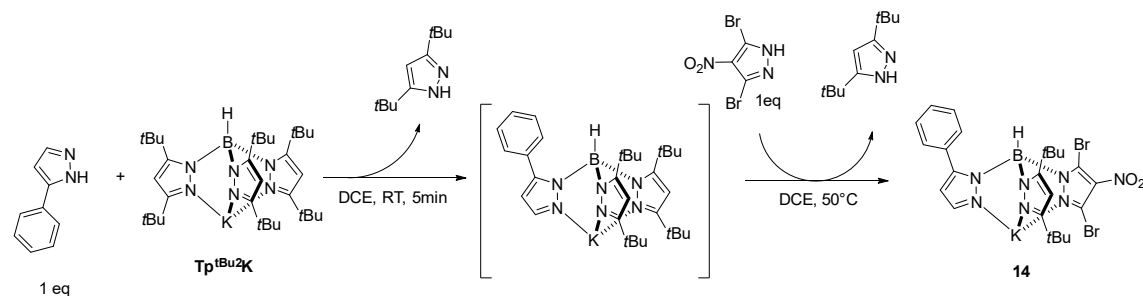


Scheme 6. First metathesis of the three pyrazole arms of **Tp^{tBu}2K**. The first displacement was performed at room temperature while substitution of the two remaining *tert*-butylpyrazole required higher temperatures.



arms by more electron-deficient pyrazoles, Scheme 6. While the first substitution occurred at 50 °C in the case of **Tp^{*}K**, it happened instantaneously at room temperature with **Tp^(tBu)2K** and the ester-bearing dirbomopyrazole **12**. The two remaining *tert*-butylpyrazole arms could be displaced with an excess of perbromopyrazole at 95 °C overnight. Although in low yield, the resulting heteroleptic Tp **13** could be purified by chromatography column on silica gel and showed promising stability. Based on this procedure, a Tp chiral at boron was synthesized, Scheme 7. Displacement of the first *tert*-butylpyrazole arm by 3-Phenyl-1H-pyrazol followed by the displacement of a second *tert*-butylpyrazole by 3,5-Dibromo-4-nitro-1H-pyrazole upon heating at 50 °C provided the racemic at boron Tp **14**.

Scheme 7. Synthesis of a heteroleptic Tp ligand, chiral-at-boron. The compound was synthesized as a racemate and resolved by preparative chiral HPLC prior to crystallization from a diethyl ether solution.



Following chiral resolution of the racemic mixture by preparative HPLC, the enantiopure Tp **14** could be crystallized from a diethyl ether solution as a protonated salt and afforded X-ray quality crystals, Figure 1. In contrast to what is usually observed with Tp metal complexes, the phenyl substituent points away from the metal coordination site. This could potentially be a consequence of the small size of the proton, allowing more flexibility to the Tp skeleton.

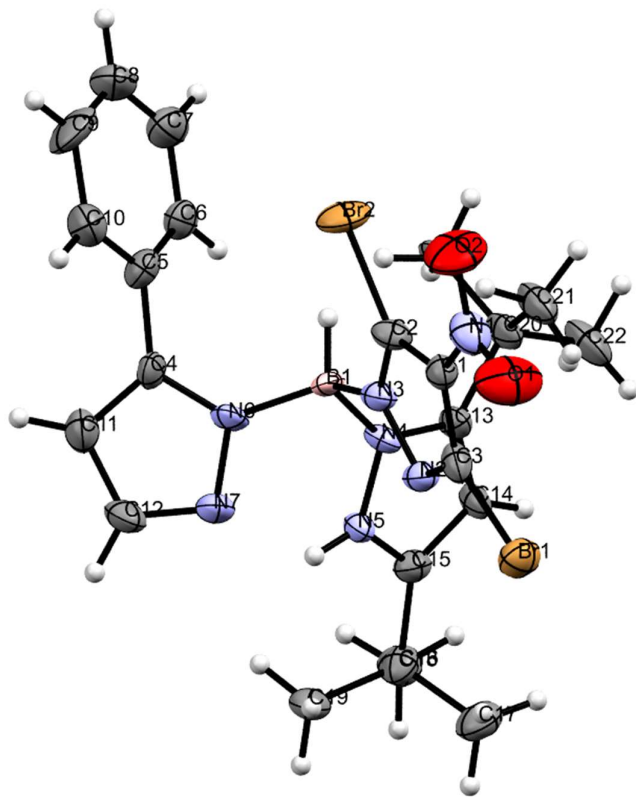


Figure 1. Molecular structure of the enantiopure Tp **14** chiral at the boron synthesized *via* pyrazole metathesis.

Trial and error led us to perform the first pyrazole metathesis with the pre-activated ester-bearing dibromopyrazole **15** to achieve the monosubstituted Tp **16**, Scheme 8. Following the displacement of the two remaining *tert*-butylpyrazole groups to afford the intermediate **17**,

Scheme 8. Synthesis of **Biot**^{C⁵}–**Tp**^{Br³}**Cu** via pyrazole metathesis.

transmellation with cuprous chloride in MeCN yielded the copper(I) complex **18**. Upon coupling with **Biot**^{C5}**NH**₃**Cl**, the cofactor **Biot**^{C5}-**Tp**^{Br3}**Cu** was obtained.

Binding of **Biot**^{C5}-**Tp**^{Br3}**Cu** was assessed *via* a competitive binding assay monitored by CD (circular dichroism) spectroscopy, Figure 2. Sav was loaded with a large excess of HABA ($\lambda_{\text{max}} = 506 \text{ nm}$, $K_d = 3,16 \cdot 10^{-3} \text{ M}$) and aliquots of cofactor were added.⁴¹ A control experiment with biotin ($K_d \approx 10^{-14} \text{ M}$)⁴² was performed and displayed full displacement of HABA after addition of nearly four equivalents relative to the tetramer. A similar curve was obtained when the titration was performed with **Biot**^{C5}-**Tp**^{Br3}**Cu**.

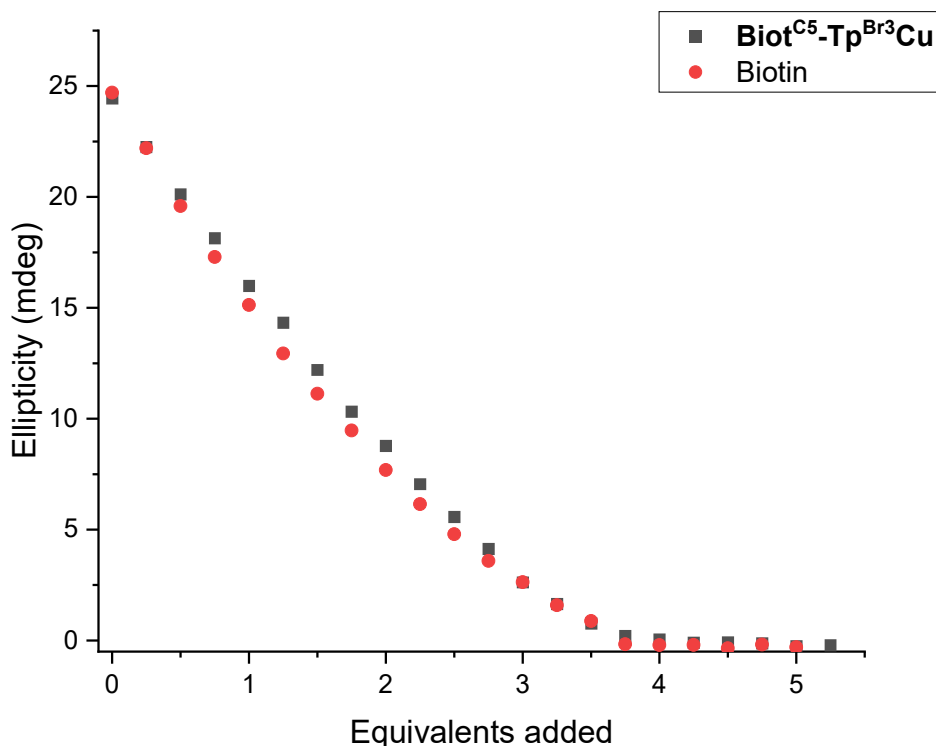
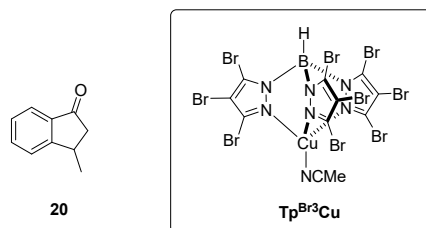


Figure 2. HABA titration of Sav WT with Biotin and **Biot**^{C5}-**Tp**^{Br3}**Cu** monitored by CD spectroscopy.

Intermolecular carbene insertion in aqueous medium being particularly challenging, we selected the intramolecular substrate **19** for our initial studies. In presence of 5 mol% **Tp**^{Br3}**Cu**, carbene formation and subsequent insertion into the benzylic C–H bond could be performed in DCM to afford the cyclopentenone **20** in quantitative yield, Scheme 9.

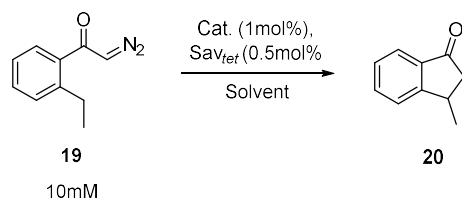
Our initial catalytic experiments aimed at establishing the compatibility of the reaction with water and the ArM, Table 1. While **Tp**^{Br3}**Cu** delivered almost 16 TON in DCM, entry 1, performing the reaction in a 9 : 1 H₂O/MeCN mixture considerably decreased the TON to about

Scheme 9. Intramolecular carbene insertion reaction for initial development of a TpCu-based artificial metalloenzyme.



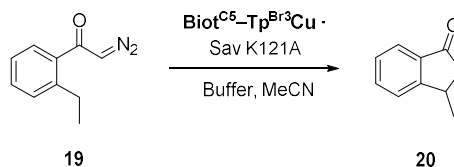
6 without completely deactivating the catalyst, entry 3. Surprisingly, the addition of Sav in did not impede the reaction and even a slight increase in activity was observed, entry 4. To our delight, the cofactor **Biot^{C5}-Tp^{Br3}Cu**, although active without being incorporated within Sav (entry 5), displayed up to 15 TON once embedded in Sav WT, entry 6. However, introduction of different amino acids at common mutation sites did not significantly influence the reaction, entry 7 to 13. It is also worth mentioning that, although a chiral center is formed during the reaction, no enantioselectivity was observed.

Table 1. Initial screening experiments with Tp^{Br3}Cu and **Biot^{C5}-Tp^{Br3}Cu** in presence or absence of Sav.



Entry	Catalyst	Sav	Solvent	TON
1	CuTpBr ₃	-	DCM	15,7
2	-	-	H ₂ O/MeCN (9:1)	2,0
3	CuTpBr ₃	-	H ₂ O/MeCN (9:1)	5,8
4	CuTpBr ₃	WT	H ₂ O/MeCN (9:1)	8,2
5	Biot ^{C5} -Tp ^{Br3} Cu	-	H ₂ O/MeCN (9:1)	9,2
6	Biot ^{C5} -Tp ^{Br3} Cu	WT	H ₂ O/MeCN (9:1)	14,9
7	Biot ^{C5} -Tp ^{Br3} Cu	K121A	H ₂ O/MeCN (9:1)	16,6
8	Biot ^{C5} -Tp ^{Br3} Cu	K121D	H ₂ O/MeCN (9:1)	16,2
9	Biot ^{C5} -Tp ^{Br3} Cu	K121R	H ₂ O/MeCN (9:1)	14,4
10	Biot ^{C5} -Tp ^{Br3} Cu	L124H	H ₂ O/MeCN (9:1)	13,9
11	Biot ^{C5} -Tp ^{Br3} Cu	S112A	H ₂ O/MeCN (9:1)	13,1
12	Biot ^{C5} -Tp ^{Br3} Cu	S112E	H ₂ O/MeCN (9:1)	15,9
13	Biot ^{C5} -Tp ^{Br3} Cu	S112R	H ₂ O/MeCN (9:1)	11,5

The development of a high-throughput screening strategy often relies on the use of low catalyst loading, typically <10 μM. With this goal in mind, we set out to optimize the reaction conditions using DOE (design of experiment). A central composite design was selected with four continuous variables: substrate concentration (1 to 10 mM), ArM concentration (1 to 50 μM),

Table 2. DOE screening experiment of **Biot^{C5}-TazCu** · Sav K121A.

Entry	[Subs] (mM)	[ArM] (μM)	MeCN (%vol)	pH	Yield (%)	TON
1	1,0	1,0	0%	6,40	9,9	99
2	1,0	1,0	0%	8,50	7,1	71
3	1,0	50,0	0%	6,40	16,3	3
4	10,0	1,0	0%	6,40	14,9	1487
5	1,0	1,0	30%	6,40	0,0	0
6	1,0	50,0	0%	8,50	27,5	5
7	10,0	1,0	0%	8,50	16,5	1650
8	1,0	1,0	30%	8,50	0,0	0
9	10,0	50,0	0%	6,40	15,4	30
10	1,0	50,0	30%	6,40	17,2	3
11	10,0	1,0	30%	6,40	2,7	271
12	10,0	50,0	0%	8,50	17,2	34
13	1,0	50,0	30%	8,50	3,1	0
14	10,0	1,0	30%	8,50	3,1	311
15	10,0	50,0	30%	6,40	14,7	29
16	10,0	50,0	30%	8,50	9,2	18
17	5,5	25,5	15%	7,45	16,0	34
18	5,5	25,5	15%	7,45	16,0	34
19	5,5	25,5	0%	7,45	15,4	33
20	5,5	25,5	30%	7,45	5,4	11
21	1,0	25,5	15%	7,45	12,6	4
22	10,0	25,5	15%	7,45	17,1	67
23	5,5	1,0	15%	7,45	2,1	114
24	5,5	50,0	15%	7,45	17,1	18
25	5,5	25,5	15%	6,40	17,4	37
26	5,5	25,5	15%	8,50	15,6	33

Abbreviations : [Subs] = substrate concentration, [ArM] = catalytic sites concentration

co-solvent (0 to 30 %) and pH (6.4 to 8.5), Table 2. The screening was designed and analyzed with a trial version of the statistical software JMP. Although the software could not extract a fully satisfying model from the obtained data, some trends could be clearly observed: A higher substrate concentration as well as a low ArM concentration provided higher TON. Surprisingly, despite of the insolubility of the substrate, a lower MeCN concentration was beneficial for the TON as well as the yield. Unlike the other variables, the pH seemed to have a rather limited impact on the reaction outcome. Hence, TON of up 1650 and 16.5 % yield could be achieved with 10 mM substrate, 1 μM ArM, 0 % MeCN and pH = 8.5.

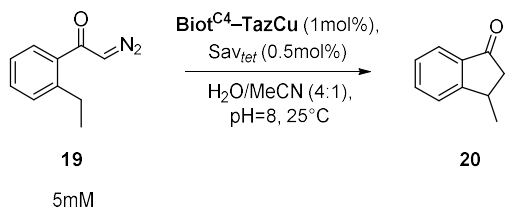
Although the DOE optimization demonstrated a high potential for the improvement of the ArM activity, the introduction of mutations at various sites of Sav induced an insufficient level of response for efficient genetic optimization. Critical analysis of the well-studied and structurally comparable Tp^{Br3}TI revealed a considerable steric shielding of the metal center by the ligand. Cone and wedge angles of 234 ° and 60 ° respectively,² only providing limited opportunities to

the second coordination sphere to exert an influence on the active site following substrate binding. Additionally, the hydrophobicity of the ligand substituents offer limited interactions to the protein to precisely locate **Biot^{C5}-Tp^{Br3}Cu**.

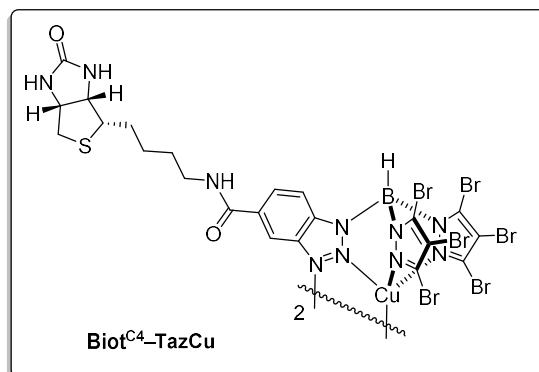
Building on past experimental evidence and the above analysis, we surmised that a more polar and sterically less-crowded cofactor may increase the chances of regio- and stereoselective catalysis. Thus, **Biot^{C4}-TazCu** was synthesized (see Chapter 4 for synthetic details).

To our delight, preliminary screening of various mutants at position K121 and S112 with 1 mol% of **Biot^{C4}-TazCu** revealed a critical influence of the amino acid at position K121 on catalysis, Table 3. While no activity was initially observed with WT Sav, entry 1, mutating the native lysine residue to an alanine allowed the reaction to proceed, entry 2. Introduction of other amino acids at position K121 and S112 revealed the following trends: Positively charged residues (Lys, His and Arg) systematically deactivated the cofactor, entry 1, 11 and 12. Hence, the tested *single* mutants at position S112 remained inactive, entry 13-15. On the other hand, apolar (Ile) and aromatic residues (Phe, Trp) displayed the highest levels of activity, entry 4, 7 and 11. Lower activities were observed with methionine and anionic (Asp and Glu) residues, entry 5, 9 and 10. Unfortunately, although mutations at position K121 were critical for the reaction, racemic mixtures were still systematically obtained.

Table 3. Purified Sav single mutant screening with **Biot^{C4}-TazCu**.



Entry	Sav	TON
1	WT	NR
3	K121A	5,0
4	K121I	7,1
5	K121M	3,5
6	K121F	9,9
7	K121W	7,9
8	K121Y	5,2
9	K121D	4,4
10	K121E	3,8
11	K121H	NR
12	K121R	NR
13	S112E	NR
14	S112H	NR
15	S112Y	NR

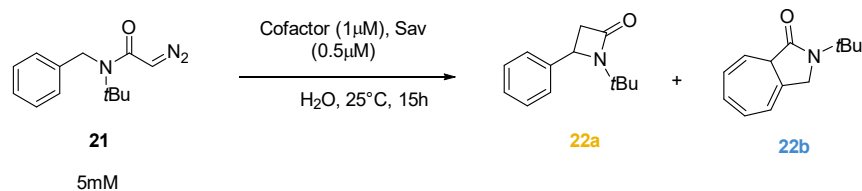


After engineering the cofactor and testing several Sav variants, we focused our attention on the substrate. For the intramolecular C-H insertion of the diazoketone **19**, the configuration of

the resulting 3-methyl-indanone **10** is dictated by the orientation of the methyl group in the transition state. However, dictating the exact conformation of such small and hydrophobic group would require an extremely well-defined second coordination sphere. We surmised that substituting the methyl group by a phenyl group may increase the steric bulk and potentially improve the rigidity of the substrate inside the protein vestibule. The diazoacetamide **21** offered such feature and additionally had the advantage of decreasing the diazo-coupling side reaction.⁴³

To our delight, **Biot^{C4}-TazCu** · Sav K121F catalyzed the enantioselective C–H insertion into the benzylic position to afford the β -lactam **22a** in 425 TON and 62 : 38 e.r, Table 4, entry 2. Surprisingly, the Büchner ring expansion product **22b** was also detected with this substrate and constituted more than 50 % of TTON (529 TON). The K121I variant displayed similar enantiomeric ratio (64 : 36) and activity (693 TON) for the formation of the β -lactam **22a**, entry 3. However, the substitution of the phenylalanine to an isoleucine doubled the amount of Büchner product **22b** (1065 TON) versus K121I. No enantioselective formation of the Büchner product **22b** was detected. Large scale synthesis and purification revealed that the compound would spontaneously decompose overtime. The free **Biot^{C4}-TazCu** catalyzed the reaction as well, although without enantioselectivity, entry 1. The reaction was run with **Biot^{C5}-Tp^{Br3}Cu** · Sav K121I as well, entry 4. As we previously hypothesized, the β -lactam **22a** was obtained as a racemate. Interestingly, the cofactor afforded a higher ratio of β -lactam **22a** relative to Büchner product **22b** (1089 TON vs. 505 TON). This could be due to the higher steric shielding of the metal center and disfavor the functionalization of the aromatic ring.

Table 4. First significant levels of enantioselectivity in TpCu-based ArM-catalyzed intramolecular carbene insertion with substrate **21**.



Entry	Cofactor	Sav	TON	e.r.	TON	e.r.	TTON
1	Biot^{C4}-TazCu	-	582	49 : 51	633	51 : 49	1215
2	Biot^{C4}-TazCu	K121F	425	62 : 38	529	49 : 51	954
3	Biot^{C4}-TazCu	K121I	693	64 : 36	1065	53 : 47	1758
4	Biot^{C5}-Tp^{Br3}Cu	K121I	1089	50 : 50	505	49 : 51	1594

3.4 Conclusion

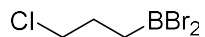
Tp complexes are one of the most studied systems in the field of coordination chemistry, particularly for enzyme modelling. However, a significant gap remained between Tp-based models and real enzymes. This chapter summarized our efforts to develop catalytically-active bioconjugated Tp complexes. A novel pyrazole metathesis procedure for the synthesis of heteroscorpionate ligands was developed and applied to afford biotinylated copper(I) heteroscorpionate cofactors for supramolecular assembly with Sav. The resulting artificial metalloenzymes displayed promising activity for intramolecular C–H insertion of carbene intermediates. We envision that this work could open new perspectives for Tp-based enzyme models and the development of ArM's catalyzing unnatural reactions.

3.5 Supporting information

3.5.1 General methods

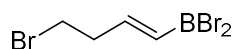
Commercially available chemicals were purchased from the following suppliers and used without further purification: Acros Organics, Alfa Aesar, Combi Blocks Fluorochem, Sigma Aldrich. **KTp^{(tBu)₂}**,⁴⁴ 3,4,5-Tribromopyrazole,⁴⁵ **CuTp^{Br₃}**,⁴⁶ **Biot^{C₄}-NH₃Cl** and **Biot^{C₅}-NH₃Cl**,⁴⁷ were synthesized according to reported procedures. Dry solvents were purchased from Acros Organics and used without further purification. The water used for catalytic experiments was purified with a Milli-Q Advantage system. All catalytic experiments were performed in 2 mL glass vials under air in non-degassed solvents. Flash chromatography was carried out on silica gel. ¹H NMR (500 MHz), ¹³C NMR (125 MHz) and ¹¹B (160 MHz) spectra were recorded on a Bruker Avance Neo spectrometer at room temperature unless stated otherwise. Chemical shifts are reported in ppm (parts per million) relative to TMS (δ = 0.00 ppm for ¹H and ¹³C) or BF₃·OEt₂ (δ = 0.00 ppm for ¹¹B) and multiplicity quoted as follows: s = singlet, d = doublet, t = triplet, q = quartet, bs = broad singlet, dd = doublet of doublet and m = multiplet. Spectra were analysed on MestReNova and calibrated relative to the residual solvent peak. Routine MS analysis were performed on a Shimadzu LCMS 2020 in H₂O (0.1% formic acid) or MeCN (0.1% formic acid) for the positive mode and MeOH for the negative mode. HRMS analysis were performed by the analytical facility of the University of Basel. Catalytic experiments were analysed by SFC (supercritical fluid chromatography) on a Waters Acquity UPC2. CD (circular dichroism) spectra were recorded on a Chirascan from Applied Photophysics at 25 °C using a quartz cell (1 cm path length). Flash chromatography was performed on a Biotage Isolera.

3.5.2 Experimental

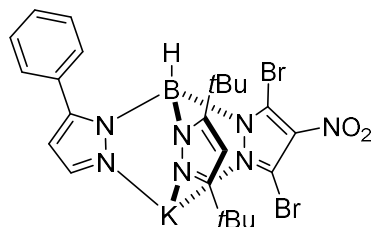


4 Dimethylethylsilane (0.528 mL, 4 mmol) and allyl chloride (0.340 mL, 4 mmol) were dissolved in Hexane (5mL) and added dropwise to boron tribromide (0.378 mL, 4 mmol) in Hexane (1 mL) at -55 °C under nitrogen. The reaction was stirred 1 h at -78 °C and conversion assessed by NMR. The mixture was then carefully distilled down to 20 mbar at room temperature to remove the volatile impurities, giving the dibromoborane **4** as a brownish liquid in quantitative yield.

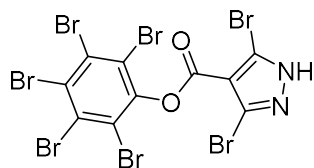
¹H NMR (500 MHz, CDCl₃, 298 K) δ 3.58 (t, 2H), 2.12 (m, 2 H), 1.75 (t, 2 H). ¹¹B NMR (160 MHz, CDCl₃, 298 K) δ 64.16 (br. s, 1B).



7 The dibromoborane **7** was synthesized according to the same procedure as **4** using 4-Bromo-1-butyne instead of allyl chloride. The crude product was used for the next step without further purification.



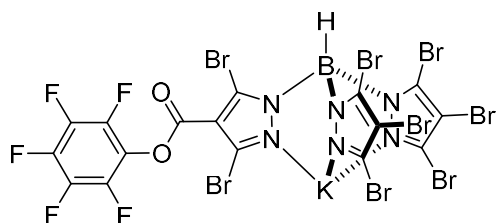
14 **Tp^{tBu}₂K** (177 mg, 0.3 mmol) was added to a solution of 3-Phenyl-1H-pyrazol (43 mg, 0.3 mmol) in DCE (8 mL). The reaction was stirred 5 minutes and 3,5-Dibromo-4-nitro-1H-pyrazole (81 mg, 0.3 mmol) was added. The reaction was heated to 50 °C, and the formation of the product was closely monitored by ESI-MS in negative mode. Once maximum product concentration was reached, the solvent was removed under reduced pressure and purified by column chromatography (DCM/MeOH, 100:0 to 85:15). The racemic mixture was purified by preparative HPLC using a ReproSil Chiral-OM column with Heptane and iPrOH. X-ray quality crystals of the proton salt were obtained by slow evaporation of a diethyl ether solution. X-ray data can be found in section 3.5.4.



15

Pentafluorophenyl trifluoroacetate (0.155 mL, 0.9 mmol) was added dropwise at 0 °C to a solution of 3,5-dibromo-1H-pyrazole-4-carboxylic acid (243 mg, 0.9 mmol) and triethylamine (0.190 mL, 1.35 mmol) in dry DMF (10 mL). The reaction was stirred (1.5 h at 0 °C) and the DMF was removed under reduced pressure. The crude mixture was dissolved in dichloromethane (30 mL) and washed with water once. The organic layer was dried over MgSO₄ and the solvent removed under reduced pressure. The crude product was purified by flash chromatography with DCM/MeOH (100:0 to 97:3) to afford 370 mg of **15** as an off-white solid (94 % yield).

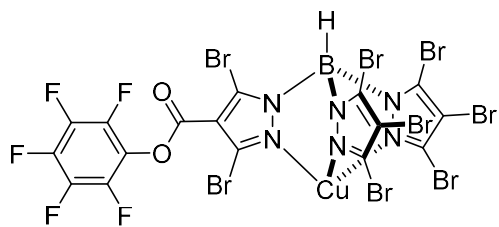
¹⁹F NMR (471 MHz, CDCl₃, 298 K) δ -155.22 (d, 2F), -160.82 (t, 1F), -165.47 (t, 2F). HRMS (ESI negative mode, m/z): calculated for C₁₀Br₂F₅N₂O₂ [M]⁻ 434.8232; found 434.8239.



17

The tris(pyrazolyl)borate **KTp**^{(tBu)₂} (536 mg, 0.91 mmol) was added in one portion to a solution of dibromopyrazole-PFP (**15**) (305 mg, 0.7 mmol) in dry DCM (30 mL) and the reaction was stirred for 15 min at RT. The solvent was removed under reduced pressure at a temperature of 25 °C. The residue was dissolved in dry dioxane (30 mL). Tribromopyrazole (747 mg, 2.45 mmol) was added in one portion and the flask equipped with a reflux condenser. The reaction stirred at 95 °C for 5 h. The solvent was removed under reduced pressure and the crude product purified by flash chromatography with EtOAc/petroleum ether (0:100 to 40:60). A second flash chromatography with DCM/MeCN (98:2) led to 92 mg of PFP-bearing Tp **17** (12 % yield).

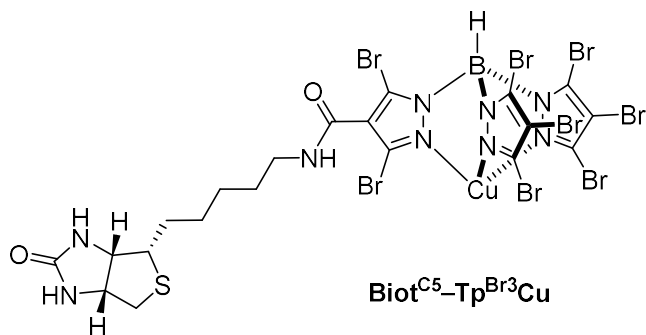
¹⁹F NMR (471 MHz, CD₂Cl₂, 298 K) δ -152.69 (d, 2F), -158.81 (t, 1F), -163.23 (t, 2F). HRMS (ESI negative mode, m/z): calculated for C₁₆HBBBr₈F₅N₆O₂ [M]⁻ 1054.3569; found 1054.3599.



18

CuCl (4.9 mg, 0.050 mmol) in dry MeCN (1 mL) was added dropwise to a solution of the Tp **16** (49.5 mg, 0.045 mmol) in dry MeCN (1 mL) at RT. A white precipitate of KCl formed after a few minutes. The reaction was stirred overnight at RT under nitrogen. The reaction mixture was filtered through a pad of celite and the solvent was removed under reduced pressure. The crude product was dissolved with DCM and filtered through a pad of celite (2x). The solvent was removed under reduced pressure and 45 mg of PFP-Tp^{Br3}Cu **18** were afforded as a beige solid (89 % yield).

¹⁹F NMR (471 MHz, CD₂Cl₂, 298 K) δ -152.66 (d, 2F), -158.72 (t, 1F), -163.18 (t, 2F).

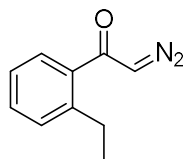


Biot^{C5}-Tp^{Br3}Cu

A suspension of **biotin^{C5}NH₃Cl** (8.0 mg, 0.03 mmol) in dry DMF (0.5 mL) was added to a solution of the PFP-Tp^{Br3}Cu **18** (22.4 mg, 0.02 mmol), and triethylamine (8.4 μL, 0.06 mmol) in dry DMF (0.5 mL) at RT. The reaction was stirred at 35 °C for a few hours. End of the reaction was monitored with the disappearance of the starting material by ESI-MS in the negative mode. The solvent was then removed under reduced pressure and the crude product was dried under high vacuum. The crude product was dissolved in DCM/MeOH (1:3) and diethyl ether was carefully added until a first precipitate (mainly biotin^{C5}NH₂) was observed. The mixture was centrifuged and the supernatant separated. More diethyl ether was added until an abundant precipitate formed (**Biot^{C5}-Tp^{Br3}Cu**). The mixture was centrifuged and the supernatant was removed. The purity

of the product was assessed by ESI-MS and the precipitation repeated if necessary. 7 mg of **Biot**^{C5}-**Tp**^{Br3}**Cu** were afforded as a white solid (30 % yield).

¹H NMR (600 MHz, DMF-*d*₇, 298 K) δ 6.39 (m., 2H), 4.50 (m, 1 H), 4.33 (m, 1 H), 3.30 (br. s, 2 H), 3.12 (t, 1 H), 3.00 (br. s, 1 H), 2.81 (br. s, 1 H), 1.77 (m, 2 H), 165-1.45 (m, 6H). ¹³C NMR (125 MHz, DMF-*d*₇, 298 K) δ 163.32 (1C), 61.71 (1C), 60.17 (1C), 40.85 (1C), 39.33 (1C), 28.94 (1C), 27.09 (1C). HRMS (ESI negative mode, m/z): calculated for C₂₀H₁₉BBr₈CuN₉O₂S [M]⁻: 1161.4089; found 1161.4073.



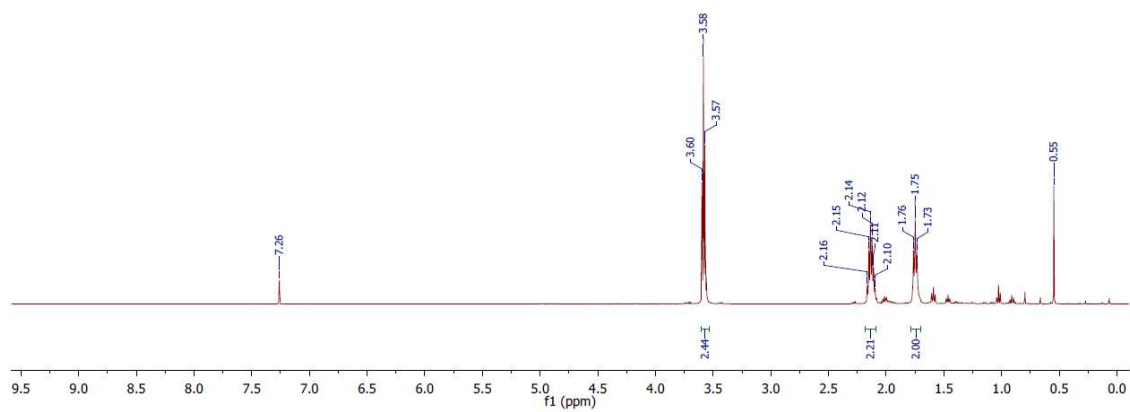
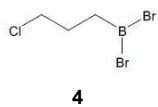
19 The diazoketone **19** was synthesized according to a reported procedure.⁴⁸

Oxalyl chloride (0.643 mL, 7.5 mmol) was added dropwise to a solution of 2-ethylbenzoic acid (750 mg, 5 mmol) in DCM (8 mL) at room temperature. After 1 h of stirring, the reaction mixture was concentrated under reduced pressure to give the corresponding acyl chloride, which was used without purification. The crude acyl chloride was dissolved in MeCN (35 mL) and TMS diazomethane (2 M in Et₂O, 3 mL, 6 mmol) was added dropwise at 0 °C. The reaction was stirred for 24 h and the volatiles were removed under reduced pressure. The crude product purified by flash chromatography with EtOAc/petroleum ether (0:100 to 15:85) and gave the diazoketone **19** as a yellow oil (55 % yield).

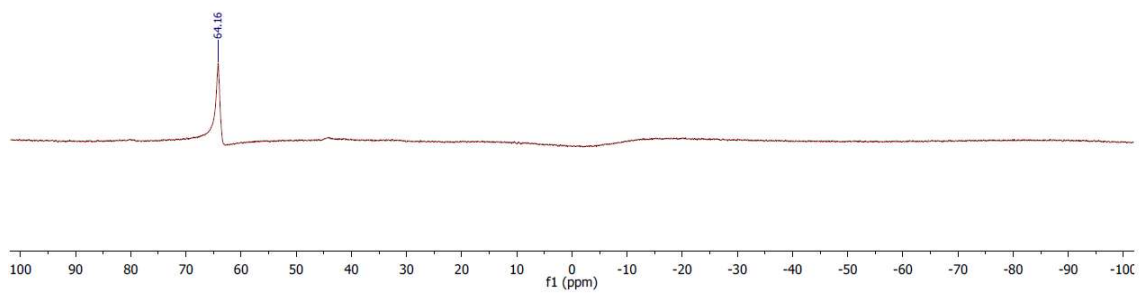
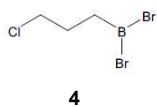
The NMR signals corresponded to the literature characterization. ¹H NMR (500 MHz, CDCl₃, 298 K) δ 7.36 (m, 2H), 7.29 (d, 1 H), 7.23 (m, 1 H), 5.56 (br. s, 1 H), 2.86 (q, 2 H), 1.24 (t, 3 H).

3.5.3 NMR and MS Spectra

rumocoR-.574.1.1.1r
Kuerzel CRU
Gruppe Ward
Nummer 567dist

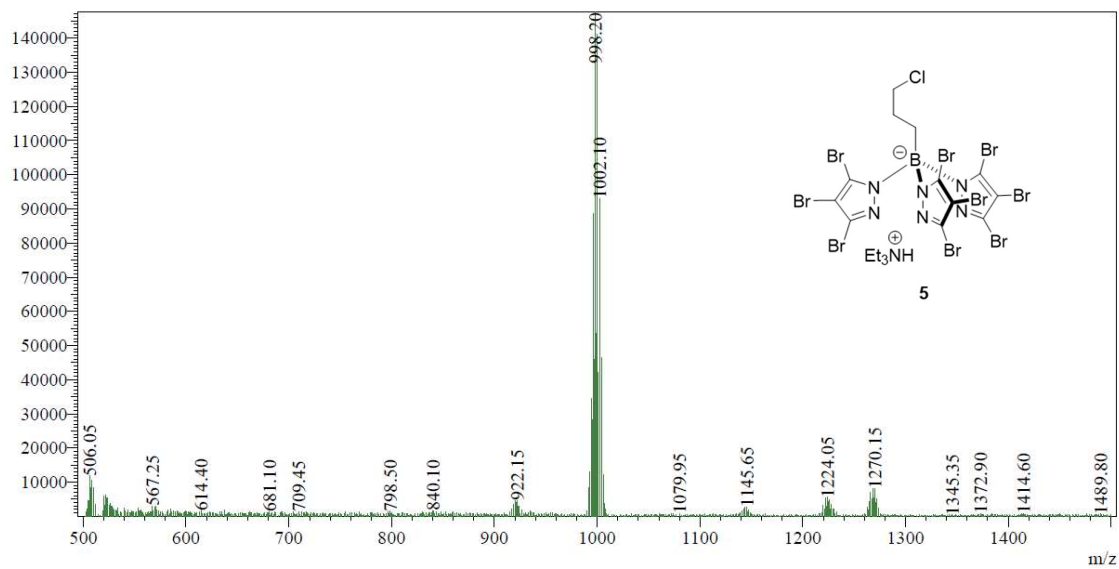


rumocoR-.574.2.1.1r
Kuerzel CRU
Gruppe Ward
Nummer 567dist



MS Spectrum Negative Mode

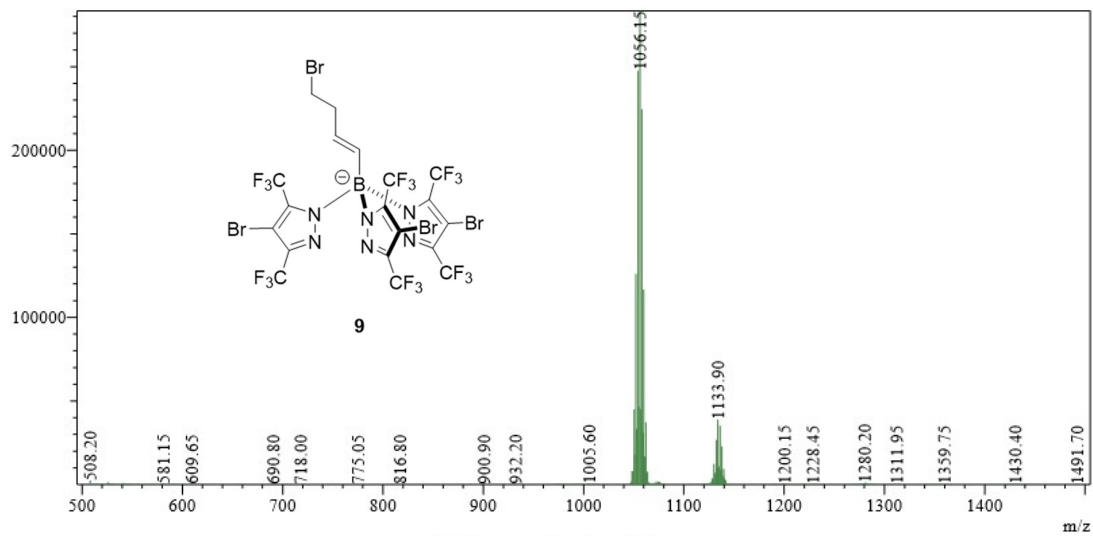
Line#:1 R.Time:----(Scan#:----)
 MassPeaks:974
 Spectrum Mode:Averaged 1.571-2.951(944-1772) Base Peak:998.20(147537)
 BG Mode:Averaged 0.301-1.111(182-668) Segment 1 - Event 2



MS Spectrum Negative Mode

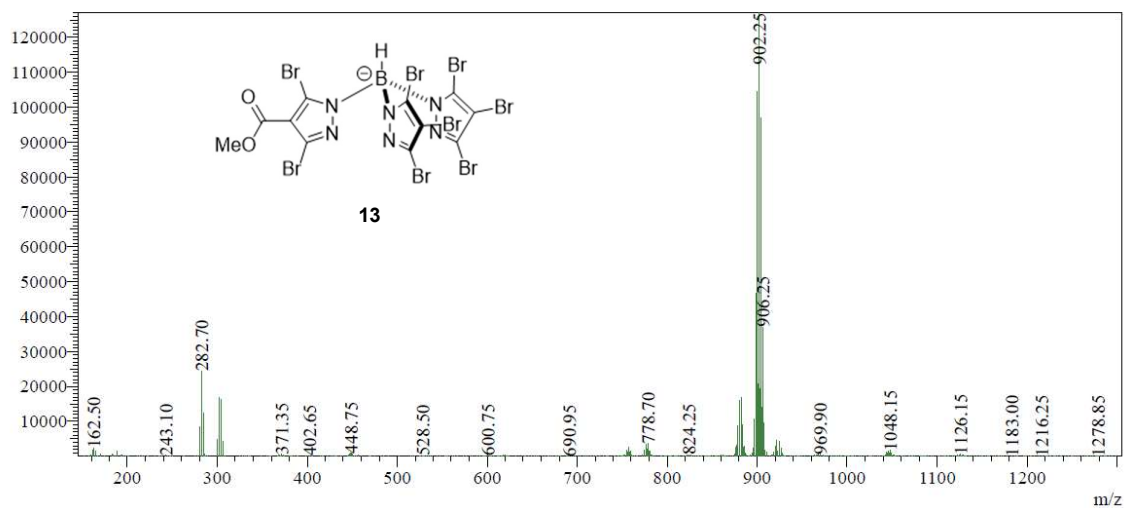
MS Spectrum Negative Mode

Line#:1 R.Time:----(Scan#:----)
 MassPeaks:775
 Spectrum Mode:Averaged 1.901-2.711(1142-1628) Base Peak:1056.15(283398)
 BG Mode:Averaged 0.325-1.395(196-838) Segment 1 - Event 2

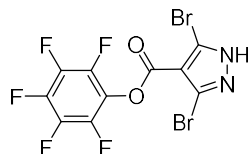


MS Spectrum Negative Mode

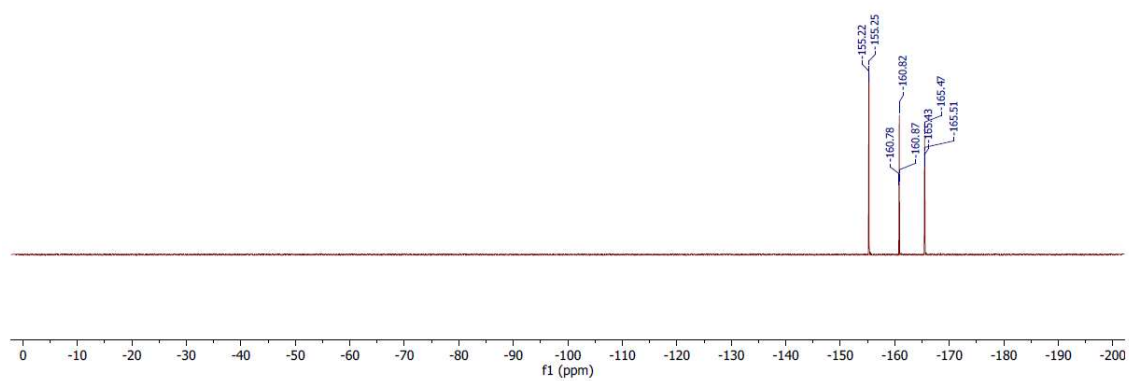
Line#:2 R.Time:----(Scan#:----)
MassPeaks:578
Spectrum Mode:Averaged 1.925-2.938(1156-1764) Base Peak:902.25(127033)
BG Mode:Averaged 0.778-1.778(468-1068) Segment 1 - Event 2



rumocoR-.1241.1.fid
Kuerzel CRU
Gruppe Ward
Nummer 1412
group Ward



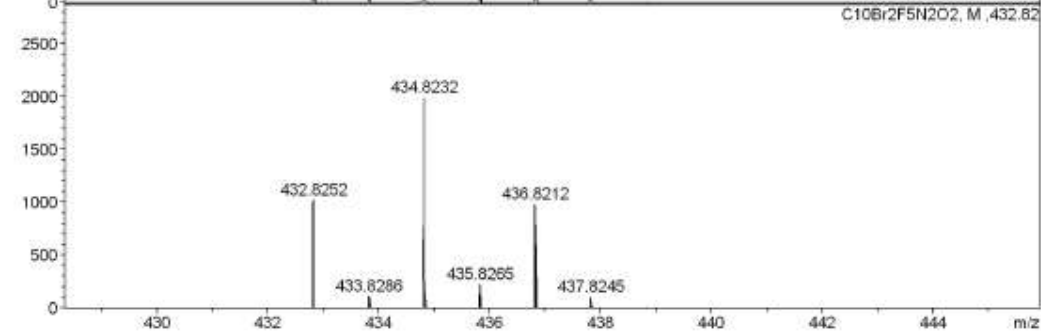
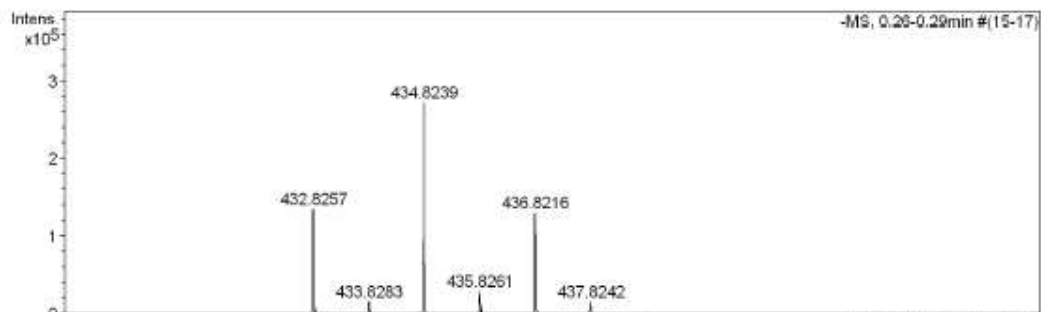
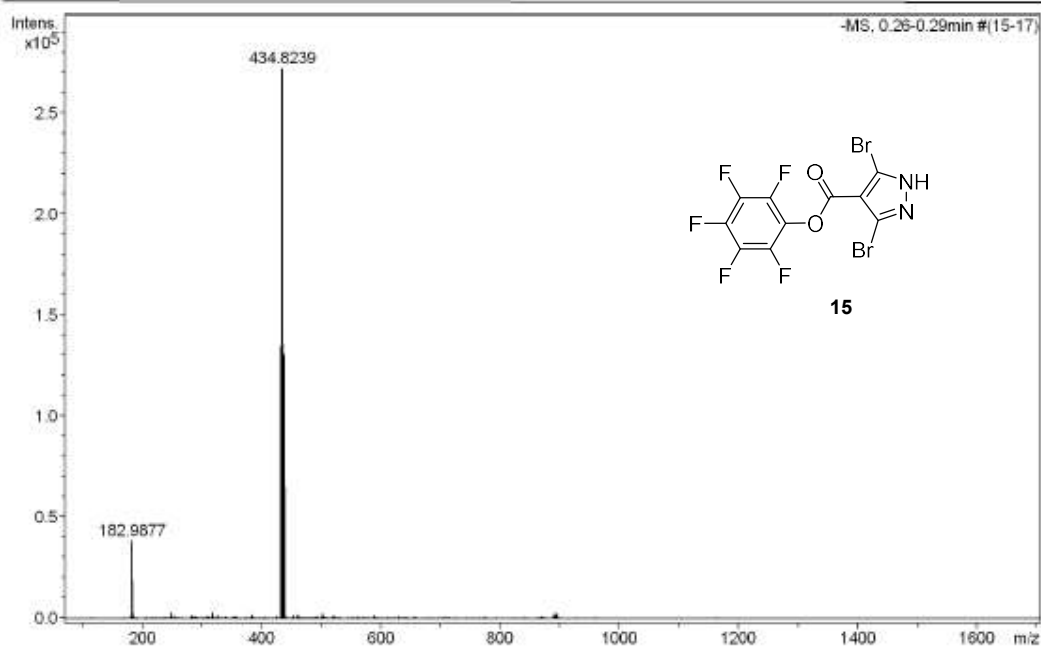
15



High Resolution Mass Spectrometry Report

Sample Name **cru1412 neg**
Comment

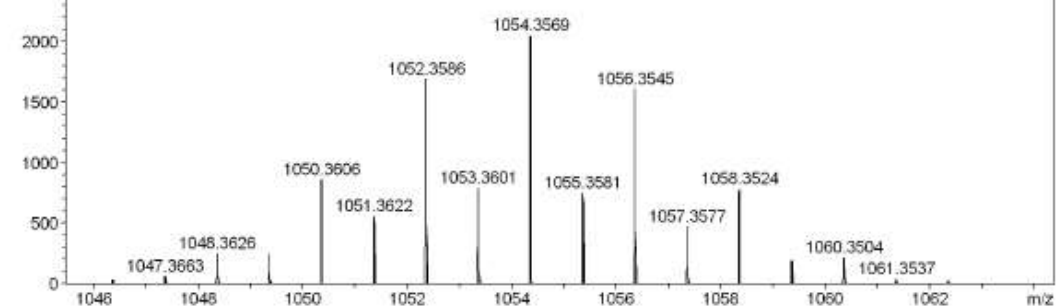
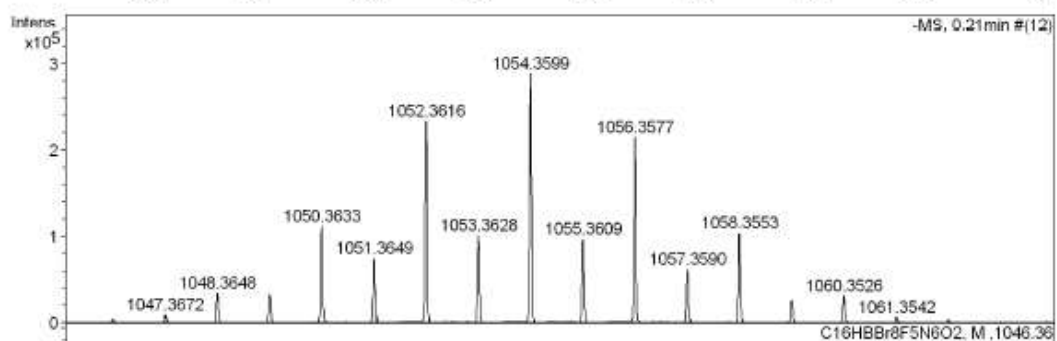
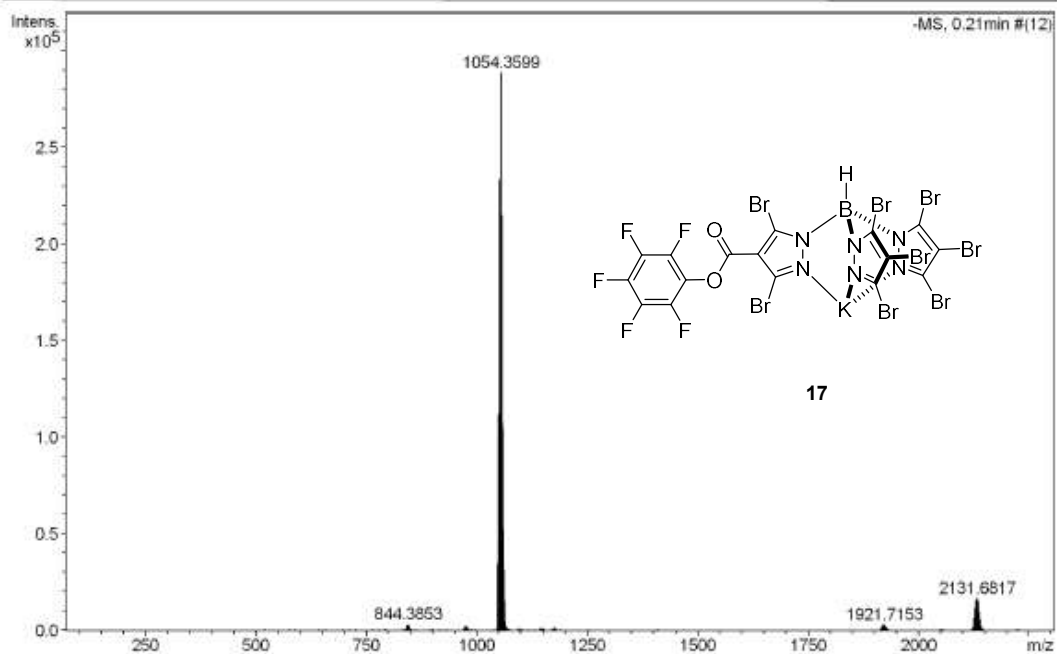
Instrument **maXis 4G**
Method **ms_nocolumn_mid_neg.m**



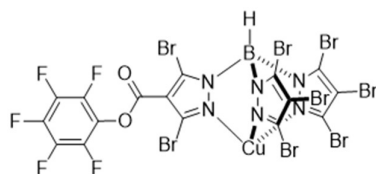
High Resolution Mass Spectrometry Report

Sample Name **cru1415 neg**
Comment

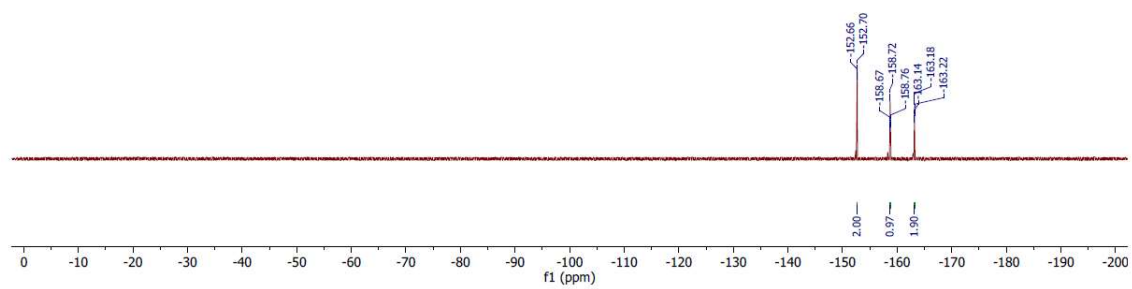
Instrument **maXis 4G**
Method **ms_nocolumn_high_neg_use_acn.m**

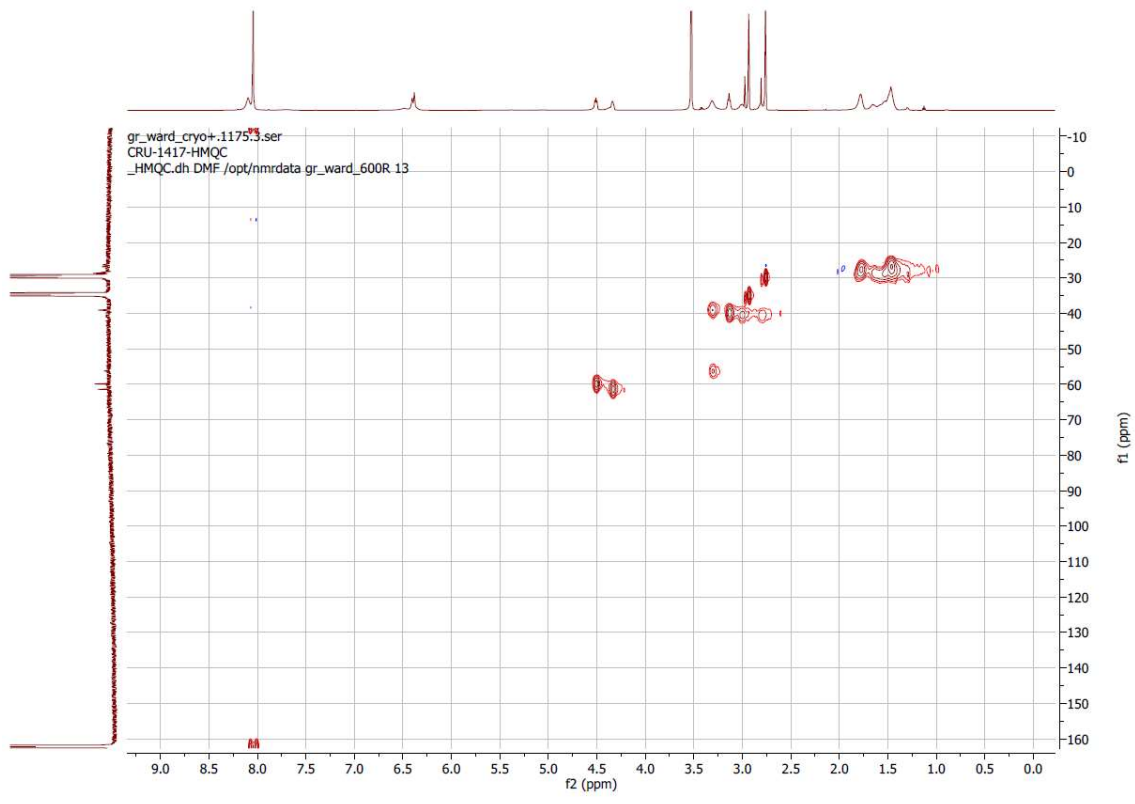
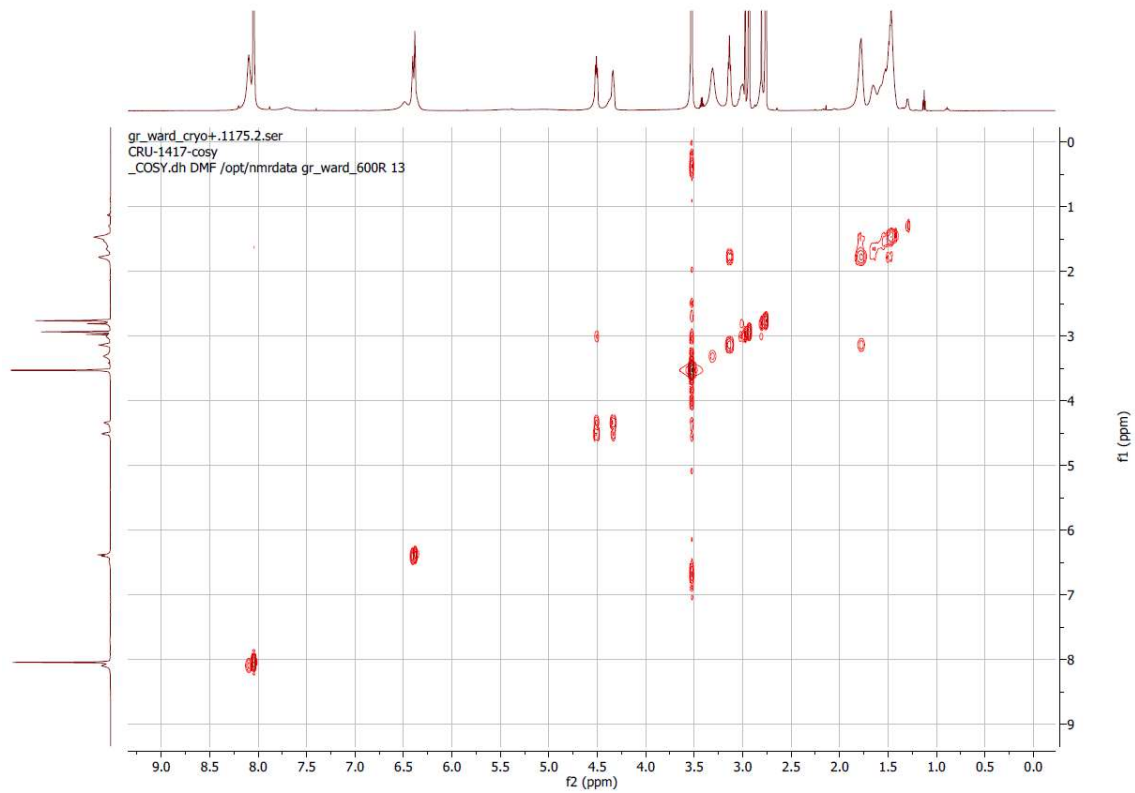


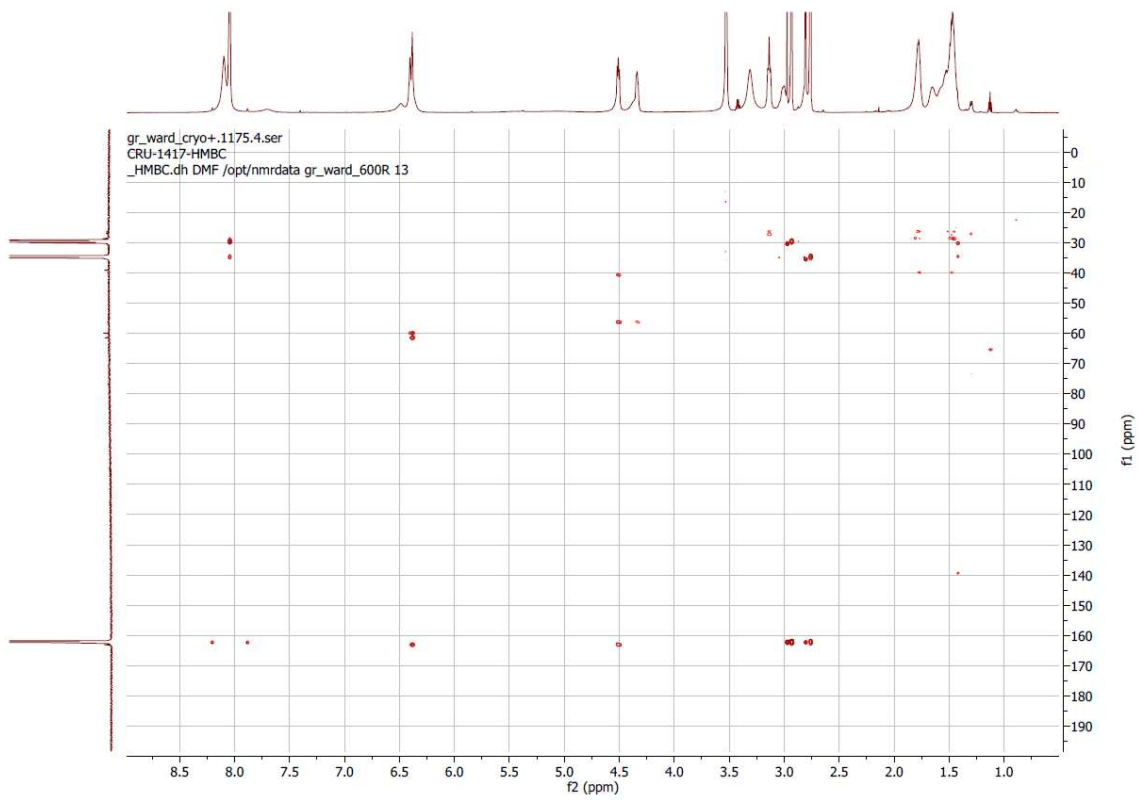
rumocoR-1242.1.fid
Kuerzel CRU
Gruppe Ward
Nummer 1416
group Ward



18



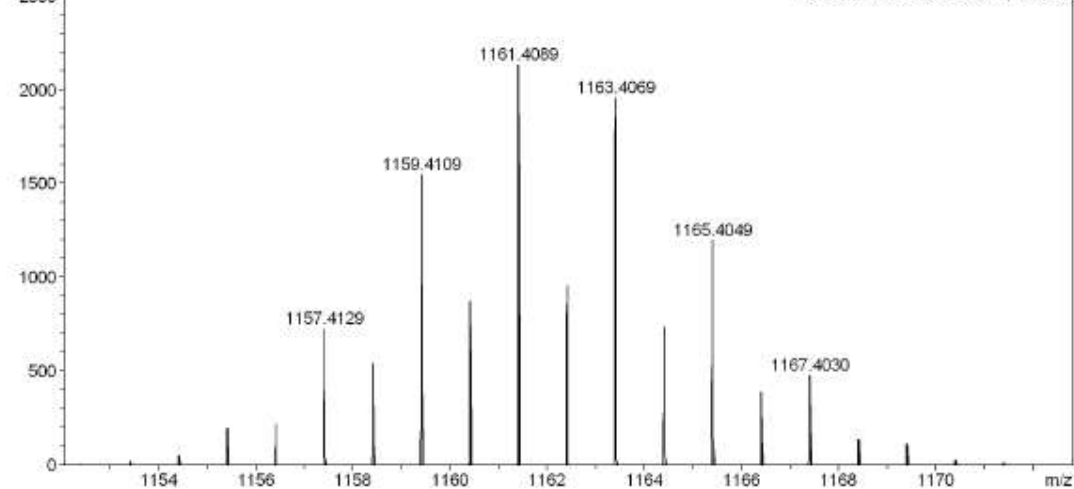
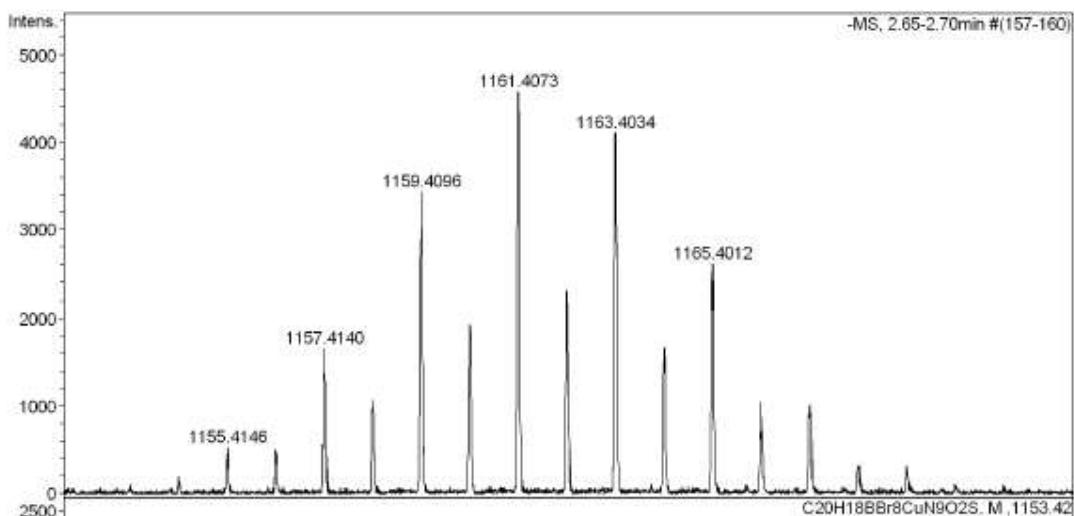
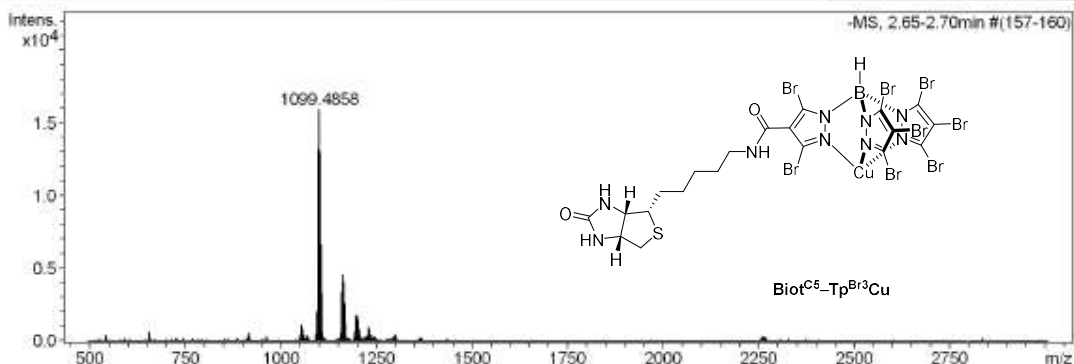




High Resolution Mass Spectrometry Report

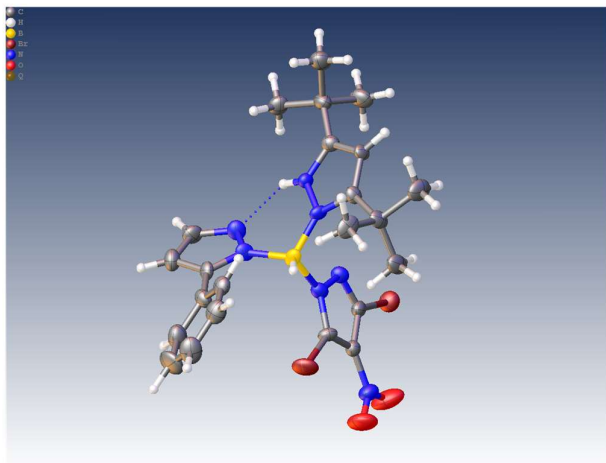
Sample Name **cru 1417**
Comment analyzed in MeOH

Instrument **maXis 4G**
Method **34 Direct_neg_high.m**



3.5.4 X-ray reports

X-Ray Crystallographic Information for **14**



Experimental. Single colourless block crystals of **CRU1037_150K** were used as supplied. A suitable crystal with dimensions $0.22 \times 0.17 \times 0.10 \text{ mm}^3$ was selected and mounted on a mylar loop in perfluoroether oil on a STOE STADIVARI diffractometer. The crystal was kept at a steady $T = 150 \text{ K}$ during data collection. The structure was solved with the ShelXT 2018/2 (Sheldrick, 2018) solution program using dual methods and by using Olex2 (Dolomanov et al., 2009) as the graphical interface. The model was refined with ShelXL 2018/3 (Sheldrick, 2015) using full matrix least squares minimisation on F^2 .

Crystal Data. $\text{C}_{23}\text{H}_{28}\text{BBr}_2\text{N}_7\text{O}_2$, $M_r = 605.15$, orthorhombic, $P2_12_12_1$ (No. 19), $a = 11.3782(5) \text{ \AA}$, $b = 12.3267(5) \text{ \AA}$, $c = 19.2984(11) \text{ \AA}$, $\alpha = \beta = \gamma = 90^\circ$, $V = 2706.7(2) \text{ \AA}^3$, $T = 150 \text{ K}$, $Z = 4$, $Z' = 1$, $\mu(\text{GaK}\alpha) = 2.689$, 37501 reflections measured, 5394 unique ($R_{\text{int}} = 0.1526$) which were used in all calculations. The final wR_2 was 0.0802 (all data) and R_1 was 0.0438 ($I \geq 2 \sigma(I)$).

Compound	CRU1037_150K
Formula	$\text{C}_{23}\text{H}_{28}\text{BBr}_2\text{N}_7\text{O}_2$
$D_{\text{calc.}} / \text{g cm}^{-3}$	1.485
μ / mm^{-1}	2.689
Formula Weight	605.15
Colour	colourless
Shape	block
Size/ mm^3	$0.22 \times 0.17 \times 0.10$
T / K	150
Crystal System	orthorhombic
Flack Parameter	0.04(4)
Hooft Parameter	0.05(5)
Space Group	$P2_12_12_1$
$a / \text{Å}$	11.3782(5)
$b / \text{Å}$	12.3267(5)
$c / \text{Å}$	19.2984(11)
$\alpha / ^\circ$	90
$\beta / ^\circ$	90
$\gamma / ^\circ$	90
$V / \text{Å}^3$	2706.7(2)
Z	4
Z'	1
Wavelength/ Å	1.34143
Radiation type	$\text{GaK}\alpha$
$\theta_{\text{min}} / ^\circ$	3.702
$\theta_{\text{max}} / ^\circ$	56.719
Measured Refl's.	37501
Indep't Refl's	5394
Refl's $I \geq 2 \sigma(I)$	2840
R_{int}	0.1526
Parameters	322
Restraints	0
Largest Peak	0.437
Deepest Hole	-0.365
GooF	0.689
wR_2 (all data)	0.0802
wR_2	0.0745
R_1 (all data)	0.0898
R_1	0.0438

Bond Lengths of **14** in Å

Atom	Atom	Length/Å
Br1	C3	1.876(9)
Br2	C2	1.874(7)
N4	N5	1.365(9)
N4	C13	1.354(9)
N4	B1	1.531(12)
N5	C15	1.332(10)
N3	N2	1.373(8)
N3	C2	1.336(9)
N3	B1	1.621(11)
N2	C3	1.283(10)
N6	N7	1.362(9)
N6	C4	1.346(10)
N6	B1	1.522(12)
N7	C12	1.333(10)
N1	O1	1.219(9)
N1	O2	1.210(8)
N1	C1	1.428(10)
C2	C1	1.340(10)
C14	C13	1.378(12)
C14	C15	1.374(11)
C13	C20	1.524(12)
C6	C7	1.369(11)
C6	C5	1.353(12)
C1	C3	1.419(10)
C4	C5	1.504(12)
C4	C11	1.368(12)
C7	C8	1.370(13)
C5	C10	1.374(12)
C15	C16	1.528(12)
C21	C20	1.528(13)
C17	C16	1.529(13)
C16	C19	1.528(12)
C16	C18	1.544(13)
C20	C23	1.532(13)
C20	C22	1.546(12)
C11	C12	1.406(13)
C8	C9	1.342(13)
C10	C9	1.406(13)

3.6 References

- (1) Trofimenko, Swiatoslaw. Boron-Pyrazole Chemistry. IV. Carbon- and Boron-Substituted Poly[(1-Pyrazolyl) Borates]. *Journal of the American Chemical Society* **1967**, *89* (24), 6288–6294. <https://doi.org/10.1021/ja01000a053>.
- (2) S. Trofimenko. *Scorpionates: The Coordination Chemistry of Polypyrazolylborate Ligands*; Imperial College Press, 1999.
- (3) Pettinari, C. *Scorpionates II: Chelating Borate Ligands*; Imperial College Press, 2008.
- (4) Tellers, D. M.; Skoog, S. J.; Bergman, R. G.; Gunnoe, T. B.; Harman, W. D. Comparison of the Relative Electron-Donating Abilities of Hydridotris(Pyrazolyl)Borate and Cyclopentadienyl Ligands: Different Interactions with Different Transition Metals. *Organometallics* **2000**, *19* (13), 2428–2432. <https://doi.org/10.1021/om000043o>.
- (5) Calabrese, J. C.; Trofimenko, S.; Thompson, J. S. A New Class of Polypyrazolylborate Ligands. *J. Chem. Soc. Chem. Commun.* **1986**, No. 14, 1122. <https://doi.org/10.1039/c39860001122>.
- (6) Trofimenko, S.; Calabrese, J. C.; Thompson, J. S. Novel Polypyrazolylborate Ligands: Coordination Control through 3-Substituents of the Pyrazole Ring. *Inorg. Chem.* **1987**, *26* (10), 1507–1514. <https://doi.org/10.1021/ic00257a010>.
- (7) Murtuza, S.; Casagrande, O. L.; Jordan, R. F. Ethylene Polymerization Behavior of Tris(Pyrazolyl)Borate Titanium(IV) Complexes. *Organometallics* **2002**, *21* (9), 1882–1890. <https://doi.org/10.1021/om010530j>.
- (8) Lin, Y.; Zhu, D.-P.; Du, Y.-R.; Zhang, R.; Zhang, S.-J.; Xu, B.-H. Tris(Pyrazolyl)Borate Cobalt-Catalyzed Hydrogenation of C=O, C=C, and C=N Bonds: An Assistant Role of a Lewis Base. *Org. Lett.* **2019**, *21* (8), 2693–2698. <https://doi.org/10.1021/acs.orglett.9b00679>.
- (9) Meucci, E. A.; Nguyen, S. N.; Camasso, N. M.; Chong, E.; Ariafard, A.; Canty, A. J.; Sanford, M. S. Nickel(IV)-Catalyzed C–H Trifluoromethylation of (Hetero)Arenes. *Journal of the American Chemical Society* **2019**. <https://doi.org/10.1021/jacs.9b06383>.
- (10) Morilla, M. E.; Molina, M. J.; Díaz-Requejo, M. M.; Belderráin, T. R.; Nicasio, M. C.; Trofimenko, S.; Pérez, P. J. Copper-Catalyzed Carbene Insertion into O–H Bonds: High Selective Conversion of Alcohols into Ethers. *Organometallics* **2003**, *22* (14), 2914–2918. <https://doi.org/10.1021/om030243a>.
- (11) Caballero, A.; Despagnet-Ayoub, E.; Díaz-Requejo, M. M.; Díaz-Rodríguez, A.; González-Núñez, M. E.; Mello, R.; Muñoz, B. K.; Ojo, W.-S.; Asensio, G.; Etienne, M.; Pérez, P. J. Silver-Catalyzed C–C Bond Formation Between Methane and Ethyl Diazoacetate in Supercritical CO₂. *Science* **2011**, *332* (6031), 835–838. <https://doi.org/10.1126/science.1204131>.

- (12) Iglesias, M. J.; Nicasio, M. C.; Caballero, A.; Pérez, P. J. Silver-Catalyzed Silicon–Hydrogen Bond Functionalization by Carbene Insertion. *Dalton Trans.* **2012**, 42 (4), 1191–1195. <https://doi.org/10.1039/C2DT31460F>.
- (13) Li, M.-L.; Yu, J.-H.; Li, Y.-H.; Zhu, S.-F.; Zhou, Q.-L. Highly Enantioselective Carbene Insertion into N–H Bonds of Aliphatic Amines. *Science* **2019**, 366 (6468), 990–994. <https://doi.org/10.1126/science.aaw9939>.
- (14) Lovely, C. J.; Browning, R. G.; Badarinarayana, V.; Dias, H. V. R. A Silver-Catalyzed Büchner Reaction. *Tetrahedron Lett.* **2005**, 46 (14), 2453–2455. <https://doi.org/10.1016/j.tetlet.2005.02.052>.
- (15) Kulkarni, N. V.; Das, A.; Jayaratna, N. B.; Yousufuddin, M.; Dias, H. V. R. Zinc-Mediated Carbene Insertion to C–Cl Bonds of Chloromethanes and Isolable Zinc(II) Isocyanide Adducts. *Inorg. Chem.* **2015**, 54 (11), 5151–5153. <https://doi.org/10.1021/acs.inorgchem.5b00929>.
- (16) Conde, A.; Mar Díaz-Requejo, M.; Pérez, P. J. Direct, Copper-Catalyzed Oxidation of Aromatic C–H Bonds with Hydrogen Peroxide under Acid-Free Conditions. *Chem. Commun.* **2011**, 47 (28), 8154. <https://doi.org/10.1039/c1cc12804c>.
- (17) Conde, A.; Vilella, L.; Balcells, D.; Díaz-Requejo, M. M.; Lledós, A.; Pérez, P. J. Introducing Copper as Catalyst for Oxidative Alkane Dehydrogenation. *J. Am. Chem. Soc.* **2013**, 135 (10), 3887–3896. <https://doi.org/10.1021/ja310866k>.
- (18) Fructos, M. R.; Trofimenko, S.; Díaz-Requejo, M. M.; Pérez, P. J. Facile Amine Formation by Intermolecular Catalytic Amidation of Carbon–Hydrogen Bonds. *J. Am. Chem. Soc.* **2006**, 128 (36), 11784–11791. <https://doi.org/10.1021/ja0627850>.
- (19) Maestre, L.; Dorel, R.; Pablo, Ó.; Escofet, I.; Sameera, W. M. C.; Álvarez, E.; Maseras, F.; Díaz-Requejo, M. M.; Echavarren, A. M.; Pérez, P. J. Functional-Group-Tolerant, Silver-Catalyzed N–N Bond Formation by Nitrene Transfer to Amines. *J. Am. Chem. Soc.* **2017**, 139 (6), 2216–2223. <https://doi.org/10.1021/jacs.6b08219>.
- (20) Ponduru, T. T.; Sun, Z.; Cundari, T. R.; Dias, H. V. R. Nitrene Insertion into Aromatic and Benzylic C–H Bonds Catalyzed by Copper Complexes of Fluorinated Bis- and Tris(Pyrazolyl)Borates. *ChemCatChem* **2019**, 11 (19), 4966–4973. <https://doi.org/10.1002/cctc.201901087>.
- (21) Perez, P. J.; Brookhart, M.; Templeton, J. L. A Copper(I) Catalyst for Carbene and Nitrene Transfer to Form Cyclopropanes, Cyclopropenes, and Aziridines. *Organometallics* **1993**, 12 (2), 261–262. <https://doi.org/10.1021/om00026a007>.
- (22) Llaveria, J.; Beltrán, Á.; Díaz-Requejo, M. M.; Matheu, M. I.; Castellón, S.; Pérez, P. J. Efficient Silver-Catalyzed Regio- and Stereospecific Aziridination of Dienes. *Angew. Chem. Int. Ed.* **2010**, 49 (39), 7092–7095. <https://doi.org/10.1002/anie.201003167>.

- (23) Fructos, M. R.; Álvarez, E.; Díaz-Requejo, M. M.; Pérez, P. J. Selective Synthesis of N-Substituted 1,2-Dihydropyridines from Furans by Copper-Induced Concurrent Tandem Catalysis. *J. Am. Chem. Soc.* **2010**, *132* (13), 4600–4607. <https://doi.org/10.1021/ja1006614>.
- (24) Muñoz-Molina, J. M.; Belderraín, T. R.; Pérez, P. J. Copper-Catalyzed Synthesis of 1,2-Disubstituted Cyclopentanes from 1,6-Dienes by Ring-Closing Kharasch Addition of Carbon Tetrachloride. *Adv. Synth. Catal.* **2008**, *350* (14–15), 2365–2372. <https://doi.org/10.1002/adsc.200800364>.
- (25) Muñoz-Molina, J. M.; Belderraín, T. R.; Pérez, P. J. An Efficient, Selective, and Reducing Agent-Free Copper Catalyst for the Atom-Transfer Radical Addition of Halo Compounds to Activated Olefins. *Inorg. Chem.* **2010**, *49* (2), 642–645. <https://doi.org/10.1021/ic901942p>.
- (26) Diaba, F.; Martínez-Laporta, A.; Bonjoch, J.; Pereira, A.; Muñoz-Molina, J. M.; Pérez, P. J.; Belderraín, T. R. Cu(I)-Catalyzed Atom Transfer Radical Cyclization of Trichloroacetamides Tethered to Electron-Deficient, -Neutral, and -Rich Alkenes: Synthesis of Polyfunctionalized 2-Azabicyclo[3.3.1]Nonanes. *Chem. Commun.* **2012**, *48* (70), 8799–8801. <https://doi.org/10.1039/C2CC34133F>.
- (27) Armstrong, W. H.; Spool, A.; Papaefthymiou, G. C.; Frankel, R. B.; Lippard, S. J. Assembly and Characterization of an Accurate Model for the Diiron Center in Hemerythrin. *J. Am. Chem. Soc.* **1984**, *106* (12), 3653–3667. <https://doi.org/10.1021/ja00324a041>.
- (28) Kitajima, N.; Tolman, W. B. Coordination Chemistry with Sterically Hindered Hydrotris(Pyrazolyl)Borate Ligands: Organometallic and Bioinorganic Perspectives. In *Progress in Inorganic Chemistry*; John Wiley & Sons, Ltd, 1995; pp 419–531. <https://doi.org/10.1002/9780470166444.ch5>.
- (29) Young, C. G.; Wedd, A. G. Metal Chemistry Relevant to the Mononuclear Molybdenum Andtungstenpterin Enzymes. *Chem. Commun.* **1997**, No. 14, 1251–1257. <https://doi.org/10.1039/A606660G>.
- (30) Vahrenkamp, H. Transitions, Transition States, Transition State Analogues: Zinc Pyrazolylborate Chemistry Related to Zinc Enzymes. *Acc. Chem. Res.* **1999**, *32* (7), 589–596. <https://doi.org/10.1021/ar9703185>.
- (31) Costas, M.; Mehn, M. P.; Jensen, M. P.; Que, L. Dioxygen Activation at Mononuclear Nonheme Iron Active Sites: Enzymes, Models, and Intermediates. *Chem. Rev.* **2004**, *104* (2), 939–986. <https://doi.org/10.1021/cr020628n>.
- (32) Burzlauff, N. Biomimetic Trispyrazolylborato Iron Complexes. *Angew. Chem. Int. Ed.* **2009**, *48* (31), 5580–5582. <https://doi.org/10.1002/anie.200900552>.

- (33) Sallmann, M.; Limberg, C. Utilizing the Trispyrazolyl Borate Ligand for the Mimicking of O_2 -Activating Mononuclear Nonheme Iron Enzymes. *Acc. Chem. Res.* **2015**, *48* (10), 2734–2743. <https://doi.org/10.1021/acs.accounts.5b00148>.
- (34) Díaz-Requejo, M. M.; Belderrain, T. R.; Nicasio, M. C.; Pérez, P. J. From Homogeneous to Heterogeneous Catalysis: Novel Anchoring of Polypyrazolylborate Copper(I) Complexes on Silica Gel through Classical and Nonclassical Hydrogen Bonds. Use as Catalysts of the Olefin Cyclopropanation Reaction. *Organometallics* **2000**, *19* (3), 285–289. <https://doi.org/10.1021/om990780o>.
- (35) Nakamizu, A.; Kasai, T.; Nakazawa, J.; Hikichi, S. Immobilization of a Boron Center-Functionalized Scorpionate Ligand on Mesoporous Silica Supports for Heterogeneous Tp-Based Catalysts. *ACS Omega* **2017**, *2* (3), 1025–1030. <https://doi.org/10.1021/acsomega.7b00022>.
- (36) Molina de la Torre, J. A.; Pérez-Ortega, I.; Beltrán, Á.; Rodríguez, M. R.; Díaz-Requejo, M. M.; Pérez, P. J.; Albéniz, A. C. Trispyrazolylborate Ligands Supported on Vinyl Addition Polynorbornenes and Their Copper Derivatives as Recyclable Catalysts. *Chem. Eur. J.* **2019**, *25* (2), 556–563. <https://doi.org/10.1002/chem.201803852>.
- (37) Zagermann, J.; Kuchta, M. C.; Merz, K.; Metzler-Nolte, N. Para-Bromophenyl[Tris(Pyrazolyl)]Borate Complexes of Group 1 Metals, Thallium and Magnesium: Synthesis and Characterization of Transfer Agents for “Third-Generation” Tp Ligands. *Eur. J. Inorg. Chem.* **2009**, *2009* (35), 5407–5412. <https://doi.org/10.1002/ejic.200900707>.
- (38) Zagermann, J.; Klein, K.; Merz, K.; Molon, M.; Metzler-Nolte, N. Synthesis and Characterization of the Azido-Functionalized Ruthenocene Analogue [TpRu(p-N₃C₆H₄)Tp]Cl and Its Attachment to Biomolecules by Copper-Catalyzed Azide–Alkyne Cycloaddition. *Eur. J. Inorg. Chem.* **2011**, *2011* (27), 4212–4219. <https://doi.org/10.1002/ejic.201100433>.
- (39) Fischer, S.; Ward, T. R.; Liang, A. D. Engineering a Metathesis-Catalyzing Artificial Metalloenzyme Based on HaloTag. *ACS Catal.* **2021**, *11* (10), 6343–6347. <https://doi.org/10.1021/acscatal.1c01470>.
- (40) Desrochers, P. J.; Besel, B. M.; Corken, A. L.; Evanov, J. R.; Hamilton, A. L.; Nutt, D. L.; Tarkka, R. M. Immobilized Boron-Centered Heteroscorpionates: Heterocycle Metathesis and Coordination Chemistry. *Inorg. Chem.* **2011**, *50* (5), 1931–1941. <https://doi.org/10.1021/ic102392x>.
- (41) Skander, M.; Humbert, N.; Collot, J.; Gradinaru, J.; Klein, G.; Loosli, A.; Sauser, J.; Zocchi, A.; Gilardoni, F.; Ward, T. R. Artificial Metalloenzymes: (Strept)Avidin as Host for Enantioselective Hydrogenation by Achiral Biotinylated Rhodium–Diphosphine

- Complexes. *J. Am. Chem. Soc.* **2004**, *126* (44), 14411–14418. <https://doi.org/10.1021/ja0476718>.
- (42) Dundas, C. M.; Demonte, D.; Park, S. Streptavidin–Biotin Technology: Improvements and Innovations in Chemical and Biological Applications. *Appl Microbiol Biotechnol* **2013**, *97* (21), 9343–9353. <https://doi.org/10.1007/s00253-013-5232-z>.
- (43) Martín, C.; Belderráin, T. R.; Pérez, P. J. Rediscovering Copper-Based Catalysts for Intramolecular Carbon–Hydrogen Bond Functionalization by Carbene Insertion. *ACS Catal.* **2009**, *7* (22), 4777. <https://doi.org/10.1039/b911589g>.
- (44) Dowling, C. M.; Leslie, D.; Chisholm, M. H.; Parkin, G. The Synthesis and Structural Characterization of the Sterically Demanding Tris (3,5-Di-*t*-Butylpyrazolyl) Hydroborato Ligand, [Tp Bu₂t]: A Highly Twisted, Propeller-Like, Ligand System. *Main Group Chem.* **1995**, *1* (1), 29–52. <https://doi.org/10.1080/13583149512331338245>.
- (45) Rheingold, A. L.; Liable-Sands, L. M.; Incarvito, C. L.; Trofimenko, S. Novel Scorpionate Ligands Devoid of C–H Bonds: BpBr₃ and TpBr₃. *J. Chem. Soc., Dalton Trans.* **2002**, No. 11, 2297–2301. <https://doi.org/10.1039/B111568P>.
- (46) Caballero, A.; Díaz-Requejo, M. M.; Belderráin, T. R.; Nicasio, M. C.; Trofimenko, S.; Pérez, P. J. Highly Regioselective Functionalization of Aliphatic Carbon–Hydrogen Bonds with a Perbromohomoscorpionate Copper(I) Catalyst. *J. Am. Chem. Soc.* **2003**, *125* (6), 1446–1447. <https://doi.org/10.1021/ja0291484>.
- (47) Soares da Costa, T. P.; Tieu, W.; Yap, M. Y.; Zvarec, O.; Bell, J. M.; Turnidge, J. D.; Wallace, J. C.; Booker, G. W.; Wilce, M. C. J.; Abell, A. D.; Polyak, S. W. Biotin Analogues with Antibacterial Activity Are Potent Inhibitors of Biotin Protein Ligase. *ACS Med. Chem. Lett.* **2012**, *3* (6), 509–514. <https://doi.org/10.1021/ml300106p>.
- (48) Ren, H.; Wulff, W. D. Trimethylsilyldiazomethane as a Versatile Stitching Agent for the Introduction of Aziridines into Functionalized Organic Molecules. *Org. Lett.* **2010**, *12* (21), 4908–4911. <https://doi.org/10.1021/ol102064b>.

4. An artificial metalloenzyme based on a copper heteroscorpionate enables sp^3 C–H functionalization *via* intramolecular carbene insertion

Corentin Rumo, Alina Stein, Juliane Klehr, Ryo Tachibana, Alessandro Prescimone, Daniel Häussinger, Thomas R. Ward*

This work was published in the *Journal of the American Chemical Society*:

J. Am. Chem. Soc. **2022**, *144*, 26, 11676–11684.

4.1 Contributions to this Work

TRW supervised the project. CR led the project. AS performed the cloning experiments and designed a part of the double saturation library. JK designed the other part of the double saturation library. RT performed the molecular modelling. AP solved the crystal structures. DH performed the NMR experiments on the cofactor.

4.2 Introduction

The selective functionalization of inert C–H bonds currently lies at the forefront of modern synthetic chemistry. It alleviates the laborious interconversion of functional groups, minimizes the number of synthetic steps and enables capitalizing on previously inaccessible bond formation strategies.^{1–3} This reduces the environmental footprint of lengthy chemical processes.

Thus far, the field of homogeneous C–H functionalization has been mostly dominated by precious metal catalysts used in combination with directing groups and is often performed at elevated temperatures.⁴ One of the recurring challenges faced with such methodologies is the reductive elimination of the stable M–C bond.⁵ An attractive approach to circumvent this limitation, is the insertion of a reactive M–X species into the C–H bond of a substrate that does not interact with the metal (Scheme S1).^{6–9} Largely developed by Pérez and coworkers, complexes bearing a tris(pyrazolyl)borate (Tp) ligand have been shown to enable the functionalization of simple alkanes with carbene, nitrene and oxo intermediates.^{9–11} The

pyrazole motif offers the possibility to readily fine-tune both steric and electronic properties of the TpM-catalyst to achieve the desired reactivity. Remarkably, perfluorinated azolylborate complexes of silver and copper catalyze the functionalization of methane in supercritical CO₂ with ethyl diazoacetate.^{12,13} However, this system occasionally yielded complex mixtures of regioisomers when substrates containing different C–H bonds were subjected to functionalization.

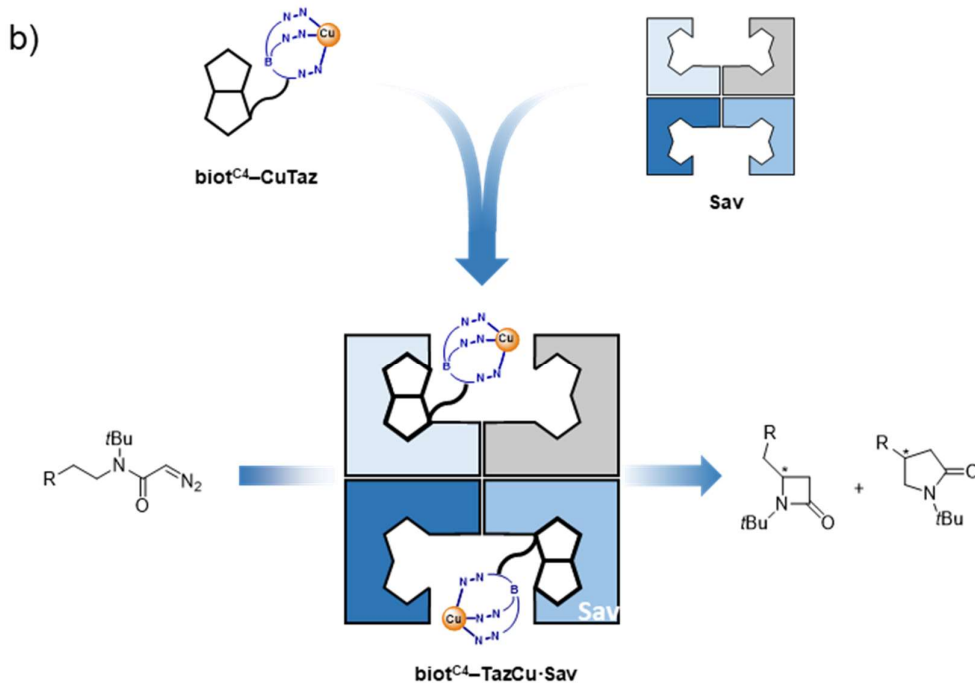
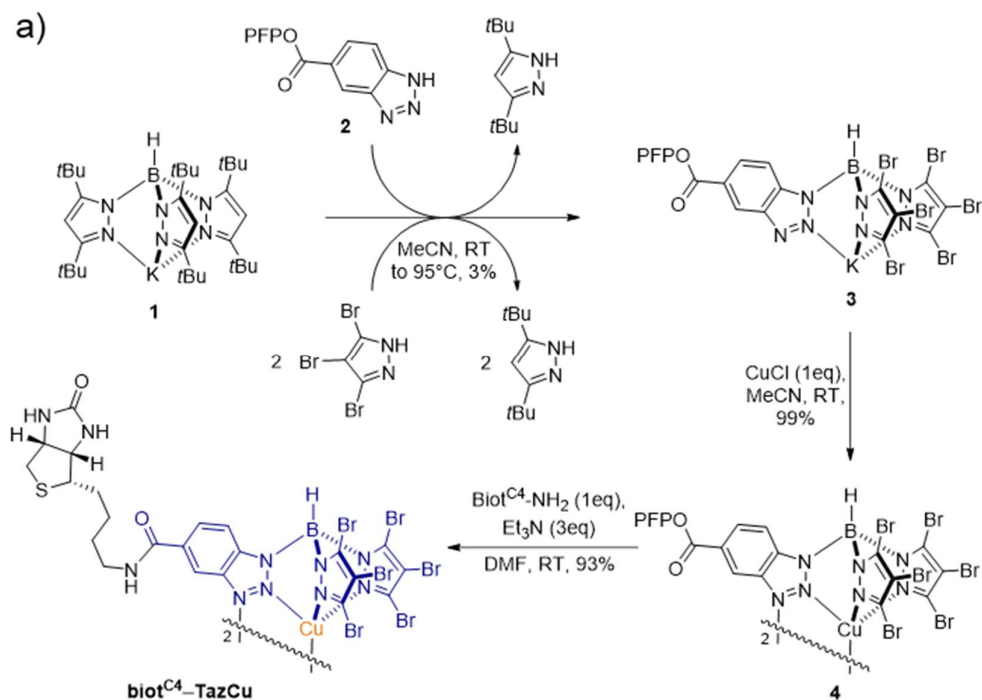
With the aim of combining the benefits of homogeneous and enzymatic catalysts, artificial metalloenzymes (ArMs) have attracted increasing attention since the pioneering work of Wilson and Whitesides.^{14–17} The anchoring of an abiotic catalytic moiety within a protein enables combining attractive assets of both homogeneous and enzymatic catalysis.^{17–21} Certain natural enzymes including S-adenosyl methionine-dependent (SAM) enzymes catalyze the alkylation of C–H bonds. They are however mainly limited to the transfer of methyl groups or highly specific C–C bonds with radical acceptors.^{22,23} Repurposed (natural) enzymes and ArMs offer an attractive means to complement SAM-dependent enzymes for C–H activation purposes.^{21,24–28} Among the most noteworthy achievements in “new-to-nature” C–C bond formation *via* C–H functionalization one should mention: engineered P411,^{29,30} repurposed P450,^{31–34} myoglobin,^{35,36} and streptavidin^{37,38} ArMs. However, examples of highly active C–H insertion biocatalysts that are based on first row transition metals and tolerate aerobic reaction conditions remain scarce. The work presented herein capitalizes on a Cu(I) heteroscorpionate complex to engineer a highly active ArM that catalyses the intramolecular insertion of carbenes into different types of C–H bonds in a regio- and enantioselective fashion.

4.3 Results and Discussion

Cofactor synthesis and computational modelling. The remarkable affinity of biotin for streptavidin ($K_d < 10^{-13}$ M) offers an attractive means to anchor any biotinylated probe within streptavidin (Sav). Several groups have relied on this tool to assemble ArMs.^{14,37–46} A common strategy for the synthesis of anchored Tp complexes relies on the introduction of a fourth substituent on the boron, replacing the hydride moiety.^{47–49} In our hands however, this strategy proved challenging as tetrasubstituted Tp-derivatives bearing electron-deficient pyrazoles revealed insufficient stability. Inspired by the work of Desrochers and coworkers on heterocycle metathesis,⁵⁰ we selected the Tp^(tBu)2K **1** as precursor for the assembly of a biotinylated, electron-deficient TpM-cofactor. The pronounced steric bulk around the boron enabled the selective substitution of the three *tert*-butyl pyrazole groups by the benzotriazole **2** bearing an *asjn* activated ester and two tribromopyrazole moieties to afford the intermediate **3** albeit in

low yield, Scheme 1a. This intermediate was characterized by X-ray crystallography (Figure S1).

Scheme 10. Artificial metalloenzyme for C–H insertion resulting from anchoring a biotinylated copper(I) heteroscorpionate complex in Sav (streptavidin). (a) Synthesis of the cofactor *via* pyrazole/triazole metathesis on $\text{Tp}^{\text{tBu}}_2\text{K}$ **1** and conjugation with a modified biotin anchor to afford the cofactor **biot^{C4}-TazCu**. PFP = pentafluorophenyl; (b) artificial metalloenzyme assembly *via* supramolecular anchoring of **biot^{C4}-TazCu** into Sav. The assembled artificial metalloenzyme catalyzes the formation of β - and γ -lactams *via* intramolecular C–H insertion of carbene intermediates.



Trans-metallation with cuprous chloride yielded compound **4**, which was also characterized by X-ray crystallography (Figure S2). Interestingly, the structure revealed that the benzotriazole coordinates to a second copper center through the third nitrogen to afford a dimeric structure. To ensure additional electron-deficient character to the cofactor, the benzotriazole was equipped with a carboxylate moiety. Coupling to biotin thus required the use of biotin-amine (i.e. **biot^{C4}-NH₂**),⁵¹ rather than biotin, which bears a valeric acid. The biotinylated cofactor **biot^{C4}-TazCu** was assembled by reacting **biot^{C4}-NH₂** with the activated ester **4** to ensure its

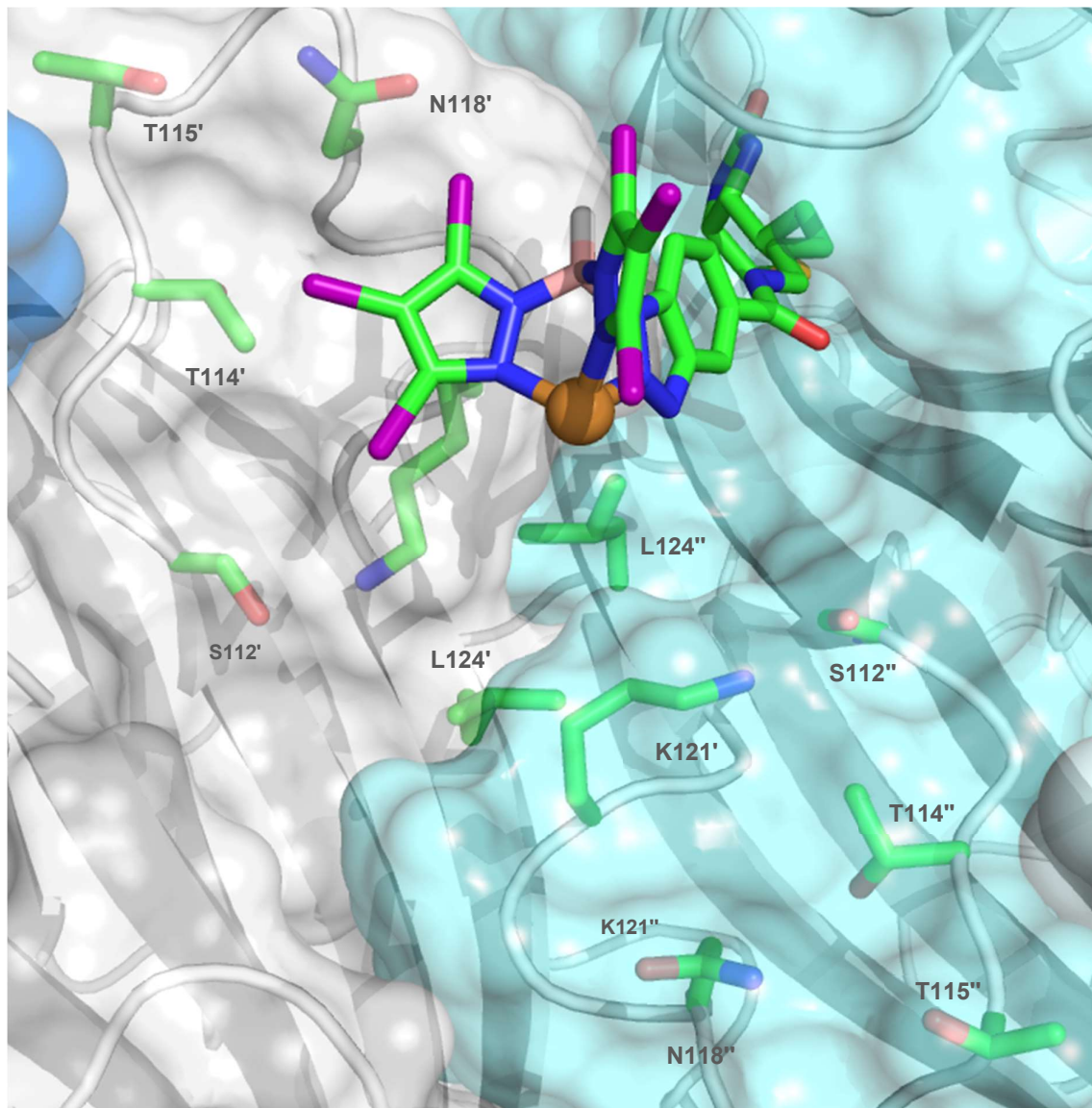


Figure 3. Close-up view of the structure resulting from modelling **biot^{C4}-TazCu** within Sav WT. The cofactor was docked into one monomer (Sav', grey), leaving the adjacent (Sav'', pale blue) binding site empty. Cu—C_β distances (Å) of the closest-lying amino acid: S112' (11.8); T114' (11.9); T115' (14.3); N118' (10.1); K121' (8.1); L124' (13.8); S112'' (10.5); T114'' (12.3); T115'' (15.6); N118'' (12.2); K121'' (9.9); L124'' (12.9). Sav is displayed as a transparent solvent-accessible surface overlaid with a cartoon representation of the 8-stranded β -barrel. Close lying residues and the **biot^{C4}-TazCu** cofactor are displayed as color-coded sticks and Cu as an orange sphere.

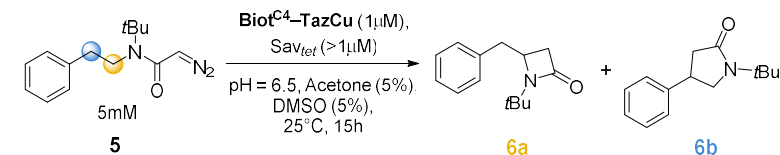
localization within Sav, Scheme 1b. HRMS and detailed NMR analysis enabled unambiguous characterization of the biotinylated cofactor **biot^{C4}–TazCu** (See SI Figures S3-S5).

The quantitative anchoring of the cofactor **biot^{C4}–TazCu** into Sav was assessed *via* CD spectroscopy, Figure S6.⁵² The overall binding affinity relying on a one-to-one binding stoichiometry with the mathematical expression derived in SI (Figure S6).⁵³ The fitted dissociation constant was $K_d = 2,37 \pm 1,40 \cdot 10^{-8} \text{ M}^{-1}$ thus leading to > 99 % of bound **biot^{C4}–TazCu** in the presence of equimolar concentrations of cofactor and tetrameric Sav. Unfortunately, all attempts to crystallize the ArM: **biot^{C4}–TazCu**·Sav WT were vain. Accordingly, we turned to QM/MM calculations to model **biot^{C4}–TazCu**·Sav WT ArM (see SI for details). Both the HABA displacement titration and the QM/MM modelling confirmed that up to four **biot^{C4}–TazCu** cofactors could be accommodated in the homotetrameric host Sav WT. Amino acids that point towards the docked Cu-center include: K121, S112 and L124 with a second, more remote shell that includes T114, T115 and N118, Figure 1. Based on the computed structure, we selected residues K121, S112 and L124 for the genetic optimization of the ArM.

Single mutant screening. Reports by Perez and coworkers suggest that sterically-hindered diazoacetamides are less prone to undergo homocoupling in copper tris(pyrazolyl)borate-catalyzed intramolecular C–H insertion reactions.⁵⁴ The diazoacetamide substrate **5** was selected for initial screening, Table 1. This reaction is of particular interest as it provides a straightforward access to β - and γ -lactams upon C–H insertion. These represent ubiquitous structural motifs in numerous pharmaceutically-relevant compounds.^{55–57} Similarly, Fasan and coworkers reported the stereoselective formation of fused γ -lactams *via* biocatalytic intramolecular cyclopropanation of diazoacetamide.⁵⁸

As the cofactor's activity was affected by the presence of cellular metabolites, we adapted a purification protocol of Sav mutants in 96-well plate based on our streamlined protocol.⁵⁹ Cytoplasmic protein overexpression was carried out in the *E. coli* strain BL21 (DE3) in 24-deep-well plates. Following cell-lysis and centrifugation, the cell-free extract was applied to an iminobiotin-sepharose resin under basic conditions (pH = 10.6, 100 mM carbonate buffer), leading to the immobilization of Sav on the resin. After washing (pH = 7.9, 100 mM MOPS buffer), elution with an acidic solution (pH = 5.5, 100 mM MES buffer) led to protonation of the iminobiotin, thus releasing Sav. Its concentration in the elution buffer was determined *via* a fluorescence assay with biotin-4-fluorescein, Figure S7. Concentrations > 5 μM Sav (tetramer, > 20 μM biotin-binding sites) were obtained for most of the Sav mutants. Early catalytic experiments revealed a decrease in performance with decreasing Sav : **biot^{C4}–TazCu** ratios (i.e. 1 : 1 vs 1 : 4). We surmise that binding of two **biot^{C4}–TazCu** in adjacent biotin-binding

Table 5. Summary of the screening results of **biot^{C4}-TazCu** · Sav K121X for the C–H insertion in the presence of substrate **5**.



Entry	SAV	TON ^a	e.r. ^c	TON ^a	e.r. ^c	r.r. (β/γ)	TTON (yield(%))
1 ^{b, c}	-	ND	-	ND	-	-	ND
2 ^c	Empty vector	91	50:50	280	50:50	24:76	371 (7,4)
3	Empty vector	112	50:50	346	49:51	24:76	458 (9,2)
4	K121A	334	49:51	577	48:52	37:63	912 (18,2)
5	K121I	741	40:60	1708	49:51	30:70	2449 (49,0)
6	K121L	594	36:64	1693	34:66	26:74	2287 (45,7)
7	K121M	109	52:48	317	45:55	26:74	426 (8,5)
8	K121V	550	41:59	1124	50:50	33:67	1674 (33,5)
9	K121F	709	37:63	1449	64:36	33:67	2157 (43,1)
10	K121W	588	38:62	870	49:51	40:60	1458 (29,2)
11	K121Y	718	39:61	923	46:54	44:56	1640 (32,8)
12	K121C	511	44:56	768	50:50	40:60	1280 (25,6)
13	K121N	312	43:57	358	45:55	47:53	670 (13,4)
14	K121Q	390	40:60	506	48:52	44:56	895 (17,9)
15	K121S	547	42:58	645	51:49	46:54	1192 (23,8)
16	K121T	329	41:59	650	45:55	34:66	979 (19,6)
17	K121D	62	48:52	146	52:48	30:70	208 (4,2)
18	K121E	421	40:60	560	52:48	43:57	980 (19,6)
19	K121H	ND	-	ND	-	-	ND
20	WT	ND	-	ND	-	-	ND
21	K121R	ND	-	ND	-	-	ND
22	K121G	455	51:49	753	49:51	38:62	1208 (24,2)
23	K121P	365	50:50	626	55:45	37:63	991 (19,8)

^aDetermined by chiral SFC (supercritical fluid chromatography) using 1,3,5-trimethoxybenzene as internal standard. ^bThe reaction was performed in DCM with 5 % DMSO and 5 % acetone. ^cThe reaction was performed with complex **4** instead of **biot^{C4}-TazCu**. ND = not detected.

sites impedes catalytic activity. Accordingly, an excess of biotin binding sites in the reaction was enforced (e.g. > four equivalents of Sav monomers vs one equivalent of cofactor).

To evaluate the effect of residual cellular debris, a culture of *E. coli* harboring an empty plasmid (i.e. no Sav overexpressed) was subjected to the above iminobiotin purification protocol. The collected eluate was evaluated in catalysis at pH 6.5 in the presence of 1 μM of either complex **4** or **biot^{C4}-TazCu** (0.02 % loading) and the diazoacetamide substrate **5**, Table 1, entry 2 and 3. A 1 : 3 mixture of racemic β : γ lactams **6a** and **6b** was obtained with a total turnover number of 371 and 458 (TTON) respectively. To our disappointment, upon incorporation in WT Sav, no conversion could be detected by SFC, Table 1 (entry 20). As both lysine residues K121 and K121' were computed to lie closest to Cu, we initiated our genetic optimization efforts by mutating this position. Gratifyingly, the ArM **biot^{C4}-TazCu** · Sav K121A proved catalytically active and afforded > 900 TTONs with a 1 : 2 r.r. (β : γ, i.e. **6a** : **6b**) but as a (near) racemate, entry 4. Next, we screened the ArMs resulting from saturation mutagenesis at position Sav

K121X, Table 1. As can be appreciated, the nature of the residue at Sav K121X significantly affects the catalytic performance. From these results, following trends emerge: Positively charged residues at position K121 (Lys, His and Arg) consistently shut down activity (entry 19, 20 and 21). We hypothesize that such close lying, potentially coordinating Lewis basic residue may coordinate to the Cu(I), and prevent the formation of the Cu-carbene moiety. On the other hand, apolar (Ile, Leu and Val) and aromatic residues (Phe, Trp and Tyr) have a beneficial effect on activity (entry 5, 6, 8, 9, 10 and 11). The ArM **biot^{C4}-TazCu** · Sav K121L provided 74 % γ -lactam with the highest enantiomeric ratios (36 : 64 and 34 : 66 for **6a** and **6b**, respectively) of the single mutants (entry 6). ArM **biot^{C4}-TazCu** · Sav K121I displayed the highest activity with 2648 TTON, corresponding to 53 % yield (i.e. assay yield, used throughout unless specified). Polar uncharged residues (Asp, Glu, Asn, Gln, Ser, Thr) generally yielded lower conversions than their apolar counterparts. Interestingly, the mutant bearing an aspartate (entry 17) impeded the reaction much more than its glutamate homologue (entry 18). Similar effects on TON and e.r. could also be observed between the two isosteric residues cysteine and serine (entry 12 and 15). Overall, a large hydrophobic residue at Sav K121I/L/F appeared essential to maximize the three figures of merit TTON, r.r. and e.r. Interestingly, the ArM also afforded non-negligible amounts Büchner ring expansion product depending on the mutant tested (see SI for details). Water insertion and diazo-coupling by-products could be detected by ESI-MS of the catalytic reactions but were not investigated further (Scheme S2). Although reported for C–H bonds of methyl groups in Rh- and TpCu-based catalysts,^{54,60} C–H insertion into the *tert*-butyl group was not detected, thus minimizing the formation of additional regioisomers.

Double saturation mutagenesis. With the aim of identifying synergistic interactions between residues K121 and S112, we set out to screen the double saturation mutagenesis library comprising the four hundred Sav isoforms Sav S112X K121X'. From the four hundred double mutants, 362 could be screened and 220 afforded detectable levels of activity (see Table S2). The general trends observed in the single mutant Sav K121X screening were confirmed for the double mutants. Positively charged residues (His, Lys and Arg) consistently impeded activity, particularly at position K121, where none of the three were tolerated, irrespective of the nature of residue S112X, Figure 2a. Proline and cysteine displayed a deleterious influence as well at both S112 and K121 positions. The unexpected difference between the homologous amino acids aspartate and glutamate was also visible in this screening. The aspartate residue proved to be less advantageous than the glutamate at both positions. An apolar side chain (aliphatic or aromatic) at position K121 turned out to be an absolute requirement to obtain a higher activity of the ArM. While the two isoforms leucine and isoleucine provided comparable levels of activity at position K121 and S112, a pronounced difference in enantioselectivity was observed, Figure 2b and 2c. The leucine residue afforded much higher levels of enantio-

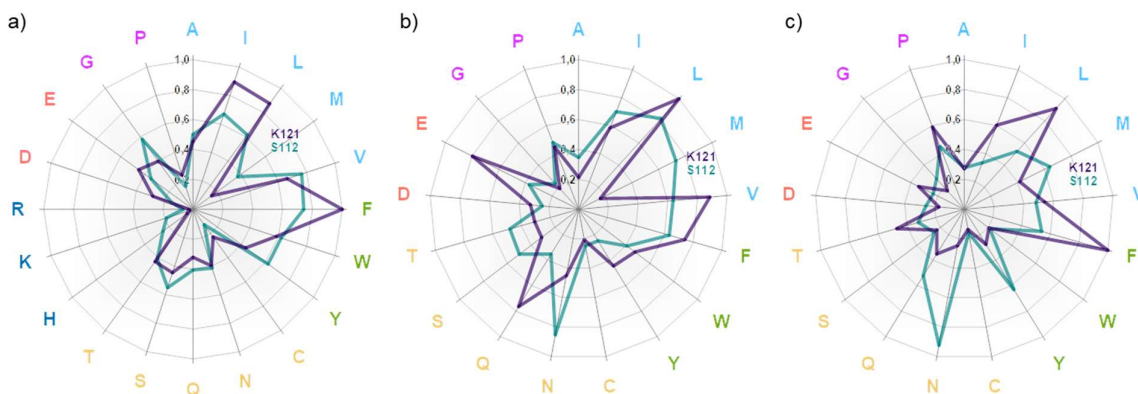


Figure 4. Relative contribution of each amino acid at position S112 and K121 to: a) TON for C–H insertion (average of all the double mutants for a respective mutation); (b) and (c) enantio-induction for the β -lactam **6a** and the γ -lactam **6b** respectively (average of the absolute enantiomeric excess value for all the double mutants with a respective mutation). Amino acids with similar properties are highlighted in the same color (light blue: apolar; green: aromatic; yellow: polar non-ionic; dark blue: basic; red: acidic; purple: special). The enantioselectivity obtained with residues H, K and R are not displayed due to the very low conversions.

induction for both the β -lactam **6a** and the γ -lactam **6b** on average. The asparagine at position S112 appeared to be crucial for enantioselectivity for both reaction products. Among other occurrences, K121V, K121E and K121Q had a positive influence for the enantioselective formation of **6a** but turned out to be less relevant for the other regioisomer **6b**.

To help identify a suitable double mutant to subject to another round of directed evolution, we analyzed e.r., r.r. and TTON by displaying the e.r. vs r.r. for the γ -lactam (+)-**6b**, Figure 3. The absolute configuration of the γ -lactam (+)-**6b** was determined as (S)-**6b** by comparison with the secondary amide (deprotected, following treatment of (+)-**6b** with TFA).⁶¹ The data reveal a clear trend for the functionalization of the benzylic position. Both enantiomers of the γ -lactam **6b** could be accessed, albeit with a higher enantioselectivity for the (S)-**6b**. Interestingly, mutation of the K121L to K121F while conserving the S112M residue allowed to invert the enantioselectivity from 28 : 72 to 91 : 9 e.r. Variants S112N-K121L and S112N-K121I revealed similar performance. Strikingly, substitution of S112N for S112Q led to an inversion of enantioselectivity (e.g. S112N K121L/I and S112Q K121L/I afford (S)-**6b** and (R)-**6b**, respectively). Of note, a pronounced difference in regioselectivity was observed between S112Q-K121L and S112Q-K121I, the former clearly favoring the formation of the γ -lactam **6b**, Figure 3.

High levels of activity, regioselectivity and enantioselectivity could be obtained with the S112N-K121V variant (86 : 14 e.r., 80 % regioselectivity and 2731 TTON). On average, the valine residue did not display as high levels of enantioselectivity as leucine or phenylalanine for **6b**,

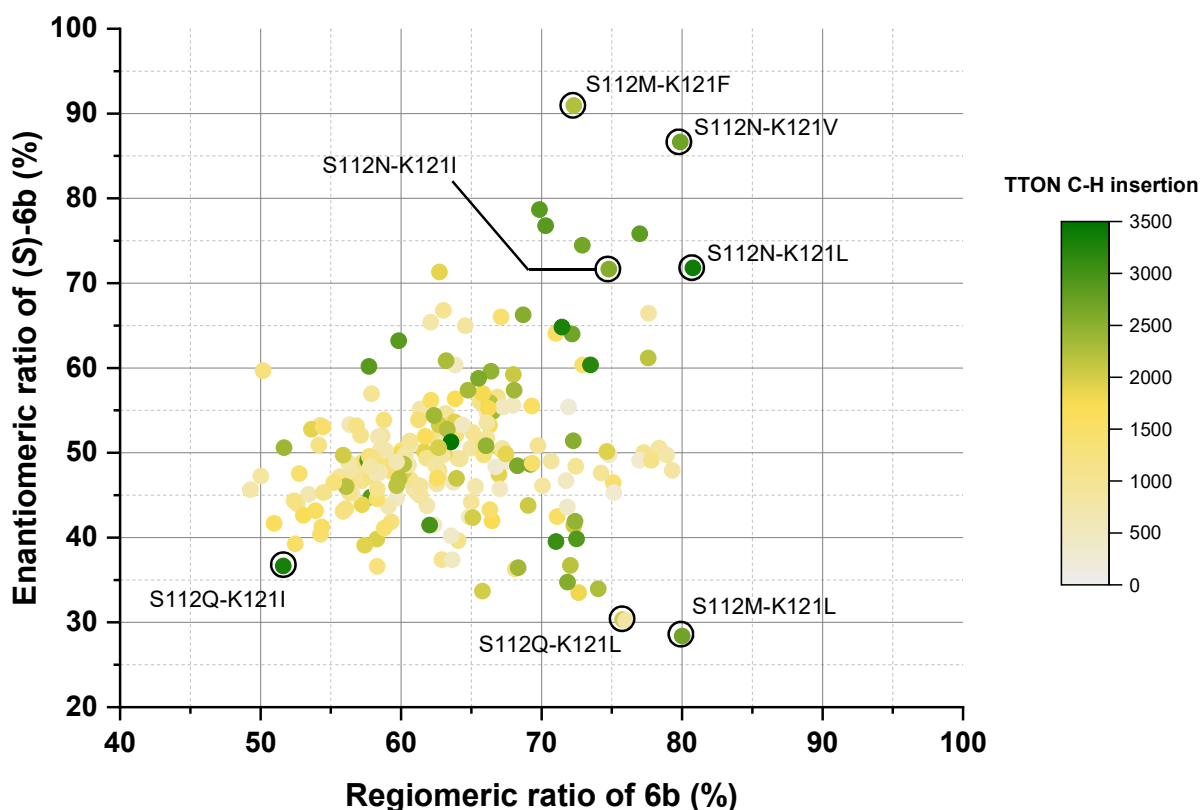


Figure 5. Graphical summary of the screening results of **biot^{C4}-TazCu · Sav S112X K121X'** for the C–H insertion of substrate **5** to afford lactams **6a** and **6b**. The axes display the enantiomeric- and the regiomic ratios of the γ -lactam (S)-**6b**. Key mutations leading to high e.r. and r.r. include asparagine and methionine at position S112 and a hydrophobic residue at K121.

Figure 2c. This finding highlights the importance of cooperative effects between sites and would not have been identified with an iterative single site saturation strategy.

The β -lactam **6a** product could not be obtained in > 51% r.r. and modest conversion (<10%, < 500 TON). The higher bond dissociation energy of the amide's vicinal C–H bond (BDE \approx 93 kcal/mol vs 87 kcal/mol for the benzylic C–H bond, predicted with ALFABET from the corresponding acetamide)⁶² and the ring strain in the transition state leading the 4-membered β -lactam **6a** both favor the formation of the γ -lactam **6b**. In some occurrences, considerable amounts of Büchner ring-expansion product were detected. This was particularly pronounced when position S112 contained an aromatic residue (i.e. S112Y or S112F: up to 1783 TON for S112F-K121I, Figure S8, Table S2). The second coordination sphere of Sav could also induce enantioselectivity for this transformation (up to 24 : 76 e.r. for S112F-K121I). Detailed data for selected mutants are collected in Table S3.

L124 saturation mutagenesis and substrate scope. Critical inspection of the results of the double saturation mutagenesis screening led us to select the double mutant Sav S112N-

K121V for the next round of directed evolution, focusing on residue Sav L124. A library encoding all twenty amino acids was prepared, relying on NDT, VMA, ATG and TGG codons. The screening revealed that the size of the amino acid at position L124 had a significant impact on both the e.r and r.r. The triple mutant Sav S112N-K121V-L124I led to slightly improved e.r. (88 : 12) and r.r (14 : 86) for the γ -lactam (*S*)-**6b**, Figure 4. Strikingly, substitution of the bulky hydrophobic L121I residue by a glycine, Sav S112N-K121V-L124G, led to the preferential formation of the β -lactam **6a** with 65 : 35 r.r. (compared to 19 : 81 for the parent double mutant) at the cost of a lower TTON. Interestingly, the enantioselectivity was reversed, favoring the β -lactam (*-*)-**6a** (identified as the (*R*)-enantiomer by VCD spectrometry, see SI for details). Attempts to further improve the catalytic performance by applying site-saturation mutagenesis at positions T114, T115 and N118 did not lead to any improvement for either TTON, r.r. or e.r. To further investigate the performance of the earth-abundant ArM, we selected substrates with either a shorter or longer aliphatic chain, Table 2. Substrate **7** yielded the corresponding β -lactam (+)-**8a** (corresponding to (*R*)-**8a**)⁶³ in 1290 TON and e.r. of 79 : 21 with **biot**^{C4}—**TazCu**·Sav S112N-K121L. To verify if the selective formation of the γ -lactam **6b** was

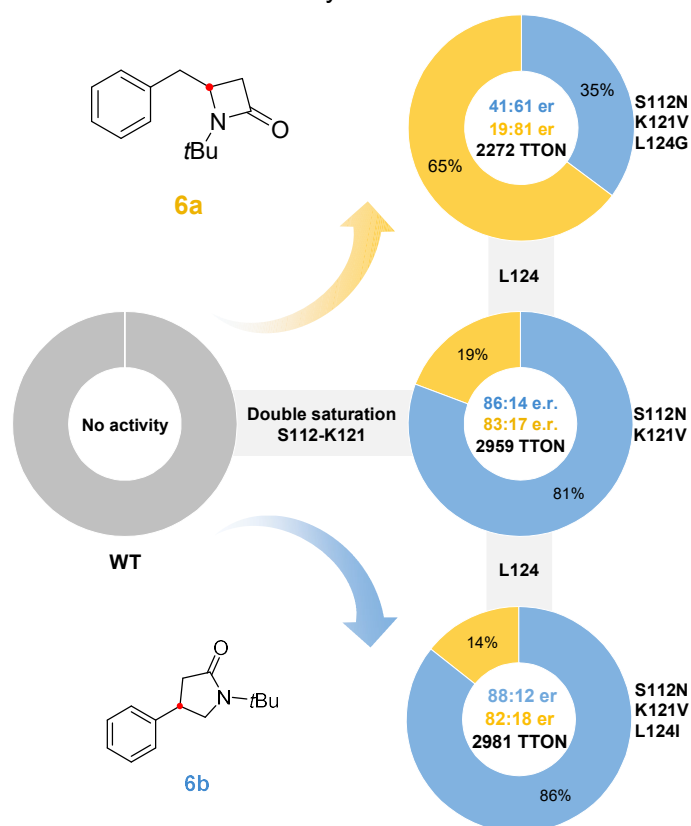
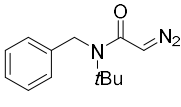
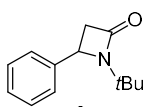
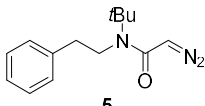
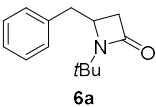
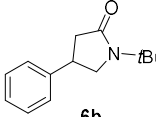
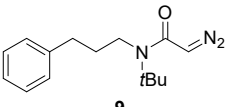
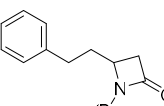
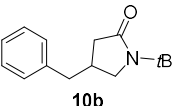
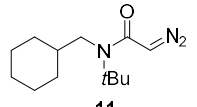
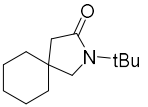


Figure 6. Evolutionary lineage of the ArM for regio- and enantioselective C–H insertion. Initial double saturation mutagenesis on WT Sav to identify improved double mutants was followed by single-site saturation mutagenesis at position L124. Mutation of L124 with an isoleucine slightly increased the selectivity of the ArM for the γ -lactam (*S*)-**6b**, while a glycine residue favors the β -lactam (*-*)-**6a**. The data are the average of biological triplicates.

Table 6. Selected results for the intramolecular C–H insertion catalyzed by **biot**^{C4}–**TazCu** · Sav mutants.^a

Substrate	Product	Mutant	e.r. (+/-)	r.r. (β/γ)	TTON (Yield (%)) ^b
		S112N-K121L	79:21	-	1290 (25.8)
		S112N-K121V-L124G	19:81	65:35	2272 (45.4)
		S112N-K121V-L124I	88:12	14:86	2981 ^c (59.6)
		S112N-K121V-L124G	37:63	28:72	2623 (52.5)
		S112N-K121V	27:73	12:88	3585 (71.7)
		S112N-K121L	-	0:100	4627 (92.5) ^d

^aConditions : 5 mM substrate, 1 μM **biot**^{C4}–**TazCu**, >1 μM Sav_{tet}, 35 mM MES pH 5.5, 10 % acetone, 5 % DMSO, 15 h at 25 °C under air. ^b47% yield on preparative scale (12 mg), see Figure S9 and S10. ^cYield determined by ¹H-NMR with 1,3,5-trimethoxybenzene as internal standard.

caused by the lower BDE of the benzylic C–H bond (BDE ≈ 87 kcal/mol, predicted with ALFABET from the corresponding acetamide),⁶² we also subjected substrate **9** bearing a propylene spacer (BDE ≈ 96 kcal/mol for the homobenzylic C–H bond) to the transformation. To our delight, the γ-lactam **10b** was obtained with 3585 TON, 88% regioselectivity and 27 : 73 e.r with **biot**^{C4}–**TazCu** · Sav S112N-K121V. However, regioselectivity could not be tuned to favor the β-lactam **10a** when **biot**^{C4}–**TazCu** · Sav S112N-K121V-L124G was used: only a modest increase from 12 % to 28 % β-lactam **10a** was observed. The ArM also catalyzed the carbene insertion into a tertiary C–H bond (BDE ≈ 93 kcal/mol)⁶² with high efficiency: **biot**^{C4}–**TazCu** · Sav S112N-K121L afforded the spirocyclic γ-lactam **12b** in 93 % yield and 4627 TON. The four-membered ring regioisomer could not be detected either by ¹H NMR or HPLC. A selection of *para*-substituted derivatives of substrate **5** was also tested. Significantly lower TON and selectivities were observed, independently of the nature of the substituent. This

highlights a preference of the ArM for unsubstituted phenyl rings. Detailed data are collected in Table S4.

4.4 Conclusion

While Tp complexes can efficiently functionalize inert sp^3 C–H bonds by insertion of a reactive carbene intermediate, the absence of interactions between the metal and the substrate render the selectivity of the reaction challenging to control. This study reveals that this challenge can be addressed by providing a well-structured second coordination sphere around the transition state. The synthesis of a modified biotin-bearing copper(I) heteroscorpionate enabled its incorporation into a genetically-evolvable host protein. The resulting ArM catalyzes the enantio- and regioselective formation of β - and γ -lactams *via* the insertion of a carbene intermediate into secondary and tertiary sp^3 C–H bonds. Double saturation mutagenesis and directed evolution at a third position shed light on individual amino acid contributions to the cofactor's activity. TONs up to 4627 (corresponding to 93% yield) in the case of the C–H insertion into a cyclohexyl substituent were achieved. We envision that the use of the highly versatile scorpionate complexes for ArMs could open new opportunities to expand the enzymatic repertoire of C–H functionalization strategies, based on earth-abundant metal cofactor.

4.5 Supporting information

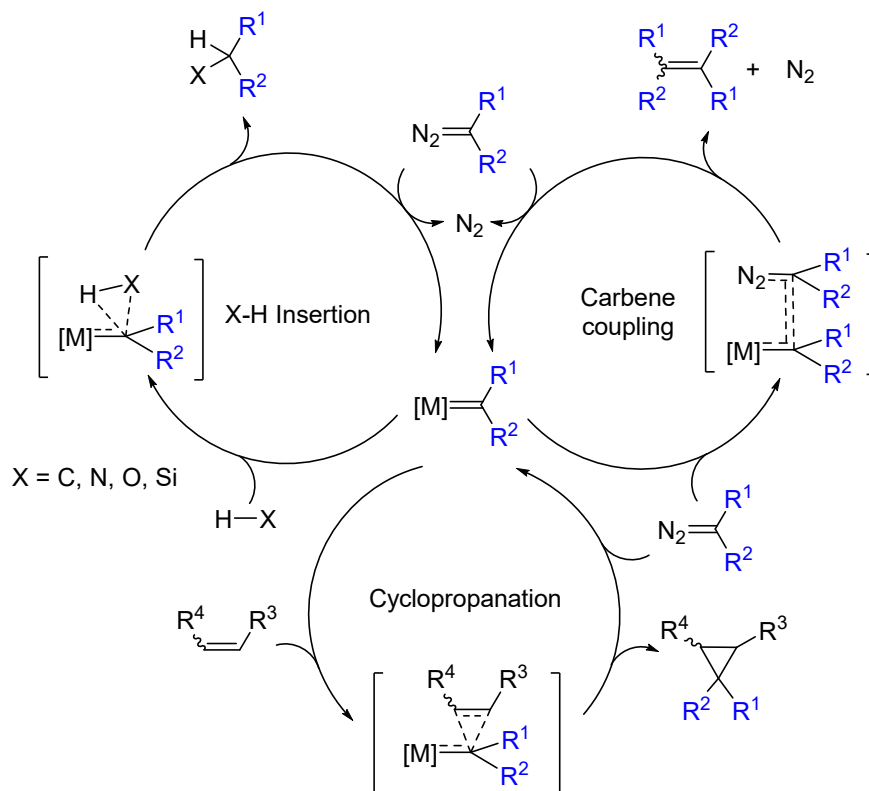
4.5.1 General methods

Commercially available chemicals were purchased from the following suppliers and used without further purification: Acros Organics, Alfa Aesar, Combi Blocks Fluorochem, Sigma Aldrich. $\text{KTp}^{(\text{tBu})_2}$ (**1**),⁶⁴ 3,4,5-Tribromopyrazole,⁶⁵ $\text{CuTp}^{\text{Br}_3}$,⁶⁶ and $\text{Biot}^{\text{C}_4}\text{-NH}_3\text{Cl}$,⁵¹ were synthesized according to reported procedures. Dry solvents were purchased from Acros Organics and used without further purification. The water used for all biological and catalytic experiments was purified with a Milli-Q Advantage system. All catalytic experiments were performed in 2 mL glass vials under air in non-degassed solvents. Flash chromatography was carried out on silica gel. The relative configuration of all chiral compounds was determined by separation of the corresponding racemic mixture *via* preparative HPLC. Compounds **6a**, **7a**, and **8b** were separated with a semi-preparative Chiralpak IH column using

Hexane/isopropanol. Compounds **7b** and **8a** were separated with a semi-preparative Dr. Maisch chiral OM column using Hexane/isopropanol. VCD spectroscopy was performed by WuXiAppTec, Wuhan China.

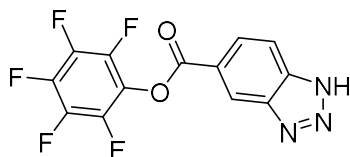
^1H NMR (500 MHz), ^{13}C NMR (125 MHz) and ^{19}F (471 MHz) spectra were recorded on a Bruker Avance Neo spectrometer at room temperature unless stated otherwise. Chemical shifts are reported in ppm (parts per million) relative to TMS ($\delta = 0.00$ ppm for ^1H and ^{13}C) or CFCl_3 ($\delta = 0.00$ ppm for ^{19}F) and multiplicity quoted as follows: s = singlet, d = doublet, t = triplet, q = quartet, bs = broad singlet, dd = doublet of doublet and m = multiplet. Spectra were analysed on MestReNova and calibrated relative to the residual solvent peak or TMS. Routine MS analysis were performed on a Shimadzu LCMS 2020 in H_2O (0.1% formic acid) or MeCN (0.1% formic acid) for the positive mode and MeOH for the negative mode. HRMS analysis were performed by the analytical facility of the University of Basel. Catalytic experiments were analysed by SFC (supercritical fluid chromatography) on a Waters Acquity UPC2. Fluorescence assays were performed on a Tecan fluorimeter Infinite M1000Pro and the corresponding samples were prepared in 96-well plate ThermoFischer Scientific Nunclon 96 Flat Black. CD (circular dichroism) spectra were recorded on a Chirascan from Applied Photophysics at 25 °C using a quartz cell (1 cm path length). Optical rotations were acquired using an Anton Paar MCP100 polarimeter in a 10 cm cell. Flash chromatography was performed on a Biotage Isolera. Preparative chromatography was performed on a Büchi Pure chromatography system.

4.5.2 Carbene Insertion



Scheme S1. Proposed mechanisms of selected TpM-catalyzed carbene transfer reactions.⁶⁷

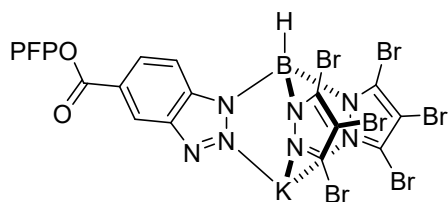
4.5.3 Cofactor synthesis



2

Pentafluorophenyl trifluoroacetate (1.03 mL, 6 mmol) was added dropwise at 0°C to a solution of benzotriazole-5-carboxylic acid (979 mg, 6 mmol) and triethylamine (1.26 mL, 9 mmol) in dry DMF (20 mL). The reaction was stirred (1.5 h at 0 °C) and the DMF was removed under reduced pressure. The crude mixture was dissolved in dichloromethane (30 mL) and washed with water once. The organic layer was dried over MgSO₄ and the solvent removed under reduced pressure to afford a reddish solid. The crude product was purified by flash chromatography (DCM/MeOH, 0 to 7 %) to afford 831 mg of benzotriazole **2** as an off-white solid in 42 % yield.

^1H NMR (600 MHz, CD_3OD , 298 K) δ 8.90 (s, 1H), 8.28 (d, 1H), 8.03 (d, 1H). ^{13}C NMR (125 MHz, CD_3OD , 298 K) δ 128.43 (1C), 122.15 (1C), 114.90 (1C). ^{19}F NMR (471 MHz, CD_3OD , 298 K) δ 155.52 (d, 2F), 160.97 (t, 1F), 165.53 (t, 2F). HRMS (ESI positive mode, m/z): calculated for $\text{C}_{13}\text{H}_5\text{F}_5\text{N}_3\text{O}_2$ $[\text{M}-\text{H}]^+$ 330.0296; found 330.0325.



3

Benzotriazole-PFP (**2**) (411 mg, 1.25 mmol) was placed in a glass pressure tube and dissolved in dry MeCN (15 mL). The tris(pyrazolyl)borate $\text{KTp}^{(\text{tBu})_2}$ (**1**) (736 mg, 1.25 mmol) was added in one portion and the reaction stirred for 10 min at RT. Tribromopyrazole (1.91g, 6.25 mmol) was added in one portion and the pressure tube was sealed. The reaction was heated to 95 °C for 4 h. The solvent was removed under reduced pressure and the crude mixture was purified by flash chromatography using EtOAc/petroleum ether (0:100 to 30:70). In case mixed fractions of the product and the substrate **2** were obtained, a second column with MeCN/DCM (0:100 to 30:70) was performed to afford 35 mg of **3** (3 % yield) after MS analysis (negative mode in MeOH) of each individual fraction.

^1H NMR (400 MHz, CD_3OD , 298 K) δ 8.85 (s, 1H), 8.10 (d, 1H), 7.49 (d, 1H). ^{13}C NMR (125 MHz, CD_3OD , 298 K) δ 127.50 (1C), 123.36 (1C), 115.03 (1C). ^{19}F NMR (471 MHz, CD_3OD , 298 K) δ 155.65 (d, 2F), 161.66 (t, 1F), 166.13 (t, 2F). HRMS (ESI positive mode, m/z): calculated for $\text{C}_{19}\text{H}_5\text{BBr}_6\text{F}_5\text{N}_7\text{O}_2\text{Na}$ $[\text{M}-\text{H}]^+$ 971.5449; found 971.5438.

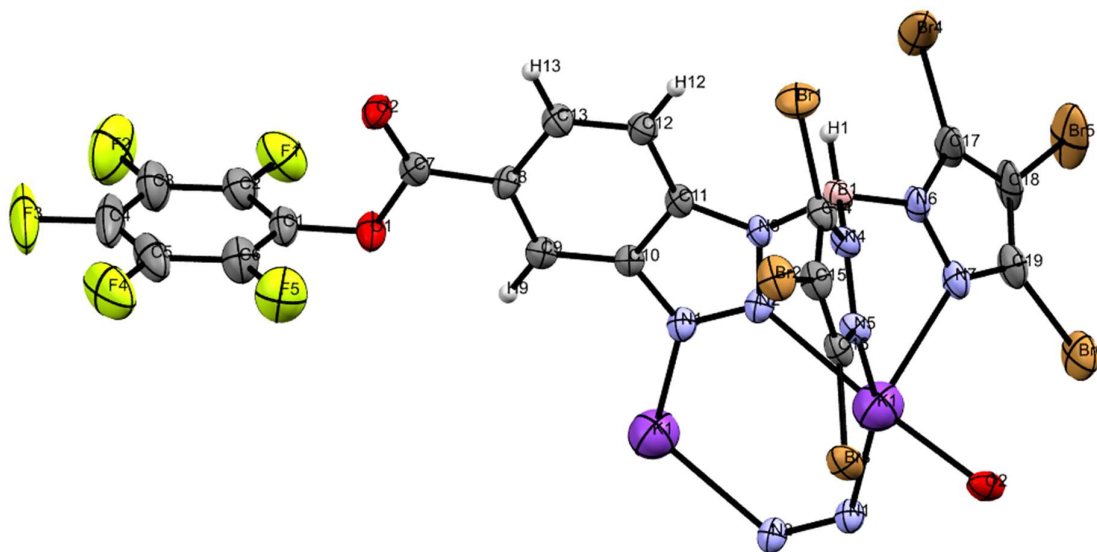
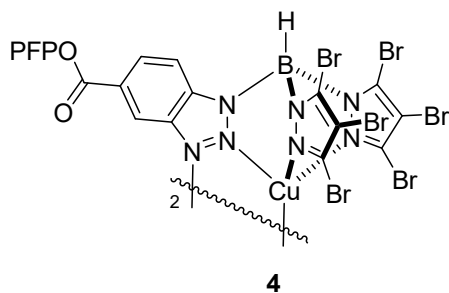


Figure S1: Molecular structure of **3** (CCDC: 2151848). Single crystals were obtained by slow evaporation of a diethyl ether solution. See section 4.5.15 for detailed X-ray data.



The heteroscorpionate **3** (35 mg, 0.035 mmol) was dissolved in dry MeCN (4 mL) under nitrogen, and a solution of CuCl (3.5 mg, 0.035 mmol) in dry MeCN (1 mL) was added at RT. The reaction was stirred overnight. The yellow precipitate was dissolved by addition of 10 mL of DCM and the mixture was filtered through celite. The solvent was removed under reduced pressure to afford 36 mg of title compound **4** in quantitative yield.

^1H NMR (600 MHz, DMSO- d_6 , 298 K) δ 8.93 (br. s, 1H), 8.08 (br. s., 1H), 7.60 (br. s., 1 H). ^{19}F NMR (471 MHz, DMSO- d_6 , 298 K) δ 153.36 (d, 2F), 157.69 (t, 1F), 162.39 (t, 2 F). HRMS (ESI positive mode, m/z): calculated for $\text{C}_{19}\text{H}_5\text{BBr}_6\text{F}_5\text{N}_7\text{O}_2\text{Cu}$ $[\text{M}-\text{H}]^+$ 1011.4848; found 1011.4838.

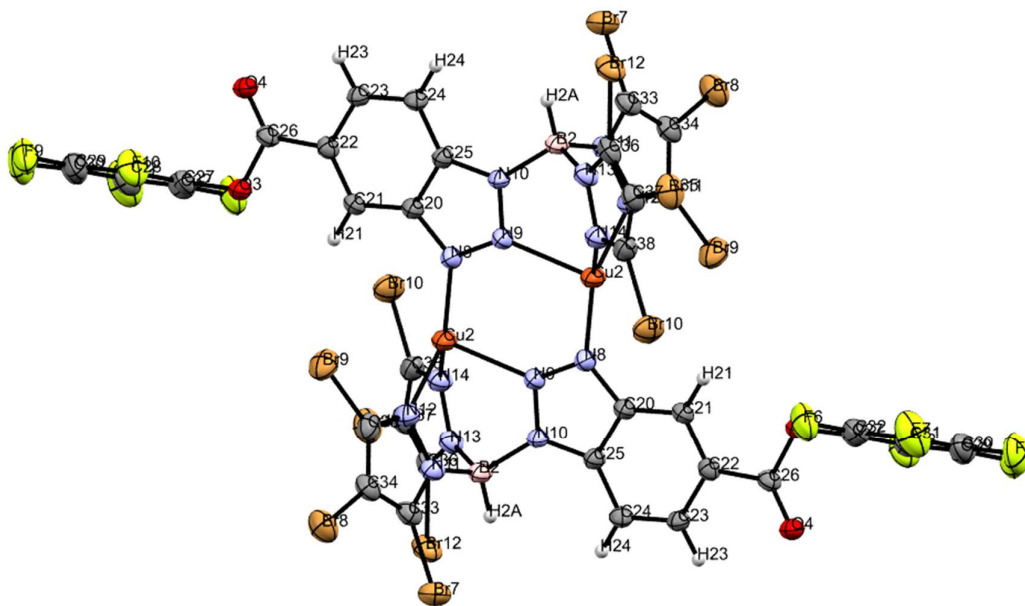
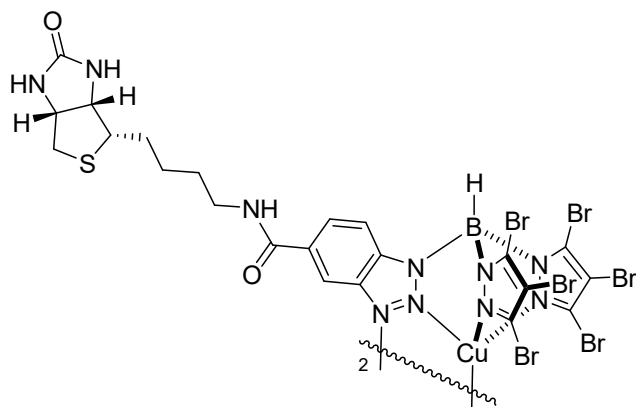


Figure S2: Molecular structure of dinuclear complex **4** (CCDC: 2151849). Single crystals were obtained with the following crystallization method: A DCM/MeCN solution of **4** in a vial was placed inside a chamber containing MeCN. Slow evaporation of the DCM and increasing concentration of MeCN afforded X-ray quality crystals. See section 4.5.15 for detailed X-ray data.



5

A suspension of biotin^{C4}-NH₃Cl (8.3 mg, 0.033 mmol) and Et₃N (12.6 μ L, 0.090 mmol) in dry DMF (1 mL) was added to a solution of the copper complex **4** (30.3 mg, 0.030 mmol) in dry DMF (2 mL) under nitrogen. The reaction was stirred 5 h at RT and the conversion assessed by MS (negative mode). The solvent was removed under reduced pressure and the residue was dried for one hour under high vacuum.

The crude product was then washed (suspended, sonicated and centrifuged) three times with DCM and once with MeOH to afford 29 mg of **Biot^{C4}—TazCu** (93 % yield) as a pale yellow-green powder. Although the compound displayed very good stability under air, it was stored at 5 °C under nitrogen.

¹H NMR (600 MHz, DMF-d₇, 248 K) δ 9.27 (br. s, 1H), 9.21 (s, 1H), 8.55 (d, 1H), 8.35 (d, 1H), 6.75 (br. s, 1H), 6.65 (br. s., 1H), 5.87 (br. s, 1H), 4.51 (s, 1H), 4.33 (s, 1H), 3.51 (m, 1H), 3.42 (m, 1H), 3.24 (m, 1H), 2.93 (m, 1H), 2.70 (m, 1H), 1.76 – 1.47 (m, 6H). ¹³C NMR (125 MHz, DMF-d₇, 248 K) δ 164.99 (1C), 163.62 (1C), 143.16 (1C), 138.84 (1C), 133.27 (1C), 129.26 (1C), 117.76 (1C), 112.83, (1C), 61.58 (1C), 60.02 (1C), 56.50 (1C), 40.53 (1C), 39.76, (1C), 29.73 (1C), 28.59 (1C), 26.83 (1C). HRMS (ESI positive mode, m/z): calculated for C₄₄H₄₀B₂Br₁₂Cu₂N₂₀O₄S₂Na [M-Na]⁺ 2108.1711; found 2108.1737.

4.5.4 NMR experiments on the cofactor

Biot^{C4}—TazCu showed relatively broad resonances in the proton NMR (600 MHz, DMF-d₇, 298 K) suggesting a dynamic process. Therefore, variable temperature spectra were recorded in the range between 378 and 238 K. While the high temperature proton spectra clearly displayed a coalescent phenomenon, it was not possible to reach the fast exchange regime with sharp peaks due to sample instabilities above 378 K, Figure S3. In contrast, on cooling the sample, two sets of signals were obtained – one with very well resolved, sharp lines, and another, relatively broad set, suggesting a borotropic rearrangement of the benzotriazole.⁶⁸ At 248 K, the best resolution was obtained in the proton spectra, Figure S4. Accordingly, all 2-

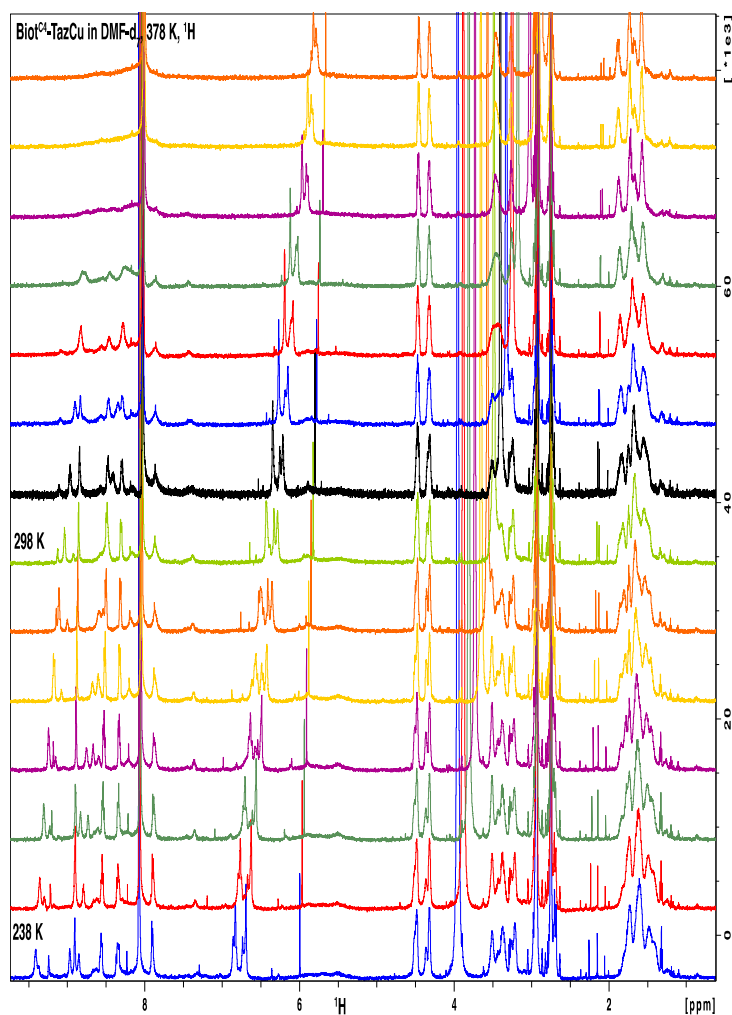


Figure S3. ^1H -NMR recorded in DMF- d_7 at a temperature ranging from 238 K to 378 K.

dimensional NMR experiments (NOESY, HSQC, HMBC) were recorded at 248 K. The borane-H appeared as a broad featureless hump at ca. 5.9 ppm due to coupling with the quadrupolar nuclei ^{11}B and ^{10}B . On decoupling at a ^{11}B shift of -10 ppm during the acquisition (inverse gating), a sharp resonance at 5.87 ppm was observed (see section IX).

HSQC spectra (see section IX) at 248 K showed the expected number and chemical shifts for all C–H carbon atoms, whereas the second set of peaks was too broad for efficient H–C magnetisation transfer and, thus, did not yield any cross peaks. HMBC spectra (not displayed) at 248 K corroborated the connectivity of **Biot^{C4}–TazCu**. A ^{11}B -decoupled noesy (see section IX) spectrum allowed the unambiguous assignment of all protons, where key NOEs are highlighted, Figure S5.

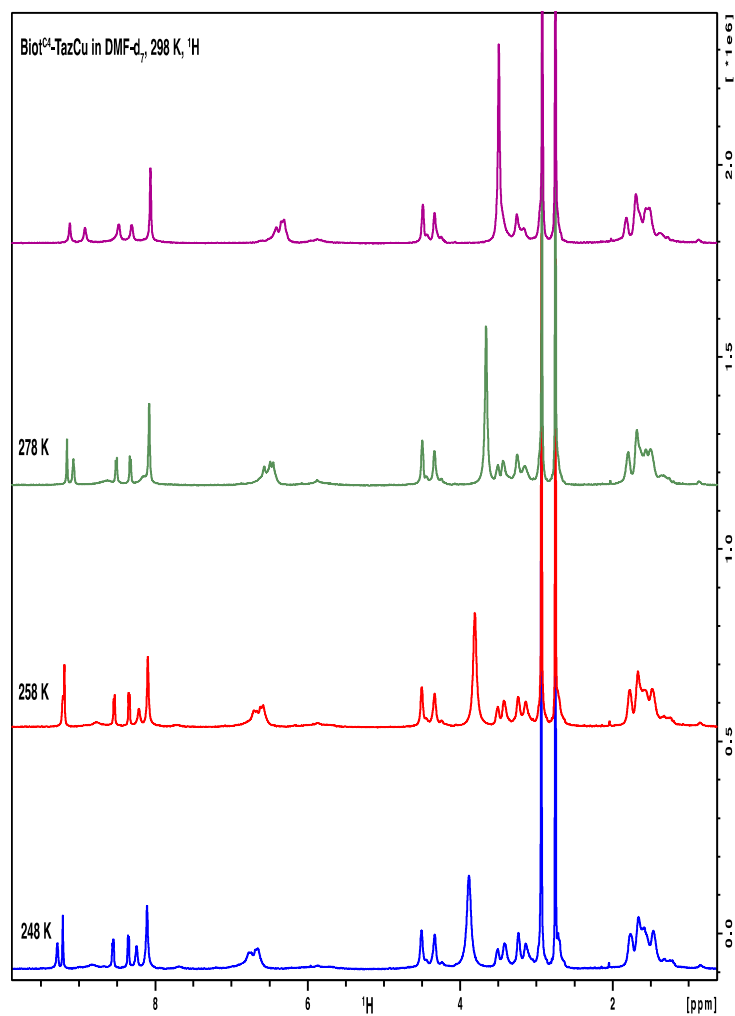


Figure S4. Close-up view of the ^1H -NMR spectra at 248, 258, 278 and 298 K.

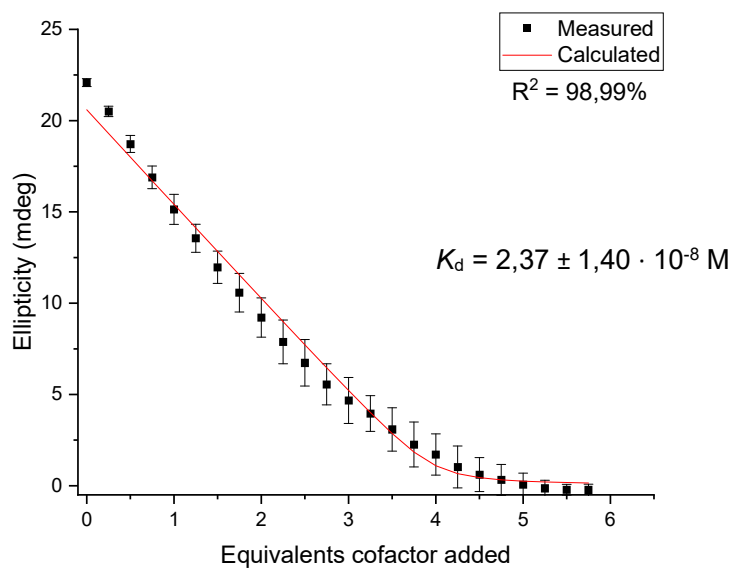


Figure S6: Determination of the binding constant of **Biot^{C4}-TazCu** for streptavidin by monitoring the CD signal at 506 nm resulting from HABA displacement. The black squares correspond to the measured CD signal. The red curve corresponds to the fitting, relying on the same K_d for all four binding events.

The fitting was performed as described by Wang: *A mathematical expression for describing competitive binding of two different ligands to a protein molecule.*⁵³

$$A = (K_a + K_b + C_a + X - C_p)$$

$$B = (K_b \cdot (C_a - C_p) + K_a \cdot (X - C_p) + K_a \cdot K_b)$$

$$\theta = (\arccos((-2 \cdot (K_a + K_b + C_a + X - C_p)^3 + 9 \cdot (K_a + K_b + C_a + X - C_p) \cdot (K_b \cdot (C_a - C_p) + K_a \cdot (X - C_p) + K_a \cdot K_b) - 27 \cdot (-K_a \cdot K_b \cdot C_p)) / (2 \cdot \sqrt{((K_a + K_b + C_a + X - C_p)^2 - 3 \cdot (K_b \cdot (C_a - C_p) + K_a \cdot (X - C_p) + K_a \cdot K_b))^3})))$$

$$C_{\text{bound}} = C_a \cdot (2 \cdot \sqrt{A^2 - 3 \cdot B}) \cdot \cos(\theta/3) - A / (3 \cdot K_a + (2 \cdot \sqrt{A^2 - 3 \cdot B}) \cdot \cos(\theta/3) - A)$$

$$C_{\text{free}} = C_a - C_{\text{bound}}$$

$$Y = C_{\text{bound}} \cdot E_{\text{bound}} + \text{Baseline}$$

Abbreviations:

$$K_a = K_{\text{HABA}}$$

$$K_b = K_{\text{Cofactor}}$$

$$C_a = [\text{HABA}]_{\text{total}}$$

$$X = [\text{Cofactor}]_{\text{total}}$$

$$C_p = [\text{Sav}_{\text{mono}}]_{\text{total}}$$

$$C_{\text{bound}} = [\text{HABA} \cdot \text{Sav}]$$

E_{bound} = Extinction coefficient

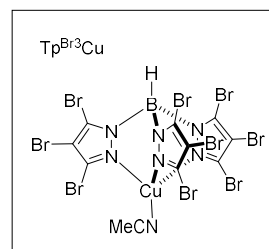
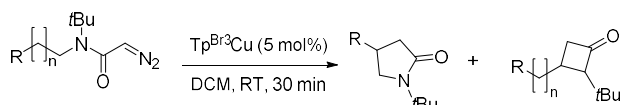
Y = Calculated signal

4.5.6 QM/MM calculations

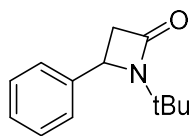
For the protein structure, the crystal structure (PDB 6FH8, tetramer, biological assembly) was processed with PDB2PQR server⁶⁹ to assign H atoms at pH 7.4. Then the pair of the catalyst structures were added to one of the dimers with the coordination of biotin moiety fixed to the crystal structure. The protein-catalyst hybrid structures were optimized by a 2-layer ONIOM method with Gaussian09.⁷⁰ The calculations were performed at the level of ONIOM(PM6:UFF) without any symmetry consideration. The high layer included the catalyst moiety of the molecule. For the low layer, atomic charges of the catalyst were calculated at the level B3LYP/6-31G(d). In the structural optimization, only the atoms within 8 Å of the high layer atoms were allowed to relax.

4.5.7 Substrates and catalysis products

Substrates were synthesized according to a reported procedure⁷¹. The catalysis products were synthesized on a large scale with following procedure:



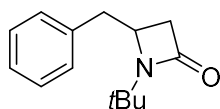
A solution of TpBr_3Cu (0.05 mmol, 50 mg) in dry DCM (2 mL) was slowly added to a solution of diazo compound (1 mmol) in dry DCM (35 mL). Nitrogen evolution was immediately visible. After 1 h, the solvent was removed under reduced pressure and the crude product was purified by flash chromatography with petroleum-ether/EtOAc (100:0 to 70:30).



8a The NMR signals correspond to the literature characterization.⁷¹

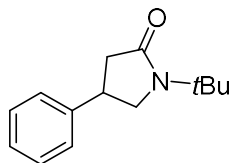
¹H NMR (400 MHz, CDCl₃, 298 K) δ 7.40 – 7.28 (m, 5H), 4.56 (m, 1H), 3.23 (dd, 1H), 2.66 (dd, 1H), 1.24 (s, 9H). ¹³C NMR (125 MHz, CDCl₃, 298 K) δ 167.59, 141.40, 128.95, 128.35, 126.50, 54.80, 53.28, 46.17, 28.31.

Chiral HPLC: Chiralpak IF[®], 4.6 x 250 mm; isocratic, 7 % MeOH in CO₂, 2 mL/min, 210 nm; t_r ((-)-**8a**) = 4.14 min, t_r ((+)-**8a**) = 4.54 min. [α]_D²⁵: -123.4 ° (c = 0.44, CHCl₃); lit. (S)-**7a**: [α]_D²⁵: -127.7 ° (c = 0.5, CHCl₃).⁶³



6a ¹H NMR (400 MHz, CDCl₃, 298 K) δ 7.31 (t, 2H), 7.24 (t, 1H), 7.17 (d, 2H), 3.82 (m, 1H), 3.39 (dd, 1H), 2.76 (dd, 1H), 2.64 (dd, 1H), 2.47 (dd, 1H), 1.43 (s, 9H). ¹³C NMR (125 MHz, CDCl₃, 298 K) δ 166.73, 137.39, 128.89, 128.85, 126.93, 54.30, 51.41, 42.06, 41.21, 28.65. HRMS (ESI positive mode, m/z): calculated for C₁₄H₁₉NONa [M-Na]⁺ 240.1359; found 240.1362.

Chiral HPLC: Chiralpak IF[®], 4.6 x 250 mm; isocratic, 7 % MeOH in CO₂, 2 mL/min, 210 nm; t_r ((-)-**6a**) = 5.08 min, t_r ((+)-**6a**) = 6.1 min. [α]_D²⁰: -73.8 ° (c = 0.26, CHCl₃).

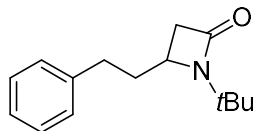


6b The NMR signals correspond to the literature characterization.⁷²

¹H NMR (400 MHz, CDCl₃, 298 K) δ 7.34 (t, 2H), 7.24 (m, 3H), 3.86 (t, 1H), 3.49 – 3.40 (m, 2H), 2.80 (dd, 1H), 2.58 (dd, 1H), 1.43 (s, 9H). ¹³C NMR (125 MHz, CDCl₃, 298 K) δ 174.44, 142.7, 128.97, 127.15, 126.86, 54.38, 53.36, 40.78, 37.18, 27.92.

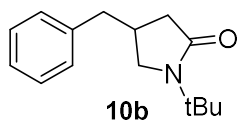
Chiral HPLC: Chiralpak IF[®], 4.6 x 250 mm; isocratic, 7 % MeOH in CO₂, 2 mL/min, 210 nm; t_r ((+)-**6b**) = 6.47 min, t_r ((-)-**6b**) = 7.64 min. [α]_D²⁰: 24.4 (c = 0.44, CHCl₃).

Removal of the *tert*-butyl group in TFA at 140 °C for 5 h to afford 4-Phenyl-2-pyrrolidinone. $[\alpha]_D^{20}$: 33.7 ° (c = 0.16, MeOH); lit. (S)-4-Phenyl-2-pyrrolidinone: $[\alpha]_D^{22}$: 37.5 ° (c = 0.5, CHCl₃).⁷³



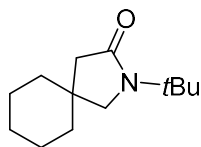
10a ¹H NMR (400 MHz, CDCl₃, 298 K) δ 7.32 (t, 2H), 7.22 (t, 1H), 7.18 (d, 2H), 3.62 (m, 1H), 2.89 (dd, 1H), 2.67 (m, 1H), 2.57 (m, 1H), 2.42 (dd, 1H), 2.30 (m, 1H), 1.76 (m, 1H), 1.34 (s, 9H). ¹³C NMR (125 MHz, CDCl₃, 298 K) δ 166.67, 140.89, 128.74, 126.36, 54.10, 50.44, 41.05, 37.04, 31.99, 28.56. HRMS (ESI positive mode, m/z): calculated for C₁₅H₂₁NONa [M-Na]⁺ 254.1515; found 254.1517.

Chiral HPLC: Chiralpak IF[®], 4.6 x 250 mm; isocratic, 7 % MeOH in CO₂, 2 mL/min, 210 nm; t_r ((-)-**10a**) = 5.45 min, t_r ((+)-**10a**) = 5.82 min. $[\alpha]_D^{25}$: 65.5 ° (c = 0.40, CHCl₃).



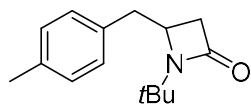
10b ¹H NMR (400 MHz, CD₂Cl₂, 298 K) δ 7.29 (t, 2H), 7.21 (t, 1H), 7.18 (d, 2H), 3.45 (dd, 1H), 3.11 (dd, 1H), 2.72 (dd, 1H), 2.67 (dd, 1H), 2.50 (m, 1H), 2.37 (dd, 1H), 2.06 (dd, 1H), 1.34 (s, 9H). ¹³C NMR (125 MHz, CD₂Cl₂, 298 K) δ 174.78, 140.1, 129.31, 129.01, 126.79, 51.33, 40.87, 40.00, 33.55, 27.97. HRMS (ESI positive mode, m/z): calc'd for C₁₄H₁₉NONa [M-Na]⁺ 254.1520; found 240.1362.

Chiral HPLC: Chiralpak IF[®], 4.6 x 250 mm; isocratic, 7 % MeOH in CO₂, 2 mL/min, 210 nm; t_r ((+)-**10b**) = 7.65 min, t_r ((-)-**10b**) = 8.73 min. $[\alpha]_D^{25}$: -11.9 ° (c = 0.28, MeOH).



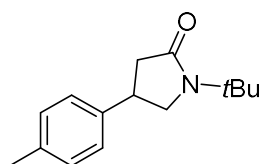
12b The NMR signals correspond to the literature characterization.⁷⁴

¹H NMR (400 MHz, CDCl₃, 298 K) δ 3.17 (s, 2H), 2.20 (s, 2H), 1.50 – 1.40 (m, 10H), 1.37 (s, 9H). ¹³C NMR (125 MHz, CDCl₃, 298 K) δ 174.45, 57.55, 53.65, 45.63, 36.82, 35.31, 27.88, 25.93, 22.96.



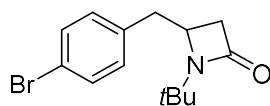
^1H NMR (400 MHz, CDCl_3 , 298 K) δ 7.13 (d, 2H), 7.06 (d, 2H), 3.80 (m, 1H), 3.35 (dd, 1H), 2.75 (dd, 1H), 2.59 (dd, 1H), 2.46 (d, 1H), 2.33 (s, 3H), 1.42 (s, 9H). ^{13}C NMR (125 MHz, CDCl_3 , 298 K) δ 166.78, 136.53, 134.28, 129.53, 128.79, 54.27, 51.51, 41.64, 41.20, 28.66, 21.17. HRMS (ESI positive mode, m/z): calculated for $\text{C}_{15}\text{H}_{21}\text{NONa}$ $[\text{M}-\text{Na}]^+$ 254.1515; found 254.1520.

Chiral HPLC: Chiralpak IF[®], 4.6 x 250 mm; isocratic, 6 % MeOH in CO_2 , 2 mL/min, 210 nm; 6.29 min, 7.30 min.



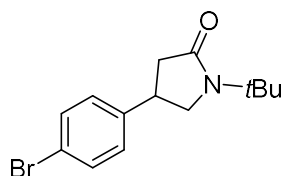
^1H NMR (400 MHz, CDCl_3 , 298 K) δ 7.14 (m, 4H), 3.84 (t, 1H), 3.43 – 3.36 (m, 2H), 2.76 (dd, 1H), 2.55 (dd, 1H), 2.33 (s, 3H), 1.42 (s, 9H). ^{13}C NMR (125 MHz, CDCl_3 , 298 K) δ 174.43, 139.75, 136.75, 129.59, 126.74, 54.22, 53.41, 40.91, 36.85, 27.92, 21.14. HRMS (ESI positive mode, m/z): calculated for $\text{C}_{15}\text{H}_{21}\text{NONa}$ $[\text{M}-\text{Na}]^+$ 254.1515; found 254.1519.

Chiral HPLC: Chiralpak IF[®], 4.6 x 250 mm; isocratic, 6 % MeOH in CO_2 , 2 mL/min, 210 nm; 9.03 min, 9.97 min.



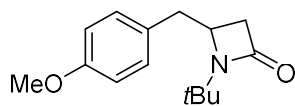
^1H NMR (400 MHz, CDCl_3 , 298 K) δ 7.45 (d, 2H), 7.05 (d, 2H), 3.79 (m, 1H), 3.34 (dd, 1H), 2.76 (dd, 1H), 2.61 (dd, 1H), 2.42 (d, 1H), 1.42 (s, 9H). ^{13}C NMR (125 MHz, CDCl_3 , 298 K) δ 166.48, 136.31, 131.99, 130.59, 120.87, 54.36, 51.05, 41.46, 41.13, 28.65. HRMS (ESI positive mode, m/z): calculated for $\text{C}_{14}\text{H}_{18}\text{BrNONa}$ $[\text{M}-\text{Na}]^+$ 318.0464; found 318.0469.

Chiral HPLC: Chiralpak IF[®], 4.6 x 250 mm; isocratic, 9 % MeOH in CO_2 , 2 mL/min, 210 nm; 7.54 min, 9.04 min.



^1H NMR (400 MHz, CDCl_3 , 298 K) δ 7.46 (d, 2H), 7.12 (d, 2H), 3.86 (t, 1H), 3.41 – 3.34 (m, 2H), 2.78 (dd, 1H), 2.51 (dd, 1H), 1.42 (s, 9H). ^{13}C NMR (125 MHz, CDCl_3 , 298 K) δ 173.96, 141.90, 132.04, 128.58, 120.90, 54.33, 53.05, 40.66, 36.66, 27.90. HRMS (ESI positive mode, m/z): calculated for $\text{C}_{14}\text{H}_{18}\text{BrNONa}$ $[\text{M}-\text{Na}]^+$ 318.0464; found 318.0466.

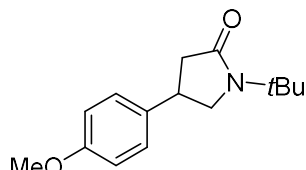
Chiral HPLC: Chiralpak IF[®], 4.6 x 250 mm; isocratic, 12 % iPrOH in CO_2 , 2 mL/min, 210 nm; 9.82 min, 11.32 min.



The NMR signals correspond to the literature characterization.⁷¹

^1H NMR (400 MHz, CDCl_3 , 298 K) δ 7.08 (d, 2H), 6.85 (d, 2H), 3.79 (s, 3H), 3.77 (m, 1H), 3.32 (dd, 1H), 2.75 (dd, 1H), 2.57 (dd, 1H), 2.45 (d, 1H), 1.42 (s, 9H). ^{13}C NMR (125 MHz, CDCl_3 , 298 K) δ 166.78, 158.56, 129.87, 129.37, 114.22, 55.40, 54.25, 51.58, 41.12, 28.65.

Chiral HPLC: Chiralpak IF[®], 4.6 x 250 mm; isocratic, 9 % MeOH in CO_2 , 2 mL/min, 210 nm; 6.19 min, 7.64 min.



^1H NMR (400 MHz, CDCl_3 , 298 K) δ 7.16 (d, 2H), 6.88 (d, 2H), 3.83 (t, 1H), 3.80 (s, 3H), 3.43 – 3.34 (m, 2H), 2.75 (dd, 1H), 2.52 (dd, 1H), 1.42 (s, 9H). ^{13}C NMR (125 MHz, CDCl_3 , 298 K) δ 174.41, 158.67, 134.79, 127.83, 114.29, 55.45, 54.20, 53.51, 41.00, 36.51, 27.91. HRMS (ESI positive mode, m/z): calculated for $\text{C}_{15}\text{H}_{21}\text{NO}_2\text{Na}$ $[\text{M}-\text{Na}]^+$ 270.1465; found 270.1468.

Chiral HPLC: Chiralpak IF[®], 4.6 x 250 mm; isocratic, 12 % iPrOH in CO_2 , 2 mL/min, 210 nm; 8.22 min, 9.89 min.

4.5.8 Directed evolution

Cloning of the Sav library: For the construction of the double site-saturation mutagenesis library at positions 112 and 121 of Sav mutants expressed in the cytoplasm, two strategies were pursued. 212 plasmids were prepared by Golden Gate cloning using primers 1 and 2 (see table below) and a pET24a plasmid containing a codon-optimized Sav-WT gene. Due to large

numbers of clones containing random sequence insertions, the remaining 188 plasmids were generated by a different approach: Polymerase chain reaction (PCR) was applied to amplify both, (i) the pET24a vector lacking any Sav target gene (using primer 3 and 4) and (ii) missing Sav variants encoded on a different library kindly provided by Tobias Vornholt (using primers 5 and 6),⁴⁶ as described below in more detail. The employment of distinct primer pairs caused the removal of the OmpA leader peptide to give rise to cytosolic Sav. The generation of final Sav-bearing pET24a constructs was completed by Gibson assembly according to the manufacturer's protocol (NEB). All PCRs described in this manuscript were carried out with 5 mM of each dNTP (Sigma Aldrich), 10 μ M of each primer (Integrated DNA Technologies), 50 ng template DNA, 1 μ L Q5 Hot Start DNA Polymerase, 10 μ L GC enhancer and 10 μ L Q5 Hot Start Buffer in 50 μ L total volume using the following conditions: a) initial denaturation: 98 °C (30 s); b) cycling (30 passes in total): 98 °C (10 s), 60 °C (20 s) and 72 °C (330 s); c) final elongation: 72 °C (300 s). PCR products for Golden Gate Cloning were cleaned up with the Monarch DNA Cleanup kit (NEB), following the manufacturer's instructions. Subsequently, DNA (5 μ g) was digested with Bsal-HF (5 μ L, NEB) and DpnI (3 μ L, NEB) in 1x CutSmart buffer (15 h at 37 °C, 50 μ L total volume). The DNA (1 μ g) was ligated with 1x T4 DNA Ligase buffer and T4 DNA ligase (1 μ L, 15 h at 16 °C, 20 μ L total volume).

For the directed evolution campaign, site-saturation mutagenesis was carried out in a one-step PCR-based approach using NNK codon degeneracy with primers 7-11. For all mutagenesis reactions, individual clones were sequence-verified by Sanger Sequencing (Microsynth AG).

Primer Number	Primer Name	Primer Sequence
1	Golden_Gate_Cloning_K121X_Forward	GATACTGGTCTCAGCAAATGCCTGGNNN AGCACACTAGTTGGTCATGATAC
2	Golden_Gate_Cloning_S112X_Reverse	GATACTGGTCTCTTTGCTTCGGTGGTGCCN NN GGTCAGCAGCC
3	Fw_GA_pET24_backbone	G TTCAGCAGTAATAAGGATCCGAATGCCA GCACCGTCG
4	Rev_GA_pET24_backbone	CCACCAGTCATACTAGCCATATGTGCATCT CCTTCTTAAAG
5	Fw_GA_cytoSAV	CTTTAAGAAGGAGATGCACATATGGCTAGT ATGACTGGTGG
6	Rev_GA_cytoSAV	CGACGGTGCTCGCATTCCGATCCTTATTAC TGCTGAACG
7	T114X-Fwd	GCTGCTGACCAATGGC NNK KACCGAAGCAA ATGCC
8	T115X-Fwd	CTGACCAATGGAACC NNK GAAAGCAAATGC C TGGGTTAG
9	T114-Rev	GGTCAGCAGCCACTGGGTATTAATGCGTG CTTC

10	L124X-Fwd	GCCTGGGTTAGCACCCNNKGTTGGTCATGA TACC
11	L124-Rev	GCTAACCCAGGCATTTGCTTC

Expression and purification in 96 well plate: General procedure: Mutant plasmids were transformed into BL21 (DE3) *E. Coli* cells in a 96-well PCR plate. The transformants were cultured in LB media supplemented with Kanamycin (50 µg/mL) overnight at 37 °C. Auto-induction media (2.4 mL/well) supplemented with Kanamycin (50 µg/mL) in four 24-well plates was then inoculated with the overnight cultures, and incubated for 24 h at 25 °C. The plates were centrifuged (3500 g, 10 min) and the medium was discarded. The cells were frozen, lysed (1 mL lysis buffer) for 2 h and frozen again overnight. Once the lysate melted, IBB buffer twice concentrated (1 mL/well) was added, and the plates were centrifuged (4200 g, 20 min). The supernatant was transferred into a 96-well plate and centrifuged once more (4200 g, 10 min). After filtration, Sav was immobilized on iminobiotin sepharose beads, washed with MOPS buffer (100 mM, pH = 7.9) and eluted with MES buffer (100 mM, pH = 5.5) twice to obtain purified Sav mutants that could be used for catalytic reactions.

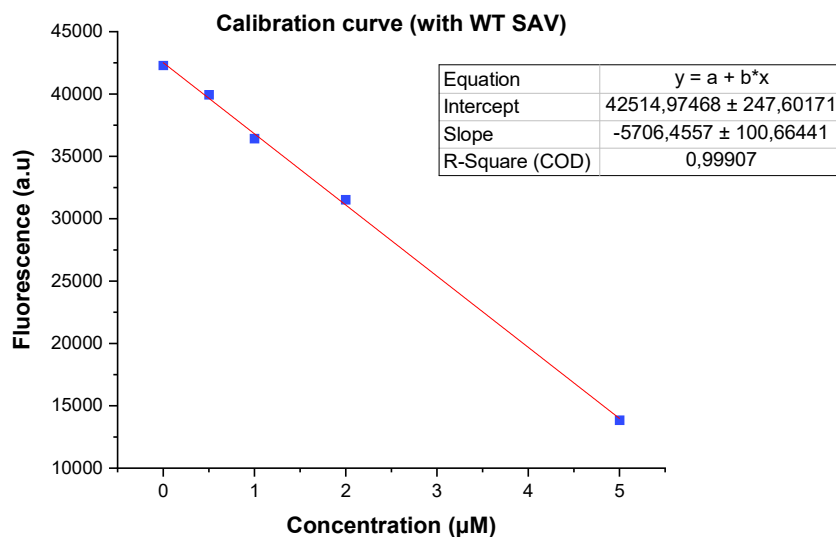
Auto-induction media composition: ZYP salts (50 mM KH₂PO₄, 50 mM Na₂HPO₄, 5 mM (NH₄)₂SO₄), ZYP sugars (0.5 % glycerol, 2.77 mM glucose monohydrate, 6.13 mM lactose) and MgSO₄ (1 mM) in yeast triptone mix (5 g/L yeast extract, 10 g/L triptone).

Lysis buffer composition: Lysozyme 1 mg/mL and DNase I in Tris(HCl) buffer (20 mM, pH = 7.5).

IBB buffer composition (twice concentrated): NaHCO₃ (100 mM, pH = 10.8) and NaCl (1 M). For IBB buffer once concentrated, dilute the above mixture twice with MQ water.

B4F Assay: General procedure: A solution of Biotin-4-Fluorescein (1 µM, 190 µL, 0.00019 µmol) in 50 mM MOPS at pH = 7 was added in a black 96-well plate. The elution fraction (10 µL) was added and mixed. Into 5 free wells, 10 µL of a 0, 0.5, 1, 2 and 5 µM Sav control solutions were added for the calibration curve. Fluorescence was measured at an excitation wavelength of 485 nm and emission wavelength of 520 nm.

a)



b)

	1	2	3	4	5	6	7	8	9	10	11	12
A	AF	AI	AK	AP	AT	AW	CF	CG	CI	CK	CM	CN
B	CQ	CS	CV	DD	DE	DI	DK	DL	DM	DN	DP	DR
C	DS	DT	DV	DY	EC	ED	EE	EF	EG	EH	EI	EP
D	ER	ES	ET	EW	EY	FD	FE	FH	FL	FN	FP	FQ
E	FS	FT	FV	FY	GA	GF	GG	GK	GL	GM	GN	GR
F	GS	GT	GV	HA	HC	HE	HF	HH	HI	HK	HL	HM
G	HN	HP	HR	HT	IC	IE	IF	IH	IK	IL	IM	IS
H	IY	KC	KD	KE	KF	KG	KI	KL	KM	KN	KP	KQ

c)

	1	2	3	4	5	6	7	8	9	10	11	12
A	4,46>5µM	>5µM	>5µM	>5µM	>5µM	1,17>5µM	1,65>5µM	4,56>5µM				
B	>5µM	>5µM	>5µM	1,08	0,86	0,61>5µM	0,45>5µM	-0,57>5µM	>5µM	>5µM		
C	>5µM	4,38	1,47	4,44	2,75	0,78>5µM	>5µM	>5µM	>5µM	>5µM	>5µM	>5µM
D	>5µM	>5µM	>5µM	-0,32	>5µM	>5µM	>5µM	4,58>5µM	>5µM			5,00
E	>5µM	>5µM	>5µM	-0,69	>5µM	-0,37	-0,42	>5µM	-0,53	>5µM	>5µM	2,00
F	>5µM	>5µM	>5µM	>5µM	>5µM	>5µM	>5µM	>5µM	>5µM	>5µM	>5µM	1,00
G	>5µM	>5µM	>5µM	>5µM	4,06	3,95	-0,53	>5µM	>5µM	1,53>5µM		0,50
H	>5µM	>5µM	>5µM	>5µM	>5µM	>5µM	>5µM	>5µM	>5µM	>5µM	>5µM	0,00

Calibration

[SAV] > 1µM

[SAV] < 0,5µM

[SAV] (µM)

Figure S7: Quantification of Sav (tetrameric) expression in 96 well plates by fluorescence quenching of B4F: (a) Calibration curve; (b) Typical quantification results for a 96 well plate of double mutants: the single letters corresponds to the amino acids at position S112X and K121X' respectively; (c) Individual expression levels. A negative value may be observed if the protein is not expressed.

HRMS and sequence of selected Sav mutants:

Mutant	Amino acid sequence	Calculated Mw (first Methionine cleaved)	Measured
Sav ^{S112N-K121L}	MASMTGGQQMGRDQAGITGTWYNQLG STFIVTAGADGALTGTYESAVGNAESRY VLTGRYDSAPATDGSGTALGWTVAWK NNYRNAHSATTWSGQYVGGAEARINTQ WLLTNGTTEANAWLSTLVGHDTFTKVK PSAASIDAAKKAGVNNGNPLDAVQQ	16436.884	16436.056
Sav ^{S112N-K121V}	MASMTGGQQMGRDQAGITGTWYNQLG STFIVTAGADGALTGTYESAVGNAESRY VLTGRYDSAPATDGSGTALGWTVAWK NNYRNAHSATTWSGQYVGGAEARINTQ WLLTNGTTEANAWVSTLVGHDTFTKVK PSAASIDAAKKAGVNNGNPLDAVQQ	16422.857	16422.766
Sav ^{S112N-K121V-L124I}	MASMTGGQQMGRDQAGITGTWYNQLG STFIVTAGADGALTGTYESAVGNAESRY VLTGRYDSAPATDGSGTALGWTVAWK NNYRNAHSATTWSGQYVGGAEARINTQ WLLTNGTTEANAWVSTIVGHDTFTKVKP SAASIDAAKKAGVNNGNPLDAVQQ	16422.857	16422.282
Sav ^{S112N-K121V-L124G}	MASMTGGQQMGRDQAGITGTWYNQLG STFIVTAGADGALTGTYESAVGNAESRY VLTGRYDSAPATDGSGTALGWTVAWK NNYRNAHSATTWSGQYVGGAEARINTQ WLLTNGTTEANAWVSTGVGHDTFTKVK PSAASIDAAKKAGVNNGNPLDAVQQ	16366.749	16366.544

4.5.9 Catalysis

Typical screening procedure: MOPS buffer (100 μ L of a 200 mM solution at pH = 7.1) and MQ water (70 μ L) were added to a purified Sav solution (100 μ L, ≥ 3 μ M tetramer, ≥ 0.0003 μ mol) in MES buffer (100 mM, pH = 5.5) in a glass vial. **Biot^{C4}-TazCu** (40 μ M, 7.5 μ L, 0.0003 μ mol) in DMSO was added. The solution was incubated for 5 min at RT. Acetone (15 μ L) and the substrate (7.5 μ L, 200 mM, 1.5 μ mol) in DMSO were added successively. The vial was sealed and incubated (25 $^{\circ}$ C, 300rpm for 15 h). A solution of internal standard (1,3,5-trimethoxybenzene, 20 μ L, 30 mM, 0.6 μ mol) in MeCN was added and the reaction was extracted twice with HPLC-grade diethyl. The organic layers were combined, dried over MgSO₄

and filtered. The crude reaction mixture was analyzed by supercritical fluid chromatography with an analytical Chiralpak® IF column (isocratic, 7 % MeOH in CO₂, 2 mL/min).

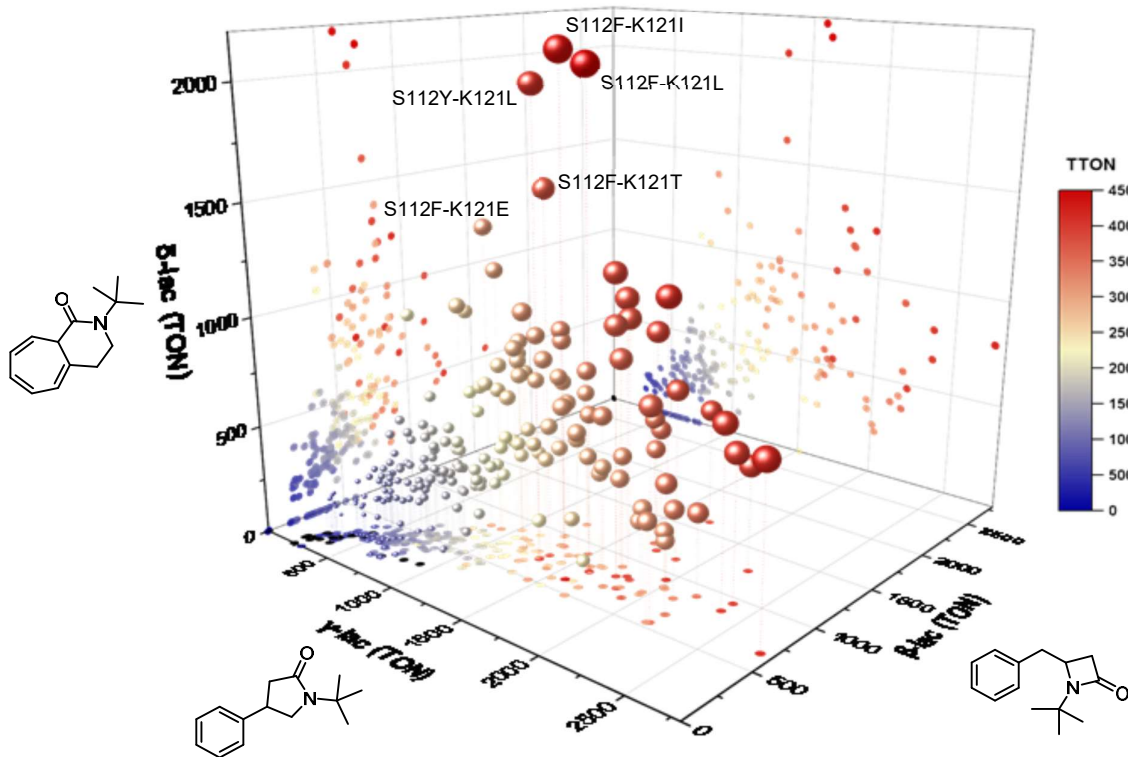


Figure S8: 3D display of the double mutant screening considering the β -, γ - and δ -lactams.

Preparative experiment: MOPS buffer (3.30 mL of a 200 mM solution at pH = 7.1) and MQ water (2.31 mL) were added to a purified Sav solution (3.30 mL, $\geq 3 \mu\text{M}$ tetramer, $\geq 0.0099 \mu\text{mol}$) in MES buffer (100 mM, pH = 5.5) in a flask. **Biot^{C4}-TazCu** (248 μL , 40 μM , 0.0099 μmol) in DMSO was added. The solution incubated for 5 min at RT. Acetone (495 μL) and the substrate (248 μL , 200 mM in DMSO, 49.5 μmol) were added. The reaction was incubated (25 °C, 200rpm for 15 h). The reaction was extracted 3x with diethyl ether (10 mL) and the combined organic layers were dried over MgSO₄. The solvent was removed under reduced pressure and the crude product was purified by flash chromatography with petroleum-

ether/EtOAc (0:100 to 20:80). The γ -lactam (+)-(*S*)-**6b** was isolated as a transparent oil in in 47% yield (5.1 mg, 2350 TON) and 86:14 e.r.

An additional preparative experiment was performed with 100 mg (50 mM) substrate with a similar procedure. Results are summarized in the following table:

Table S1. Summary of the preparative catalytic experiments with **Biot**^{C4}-**TazCu** · Sav S112N-K121V-L124I and substrate **5** to afford the γ -lactam **6b**.

Substrate loading	Catalyst loading	Isolated yield	TON
12 mg (5 mM)	1 μ M (0.02 mol%)	46.9 %	2350
100 mg (50 mM)	2.5 μ M (0.005 mol%)	25.2 %	5040

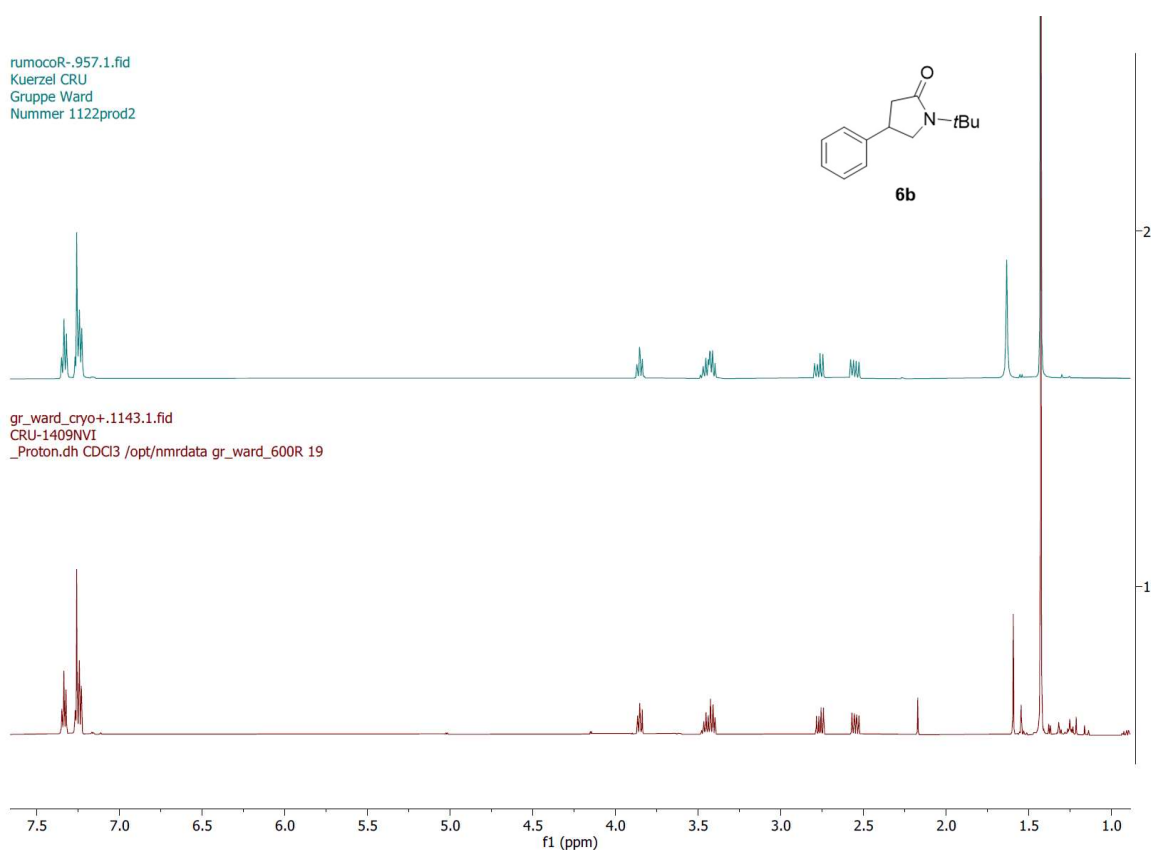


Figure S9. Preparative catalysis experiment with **Biot**^{C4}-**TazCu**·Sav S112N-K121V-L124I. (+)-(*S*)-**6b** obtained by catalytic experiment (bottom spectrum) is stacked with the pure racemic product (top spectrum).

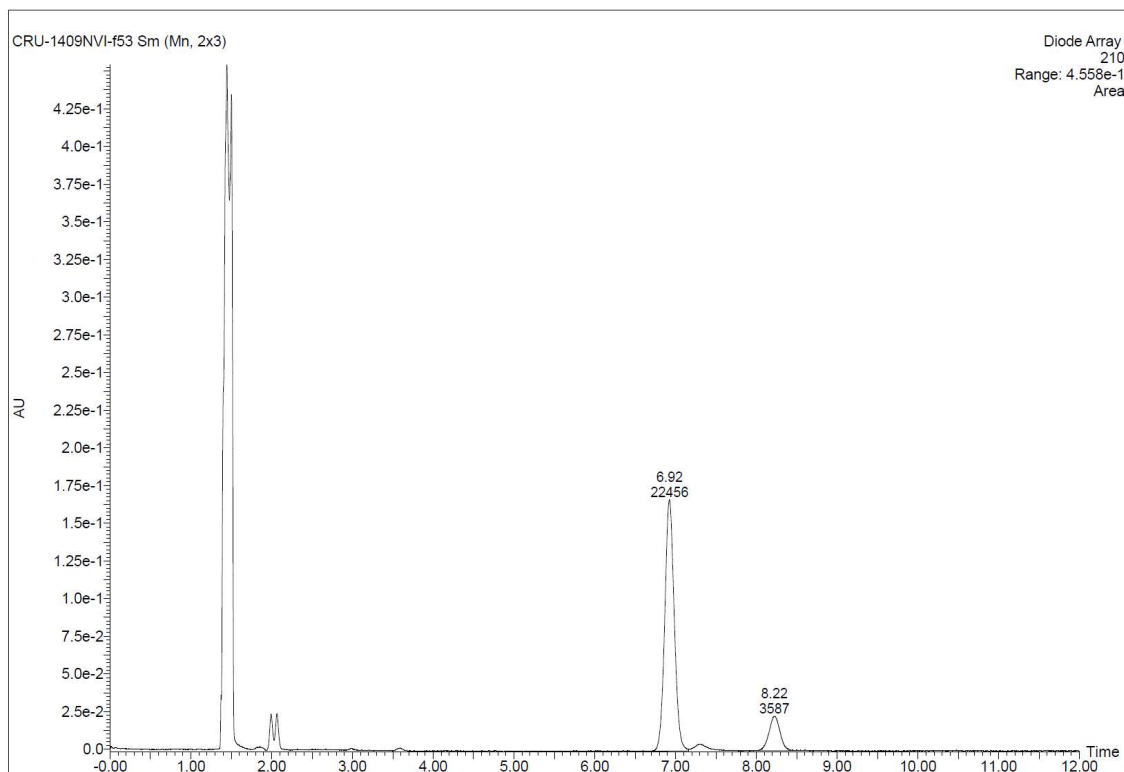


Figure S10. SFC trace of the purified γ -lactam (*S*)-6b obtained in 86:14 e.r. by catalysis experiment with **Biot^{C4}-TazCu·Sav S112N-K121V-L124I**. (*S*)-6b eluted after 6.92 min and (*R*)-6b after 8.22 min.

Double saturation mutagenesis data: The Table S2 contains the following information: Amino acids at position S112 and K121; conversion, TON and ee for the β - and γ -lactams **6a** and **6b**; conversion and TON for the Büchner ring-expansion product (CyHept); the ratio of each product; the total turnover number (TTON); the TON resulting from C–H functionalization (TON $\beta + \gamma$). ND indicates data that were below the detection threshold of the instrument. A blank indicates that the data for the mutant could not be measured due to an unsuccessful transformation.

Table S2. Complete data set of the double saturation mutagenesis.

S112	K121	β -lactam 6a			γ -lactam 6b			Büchner		β -lac	γ -lac	Büchn.	TTON	TON (β + γ)
		Conv (%)	TON	ee (%)	Conv (%)	TON	ee (%)	Conv (%)	TON					
S112A	K121A	7,83	392	3	15,80	790	13	4,85	243	27,5	55,4	17,0	1425	1182
S112A	K121C	5,70	285	-2	7,81	390	-3	2,45	123	35,7	48,9	15,4	798	675
S112A	K121D	5,92	296	-5	12,14	607	1	3,39	170	27,6	56,6	15,8	1073	903
S112A	K121E	2,17	109	-9	4,44	222	6	ND	ND	ND	ND	ND	ND	331
S112A	K121F	7,80	390	-5	13,41	671	9	8,25	412	26,5	45,5	28,0	1473	2228
S112A	K121G	9,41	471	-9	20,53	1026	10	3,42	171	28,2	61,5	10,3	1668	1497
S112A	K121H	ND	ND	ND	ND	ND	ND	ND	ND	ND	ND	ND	ND	ND
S112A	K121I	9,81	490	-1	33,97	1699	22	13,37	669	17,1	59,5	23,4	2858	2189
S112A	K121K	ND	ND	ND	ND	ND	ND	ND	ND	ND	ND	ND	ND	ND
S112A	K121L	12,62	631	-19	33,01	1651	-17	11,69	584	22,0	57,6	20,4	2866	2282
S112A	K121M	2,84	142	-11	7,22	361	-7	ND	ND	ND	ND	ND	ND	503
S112A	K121N	11,55	578	-16	15,44	772	-2	4,99	250	36,1	48,3	15,6	1600	1350
S112A	K121P	5,80	290	1	11,31	565	7	2,81	141	29,1	56,7	14,1	996	855
S112A	K121Q	7,76	388	-12	11,02	551	4	4,88	244	32,8	46,6	20,6	1183	939
S112A	K121R	ND	ND	ND	ND	ND	ND	ND	ND	ND	ND	ND	ND	ND
S112A	K121S	10,53	527	-13	15,02	751	8	7,17	358	32,2	45,9	21,9	1636	1278
S112A	K121T	6,32	316	-7	14,58	729	2	6,26	313	23,3	53,7	23,1	1358	1045
S112A	K121V	8,14	407	-1	21,94	1097	21	18,83	941	16,6	44,9	38,5	2445	1504
S112A	K121W	7,90	395	-33	12,17	609	3	3,99	199	32,8	50,6	16,6	1203	1004
S112A	K121Y	9,94	497	-21	13,56	678	-3	4,13	207	36,0	49,1	15,0	1382	966
S112C	K121A	ND	ND	ND	ND	ND	ND	ND	ND	ND	ND	ND	ND	ND
S112C	K121C	ND	ND	ND	ND	ND	ND	ND	ND	ND	ND	ND	ND	ND
S112C	K121D	2,00	100	-8	4,17	208	-2	ND	ND	ND	ND	ND	ND	309
S112C	K121E	ND	ND	ND	ND	ND	ND	ND	ND	ND	ND	ND	ND	ND
S112C	K121F	12,95	648	-7	20,89	1045	4	6,17	308	32,4	52,2	15,4	2001	1692
S112C	K121G	ND	ND	ND	ND	ND	ND	ND	ND	ND	ND	ND	ND	ND
S112C	K121H													
S112C	K121I	6,73	337	-14	10,71	535	-10	3,24	162	32,6	51,7	15,7	1034	872
S112C	K121K	ND	ND	ND	ND	ND	ND	ND	ND	ND	ND	ND	ND	ND
S112C	K121L	ND	ND	ND	ND	ND	ND	ND	ND	ND	ND	ND	ND	ND
S112C	K121M	ND	ND	ND	ND	ND	ND	ND	ND	ND	ND	ND	ND	ND
S112C	K121N	ND	ND	ND	ND	ND	ND	ND	ND	ND	ND	ND	ND	ND
S112C	K121P	ND	ND	ND	ND	ND	ND	ND	ND	ND	ND	ND	ND	ND
S112C	K121Q	ND	ND	ND	ND	ND	ND	ND	ND	ND	ND	ND	ND	ND
S112C	K121R	ND	ND	ND	ND	ND	ND	ND	ND	ND	ND	ND	ND	ND
S112C	K121S	6,79	340	-2	10,32	516	0	3,07	153	33,7	51,1	15,2	1009	856
S112C	K121T													
S112C	K121V	6,61	330	4	12,89	645	3	8,50	425	23,6	46,1	30,3	1400	975
S112C	K121W	5,65	283	-8	8,79	440	-8	ND	ND	ND	ND	ND	ND	722
S112C	K121Y	ND	ND	ND	ND	ND	ND	ND	ND	ND	ND	ND	ND	ND
S112D	K121A	ND	ND	ND	ND	ND	ND	ND	ND	ND	ND	ND	ND	ND
S112D	K121C													
S112D	K121D	3,66	183	1	14,01	701	-4	ND	ND	ND	ND	ND	ND	884
S112D	K121E	ND	ND	ND	ND	ND	ND	ND	ND	ND	ND	ND	ND	ND
S112D	K121F													
S112D	K121G													
S112D	K121H													
S112D	K121I	5,09	255	-5	14,68	734	-5	1,89	94	23,5	67,8	8,7	1083	989
S112D	K121K	ND	ND	ND	ND	ND	ND	ND	ND	ND	ND	ND	ND	ND
S112D	K121L	ND	ND	ND	ND	ND	ND	ND	ND	ND	ND	ND	ND	ND
S112D	K121M	ND	ND	ND	ND	ND	ND	ND	ND	ND	ND	ND	ND	ND
S112D	K121N	ND	ND	ND	ND	ND	ND	ND	ND	ND	ND	ND	ND	ND
S112D	K121P	ND	ND	ND	ND	ND	ND	ND	ND	ND	ND	ND	ND	ND
S112D	K121Q													
S112D	K121R	ND	ND	ND	ND	ND	ND	ND	ND	ND	ND	ND	ND	ND
S112D	K121S	7,37	368	-11	11,70	585	-8	3,39	169	32,8	52,1	15,1	1122	953
S112D	K121T	5,39	269	-4	12,61	631	-8	2,71	135	26,0	60,9	13,1	1035	900
S112D	K121V	ND	ND	ND	ND	ND	ND	ND	ND	ND	ND	ND	ND	ND
S112D	K121W	ND	ND	ND	ND	ND	ND	ND	ND	ND	ND	ND	ND	ND
S112D	K121Y	5,74	287	-15	8,30	415	-13	ND	ND	ND	ND	ND	ND	702
S112E	K121A	4,86	243	-3	7,70	385	9	2,48	124	32,3	51,2	16,5	752	628
S112E	K121C	5,96	298	-6	9,15	457	-3	ND	ND	ND	ND	ND	ND	756
S112E	K121D	ND	ND	ND	ND	ND	ND	ND	ND	ND	ND	ND	ND	ND
S112E	K121E	ND	ND	ND	ND	ND	ND	ND	ND	ND	ND	ND	ND	ND
S112E	K121F	12,03	602	-22	16,82	841	-11	6,93	346	33,6	47,0	19,4	1789	1443
S112E	K121G	13,46	673	12	16,09	805	6	5,08	254	38,9	46,5	14,7	1732	1478
S112E	K121H	ND	ND	ND	ND	ND	ND	ND	ND	ND	ND	ND	ND	ND

S112E	K121I	23,16	1158	-5	24,76	1238	1	10,42	521	39,7	42,4	17,9	2917	2396
S112E	K121K	ND	ND	ND	ND	ND	ND	ND	ND	ND	ND	ND	ND	ND
S112E	K121L	ND	ND	ND	ND	ND	ND	ND	ND	ND	ND	ND	ND	ND
S112E	K121M	ND	ND	ND	ND	ND	ND	ND	ND	ND	ND	ND	ND	ND
S112E	K121N													
S112E	K121P	9,07	454	2	17,52	876	0	2,48	124	31,2	60,2	8,5	1454	1329
S112E	K121Q	8,52	426	-16	13,15	657	-6	3,19	159	34,3	52,9	12,8	1242	1084
S112E	K121R	ND	ND	ND	ND	ND	ND	ND	ND	ND	ND	ND	ND	ND
S112E	K121S	5,98	299	-9	8,58	429	1	ND	ND	ND	ND	ND	ND	728
S112E	K121T	4,98	249	-12	6,96	348	-5	ND	ND	ND	ND	ND	ND	597
S112E	K121V	4,67	234	-6	9,11	456	11	3,45	173	27,1	52,9	20,0	863	689
S112E	K121W	11,06	553	-22	14,11	705	-13	6,05	303	35,4	45,2	19,4	1561	1258
S112E	K121Y	9,13	457	-16	12,77	638	-9	5,62	281	33,2	46,4	20,4	1376	1095
S112F	K121A	12,62	631	8	25,59	1279	5	13,74	687	24,3	49,2	26,5	2597	1910
S112F	K121C	11,31	565	-4	16,52	826	-4	8,68	434	31,0	45,3	23,8	1825	1391
S112F	K121D	16,40	820	-39	18,53	926	-15	19,78	989	30,0	33,9	36,2	2735	1746
S112F	K121E	16,39	819	-46	17,04	852	-17	22,71	1136	29,2	30,4	40,5	2807	1671
S112F	K121F	13,08	654	6	43,78	2189	52	9,20	460	19,8	66,3	13,9	3303	2843
S112F	K121G	13,98	699	1	23,89	1194	0	8,22	411	30,3	51,8	17,8	2304	1893
S112F	K121H	ND	ND	ND	ND	ND	ND	ND	ND	ND	ND	ND	ND	ND
S112F	K121I	12,30	615	-3	31,72	1586	-27	35,66	1783	15,4	39,8	44,8	3984	2201
S112F	K121K	ND	ND	ND	ND	ND	ND	ND	ND	ND	ND	ND	ND	ND
S112F	K121L	15,04	752	36	32,45	1622	-27	34,66	1733	18,3	39,5	42,2	4107	2374
S112F	K121M	ND	ND	ND	ND	ND	ND	ND	ND	ND	ND	ND	ND	ND
S112F	K121N	14,61	731	-16	17,41	871	-18	9,44	472	35,2	42,0	22,8	2074	1601
S112F	K121P	14,16	708	46	23,84	1192	43	14,28	714	27,1	45,6	27,3	2614	1900
S112F	K121Q	14,53	727	-44	16,05	802	-22	16,74	837	30,7	33,9	35,4	2366	1529
S112F	K121R	ND	ND	ND	ND	ND	ND	ND	ND	ND	ND	ND	ND	ND
S112F	K121S	17,70	885	-16	26,41	1320	-6	16,28	814	29,3	43,7	27,0	3019	2206
S112F	K121T	15,15	757	7	26,88	1344	-6	26,35	1318	22,1	39,3	38,5	3419	2101
S112F	K121V	13,56	678	-14	19,65	983	1	11,51	576	30,3	43,9	25,7	2237	1661
S112F	K121W	14,66	733	6	23,56	1178	0	15,56	778	27,3	43,8	28,9	2689	1911
S112F	K121Y	17,64	882	1	26,11	1306	-8	12,82	641	31,2	46,2	22,7	2829	2188
S112G	K121A	10,57	529	12	13,92	696	6	4,28	214	36,8	48,4	14,9	1439	1224
S112G	K121C													
S112G	K121D													
S112G	K121E													
S112G	K121F	18,03	901	-1	34,26	1713	18	8,28	414	29,8	56,6	13,7	3028	2614
S112G	K121G	9,25	463	3	20,92	1046	-2	2,04	102	28,7	64,9	6,3	1611	1509
S112G	K121H													
S112G	K121I	ND	ND	ND	ND	ND	ND	ND	ND	ND	ND	ND	ND	ND
S112G	K121K	6,55	328	0	10,91	545	-3	ND	ND	ND	ND	ND	ND	873
S112G	K121L	14,49	724	5	36,97	1848	-31	7,95	397	24,4	62,2	13,4	2969	2573
S112G	K121M	ND	ND	ND	ND	ND	ND	ND	ND	ND	ND	ND	ND	ND
S112G	K121N	13,83	691	-14	15,44	772	-5	3,12	156	42,7	47,7	9,6	1619	1464
S112G	K121P													
S112G	K121Q													
S112G	K121R	ND	ND	ND	ND	ND	ND	ND	ND	ND	ND	ND	ND	ND
S112G	K121S	18,00	900	-16	22,80	1140	-1	6,52	326	38,0	48,2	13,8	2366	2040
S112G	K121T	12,09	604	2	20,22	1011	-6	4,76	238	32,6	54,6	12,9	1853	1615
S112G	K121V	12,21	611	7	25,32	1266	0	15,69	785	23,0	47,6	29,5	2662	1876
S112G	K121W													
S112G	K121Y	ND	ND	ND	ND	ND	ND	ND	ND	ND	ND	ND	ND	ND
S112H	K121A	5,54	277	-11	7,81	390	-5	ND	ND	ND	ND	ND	ND	668
S112H	K121C	ND	ND	ND	ND	ND	ND	ND	ND	ND	ND	ND	ND	ND
S112H	K121D	ND	ND	ND	ND	ND	ND	ND	ND	ND	ND	ND	ND	ND
S112H	K121E	14,84	742	-17	17,36	868	-14	3,95	198	41,0	48,0	10,9	1808	1610
S112H	K121F	9,50	475	-6	19,39	970	32	3,51	175	29,3	59,9	10,8	1620	1445
S112H	K121G	ND	ND	ND	ND	ND	ND	ND	ND	ND	ND	ND	ND	ND
S112H	K121H	ND	ND	ND	ND	ND	ND	ND	ND	ND	ND	ND	ND	ND
S112H	K121I	24,33	1217	-7	33,22	1661	20	9,54	477	36,3	49,5	14,2	3355	2878
S112H	K121K	ND	ND	ND	ND	ND	ND	ND	ND	ND	ND	ND	ND	ND
S112H	K121L	16,68	834	13	32,45	1623	2	7,00	350	29,7	57,8	12,5	2807	2457
S112H	K121M	ND	ND	ND	ND	ND	ND	ND	ND	ND	ND	ND	ND	ND
S112H	K121N	ND	ND	ND	ND	ND	ND	ND	ND	ND	ND	ND	ND	ND
S112H	K121P	ND	ND	ND	ND	ND	ND	ND	ND	ND	ND	ND	ND	ND
S112H	K121Q	ND	ND	ND	ND	ND	ND	ND	ND	ND	ND	ND	ND	ND
S112H	K121R	ND	ND	ND	ND	ND	ND	ND	ND	ND	ND	ND	ND	ND
S112H	K121S	ND	ND	ND	ND	ND	ND	ND	ND	ND	ND	ND	ND	ND
S112H	K121T	ND	ND	ND	ND	ND	ND	ND	ND	ND	ND	ND	ND	ND
S112H	K121V	ND	ND	ND	ND	ND	ND	ND	ND	ND	ND	ND	ND	ND
S112H	K121W													
S112H	K121Y	ND	ND	ND	ND	ND	ND	ND	ND	ND	ND	ND	ND	ND

S112I	K121A	ND	ND	ND	ND	ND	ND	ND	ND	ND	ND	ND	ND	ND
S112I	K121C	10,21	511	-6	14,08	704	-1	4,11	205	36,0	49,6	14,5	1420	1214
S112I	K121D	3,41	171	10	12,78	639	-1	ND	ND	ND	ND	ND	ND	810
S112I	K121E	19,50	975	-28	24,91	1246	-8	11,95	597	34,6	44,2	21,2	2818	2221
S112I	K121F	17,11	855	38	40,48	2024	54	3,56	178	28,0	66,2	5,8	3057	2879
S112I	K121G	ND	ND	ND	ND	ND	ND	ND	ND	ND	ND	ND	ND	ND
S112I	K121H	6,74	337	-4	11,44	572	-1	2,85	143	32,0	54,4	13,6	1052	909
S112I	K121I	24,54	1227	32	33,53	1677	-6	8,06	403	37,1	50,7	12,2	3307	2904
S112I	K121K	ND	ND	ND	ND	ND	ND	ND	ND	ND	ND	ND	ND	ND
S112I	K121L	25,49	1274	61	44,45	2222	3	7,86	393	32,8	57,1	10,1	3889	3497
S112I	K121M	5,31	266	1	10,00	500	-8	ND	ND	ND	ND	ND	ND	766
S112I	K121N	11,57	578	-11	16,45	823	0	4,49	225	35,6	50,6	13,8	1626	1401
S112I	K121P	ND	ND	ND	ND	ND	ND	ND	ND	ND	ND	ND	ND	ND
S112I	K121Q	8,56	428	-20	13,87	693	-1	4,11	205	32,3	52,2	15,5	1326	1122
S112I	K121R	ND	ND	ND	ND	ND	ND	ND	ND	ND	ND	ND	ND	ND
S112I	K121S	17,92	896	-7	29,68	1484	9	13,75	688	29,2	48,4	22,4	3068	2380
S112I	K121T	9,97	498	6	19,64	982	-13	7,81	391	26,6	52,5	20,9	1871	1480
S112I	K121V	23,15	1158	65	34,50	1725	26	16,37	818	31,3	46,6	22,1	3701	2882
S112I	K121W	5,69	285	3	14,96	748	-3	2,29	114	24,8	65,2	10,0	1147	1032
S112I	K121Y	14,95	748	-2	25,12	1256	1	8,19	410	31,0	52,0	17,0	2414	2003
S112K	K121A	ND	ND	ND	ND	ND	ND	ND	ND	ND	ND	ND	ND	ND
S112K	K121C	ND	ND	ND	ND	ND	ND	ND	ND	ND	ND	ND	ND	ND
S112K	K121D	ND	ND	ND	ND	ND	ND	ND	ND	ND	ND	ND	ND	ND
S112K	K121E	13,52	676	-11	16,05	802	-19	3,19	159	41,3	49,0	9,7	1637	1478
S112K	K121F	11,62	581	-10	12,79	639	-11	2,07	104	43,9	48,3	7,8	1324	1220
S112K	K121G	5,42	271	-6	8,02	401	-2	ND	ND	ND	ND	ND	ND	672
S112K	K121H	ND	ND	ND	ND	ND	ND	ND	ND	ND	ND	ND	ND	ND
S112K	K121I	12,03	601	-12	14,84	742	-7	2,97	148	40,3	49,8	10,0	1491	1343
S112K	K121K	ND	ND	ND	ND	ND	ND	ND	ND	ND	ND	ND	ND	ND
S112K	K121L	ND	ND	ND	ND	ND	ND	ND	ND	ND	ND	ND	ND	ND
S112K	K121M	6,76	338	0	9,27	463	-3	ND	ND	ND	ND	ND	ND	801
S112K	K121N	10,25	512	-7	12,26	613	-9	ND	ND	ND	ND	ND	ND	1125
S112K	K121P	8,02	401	-11	7,79	390	-9	ND	ND	ND	ND	ND	ND	791
S112K	K121Q	ND	ND	ND	ND	ND	ND	ND	ND	ND	ND	ND	ND	ND
S112K	K121R	ND	ND	ND	ND	ND	ND	ND	ND	ND	ND	ND	ND	ND
S112K	K121S	ND	ND	ND	ND	ND	ND	ND	ND	ND	ND	ND	ND	ND
S112K	K121T	ND	ND	ND	ND	ND	ND	ND	ND	ND	ND	ND	ND	ND
S112K	K121V	ND	ND	ND	ND	ND	ND	ND	ND	ND	ND	ND	ND	ND
S112K	K121W	ND	ND	ND	ND	ND	ND	ND	ND	ND	ND	ND	ND	ND
S112K	K121Y													
S112L	K121A	9,35	468	1	18,16	908	1	8,32	416	26,1	50,7	23,2	1792	1376
S112L	K121C	ND	ND	ND	ND	ND	ND	ND	ND	ND	ND	ND	ND	ND
S112L	K121D	10,80	540	-16	17,07	853	8	5,40	270	32,5	51,3	16,2	1663	1393
S112L	K121E	17,65	883	-48	20,42	1021	6	13,73	686	34,1	39,4	26,5	2590	1904
S112L	K121F	17,34	867	50	40,17	2009	57	4,12	206	28,1	65,2	6,7	3082	2875
S112L	K121G	9,75	488	-7	17,27	864	4	5,85	293	29,7	52,5	17,8	1645	1351
S112L	K121H	ND	ND	ND	ND	ND	ND	ND	ND	ND	ND	ND	ND	ND
S112L	K121I													
S112L	K121K	ND	ND	ND	ND	ND	ND	ND	ND	ND	ND	ND	ND	ND
S112L	K121L	18,61	930	42	44,56	2228	-20	7,23	362	26,4	63,3	10,3	3520	3159
S112L	K121M	3,12	156	7	9,78	489	-31	ND	ND	ND	ND	ND	ND	645
S112L	K121N	5,54	277	-20	7,15	358	7	ND	ND	ND	ND	ND	ND	635
S112L	K121P	4,91	246	16	8,69	435	15	ND	ND	ND	ND	ND	ND	680
S112L	K121Q	9,32	466	-47	12,03	601	-9	ND	ND	ND	ND	ND	ND	1068
S112L	K121R	ND	ND	ND	ND	ND	ND	ND	ND	ND	ND	ND	ND	ND
S112L	K121S													
S112L	K121T	10,01	501	-18	26,59	1329	-33	12,79	640	20,3	53,8	25,9	2470	1830
S112L	K121V	13,77	689	23	34,29	1715	3	19,38	969	20,4	50,8	28,7	3373	2403
S112L	K121W	11,95	597	-24	23,51	1175	7	8,29	415	27,3	53,7	19,0	2187	1773
S112L	K121Y	14,69	735	-14	28,92	1446	12	8,63	432	28,1	55,3	16,5	2613	2181
S112M	K121A	7,83	392	3	15,80	790	13	4,85	243	27,5	55,4	17,0	1425	1182
S112M	K121C	5,70	285	-2	7,81	390	-3	2,45	123	35,7	48,9	15,4	798	675
S112M	K121D	5,92	296	-5	12,14	607	1	3,39	170	27,6	56,6	15,8	1073	903
S112M	K121E	6,04	302	-14	8,89	444	-2	3,12	156	33,5	49,2	17,3	902	747
S112M	K121F	7,80	390	-5	13,41	671	9	4,87	244	29,9	51,4	18,7	1305	2228
S112M	K121G	3,72	186	-2	6,72	336	6	2,72	136	28,3	51,1	20,7	658	522
S112M	K121H	ND	ND	ND	ND	ND	ND	ND	ND	ND	ND	ND	ND	ND
S112M	K121I	9,81	490	-1	33,97	1699	22	13,37	669	17,1	59,5	23,4	2858	2189
S112M	K121K	ND	ND	ND	ND	ND	ND	ND	ND	ND	ND	ND	ND	ND
S112M	K121L	12,62	631	-19	33,01	1651	-17	11,69	584	22,0	57,6	20,4	2866	2282
S112M	K121M	2,84	142	-11	7,22	361	-7	0,00	0	28,2	71,8	0,0	503	503
S112M	K121N	11,55	578	-16	15,44	772	-2	4,99	250	36,1	48,3	15,6	1600	1350
S112M	K121P	5,80	290	1	11,31	565	7	0,00	0	33,9	66,1	0,0	855	855

S112M	K121Q	7,76	388	-12	11,02	551	4	4,88	244	32,8	46,6	20,6	1183	939
S112M	K121R	ND	ND	ND	ND	ND	ND	ND	ND	ND	ND	ND	ND	ND
S112M	K121S	10,53	527	-13	15,02	751	8	7,17	358	32,2	45,9	21,9	1636	1278
S112M	K121T	6,32	316	-7	14,58	729	2	6,26	313	23,3	53,7	23,1	1358	1045
S112M	K121V	8,14	407	-1	21,94	1097	21	18,83	941	16,6	44,9	38,5	2445	1504
S112M	K121W	7,90	395	-33	12,17	609	3	1,88	94	36,0	55,5	8,6	1098	1004
S112M	K121Y	9,94	497	-21	13,56	678	-3	4,68	234	35,3	48,1	16,6	1409	966
S112N	K121A	6,52	326	10	20,08	1004	-4	4,99	249	20,6	63,6	15,8	1579	1330
S112N	K121C	ND	ND	ND	ND	ND	ND	ND	ND	ND	ND	ND	ND	ND
S112N	K121D	3,60	180	-1	7,52	376	-9	ND	ND	ND	ND	ND	ND	556
S112N	K121E	5,83	291	-9	8,18	409	4	4,21	211	32,0	44,9	23,1	911	701
S112N	K121F	14,62	731	41	39,34	1967	49	5,37	269	24,6	66,3	9,1	2967	2698
S112N	K121G	7,70	385	-8	16,46	823	-27	4,13	207	27,2	58,2	14,6	1415	1208
S112N	K121H	ND	ND	ND	ND	ND	ND	ND	ND	ND	ND	ND	ND	ND
S112N	K121I	12,96	648	53	38,47	1923	43	16,72	836	19,0	56,4	24,5	3407	2572
S112N	K121K	ND	ND	ND	ND	ND	ND	ND	ND	ND	ND	ND	ND	ND
S112N	K121L	13,03	651	54	54,72	2736	44	12,87	644	16,2	67,9	16,0	4031	3388
S112N	K121M	ND	ND	ND	ND	ND	ND	ND	ND	ND	ND	ND	ND	ND
S112N	K121N	ND	ND	ND	ND	ND	ND	ND	ND	ND	ND	ND	ND	ND
S112N	K121P	ND	ND	ND	ND	ND	ND	ND	ND	ND	ND	ND	ND	ND
S112N	K121Q	4,39	219	-5	5,93	296	-5	3,19	159	32,5	43,9	23,6	674	516
S112N	K121R	ND	ND	ND	ND	ND	ND	ND	ND	ND	ND	ND	ND	ND
S112N	K121S	6,47	323	-10	10,27	513	10	5,42	271	29,2	46,3	24,5	1107	837
S112N	K121T	ND	ND	ND	ND	ND	ND	ND	ND	ND	ND	ND	ND	ND
S112N	K121V	10,99	550	65	43,62	2181	73	14,78	739	15,9	62,9	21,3	3470	2731
S112N	K121W	8,61	430	0	16,60	830	2	5,38	269	28,1	54,3	17,6	1529	1260
S112N	K121Y	ND	ND	ND	ND	ND	ND	ND	ND	ND	ND	ND	ND	ND
S112P	K121A	6,52	326	24	12,37	619	2	3,67	184	28,9	54,8	16,3	1129	944
S112P	K121C	4,42	221	-3	12,21	610	-3	ND	ND	ND	ND	ND	ND	832
S112P	K121D	ND	ND	ND	ND	ND	ND	ND	ND	ND	ND	ND	ND	ND
S112P	K121E	ND	ND	ND	ND	ND	ND	ND	ND	ND	ND	ND	ND	ND
S112P	K121F	9,32	466	25	22,84	1142	28	3,79	189	25,9	63,5	10,5	1797	1608
S112P	K121G	1,64	82	9	4,19	210	11	ND	ND	ND	ND	ND	ND	291
S112P	K121H	ND	ND	ND	ND	ND	ND	ND	ND	ND	ND	ND	ND	ND
S112P	K121I	2,75	137	23	8,87	443	39	0,00	0	23,6	76,4	0,0	580	581
S112P	K121K	ND	ND	ND	ND	ND	ND	ND	ND	ND	ND	ND	ND	ND
S112P	K121L	3,91	195	13	13,57	678	33	2,94	147	19,1	66,5	14,4	1020	874
S112P	K121M	ND	ND	ND	14,11	705	-1	ND	ND	ND	ND	ND	ND	705
S112P	K121N	6,72	336	9	12,06	603	-1	3,35	168	30,4	54,5	15,2	1107	939
S112P	K121P	ND	ND	ND	ND	ND	ND	ND	ND	ND	ND	ND	ND	ND
S112P	K121Q	ND	ND	ND	ND	ND	ND	ND	ND	ND	ND	ND	ND	ND
S112P	K121R	ND	ND	ND	ND	ND	ND	ND	ND	ND	ND	ND	ND	ND
S112P	K121S	ND	ND	ND	ND	ND	ND	ND	ND	ND	ND	ND	ND	ND
S112P	K121T	ND	ND	ND	ND	ND	ND	ND	ND	ND	ND	ND	ND	ND
S112P	K121V	ND	ND	ND	ND	ND	ND	ND	ND	ND	ND	ND	ND	ND
S112P	K121W	ND	ND	ND	ND	ND	ND	ND	ND	ND	ND	ND	ND	ND
S112P	K121Y	ND	ND	ND	ND	ND	ND	ND	ND	ND	ND	ND	ND	ND
S112Q	K121A	8,88	444	0	14,85	742	3	3,99	199	32,1	53,6	14,4	1385	1187
S112Q	K121C	ND	ND	ND	ND	ND	ND	ND	ND	ND	ND	ND	ND	ND
S112Q	K121D	ND	ND	ND	ND	ND	ND	ND	ND	ND	ND	ND	ND	ND
S112Q	K121E	6,32	316	-24	8,21	410	-10	2,27	114	37,6	48,8	13,5	840	726
S112Q	K121F	16,97	848	-5	29,15	1458	22	8,84	442	30,9	53,1	16,1	2748	2306
S112Q	K121G	ND	ND	ND	ND	ND	ND	ND	ND	ND	ND	ND	ND	ND
S112Q	K121H	ND	ND	ND	ND	ND	ND	ND	ND	ND	ND	ND	ND	ND
S112Q	K121I	32,28	1614	-5	34,43	1722	-27	8,90	445	42,7	45,5	11,8	3781	3336
S112Q	K121K	ND	ND	ND	ND	ND	ND	ND	ND	ND	ND	ND	ND	ND
S112Q	K121L	9,82	491	12	30,72	1536	-39	4,78	239	21,7	67,8	10,5	2266	2027
S112Q	K121M	ND	ND	ND	ND	ND	ND	ND	ND	ND	ND	ND	ND	ND
S112Q	K121N	8,83	442	-14	8,84	442	-6	2,90	145	42,9	42,9	14,1	1029	884
S112Q	K121P	6,07	303	9	9,95	497	31	ND	ND	ND	ND	ND	ND	801
S112Q	K121Q	7,09	355	-16	8,46	423	-5	ND	ND	ND	ND	ND	ND	778
S112Q	K121R	ND	ND	ND	ND	ND	ND	ND	ND	ND	ND	ND	ND	ND
S112Q	K121S	ND	ND	ND	ND	ND	ND	ND	ND	ND	ND	ND	ND	ND
S112Q	K121T	6,64	332	-8	11,23	562	-18	3,02	151	31,8	53,8	14,4	1045	894
S112Q	K121V	11,91	595	12	18,32	916	3	9,96	498	29,6	45,6	24,8	2009	1512
S112Q	K121W	13,89	694	-16	19,11	956	-15	6,75	337	34,9	48,1	17,0	1987	1650
S112Q	K121Y	7,95	397	0	9,99	500	3	3,72	186	36,7	46,2	17,2	1083	897
S112R	K121A	ND	ND	ND	ND	ND	ND	ND	ND	ND	ND	ND	ND	ND
S112R	K121C	ND	ND	ND	ND	ND	ND	ND	ND	ND	ND	ND	ND	ND
S112R	K121D	6,51	325	-11	9,18	459	1	ND	ND	ND	ND	ND	ND	785
S112R	K121E	ND	ND	ND	ND	ND	ND	ND	ND	ND	ND	ND	ND	ND
S112R	K121F	4,73	237	-14	7,45	372	-9	ND	ND	ND	ND	ND	ND	609
S112R	K121G	ND	ND	ND	ND	ND	ND	ND	ND	ND	ND	ND	ND	ND

S112R	K121H	ND	ND	ND	ND	ND	ND	ND	ND	ND	ND	ND	ND	ND
S112R	K121I	4,12	206	-14	7,27	364	21	1,81	91	31,2	55,1	13,7	661	569
S112R	K121K	ND	ND	ND	ND	ND	ND	ND	ND	ND	ND	ND	ND	ND
S112R	K121L	ND	ND	ND	ND	ND	ND	ND	ND	ND	ND	ND	ND	ND
S112R	K121M	ND	ND	ND	ND	ND	ND	ND	ND	ND	ND	ND	ND	ND
S112R	K121N	ND	ND	ND	ND	ND	ND	ND	ND	ND	ND	ND	ND	ND
S112R	K121P	ND	ND	ND	ND	ND	ND	ND	ND	ND	ND	ND	ND	ND
S112R	K121Q	ND	ND	ND	ND	ND	ND	ND	ND	ND	ND	ND	ND	ND
S112R	K121R	ND	ND	ND	ND	ND	ND	ND	ND	ND	ND	ND	ND	ND
S112R	K121S	ND	ND	ND	ND	ND	ND	ND	ND	ND	ND	ND	ND	ND
S112R	K121T	ND	ND	ND	ND	ND	ND	ND	ND	ND	ND	ND	ND	ND
S112R	K121V	ND	ND	ND	ND	ND	ND	ND	ND	ND	ND	ND	ND	ND
S112R	K121W	5,63	281	-14	9,12	456	-13	1,81	91	34,0	55,1	10,9	828	737
S112R	K121Y	ND	ND	ND	ND	ND	ND	ND	ND	ND	ND	ND	ND	ND
S112	K121A	6,69	334	-2	11,55	577	-4	4,80	240	29,0	50,1	20,8	1151	912
S112	K121C	10,23	511	-12	15,36	768	0	5,56	278	32,8	49,3	17,9	1557	1280
S112	K121D	1,24	62	-4	2,93	146	5	ND	ND	ND	ND	ND	ND	208
S112	K121E	8,73	437	-19	10,36	518	6	4,62	231	36,9	43,7	19,5	1186	954
S112	K121F	16,62	831	-12	32,88	1644	19	7,53	376	29,1	57,7	13,2	2851	2475
S112	K121G	9,10	455	2	15,06	753	-2	4,15	207	32,1	53,2	14,7	1415	1208
S112	K121H	ND	ND	ND	ND	ND	ND	ND	ND	ND	ND	ND	ND	ND
S112	K121I	16,30	815	-18	36,65	1833	-3	18,63	932	22,8	51,2	26,0	3580	2648
S112	K121K	ND	ND	ND	ND	ND	ND	ND	ND	ND	ND	ND	ND	ND
S112	K121L	11,87	594	-29	33,87	1693	-32	11,17	558	20,9	59,5	19,6	2845	2287
S112	K121M	2,18	109	4	6,35	317	-11	ND	ND	ND	ND	ND	ND	426
S112	K121N	6,25	312	-13	7,17	358	-10	2,45	123	39,4	45,2	15,5	793	671
S112	K121P	7,30	365	0	12,52	626	9	3,41	171	31,4	53,9	14,7	1162	991
S112	K121Q	7,79	390	-21	10,11	506	-4	3,90	195	35,7	46,4	17,9	1091	895
S112	K121R	ND	ND	ND	ND	ND	ND	ND	ND	ND	ND	ND	ND	ND
S112	K121S	10,93	547	-15	12,91	645	2	5,72	286	37,0	43,6	19,4	1478	1192
S112	K121T	6,73	337	-19	12,51	625	-12	6,27	314	26,4	49,0	24,6	1276	962
S112	K121V	11,00	550	-18	22,49	1124	1	12,96	648	23,7	48,4	27,9	2322	1674
S112	K121W	11,75	588	-23	17,40	870	-3	5,72	286	33,7	49,9	16,4	1744	1458
S112	K121Y	14,35	718	-23	18,45	923	-7	6,04	302	36,9	47,5	15,6	1943	1640
S112T	K121A	3,85	192	0	7,10	355	-15	ND	ND	ND	ND	ND	ND	547
S112T	K121C	ND	ND	ND	ND	ND	ND	ND	ND	ND	ND	ND	ND	ND
S112T	K121D	11,13	556	-8	15,15	757	3	4,19	210	36,5	49,7	13,8	1523	1314
S112T	K121E	12,76	638	-26	12,85	643	19	4,27	214	42,7	43,0	14,3	1495	1281
S112T	K121F	12,19	610	-16	20,79	1040	13	4,95	248	32,1	54,8	13,0	1898	1649
S112T	K121G	ND	ND	ND	ND	ND	ND	ND	ND	ND	ND	ND	ND	ND
S112T	K121H	ND	ND	ND	ND	ND	ND	ND	ND	ND	ND	ND	ND	ND
S112T	K121I	15,97	799	-3	31,75	1587	10	11,30	565	27,1	53,8	19,1	2951	2386
S112T	K121K	ND	ND	ND	ND	ND	ND	ND	ND	ND	ND	ND	ND	ND
S112T	K121L	12,86	643	-20	31,36	1568	-18	9,72	486	23,8	58,1	18,0	2697	2211
S112T														
S112T	K121N	ND	ND	ND	ND	ND	ND	ND	ND	ND	ND	ND	ND	ND
S112T	K121P	ND	ND	ND	ND	ND	ND	ND	ND	ND	ND	ND	ND	ND
S112T	K121Q	9,31	466	-30	12,13	606	-3	4,49	225	35,9	46,7	17,3	1297	1072
S112T	K121R	ND	ND	ND	ND	ND	ND	ND	ND	ND	ND	ND	ND	ND
S112T	K121S	3,72	186	-3	5,16	258	-2	ND	ND	ND	ND	ND	ND	444
S112T	K121T	5,93	297	-20	11,00	550	1	3,35	168	29,3	54,2	16,5	1015	847
S112T	K121V	11,95	598	-18	23,41	1170	10	14,25	713	24,1	47,2	28,7	2481	1768
S112T	K121W	15,64	782	-23	23,65	1182	-4	8,91	445	32,5	49,1	18,5	2409	1964
S112T	K121Y	11,00	550	-20	15,55	778	-2	4,57	228	35,3	50,0	14,7	1556	1328
S112V	K121A	9,74	487	-6	21,99	1100	11	6,83	342	25,3	57,0	17,7	1929	1587
S112V	K121C	5,16	258	-6	8,80	440	-6	ND	ND	ND	ND	ND	ND	698
S112V	K121D	ND	ND	ND	ND	ND	ND	ND	ND	ND	ND	ND	ND	ND
S112V	K121E	13,12	656	-29	17,93	897	-1	11,26	563	31,0	42,4	26,6	2116	1553
S112V	K121F	15,13	756	17	39,26	1963	28	6,12	306	25,0	64,9	10,1	3025	2719
S112V	K121G	12,21	610	-8	23,51	1176	14	6,20	310	29,1	56,1	14,8	2096	1786
S112V	K121H	ND	ND	ND	ND	ND	ND	ND	ND	ND	ND	ND	ND	ND
S112V	K121I	18,94	947	53	47,39	2370	30	10,71	535	24,6	61,5	13,9	3852	3316
S112V	K121K	ND	ND	ND	ND	ND	ND	ND	ND	ND	ND	ND	ND	ND
S112V	K121L	17,09	854	45	47,36	2368	21	13,09	654	22,0	61,1	16,9	3876	3222
S112V	K121M	5,31	265	-1	12,65	633	-12	2,36	118	26,1	62,3	11,6	1016	898
S112V	K121N	13,93	696	-8	20,86	1043	-3	6,12	306	34,0	51,0	15,0	2045	1740
S112V	K121P	8,50	425	19	15,54	777	22	5,32	266	28,9	52,9	18,1	1468	1202
S112V	K121Q													
S112V	K121R	ND	ND	ND	ND	ND	ND	ND	ND	ND	ND	ND	ND	ND
S112V	K121S	15,11	755	-3	25,41	1271	7	12,93	647	28,2	47,6	24,2	2673	2026
S112V	K121T	12,85	642	6	28,67	1434	-12	15,28	764	22,6	50,5	26,9	2840	2076
S112V	K121V	16,02	801	55	35,14	1757	33	21,54	1077	22,0	48,3	29,6	3635	2558
S112V	K121W	16,44	822	-8	28,36	1418	5	11,52	576	29,2	50,4	20,5	2816	2240

S112V	K121Y	10,79	540	-11	14,80	740	-6	6,83	342	33,3	45,6	21,1	1622	1280
S112W	K121A	14,16	708	7	26,43	1321	-15	16,43	822	24,8	46,3	28,8	2851	2029
S112W	K121C	3,67	183	-7	5,43	271	-11	ND	ND	ND	ND	ND	ND	455
S112W	K121D	6,61	331	-6	9,11	456	1	ND	ND	ND	ND	ND	ND	786
S112W	K121E	ND	ND	ND	ND	ND	ND	ND	ND	ND	ND	ND	ND	ND
S112W	K121F	17,18	859	-31	28,64	1432	3	8,38	419	31,7	52,8	15,5	2710	1828
S112W	K121G	14,46	723	5	21,58	1079	0	8,19	410	32,7	48,8	18,5	2212	1802
S112W	K121H													
S112W	K121I													
S112W	K121K													
S112W	K121L	17,89	894	-32	26,97	1348	-9	16,76	838	29,0	43,8	27,2	3080	2243
S112W	K121M													
S112W	K121N													
S112W	K121P	ND	ND	ND	ND	ND	ND	ND	ND	ND	ND	ND	ND	ND
S112W	K121Q													
S112W	K121R	5,21	261	2	18,28	914	-2	ND	ND	ND	ND	ND	ND	1175
S112W	K121S	9,56	478	-5	14,89	744	-8	8,04	402	29,4	45,8	24,7	1624	1222
S112W	K121T													
S112W	K121V													
S112W	K121W													
S112W	K121Y													
S112Y	K121A	11,79	590	-2	23,39	1169	-16	12,53	626	24,7	49,0	26,3	2385	1759
S112Y	K121C													
S112Y	K121D													
S112Y	K121E	10,58	529	-7	13,40	670	-14	8,54	427	32,5	41,2	26,3	1626	1199
S112Y	K121F													
S112Y	K121G													
S112Y	K121H	6,34	317	-2	7,98	399	-15	3,95	198	34,7	43,7	21,6	914	716
S112Y	K121I	ND	ND	ND	ND	ND	ND	ND	ND	ND	ND	ND	ND	ND
S112Y	K121K	ND	ND	ND	ND	ND	ND	ND	ND	ND	ND	ND	ND	ND
S112Y	K121L	13,86	693	28	26,67	1333	-33	33,23	1662	18,8	36,1	45,1	3688	2027
S112Y	K121M													
S112Y	K121N	16,29	814	-2	22,35	1118	-21	12,72	636	31,7	43,5	24,8	2568	1932
S112Y	K121P													
S112Y	K121Q	10,54	527	-12	14,74	737	-27	10,90	545	29,1	40,7	30,1	1809	1264
S112Y	K121R													
S112Y	K121S	8,14	407	-7	13,81	690	-25	8,51	426	26,7	45,3	28,0	1523	1097
S112Y	K121T	8,19	410	2	14,61	730	-21	17,24	862	20,5	36,5	43,1	2002	1140
S112Y	K121V													
S112Y	K121W	12,77	639	4	19,81	990	-7	12,00	600	28,7	44,4	26,9	2229	1629
S112Y	K121Y	12,10	605	-6	19,75	988	-5	7,95	398	30,4	49,6	20,0	1991	1593

Complementary data of selected Sav mutants

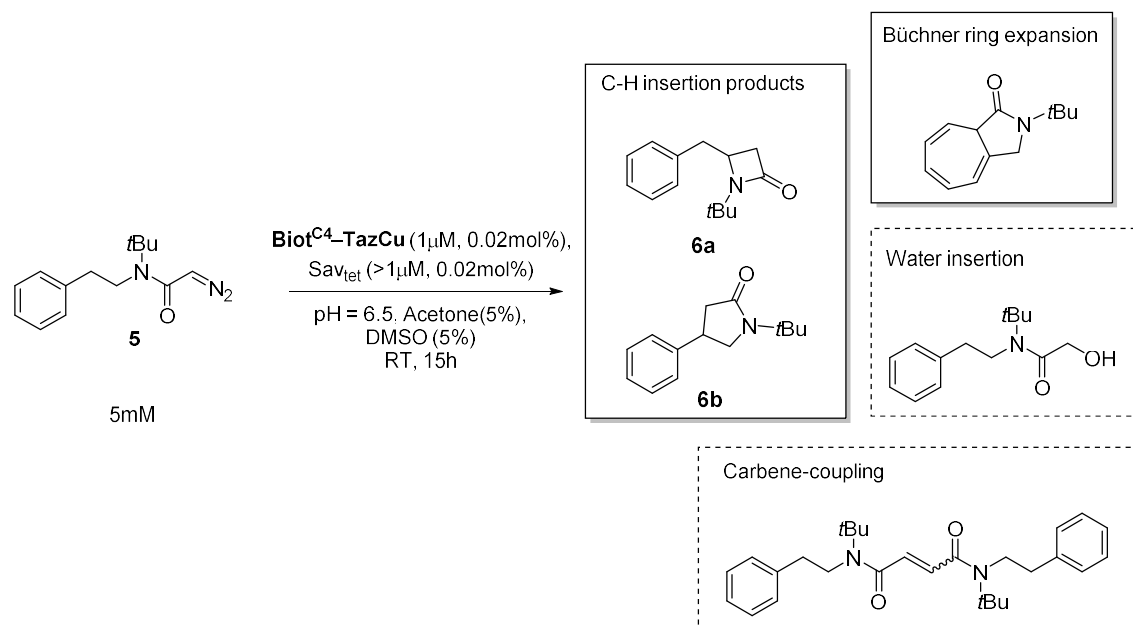


Table S3 Complementary data of selected Sav mutants

Mutant	β-lactam			γ-lactam			Büchner			Others	Total conv. ^a
	Yield(%)	TON	ee (%)	Yield(%)	TON	ee (%)	Yield(%)	TON	ee (%)	Yield(%)	
S112F-K121E	16,4	819	-46	17,0	852	-17	22,7	1136	-30	24,7	80,8
S112F-K121T	15,1	757	7	26,9	1344	-6	26,4	1318	-21	28,3	96,7
S112Y-K121L	13,9	693	28	26,7	1333	-33	33,2	1662	-9	7,5	81,3
S112F-K121L	15,0	752	36	32,4	1622	-27	34,7	1733	-20	15,8	97,9
S112F-K121I	12,3	615	-3	31,7	1586	-27	35,7	1783	-51	15,5	95,2
S112N-K121V	11,0	550	65	43,6	2181	73	14,8	739	21	22,4	91,8
S112N-K121V-L124G	29,5	1477	-62	15,9	795	-20	10,9	545	-14	23,6	79,9
S112N-K121V-L124I	8,3	417	64	51,3	2564	76	16,3	815	21	11,5	87,4

^aThe total conversion was determined based on the substrate (diazo reagent) consumption and accounts for all the reaction products and byproducts shown above (max TTON = 5000).

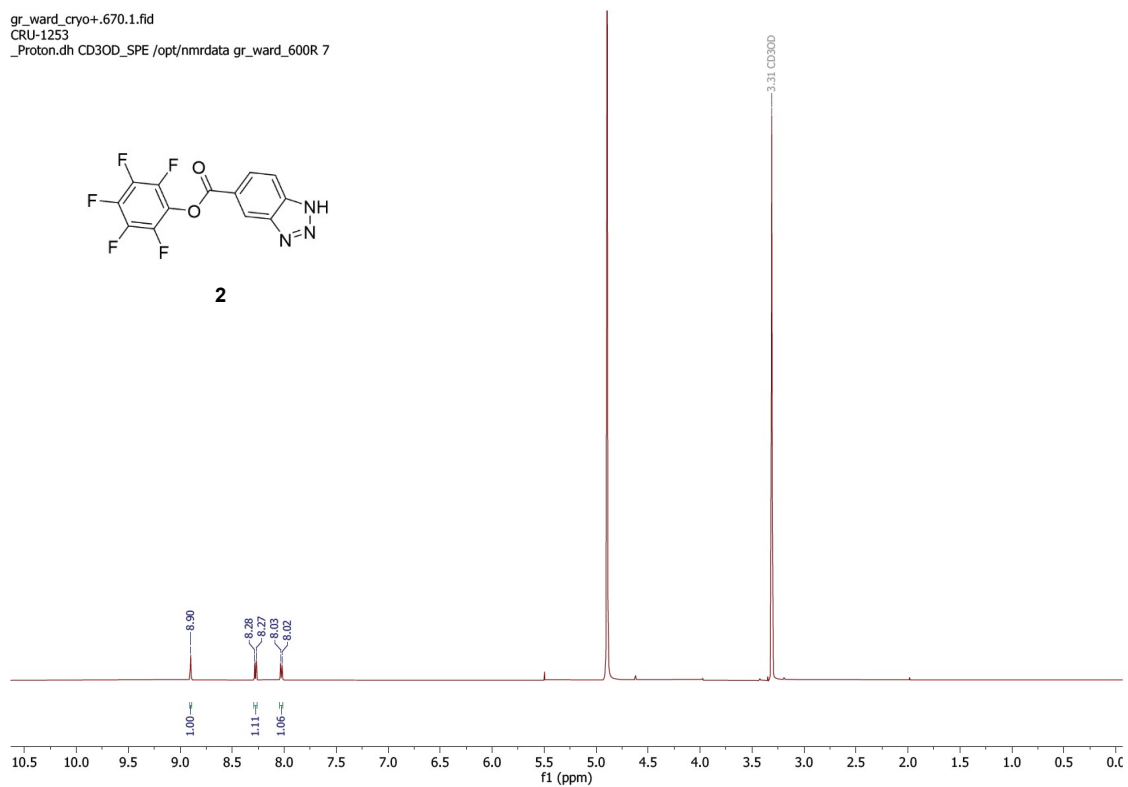
Extended substrate scope

Table S4. Extended substrate scope

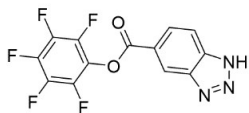
Substrate	Product	Mutant	e.r.	r.r. (β/γ)	TTON (C-H insert.)
		S112N-K121V	79:21	-	1290
		S112N-K121V-L124G	19:81	65:35	2272
		S112N-K121V-L124I	88:12	14:86	2981
		S112N-K121V-L124G	37:63	28:72	2623
		S112N-K121V	27:73	12:88	3585
		S112N-K121L	-	0:100	4627
		S112N-K121V-L124G	35:65	14:86	720
		S112N-K121L	47:53	9:91	1058
		S112N-K121V-L124G	54:46	51:50	499
		S112N-K121V	69:31	33:67	1276
		S112N-K121V-L124G	44:56	25:75	1037
		S112N-K121V-L124I	56:43	18:82	565

4.5.10 NMR and HRMS spectra

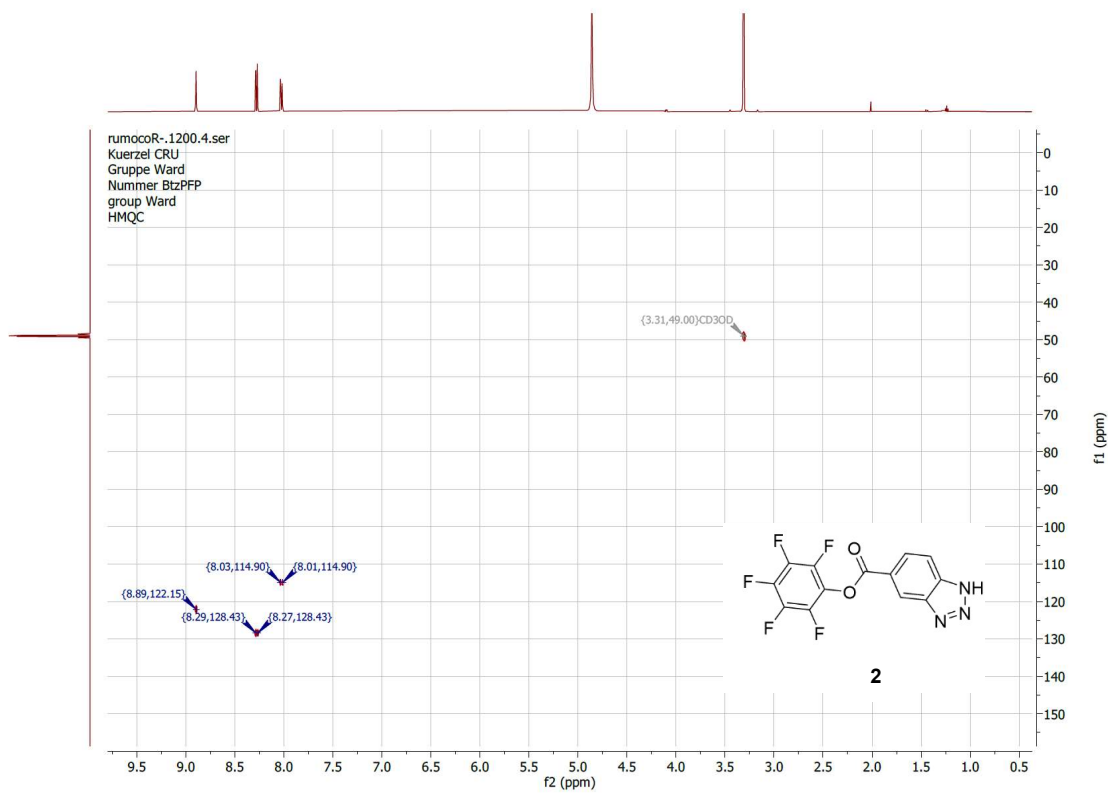
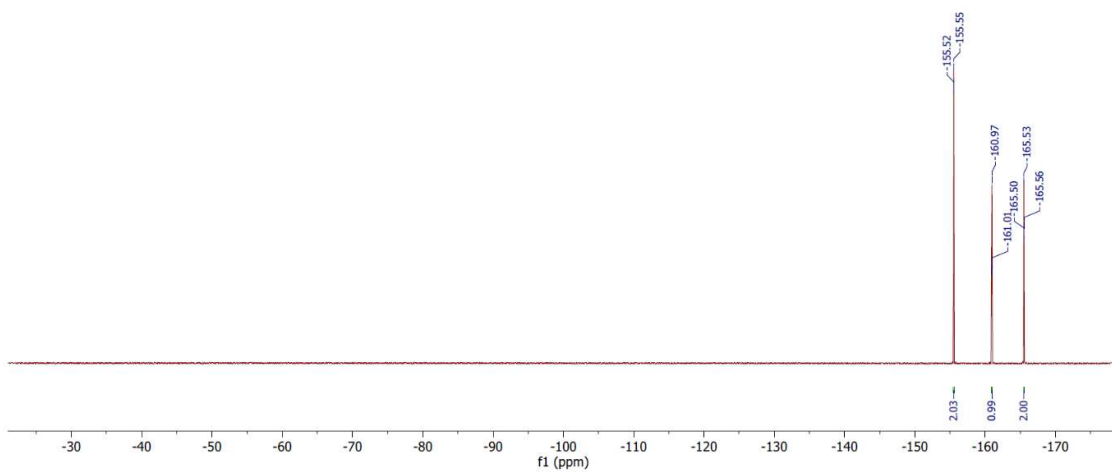
gr_ward_cryo+.670.1.fid
CRU-1253
_Proton.dh CD3OD_SPE /opt/nmrdata gr_ward_600R 7



gr_ward_cryo+.670.2.fid
CRU-1253
_F19_cpd.dh CD30D_SPE /opt/nmrdata gr_ward_600R 7



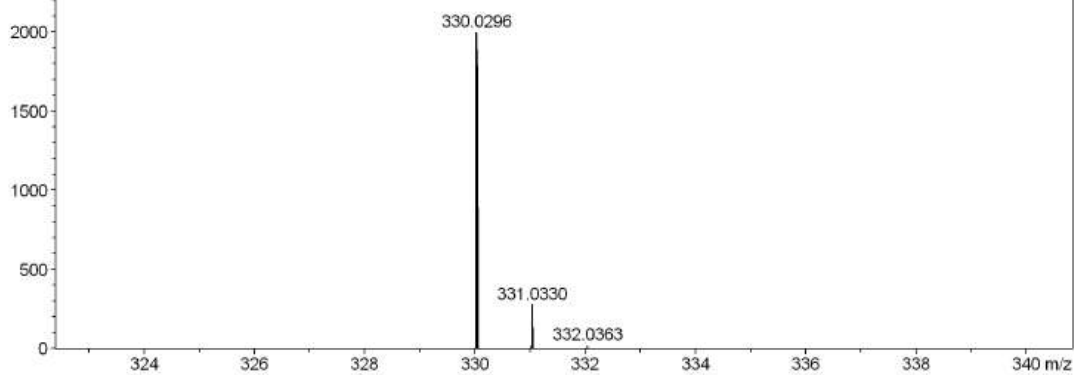
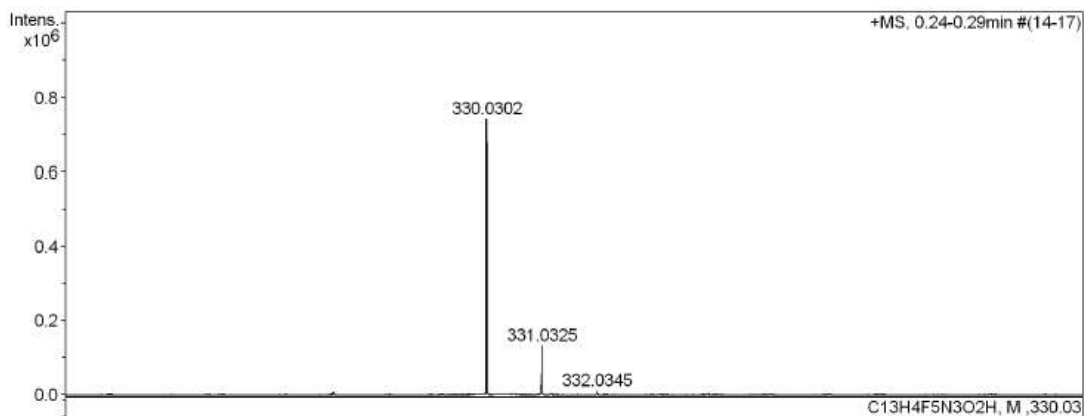
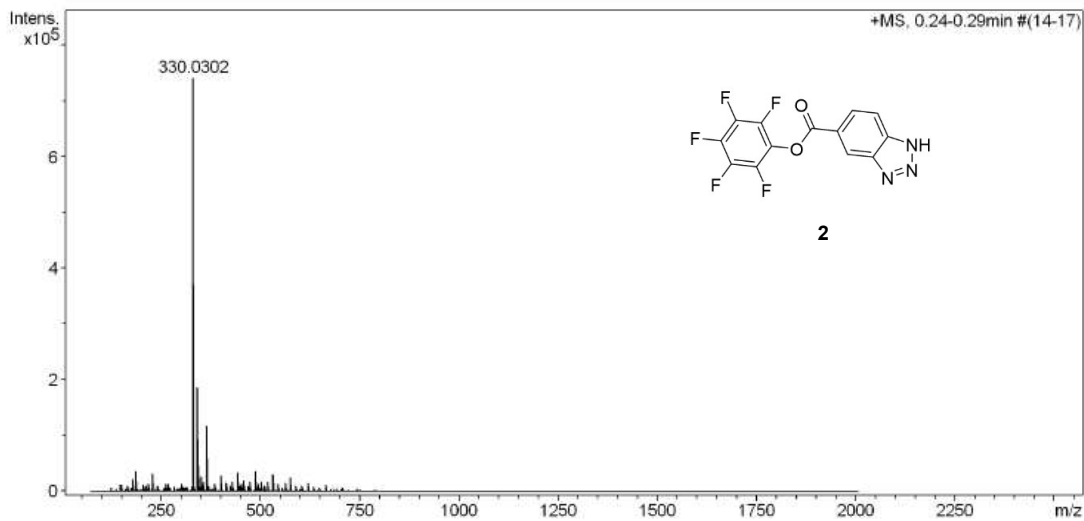
2



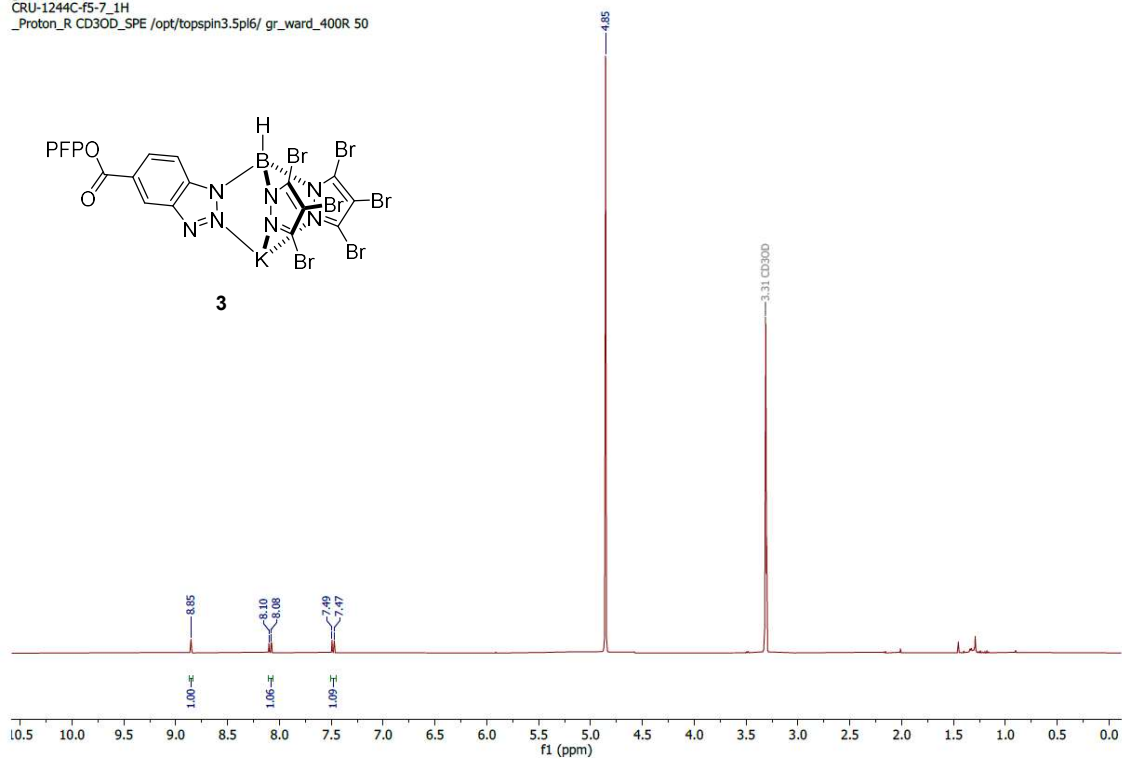
High Resolution Mass Spectrometry Report

Sample Name CRU-1243
Comment

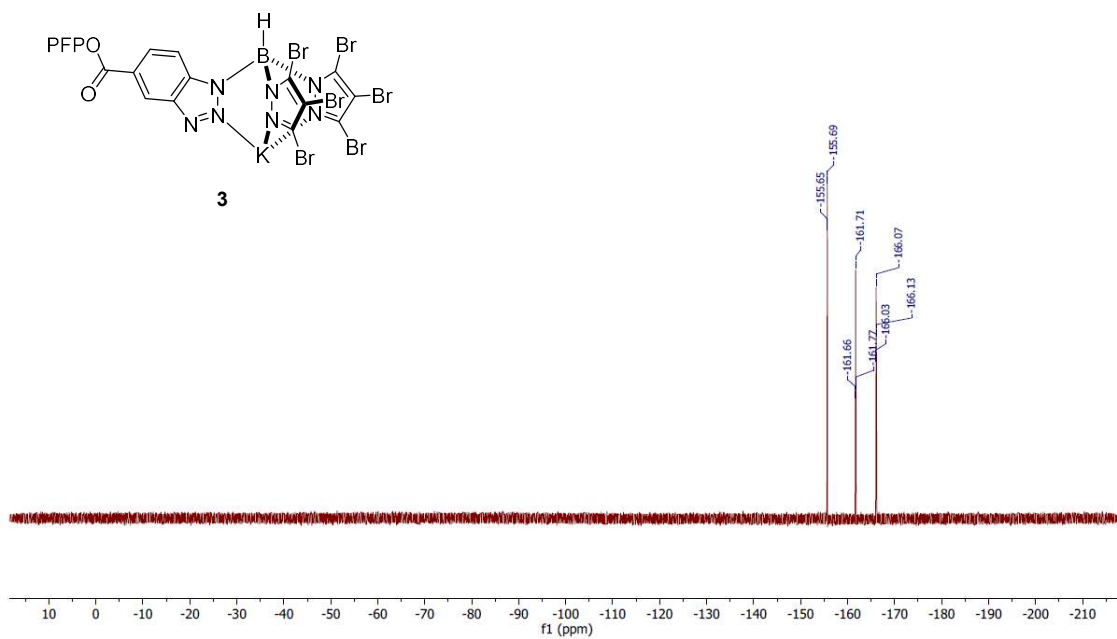
Instrument maXis 4G
Method ms_nocolumn_mid_pos.m

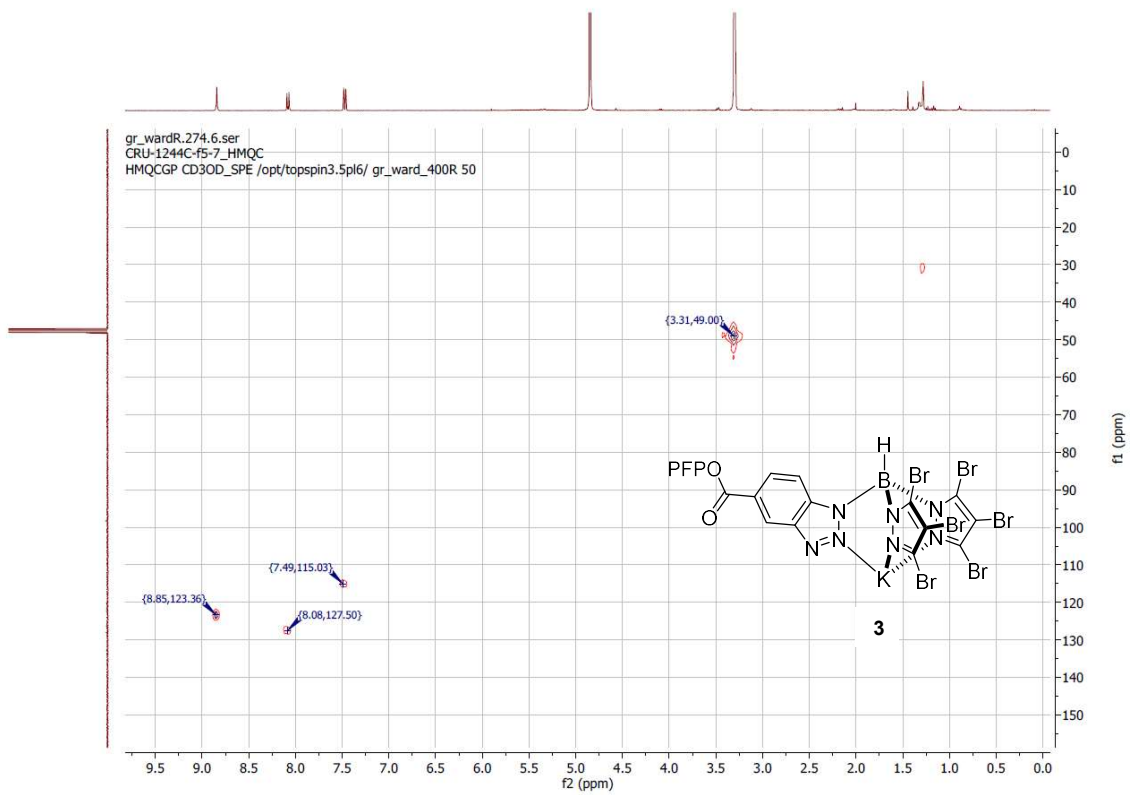


gr_wardR.274.1.fid
CRU-1244C-f5-7_1H
_Proton_R CD3OD_SPE /opt/topspin3.5pl6/ gr_ward_400R 50



gr_wardR.274.2.fid
CRU-1244C-f5-7_19F
_F19CPD CD3OD_SPE /opt/topspin3.5pl6/ gr_ward_400R 50

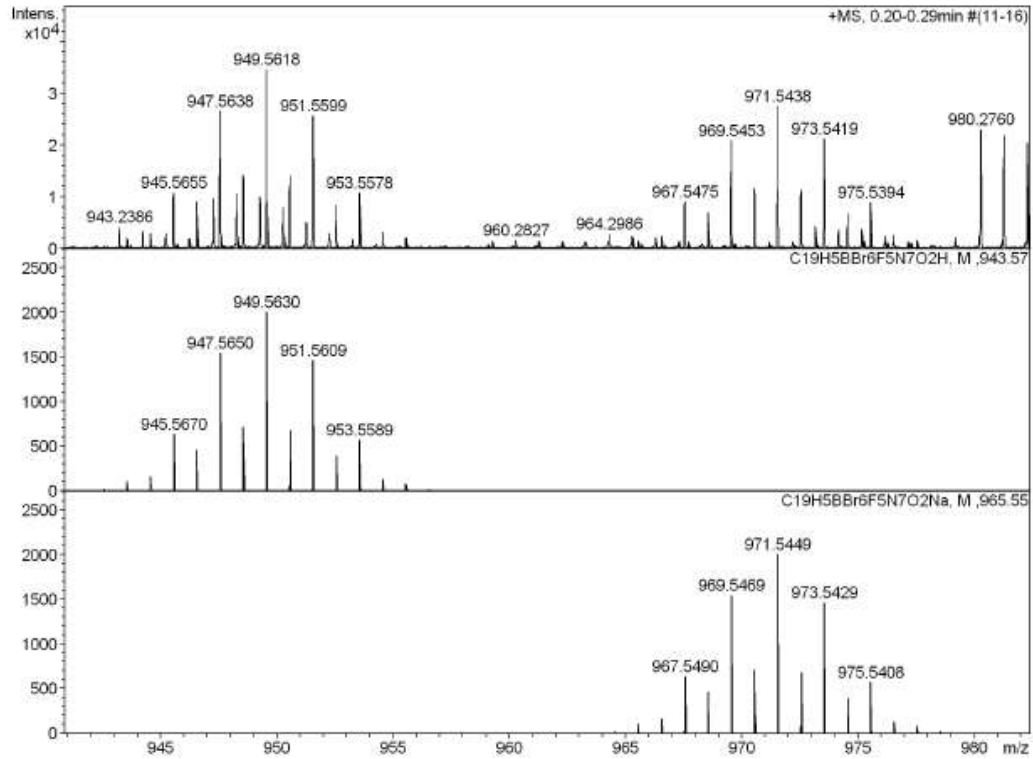
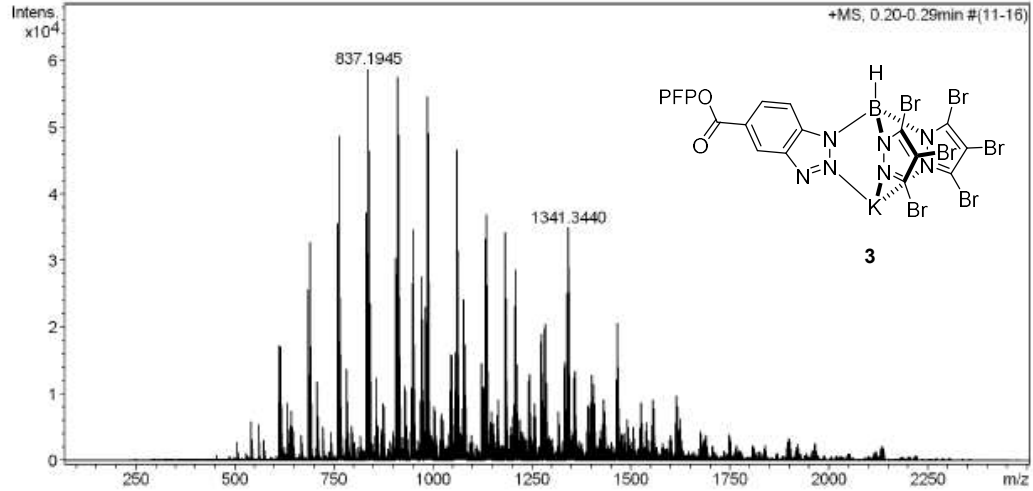




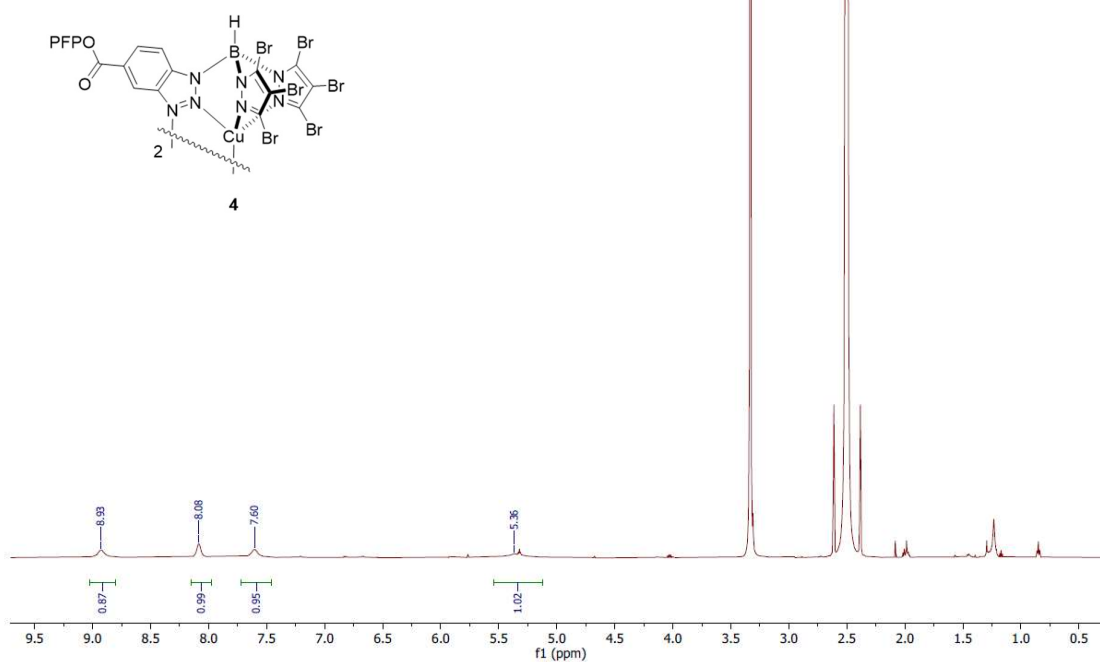
High Resolution Mass Spectrometry Report

Sample Name CRU-1244
Comment

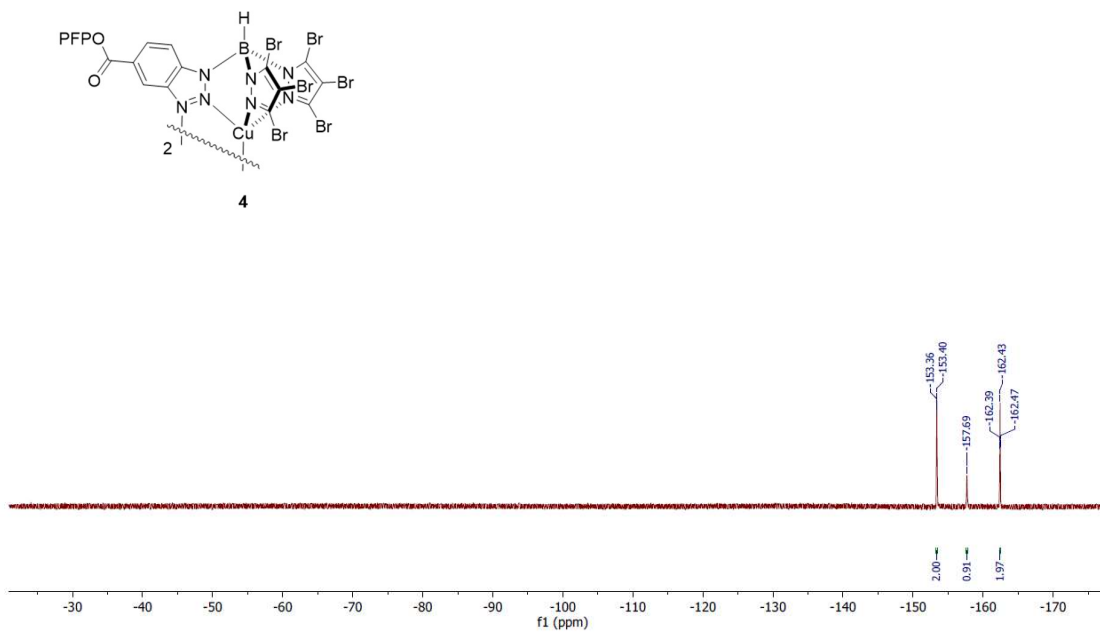
Instrument maXis 4G
Method ms_nocolumn_high_pos_use_acn.m



gr_ward_cryo+.659.1.fid
CRU-1246
_Proton.dh DMSO /opt/nmrdata gr_ward_600R 21



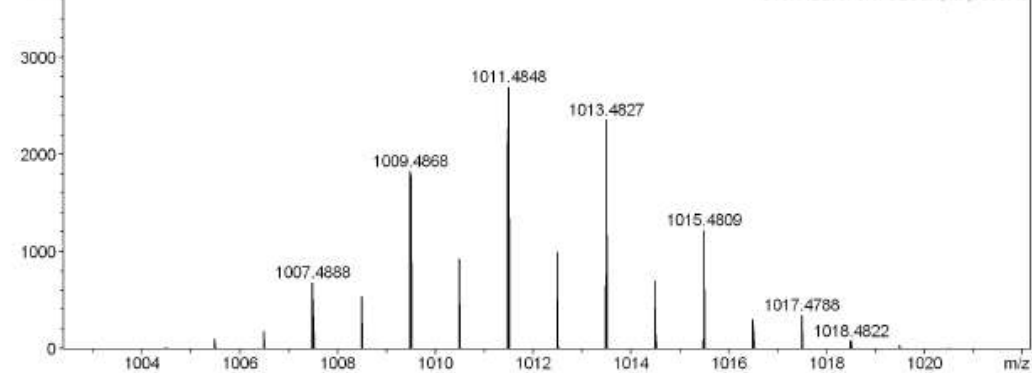
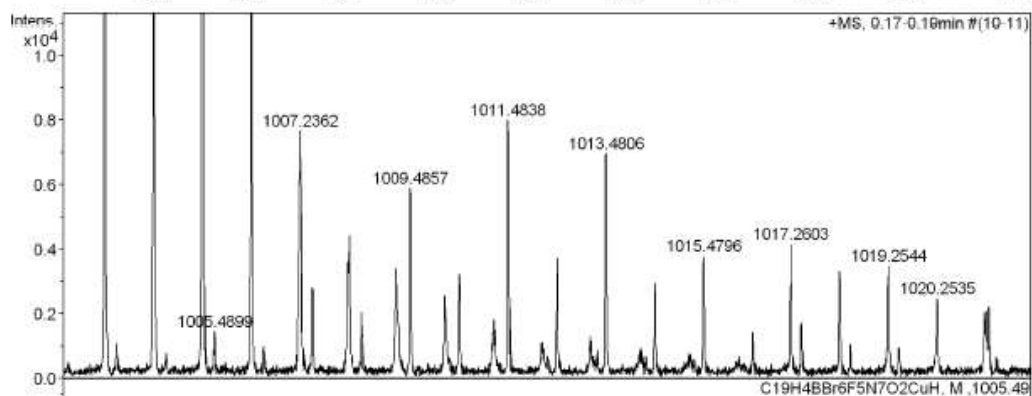
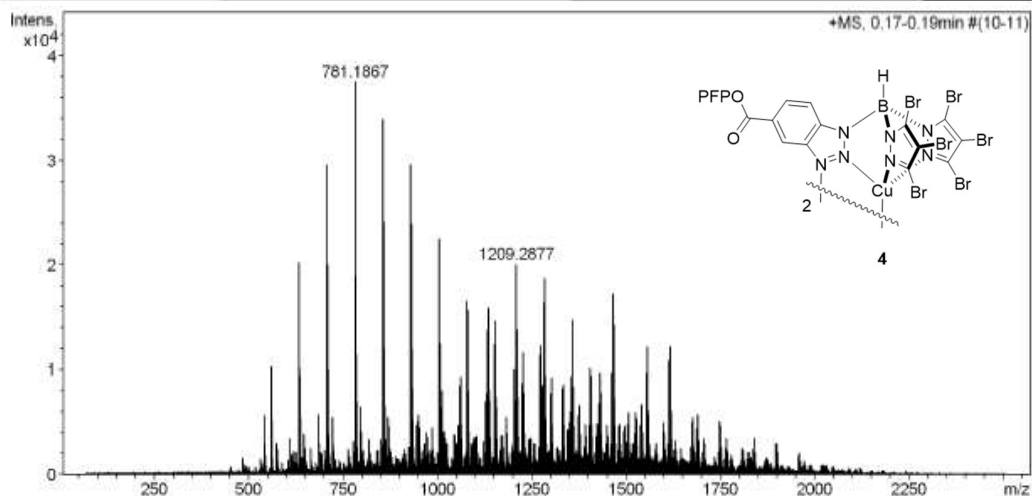
gr_ward_cryo+.659.2.fid
CRU-1246
_F19_cpd.dh DMSO /opt/nmrdata gr_ward_600R 21

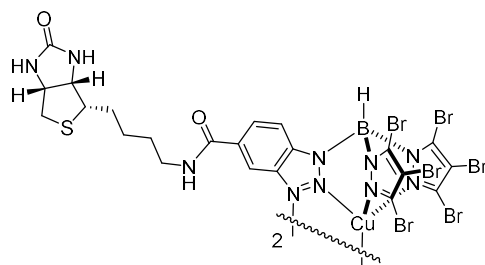


High Resolution Mass Spectrometry Report

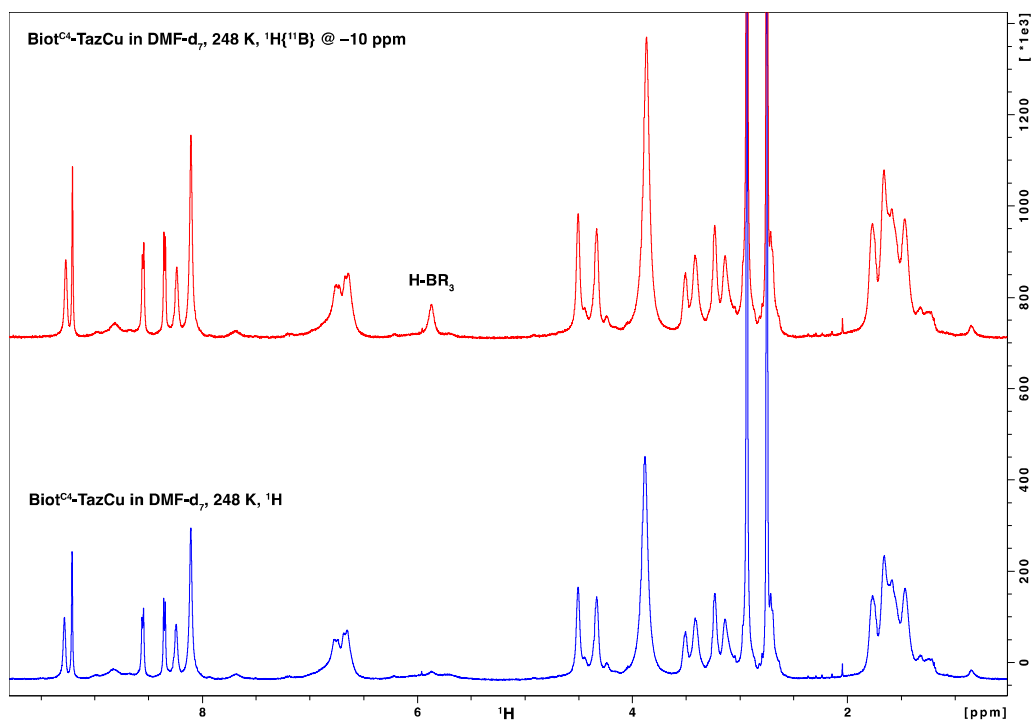
Sample Name CRU-1246
Comment

Instrument maXis 4G
Method ms_nocolumn_high_pos_use_acn.m

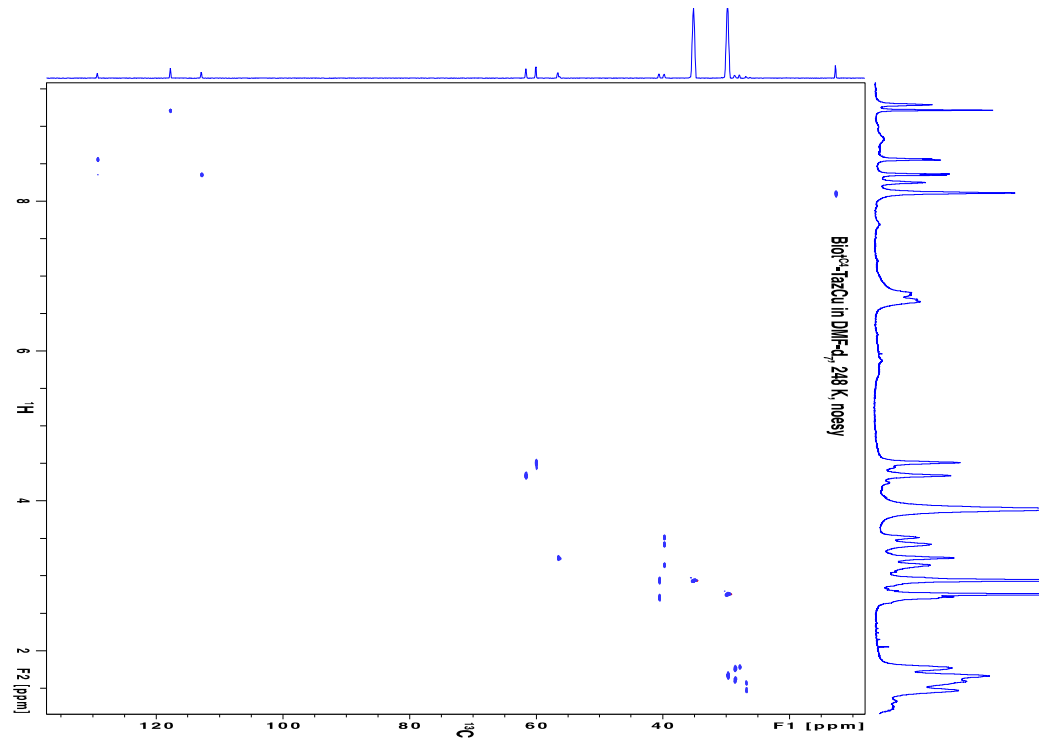
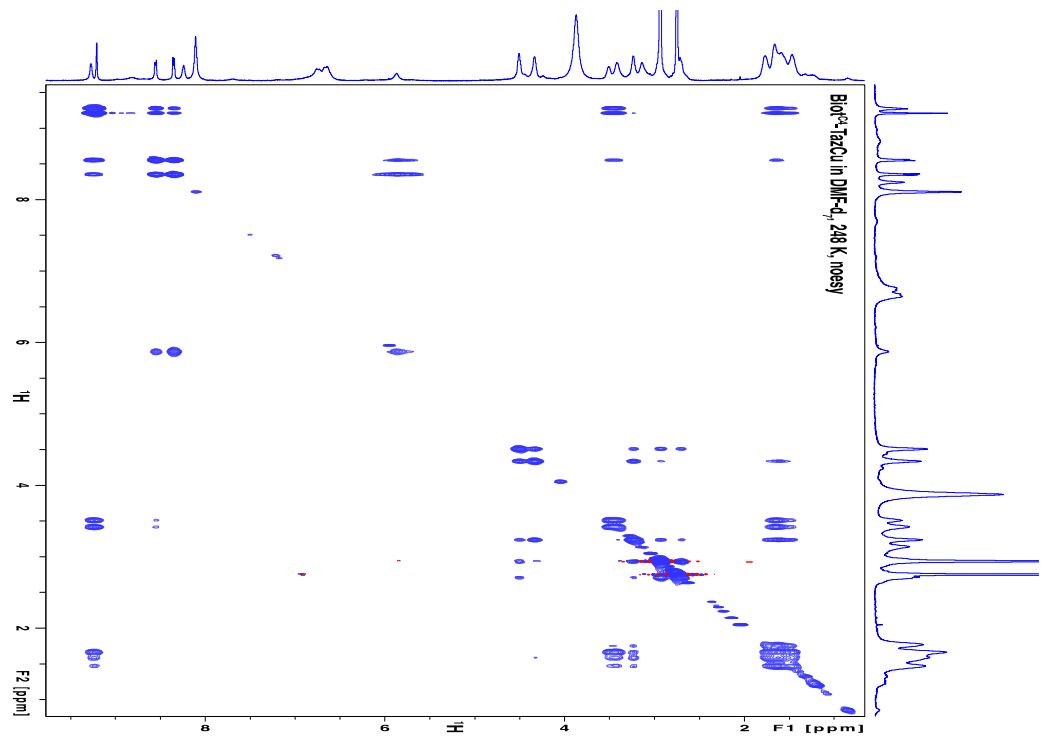




Biot^{C4}-TazCu



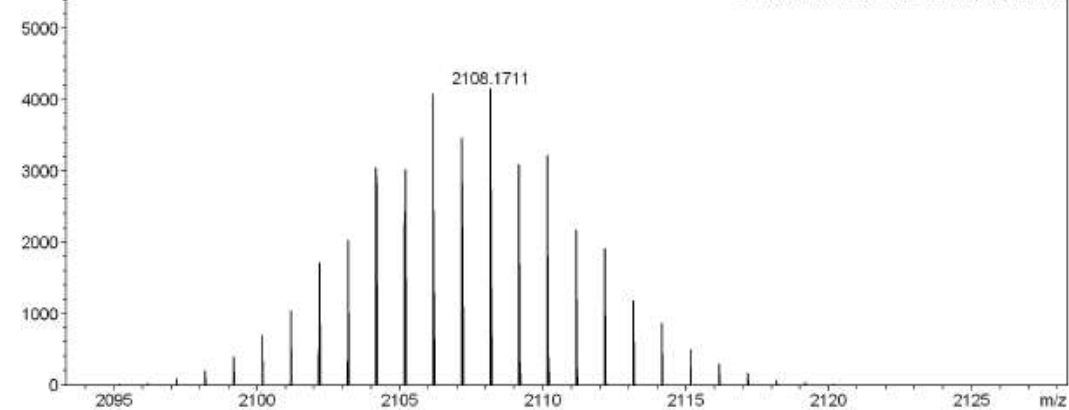
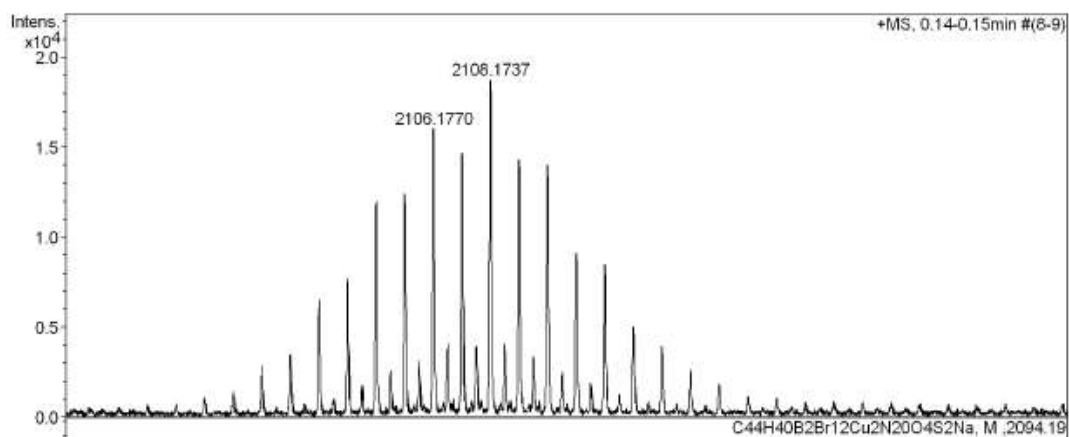
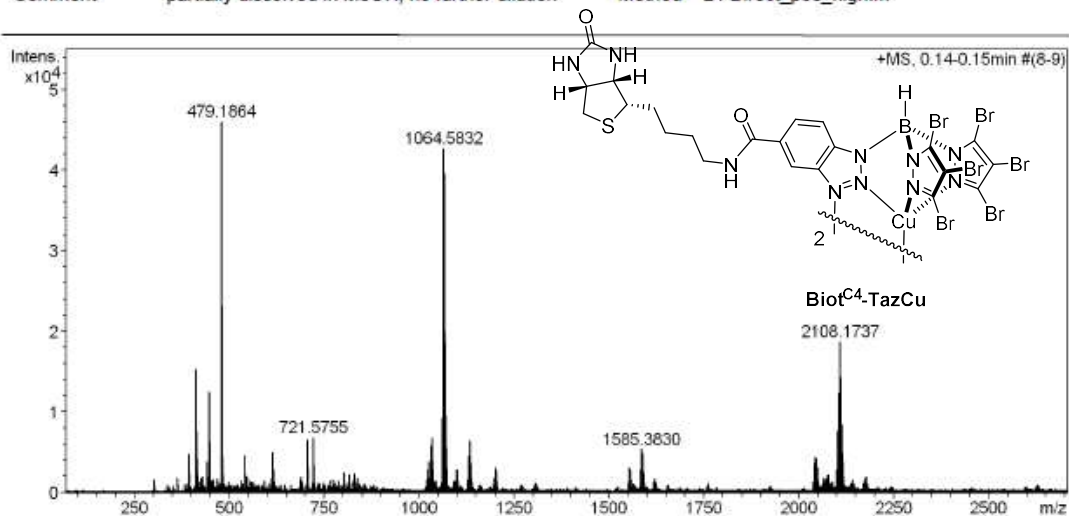
¹H-NMR spectrum, 600 MHz, upper panel with, lower panel without ¹¹B decoupling



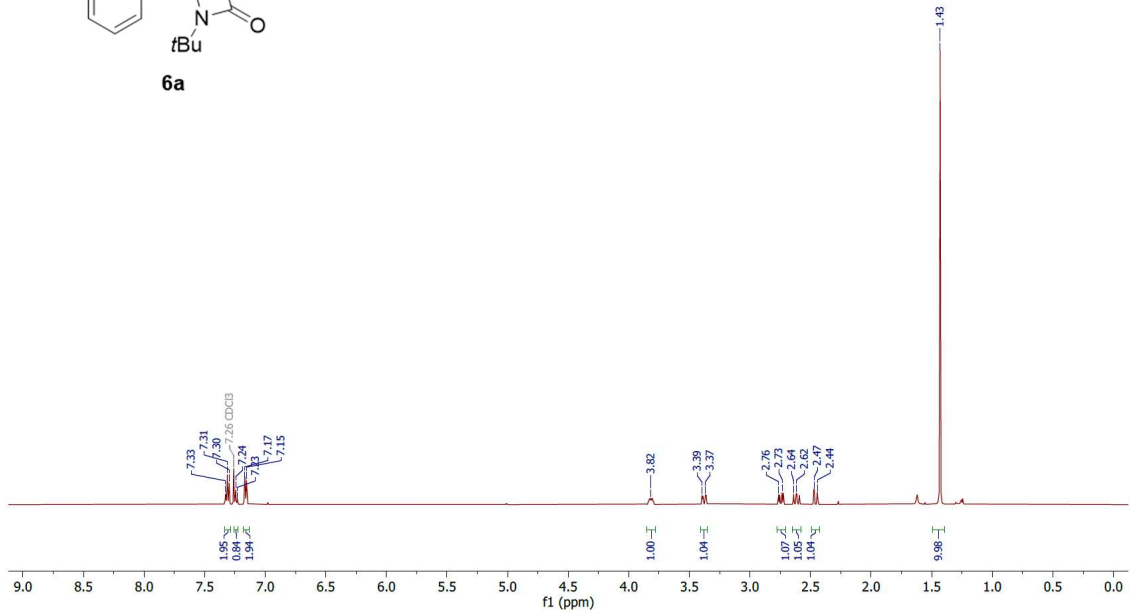
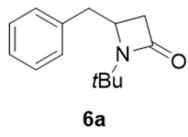
^1H - ^{13}C -HSQC spectrum, 600 MHz

High Resolution Mass Spectrometry Report

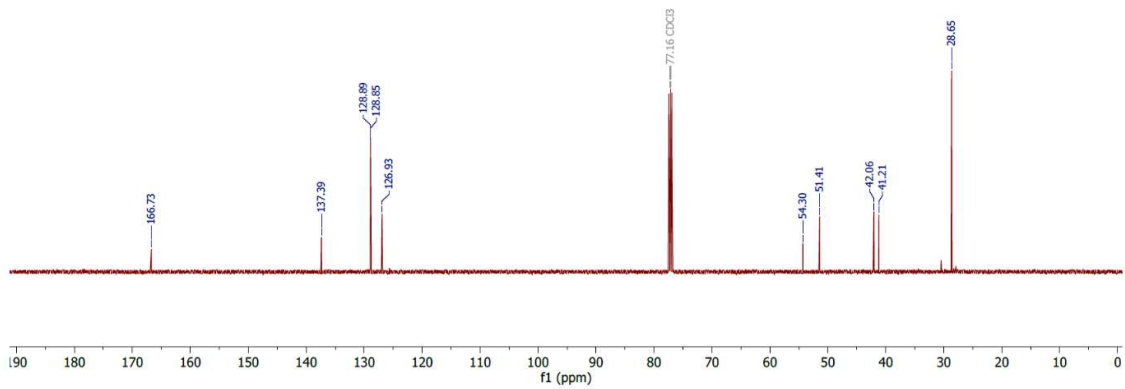
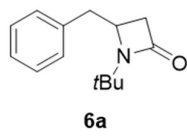
Sample Name CRU-1022 Instrument maXis 4G
Comment partially dissolved in MeOH, no further dilution Method 24 Direct_pos_high.m

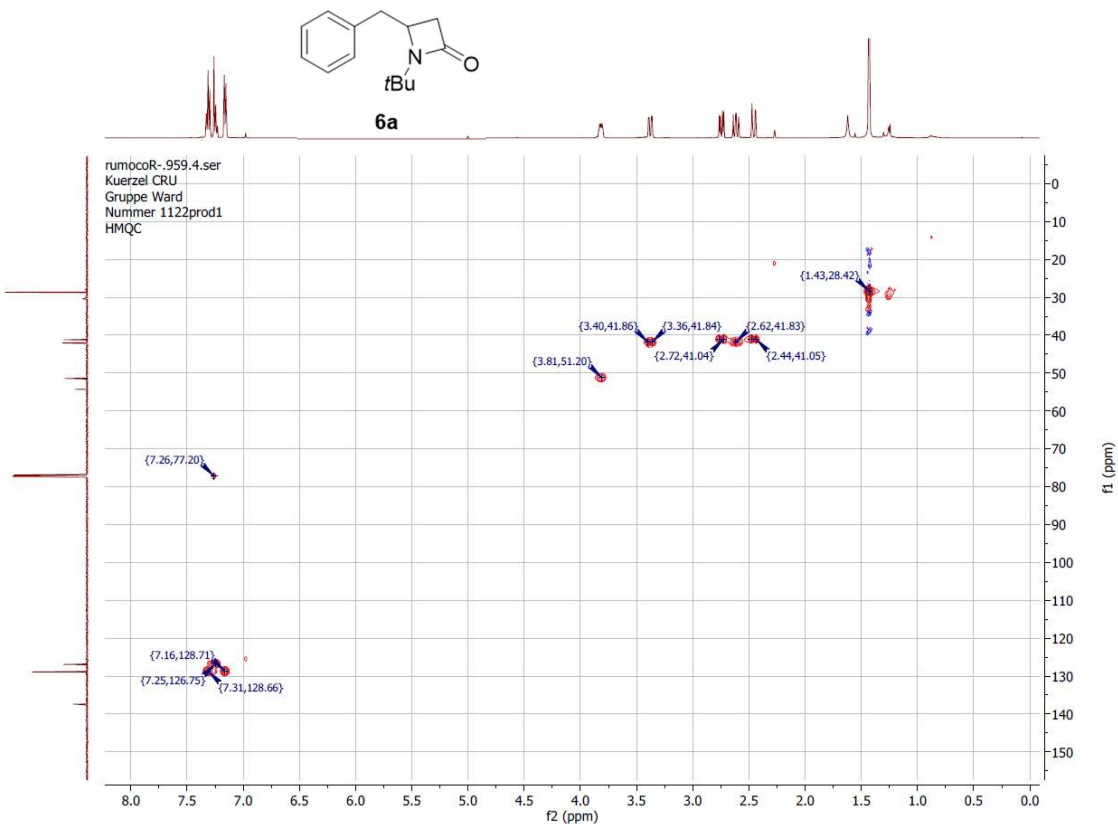
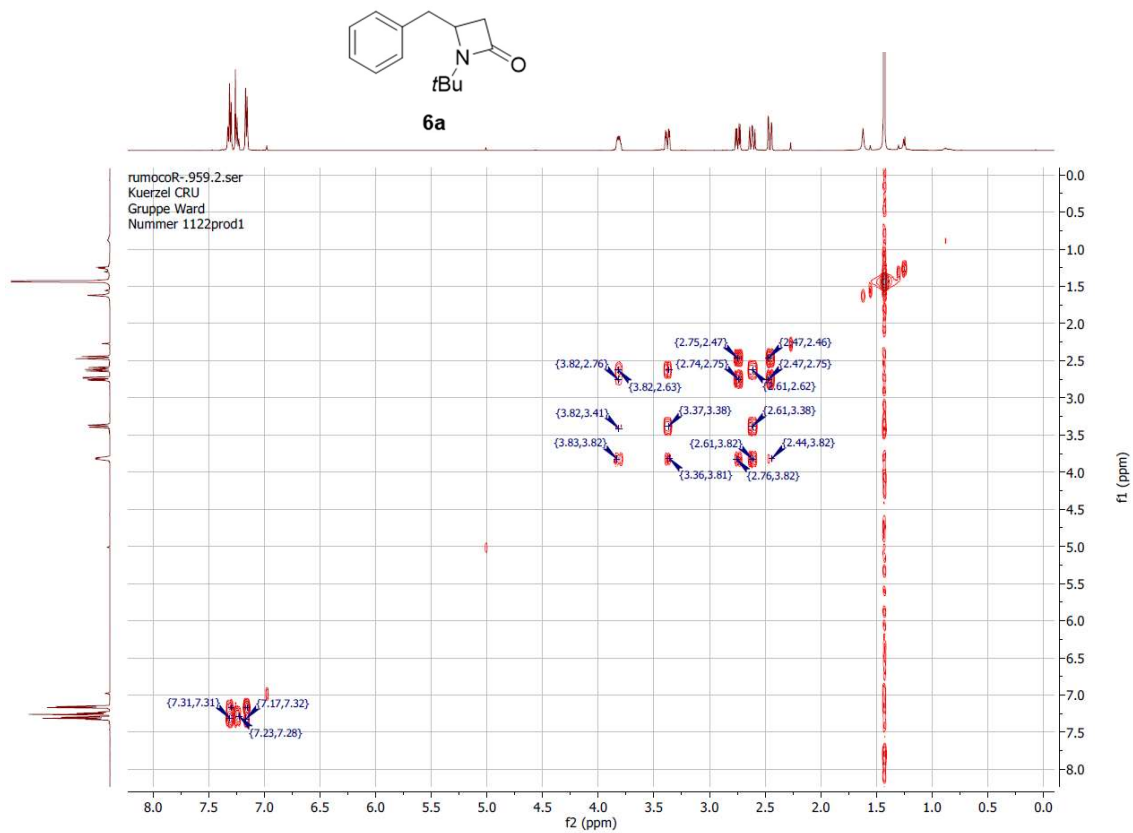


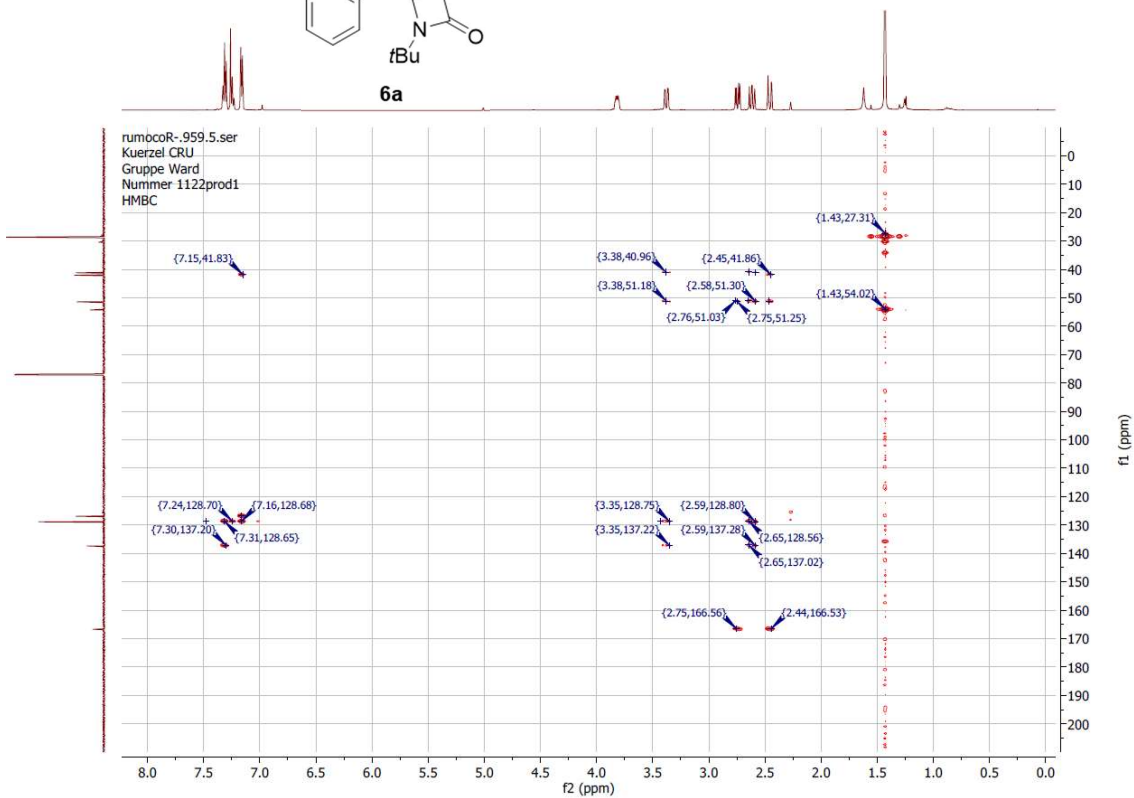
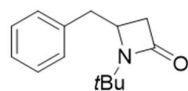
rumocoR-959.1.fid
Kuerzel CRU
Gruppe Ward
Nummer 1122prod1



rumocoR-959.3.fid
Kuerzel CRU
Gruppe Ward
Nummer 1122prod1



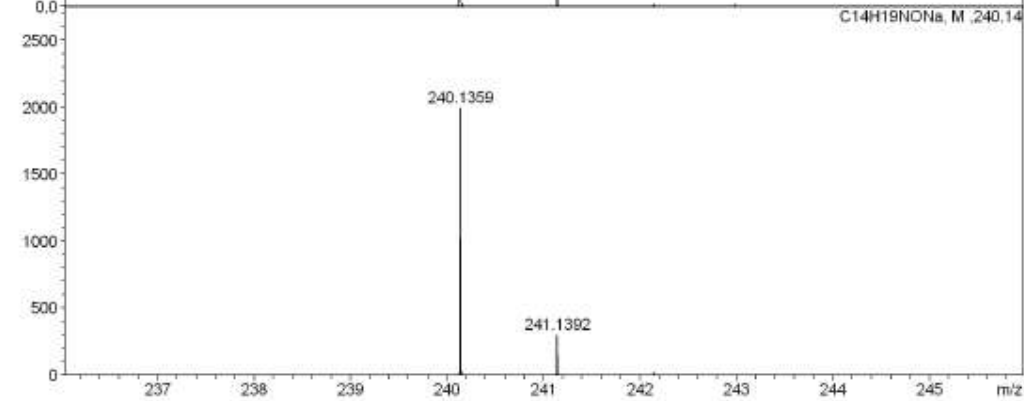
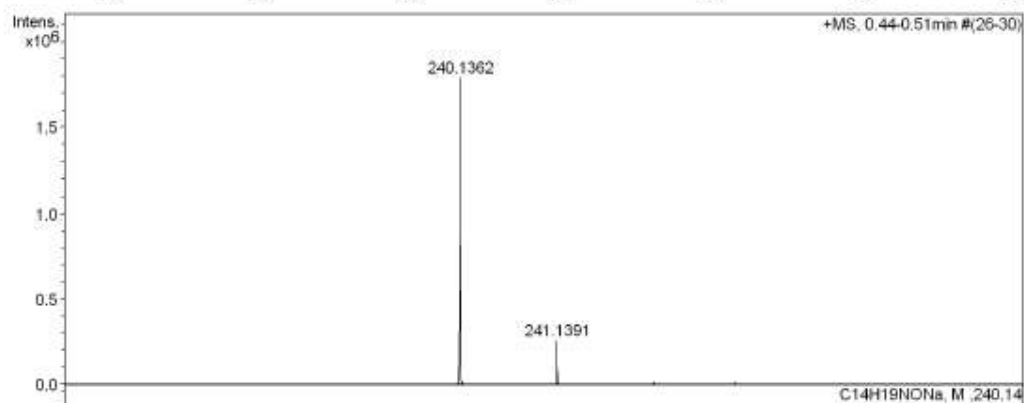
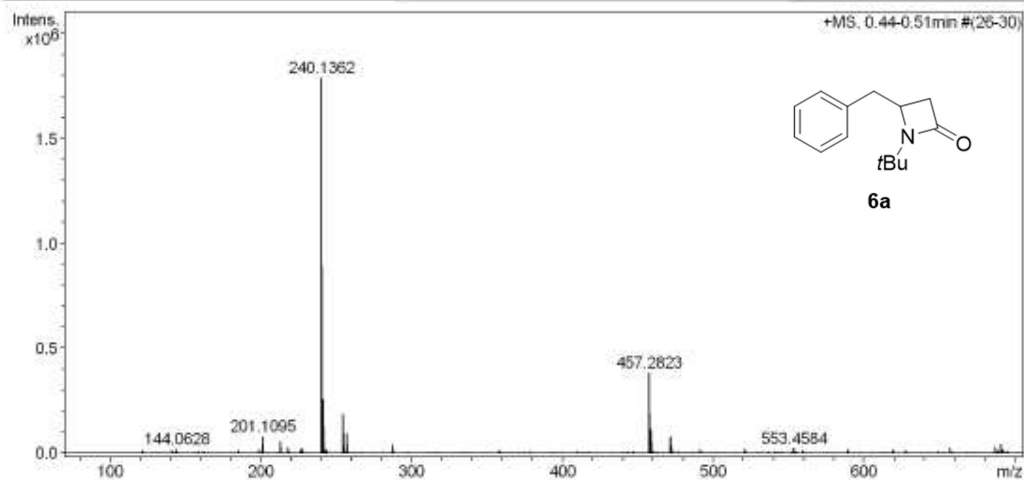




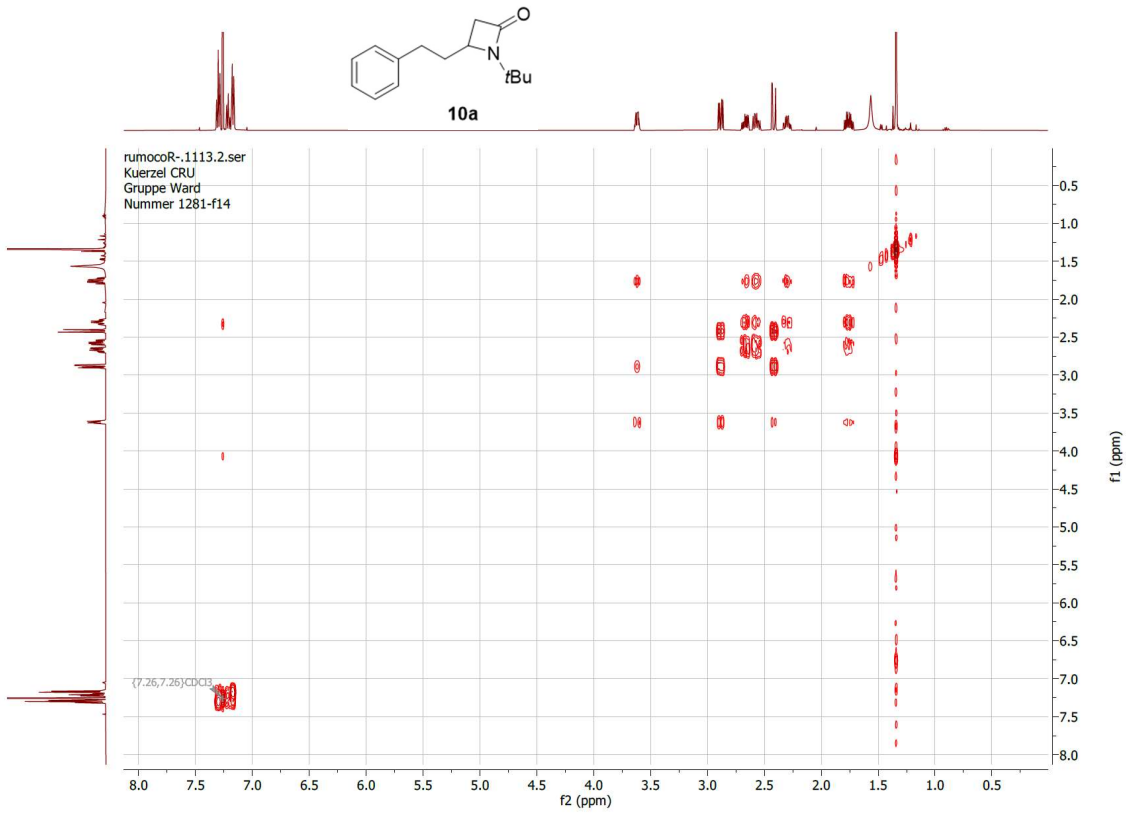
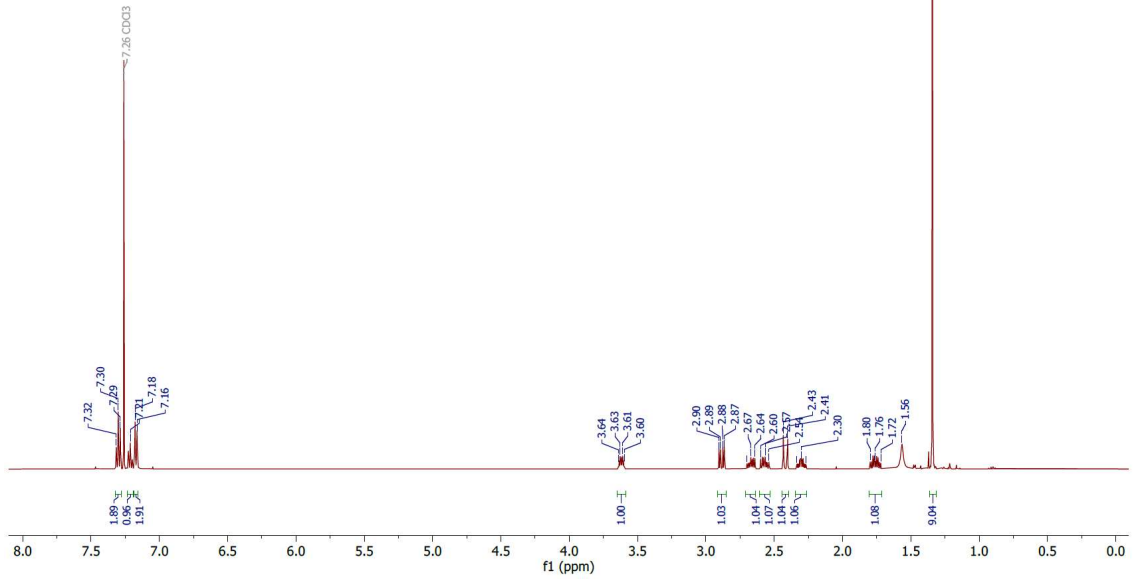
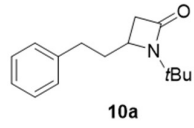
High Resolution Mass Spectrometry Report

Sample Name CRU-1122
Comment

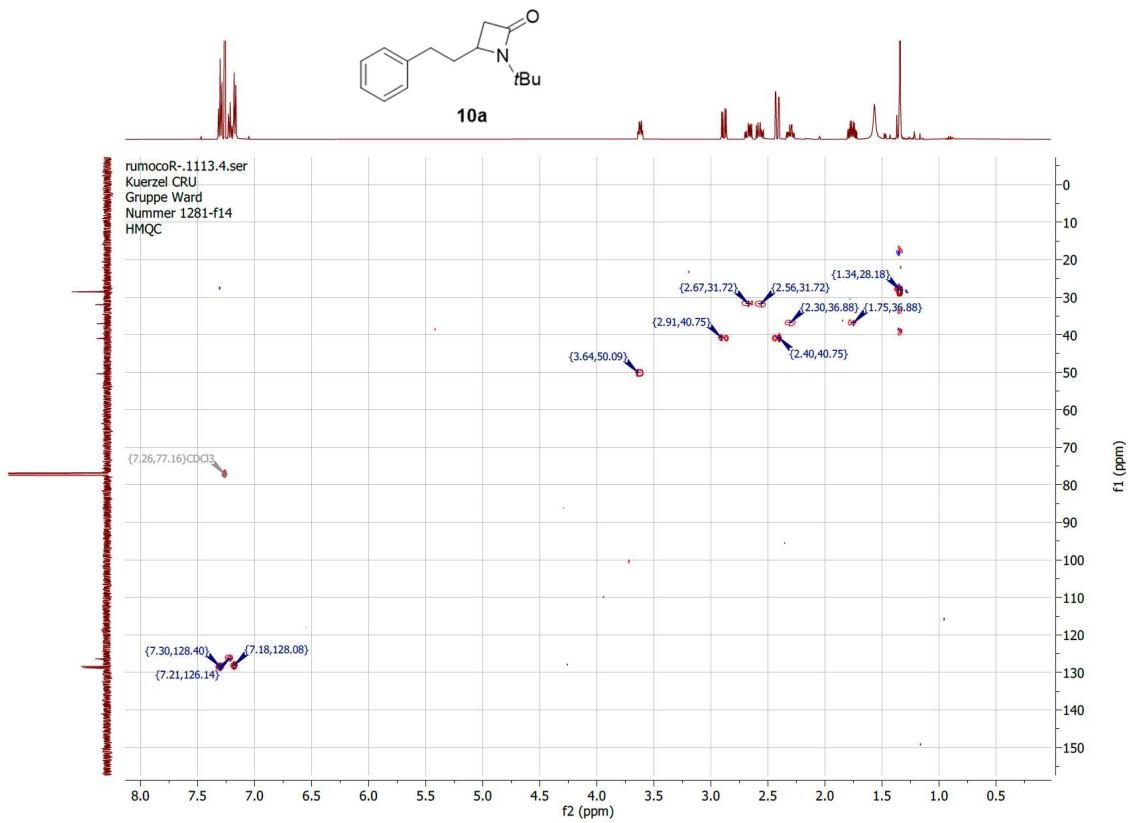
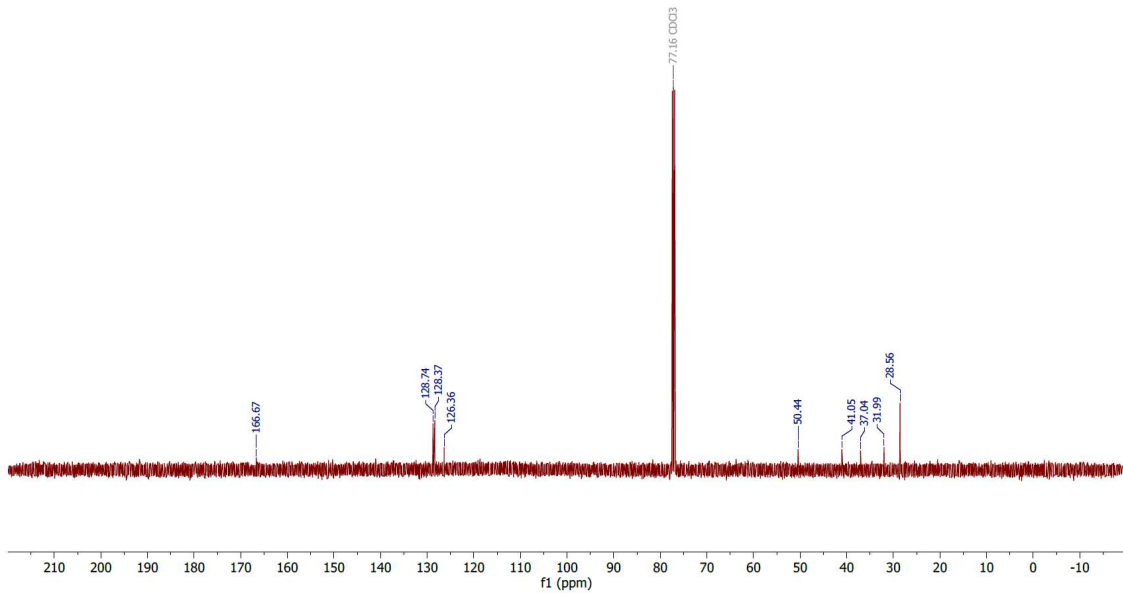
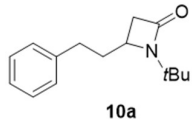
Instrument maXis 4G
Method ms_nocolumn_low_pos.m

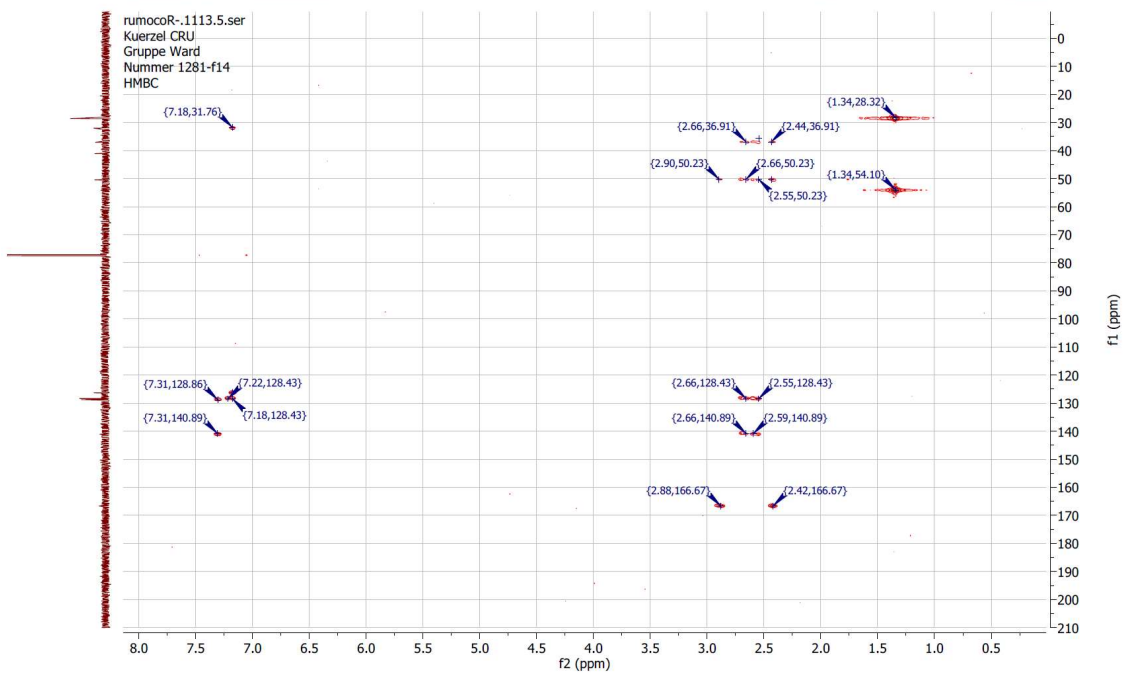
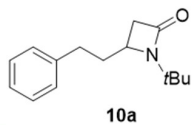


rumocoR-.1113.1.fid
Kuerzel CRU
Gruppe Ward
Nummer 1281-f14



rumocoR-.1113.3.fid
Kuerzel CRU
Gruppe Ward
Nummer 1281-f14

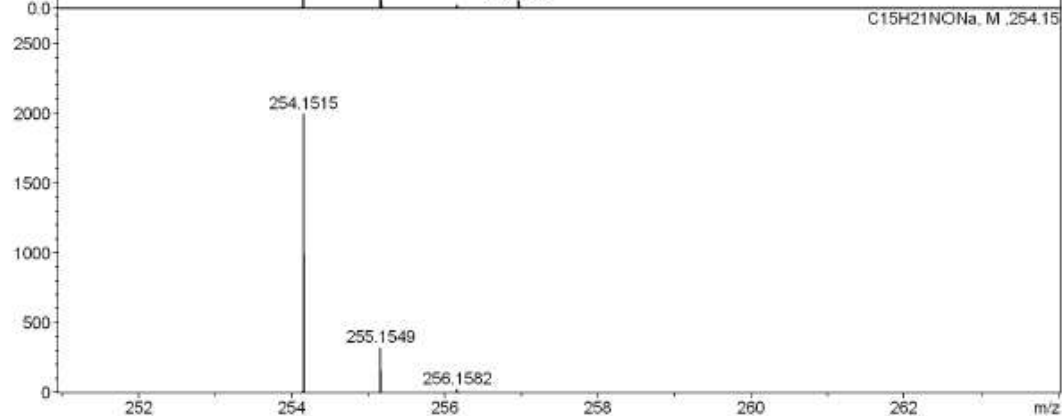
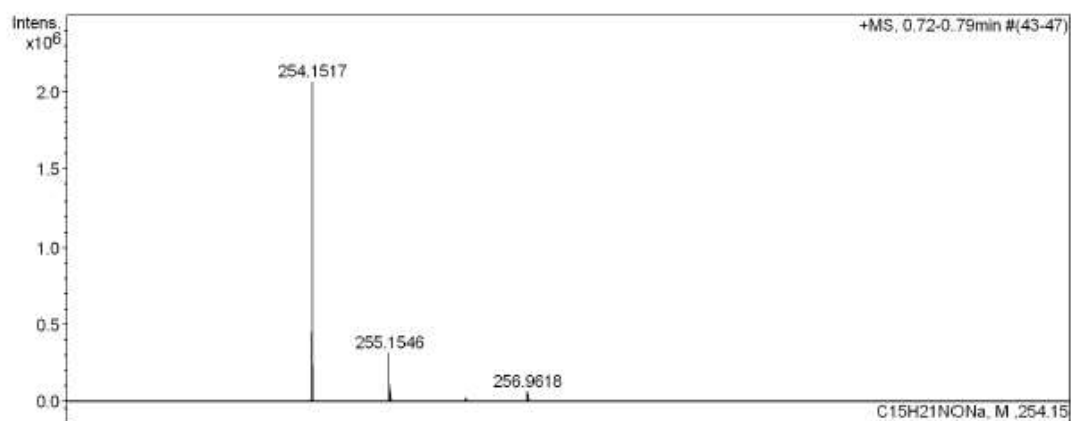
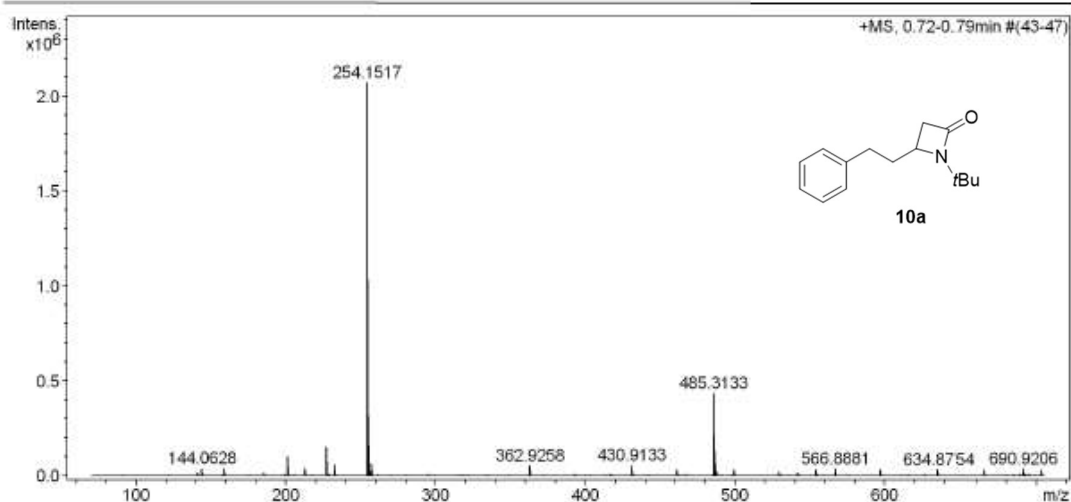




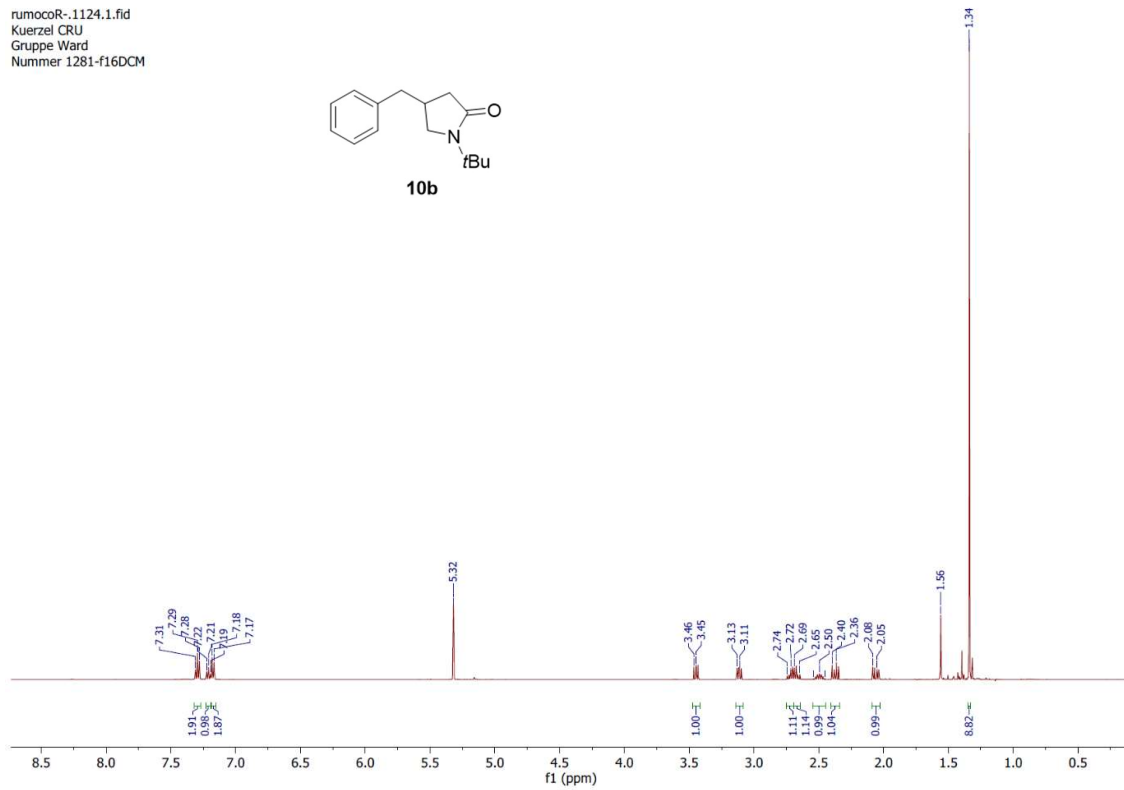
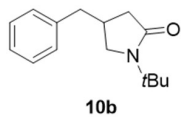
High Resolution Mass Spectrometry Report

Sample Name CRU-1401a
Comment

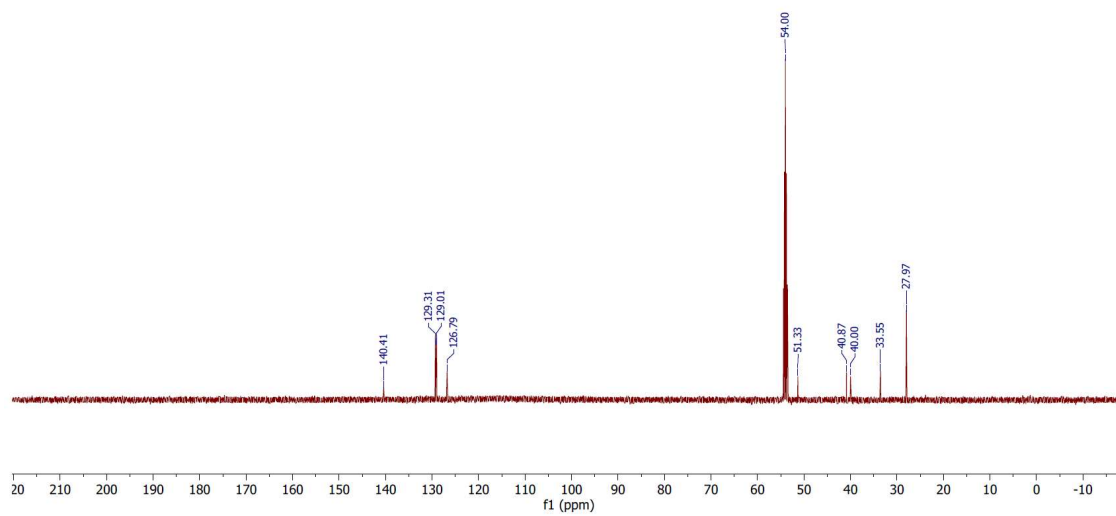
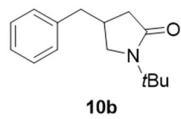
Instrument maXis 4G
Method ms_nocolumn_low_pos.m

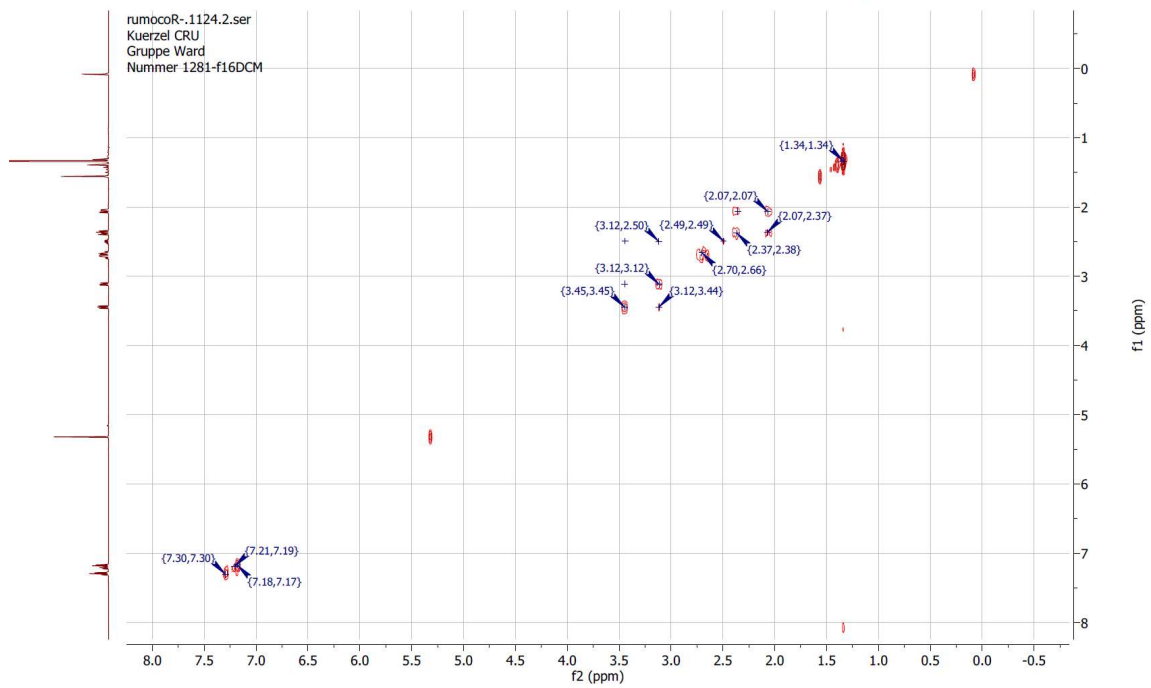
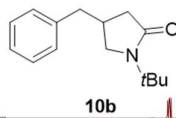
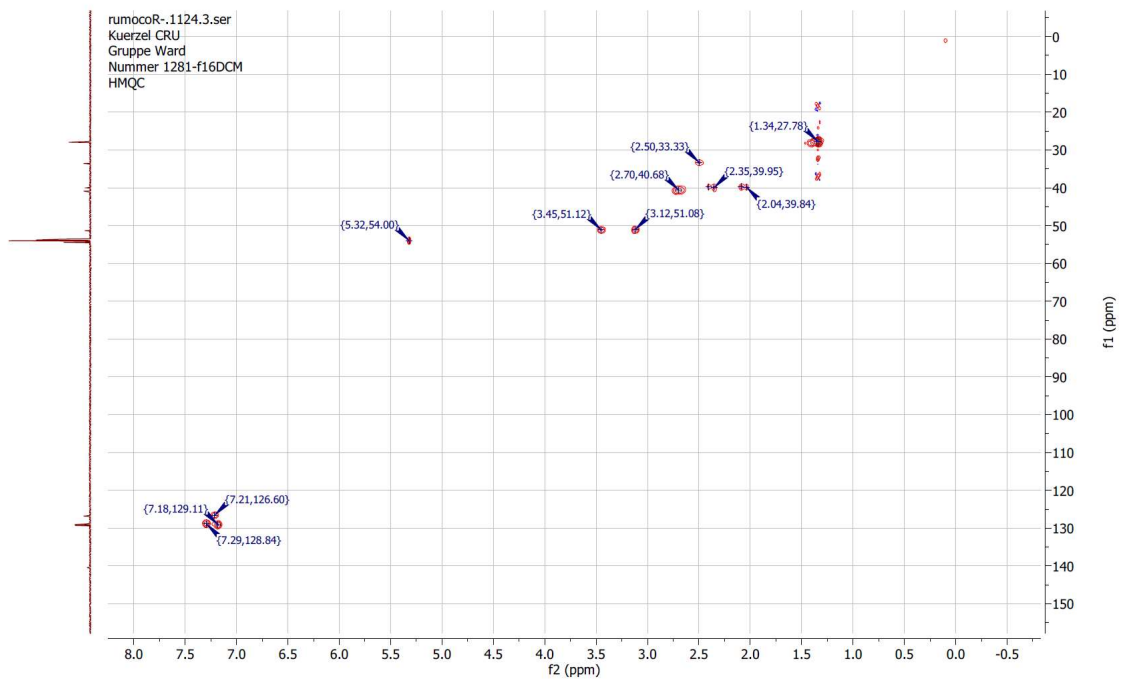
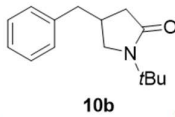


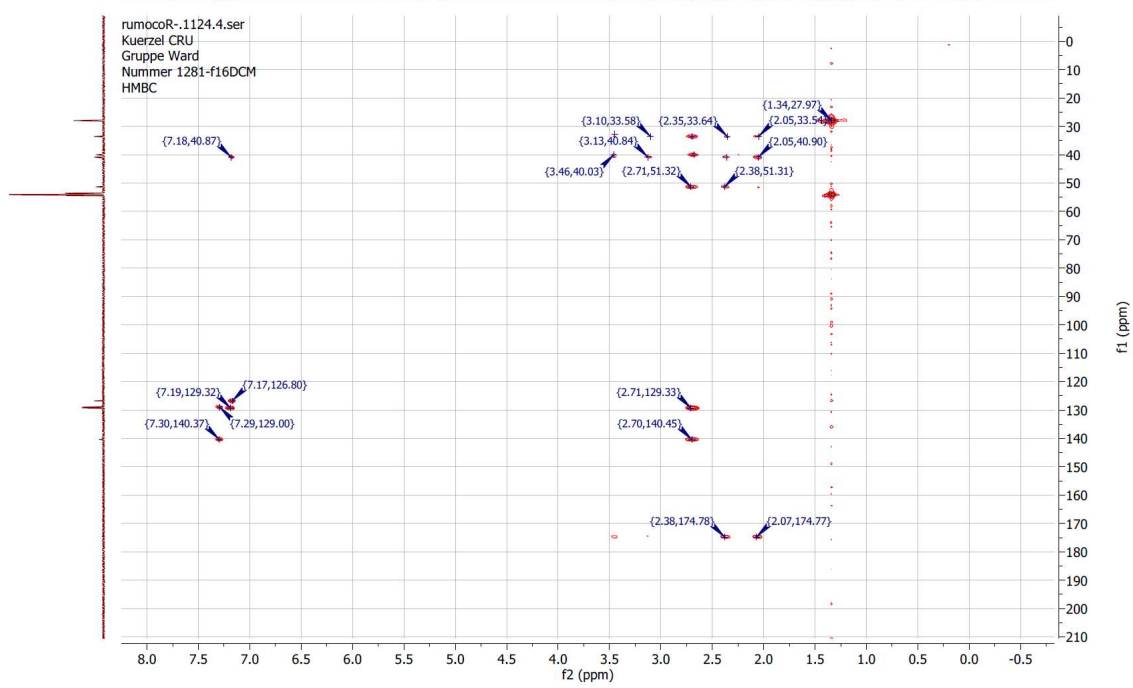
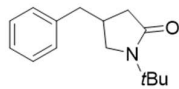
rumocoR--1124.1.fid
Kuerzel CRU
Gruppe Ward
Nummer 1281-f16DCM



rumocoR--1124.5.fid
Kuerzel CRU
Gruppe Ward
Nummer 1281-f16DCM



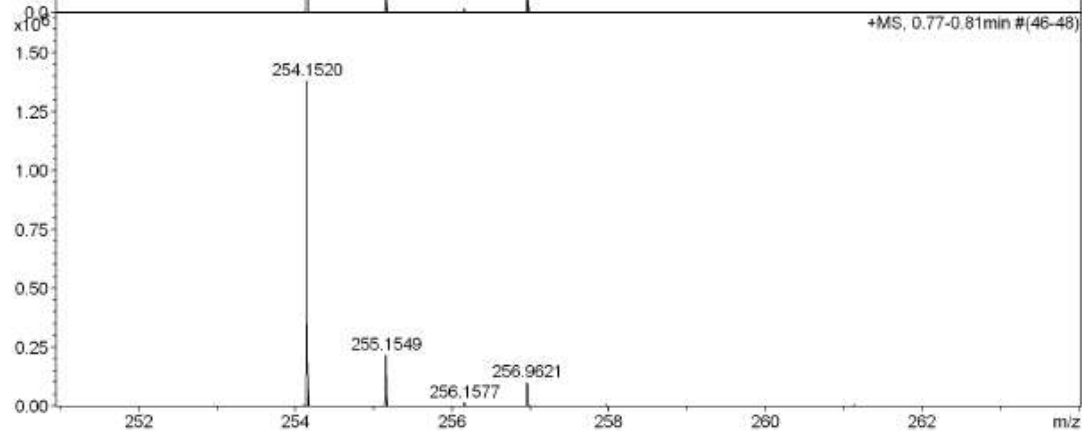
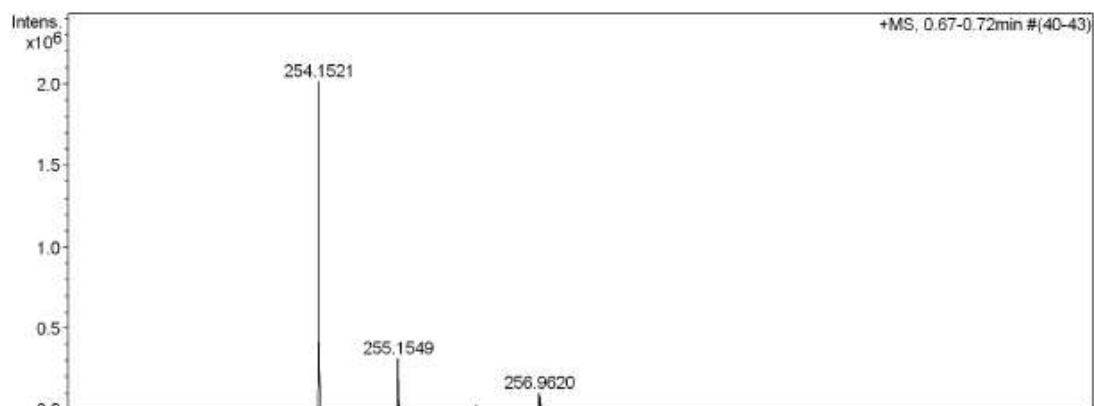
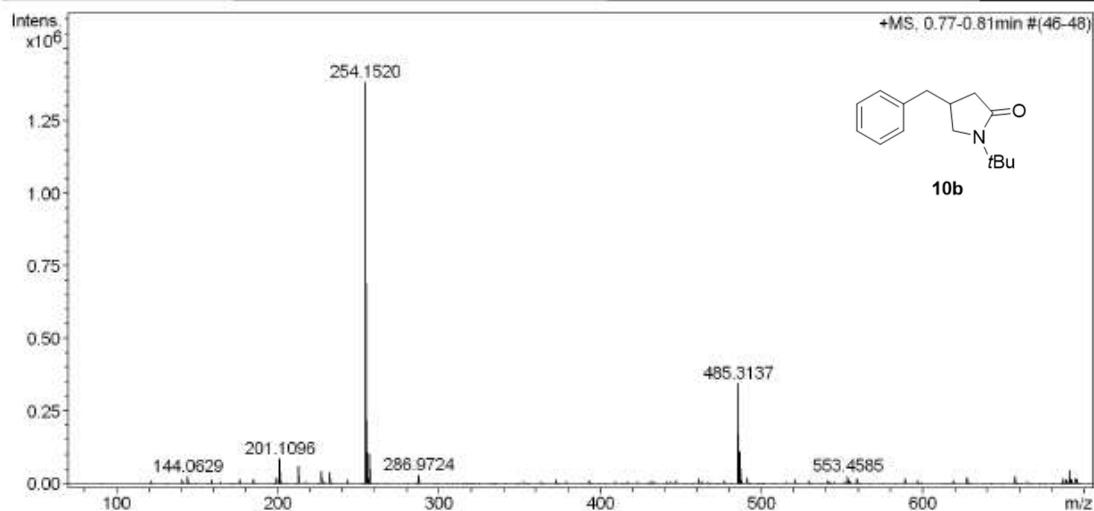




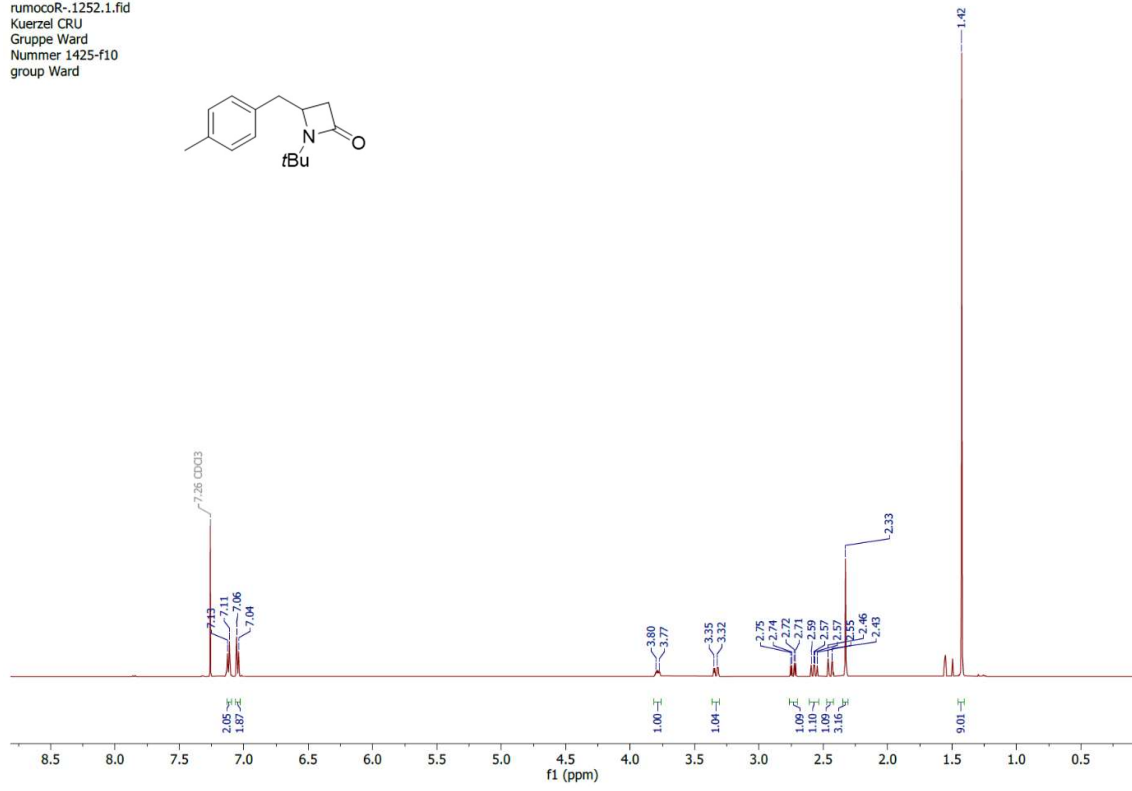
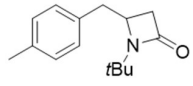
High Resolution Mass Spectrometry Report

Sample Name CRU-1401b
Comment

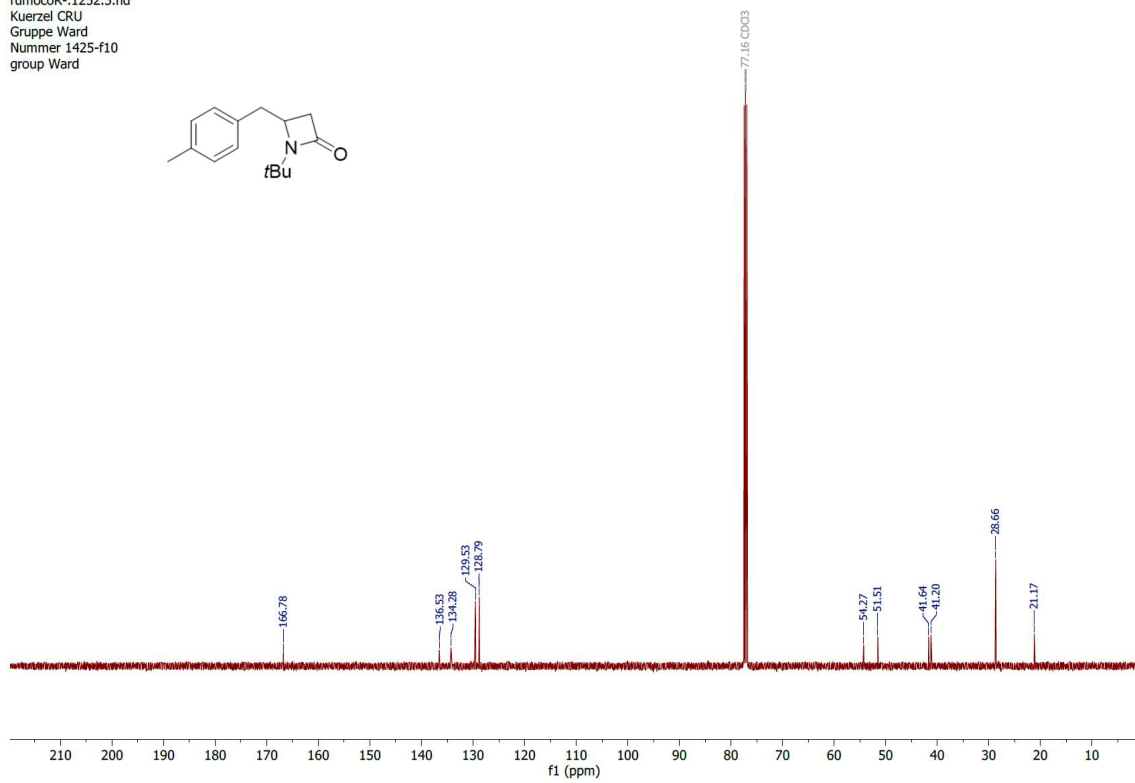
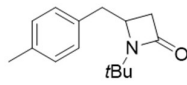
Instrument maXis 4G
Method ms_nocolumn_low_pos.m



rumocoR-1252.1.fid
Kuerzel CRU
Gruppe Ward
Nummer 1425-f10
group Ward



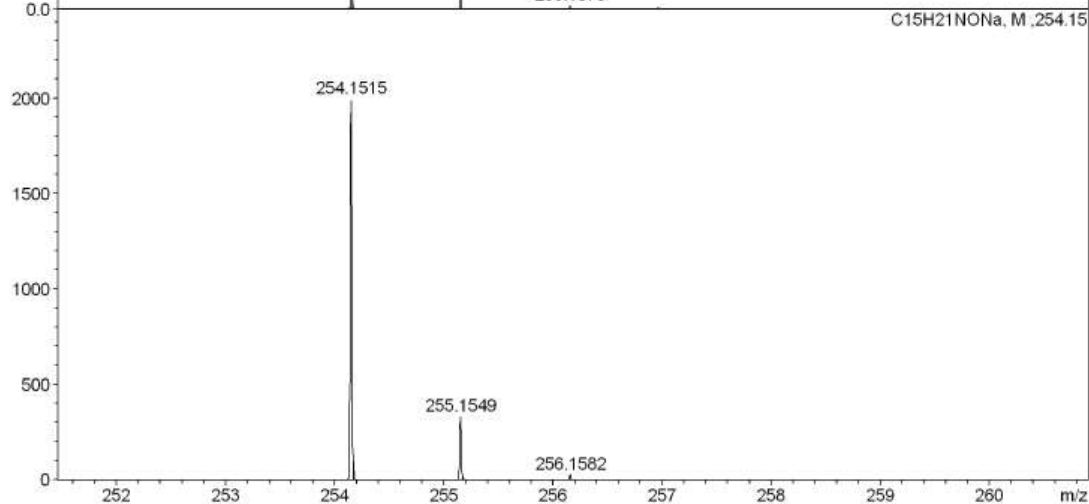
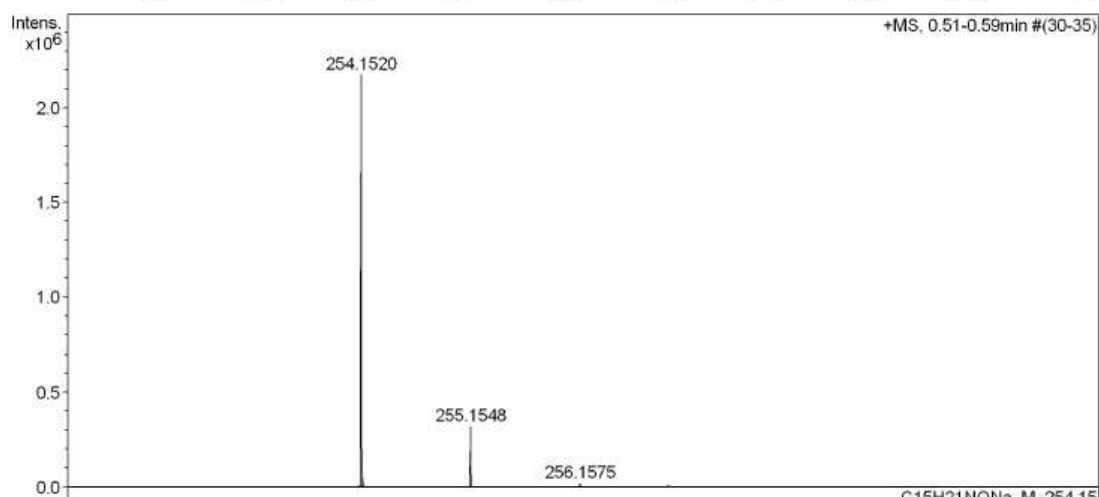
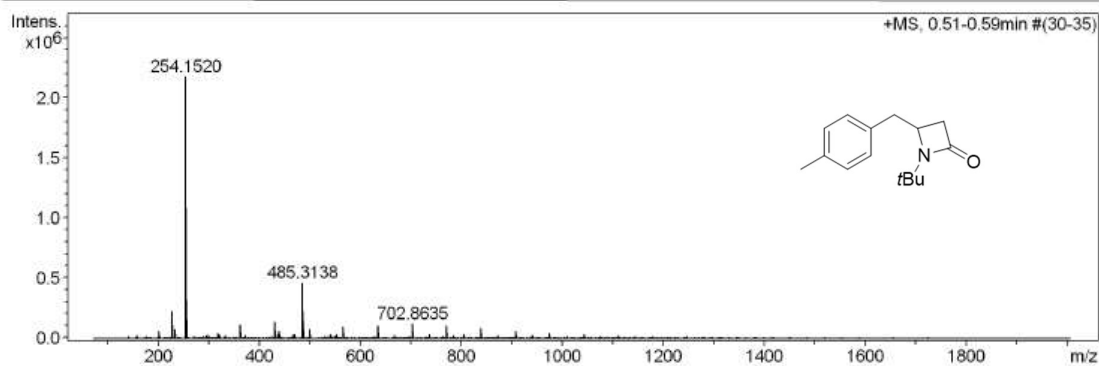
rumocoR-1252.5.fid
Kuerzel CRU
Gruppe Ward
Nummer 1425-f10
group Ward



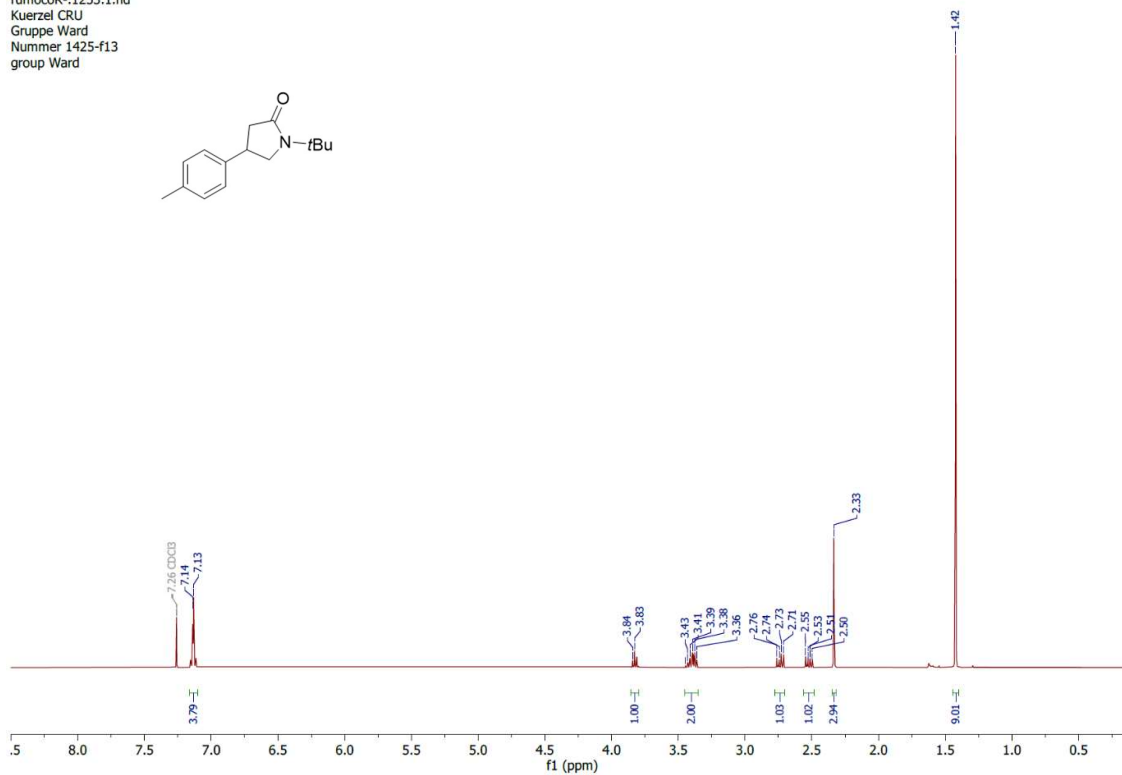
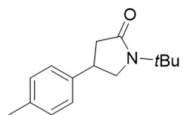
High Resolution Mass Spectrometry Report

Sample Name 1425-f10
Comment

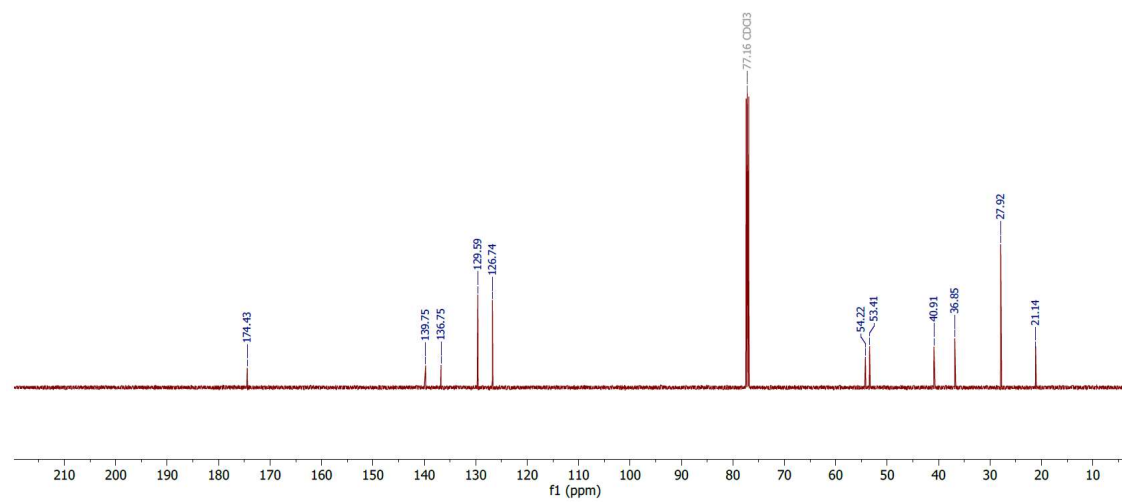
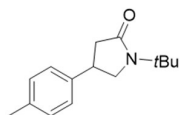
Instrument maXis 4G
Method ms_nocolumn_mid_pos.m



rumocoR-1253.1.fid
Kuerzel CRU
Gruppe Ward
Nummer 1425-f13
group Ward



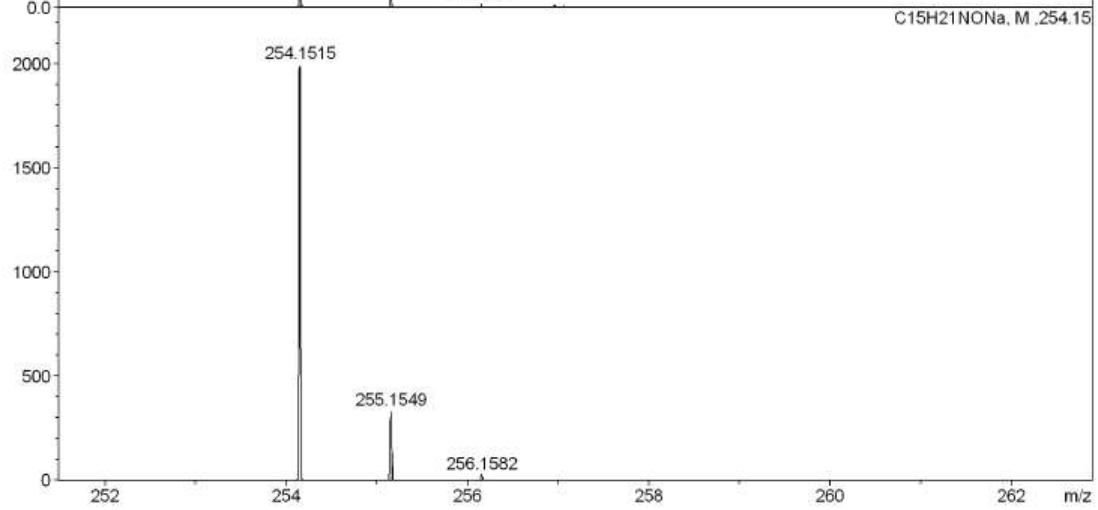
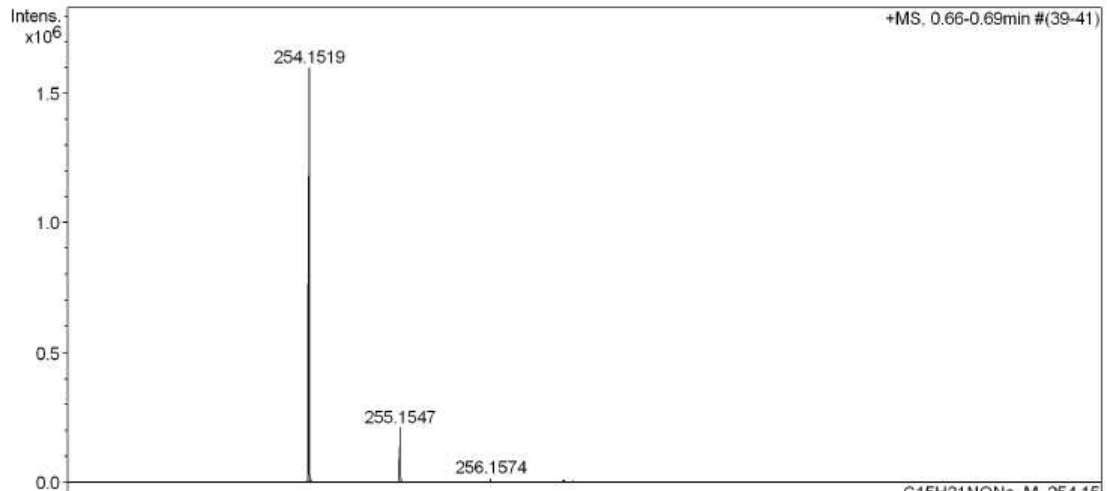
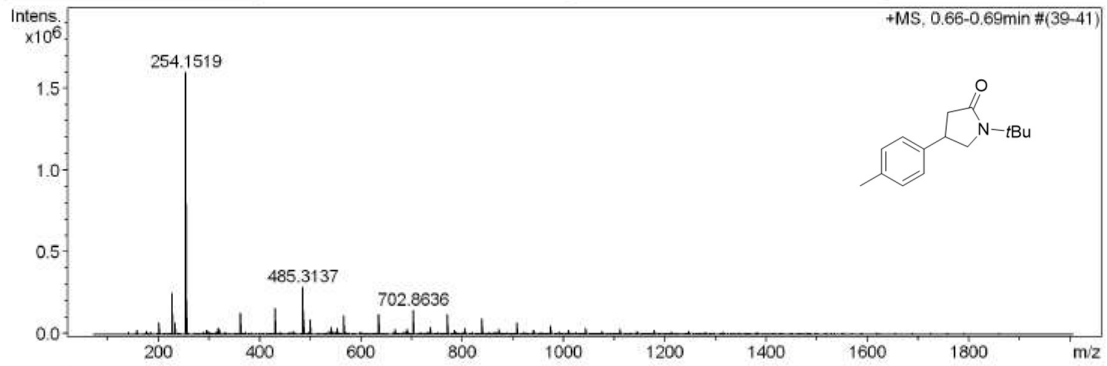
rumocoR-1253.5.fid
Kuerzel CRU
Gruppe Ward
Nummer 1425-f13
group Ward



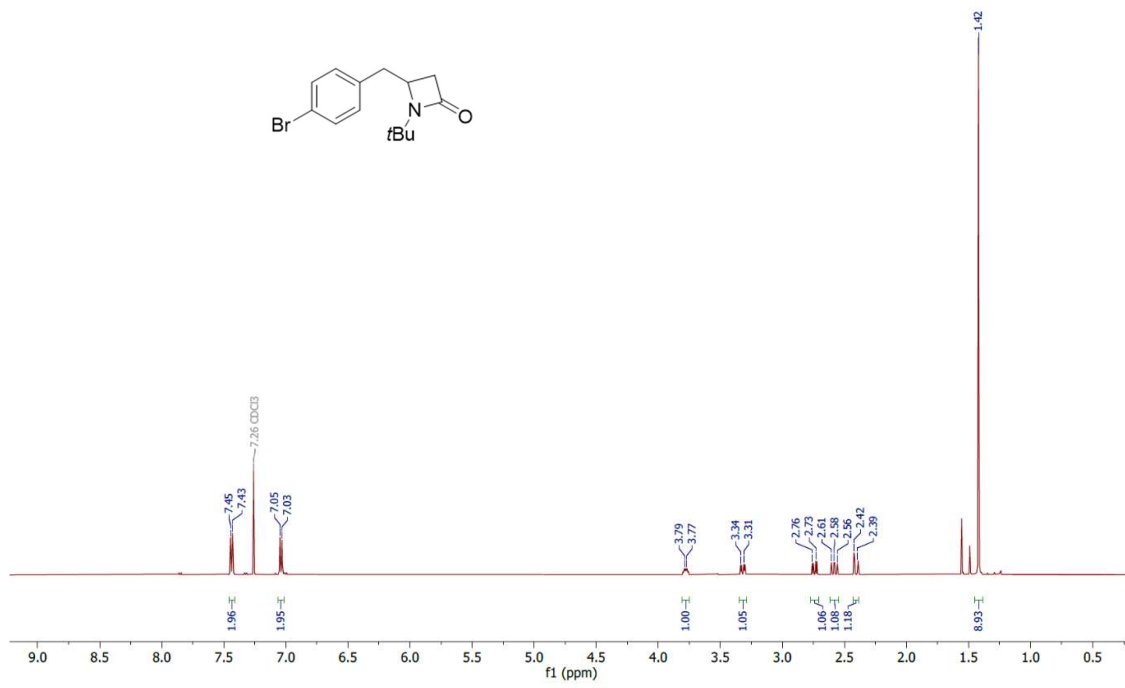
High Resolution Mass Spectrometry Report

Sample Name 1425-f13
Comment

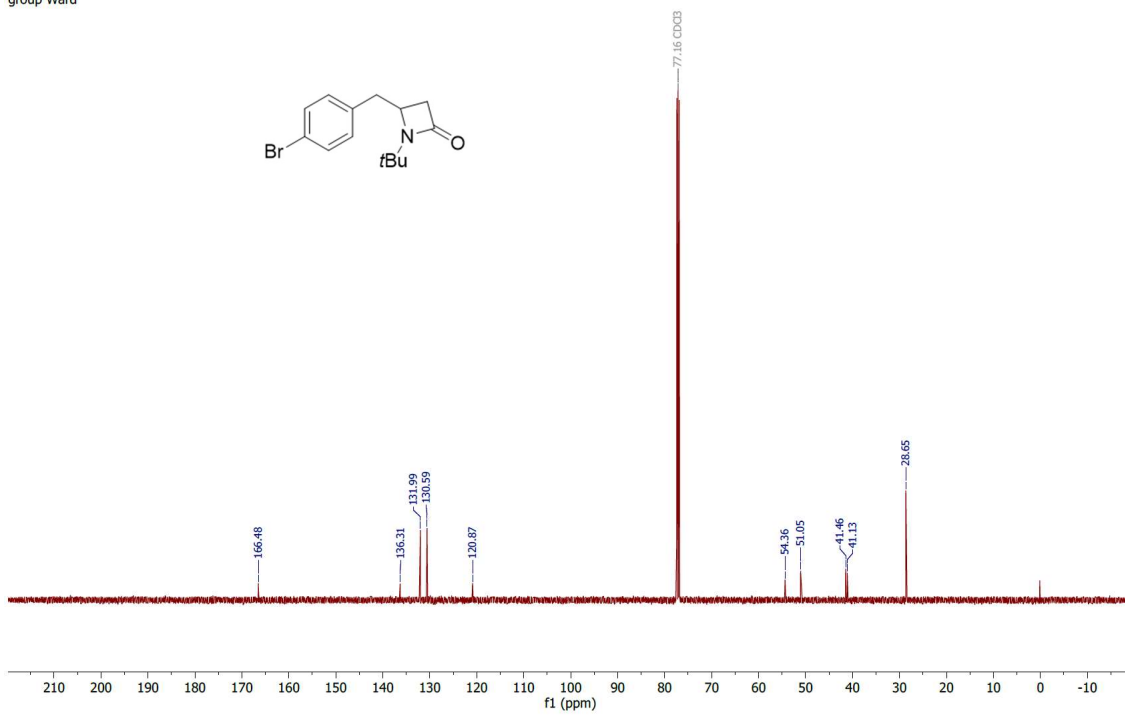
Instrument maXis 4G
Method ms_nocolumn_mid_pos.m



rumocoR-.1250.1.fid
Kuerzel CRU
Gruppe Ward
Nummer 1424-f11
group Ward



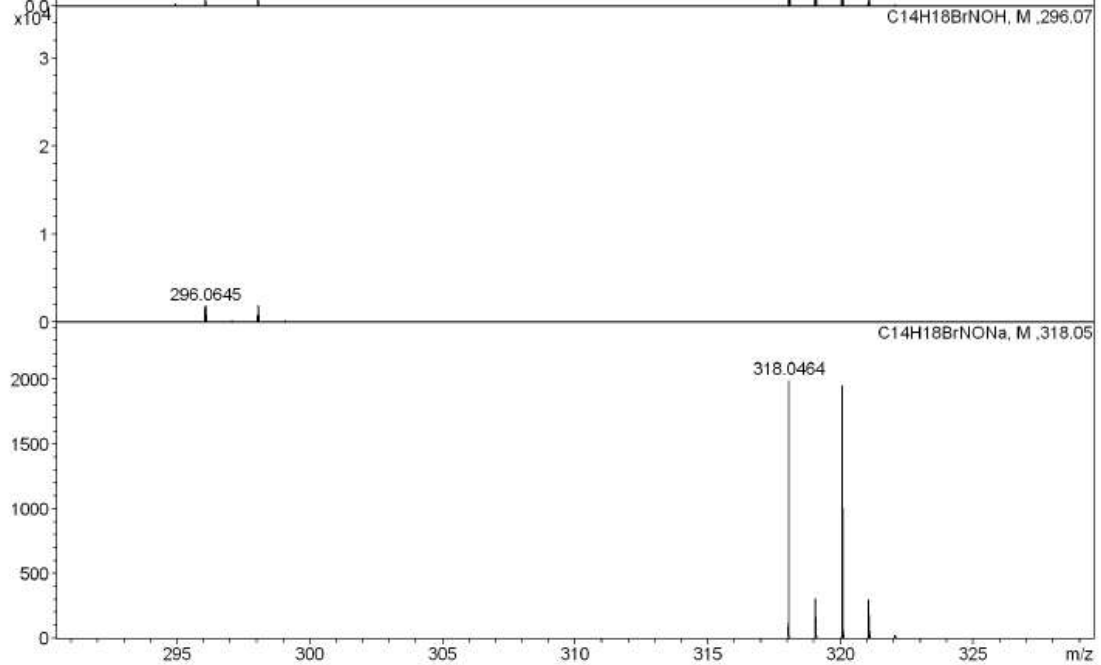
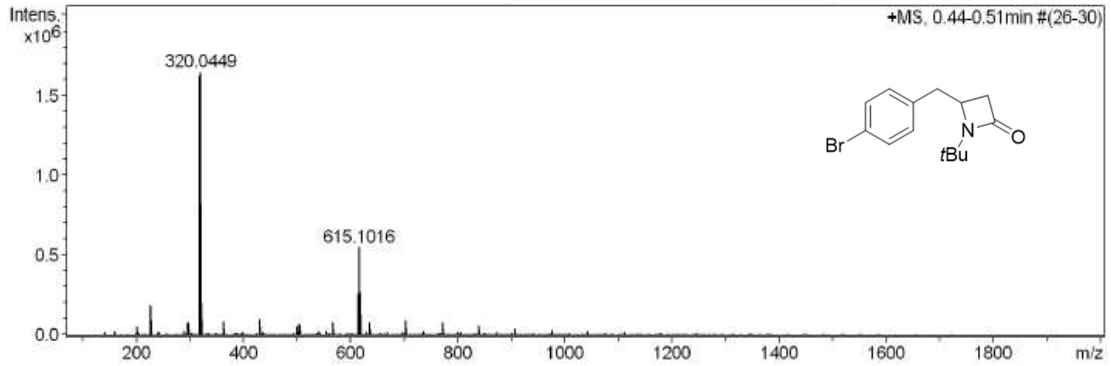
rumocoR-.1250.5.fid
Kuerzel CRU
Gruppe Ward
Nummer 1424-f11
group Ward



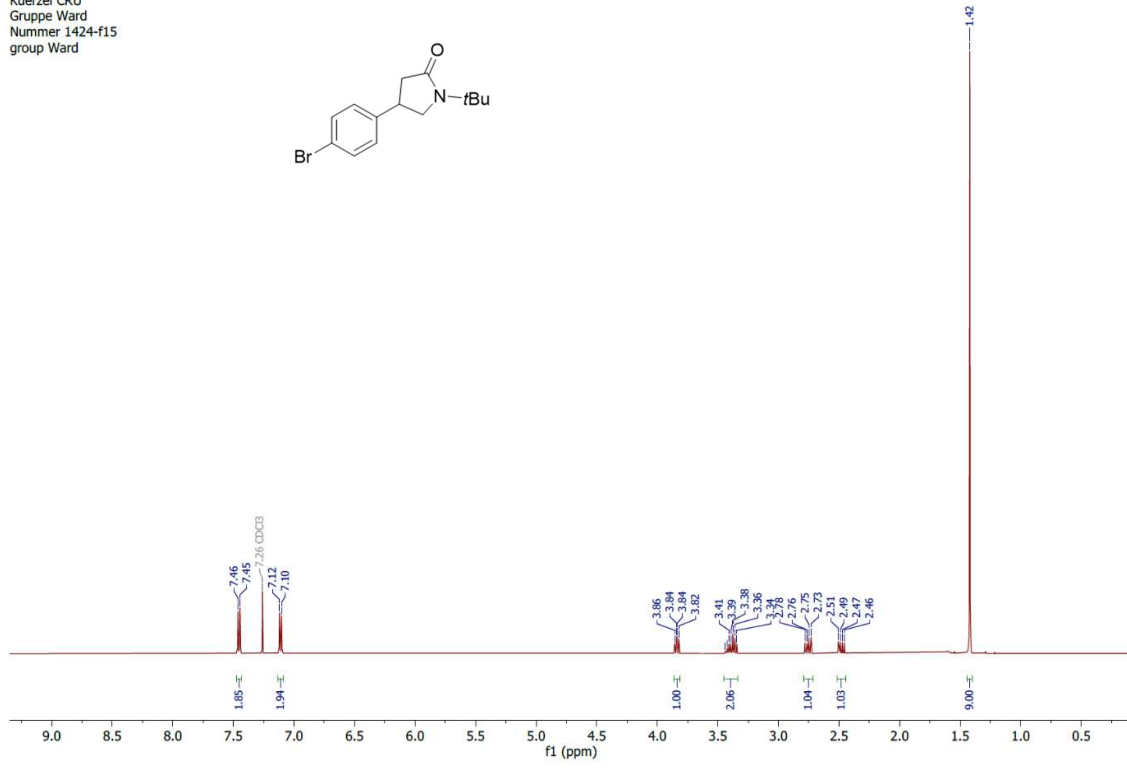
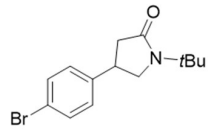
High Resolution Mass Spectrometry Report

Sample Name 1424 beta
Comment

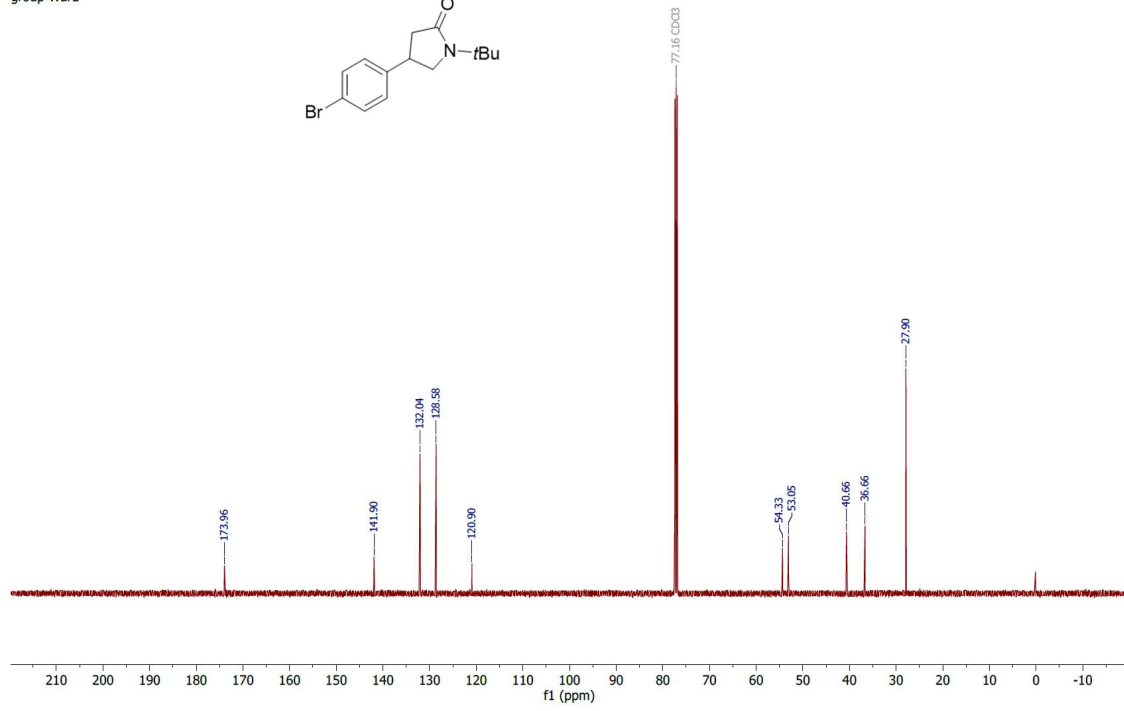
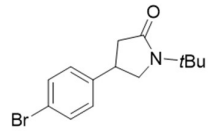
Instrument maXis 4G
Method ms_nocolumn_mid_pos.m



rumocoR-1251.1.fid
Kuerzel CRU
Gruppe Ward
Nummer 1424-f15
group Ward



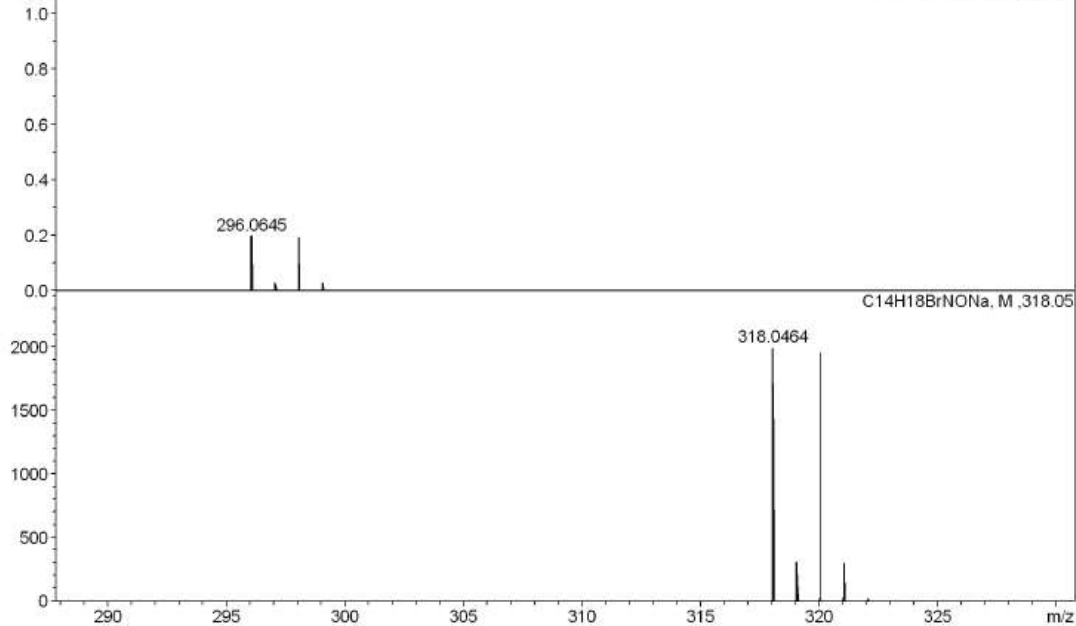
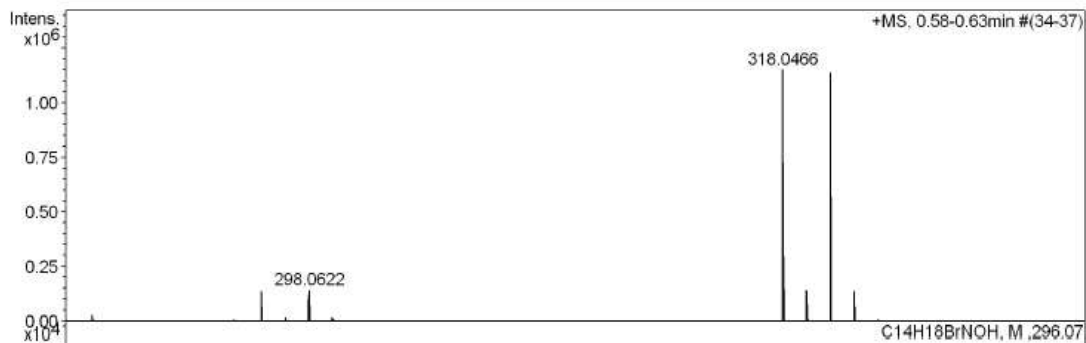
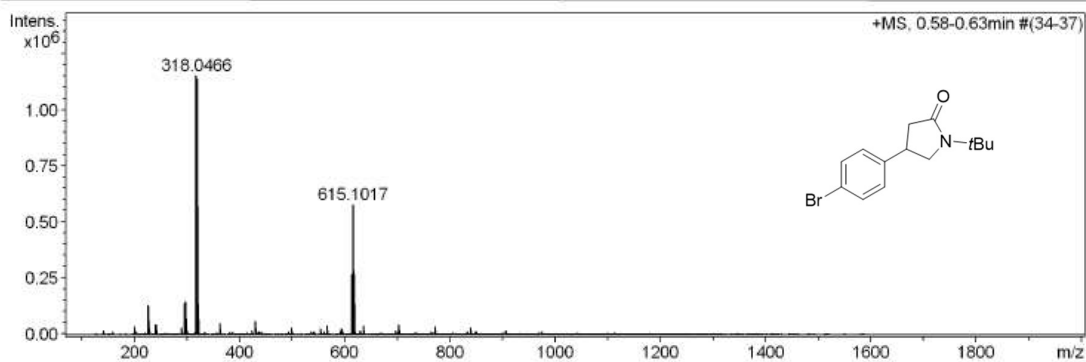
rumocoR-1251.5.fid
Kuerzel CRU
Gruppe Ward
Nummer 1424-f15
group Ward



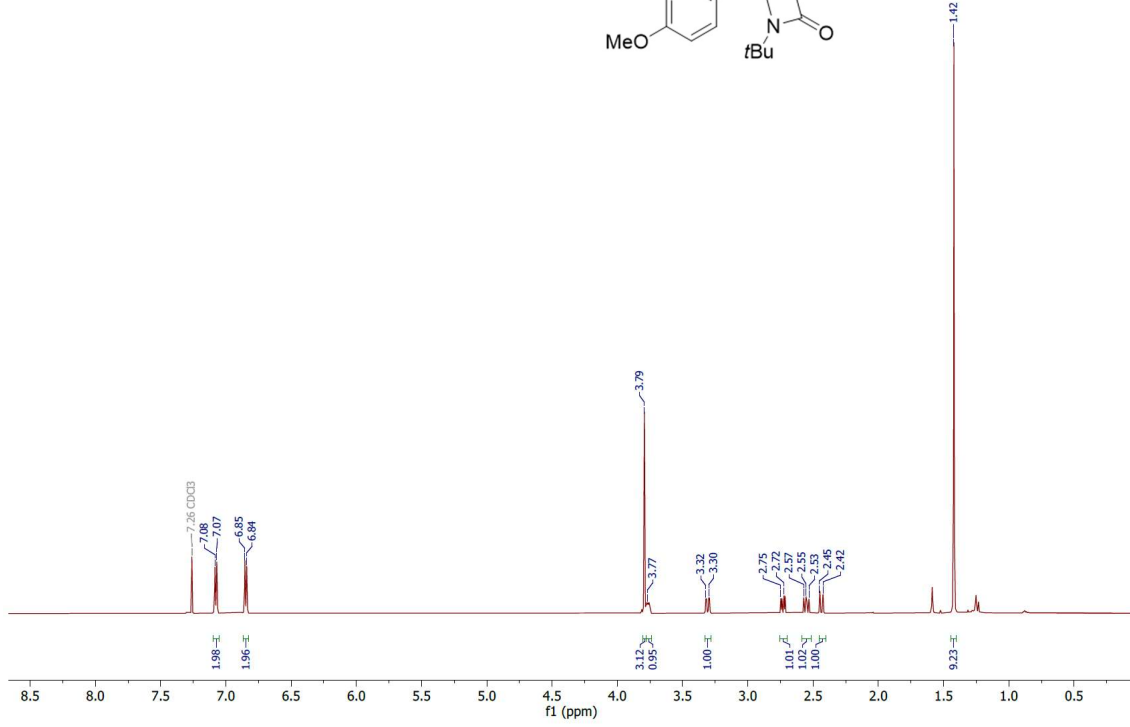
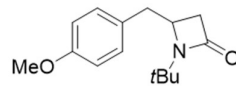
High Resolution Mass Spectrometry Report

Sample Name 1442 gamma
Comment

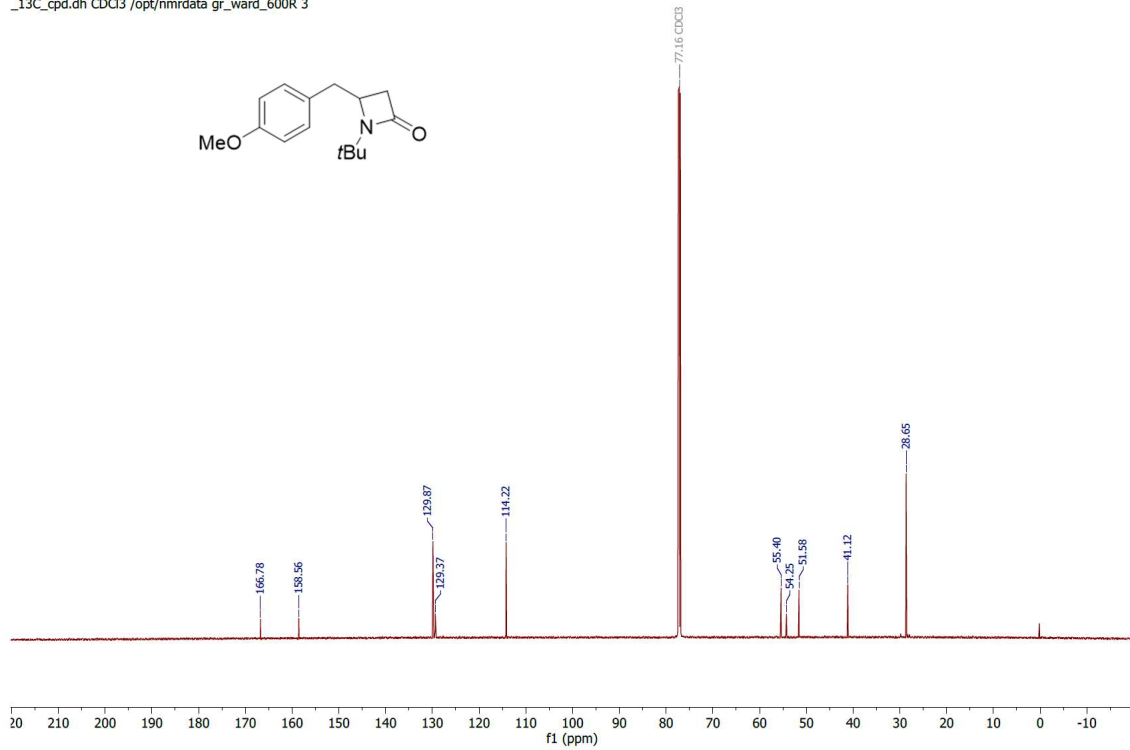
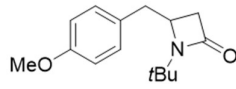
Instrument maXis 4G
Method ms_nocolumn_mid_pos.m



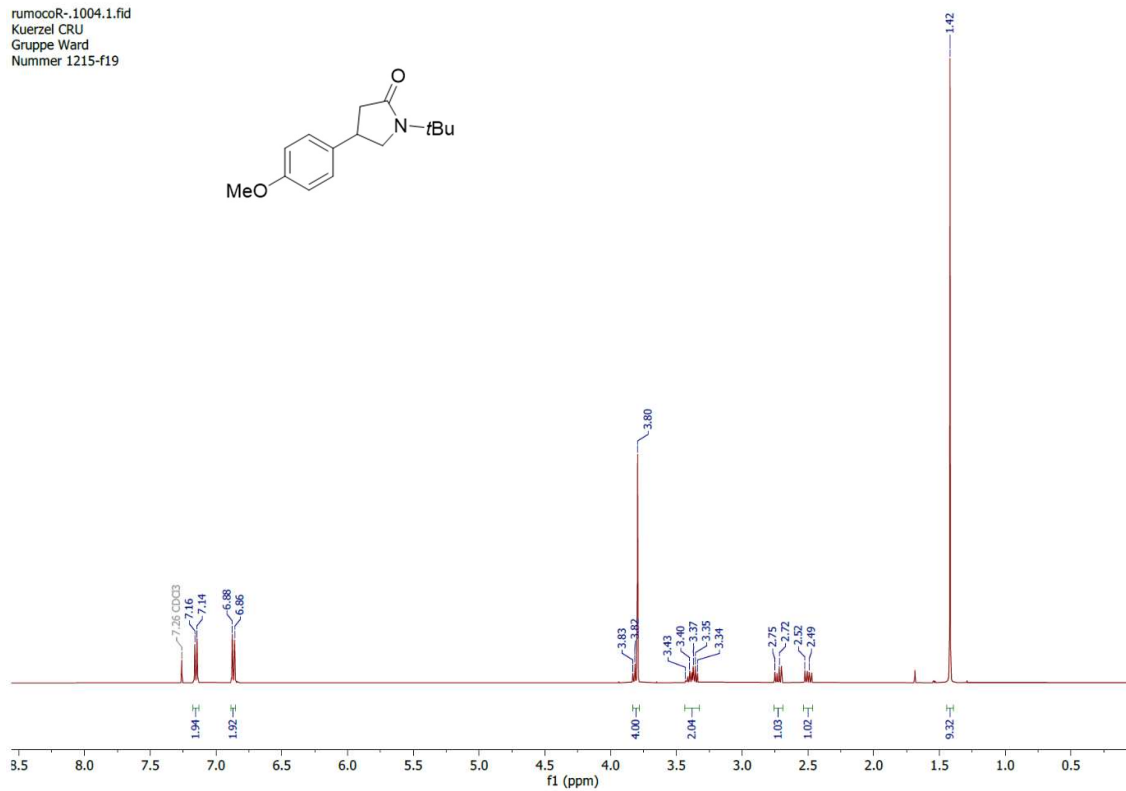
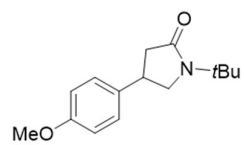
gr_ward_cryo+.422.1.fid
CRU-1215beta
_Proton.dh CDCl3 /opt/nmrdata gr_ward_600R 3



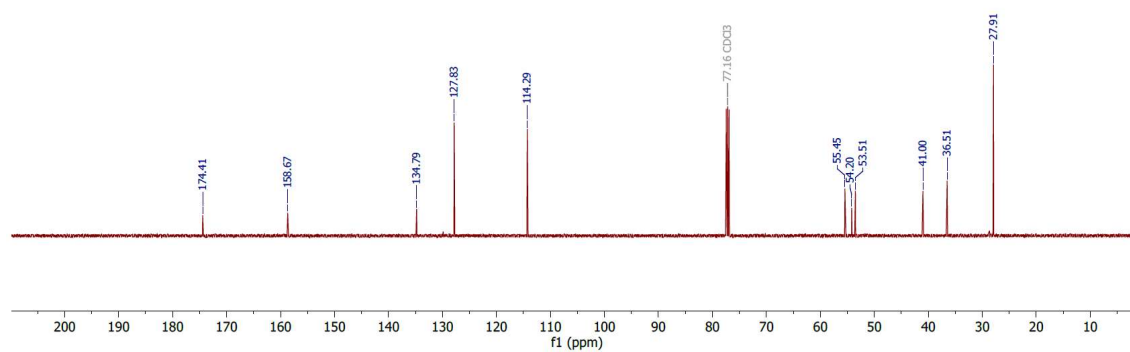
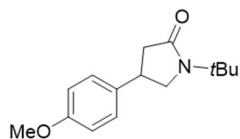
gr_ward_cryo+.422.3.fid
CRU-1215beta-cpd
_13C_cpd.dh CDCl3 /opt/nmrdata gr_ward_600R 3



rumocoR-1004.1.fid
Kuerzel CRU
Gruppe Ward
Nummer 1215-f19



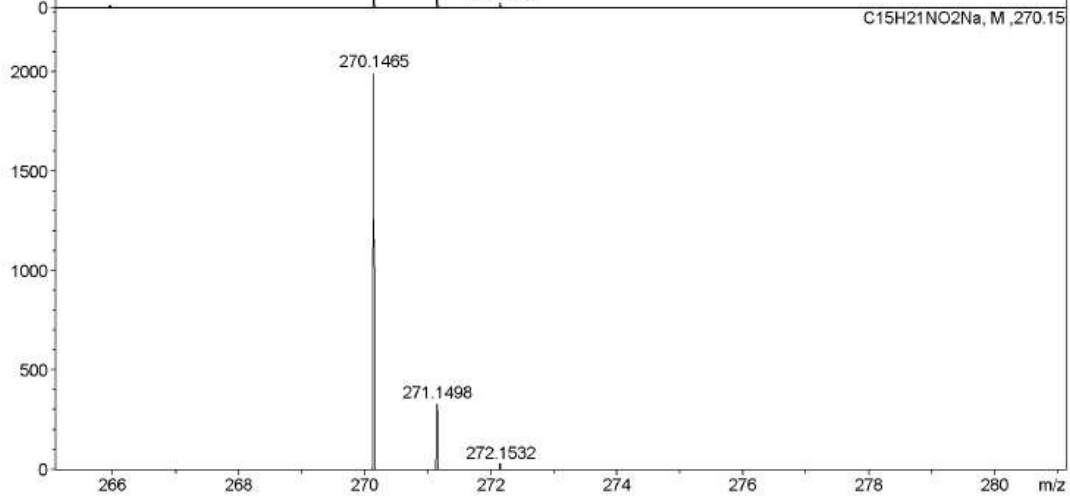
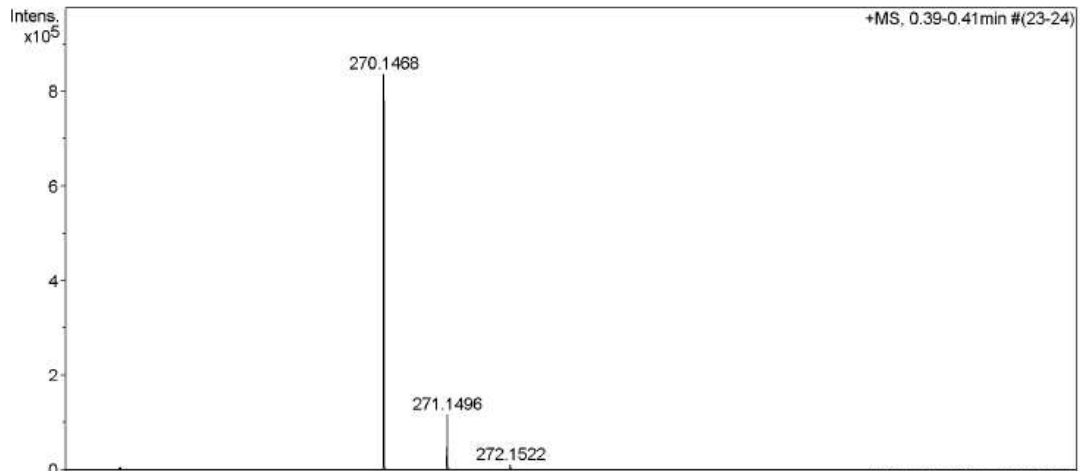
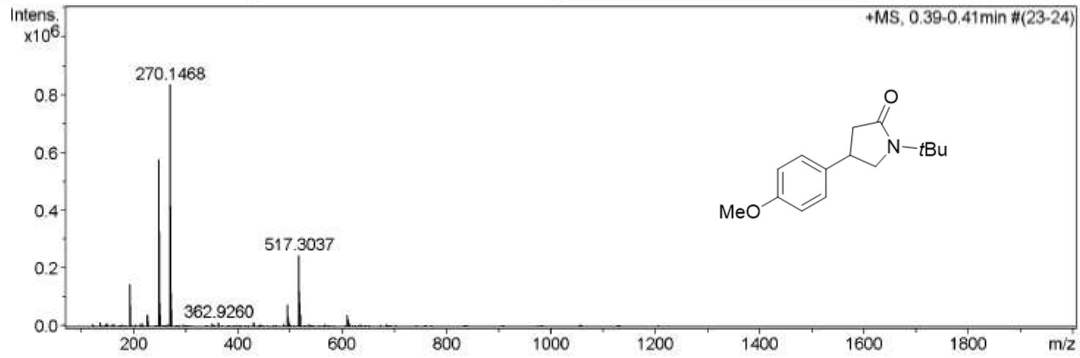
rumocoR-1004.5.fid
Kuerzel CRU
Gruppe Ward
Nummer 1215-f19



High Resolution Mass Spectrometry Report

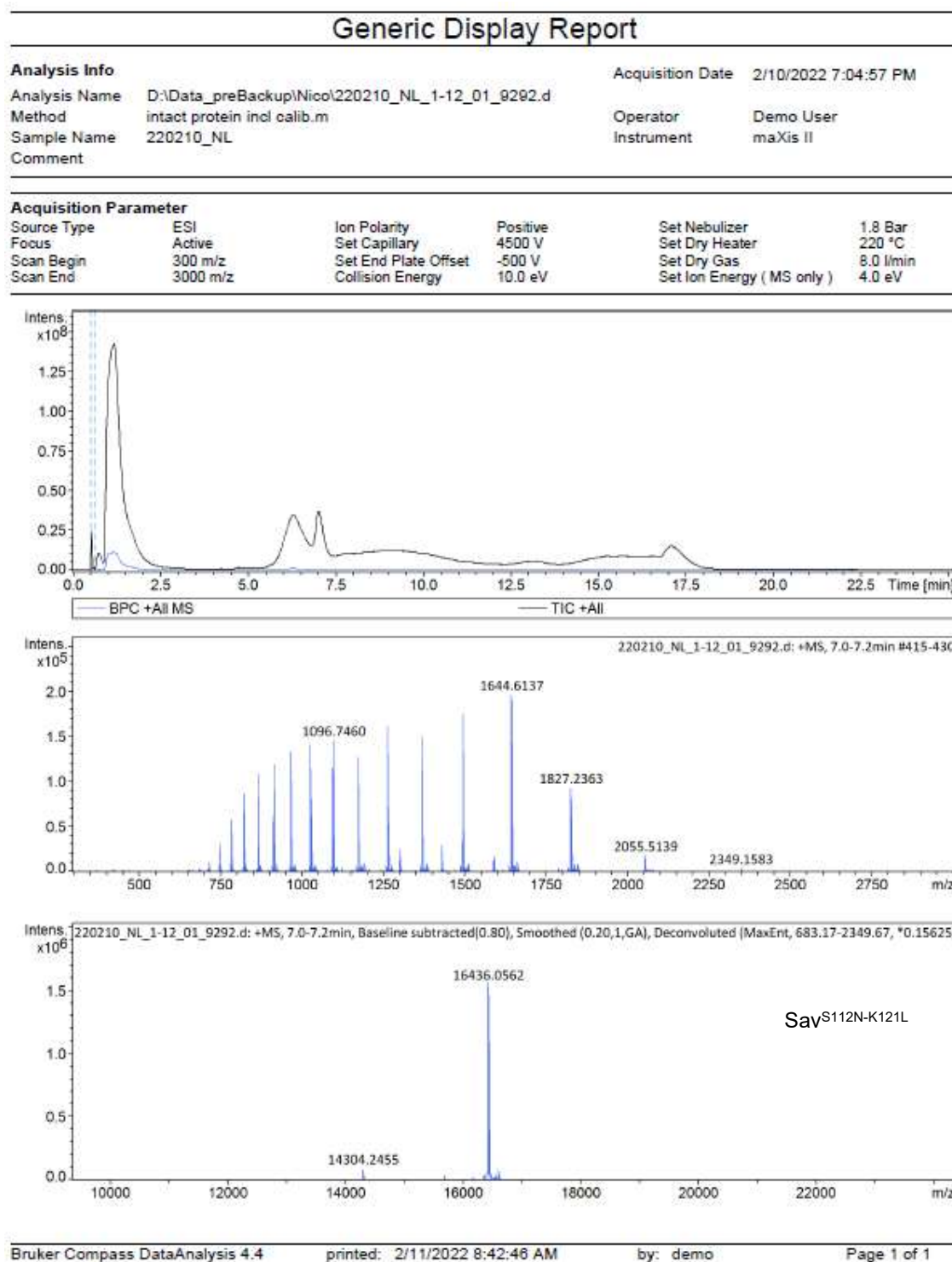
Sample Name cru 1215 gamma
Comment

Instrument maXis 4G
Method ms_nocolumn_mid_pos.m



4.5.11 Protein HRMS

Small amounts of the lysozyme used for the cell lysis could occasionally be observed on the spectra.



Generic Display Report

Analysis Info

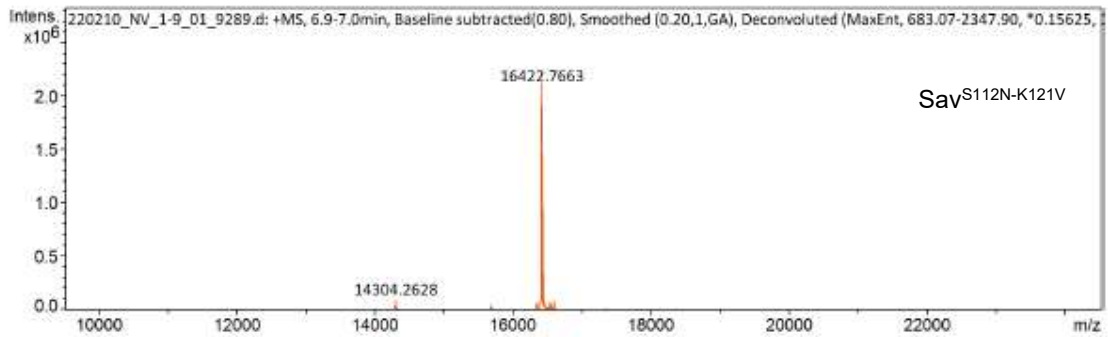
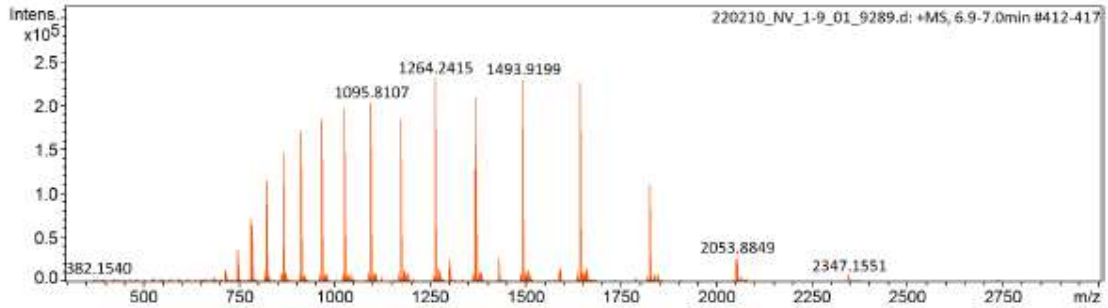
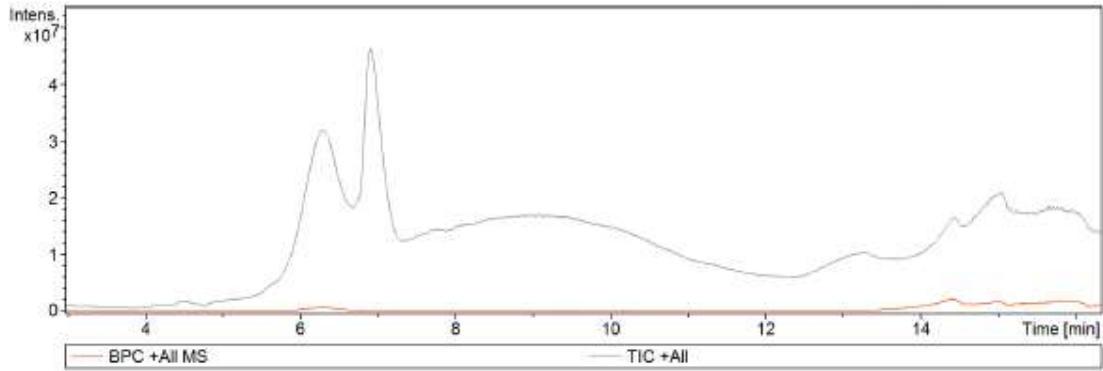
Analysis Name D:\Data_preBackup\Nico\220210_NV_1-9_01_9289.d
Method intact protein incl calib.m
Sample Name 220210_NV
Comment

Acquisition Date 2/10/2022 5:47:11 PM

Operator Demo User
Instrument maXis II

Acquisition Parameter

Source Type	ESI	Ion Polarity	Positive	Set Nebulizer	1.8 Bar
Focus	Active	Set Capillary	4500 V	Set Dry Heater	220 °C
Scan Begin	300 m/z	Set End Plate Offset	-500 V	Set Dry Gas	8.0 l/min
Scan End	3000 m/z	Collision Energy	10.0 eV	Set Ion Energy (MS only)	4.0 eV



Generic Display Report

Analysis Info

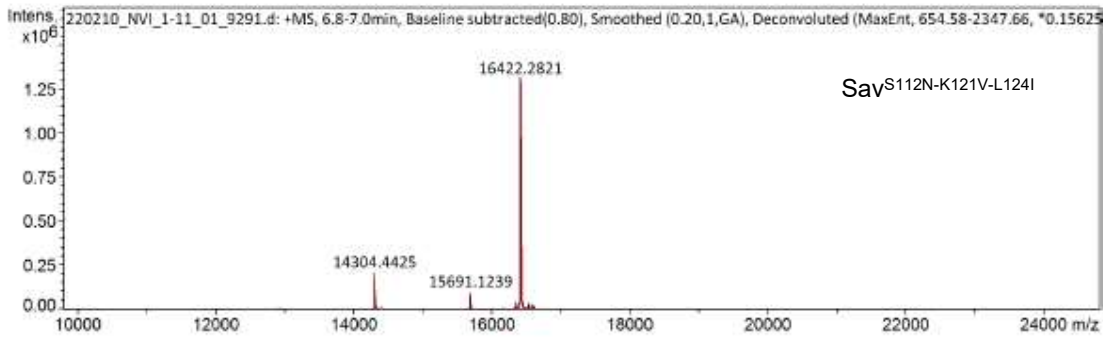
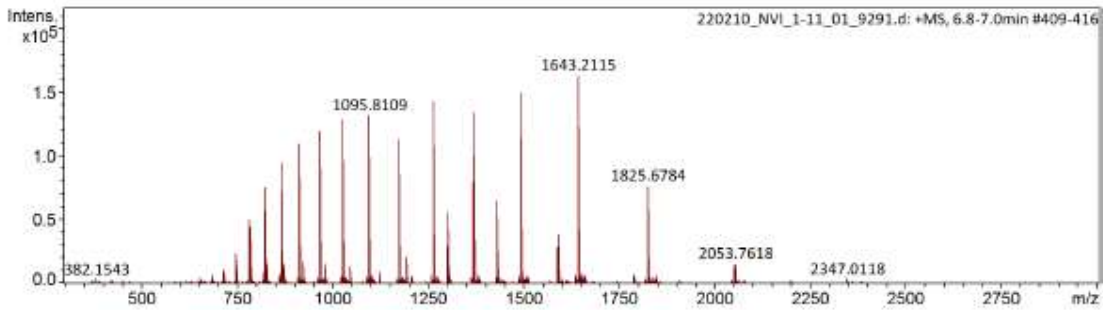
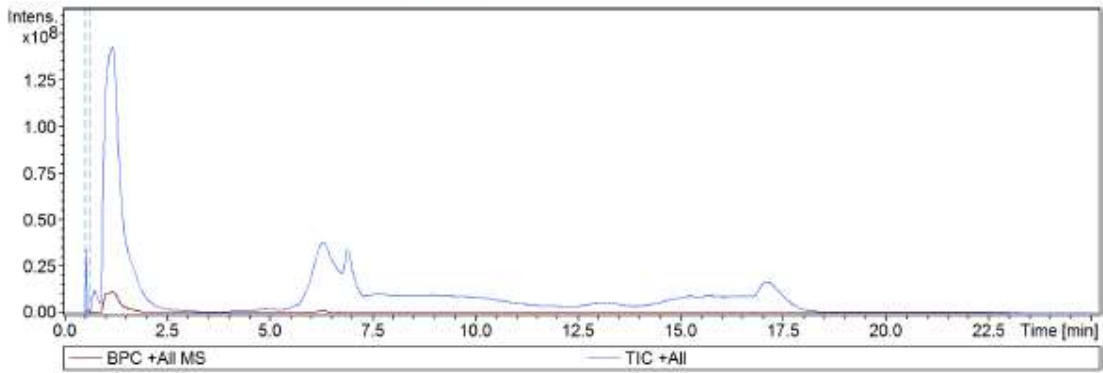
Analysis Name D:\Data_preBackup\Nico\220210_NVI_1-11_01_9291.d
 Method intact protein incl calib.m
 Sample Name 220210_NVI
 Comment

Acquisition Date 2/10/2022 6:39:01 PM

Operator Demo User
 Instrument maXis II

Acquisition Parameter

Source Type	ESI	Ion Polarity	Positive	Set Nebulizer	1.8 Bar
Focus	Active	Set Capillary	4500 V	Set Dry Heater	220 °C
Scan Begin	300 m/z	Set End Plate Offset	-500 V	Set Dry Gas	8.0 l/min
Scan End	3000 m/z	Collision Energy	10.0 eV	Set Ion Energy (MS only)	4.0 eV



Generic Display Report

Analysis Info

Analysis Name D:\Data_preBackup\Nico\220210_NVG_1-10_01_9290.d
Method intact protein incl calib.m
Sample Name 220210_NVG
Comment

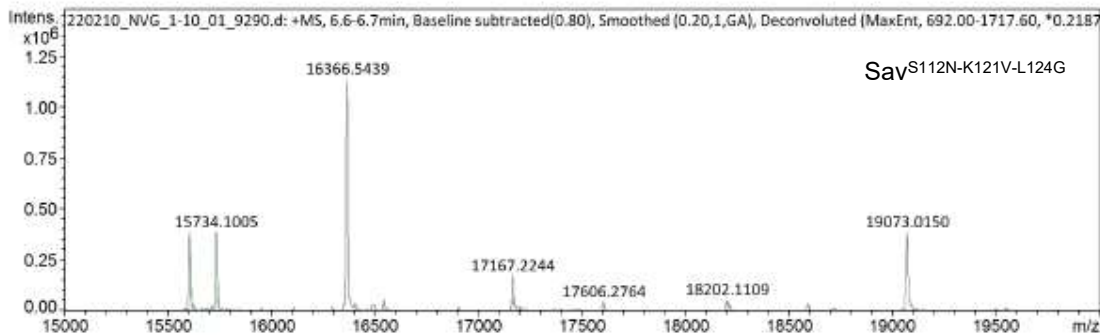
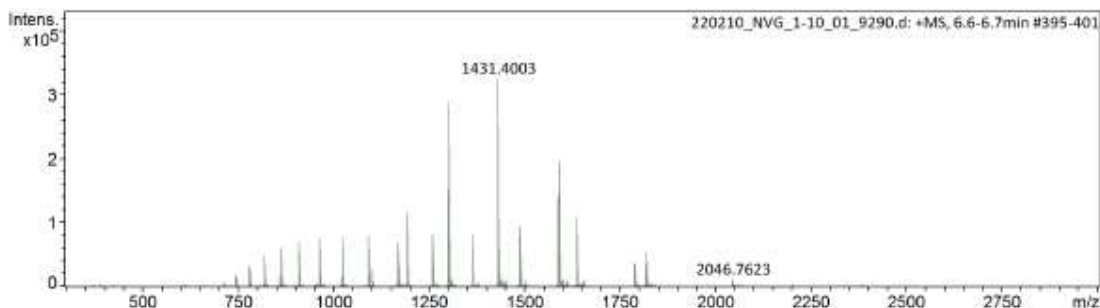
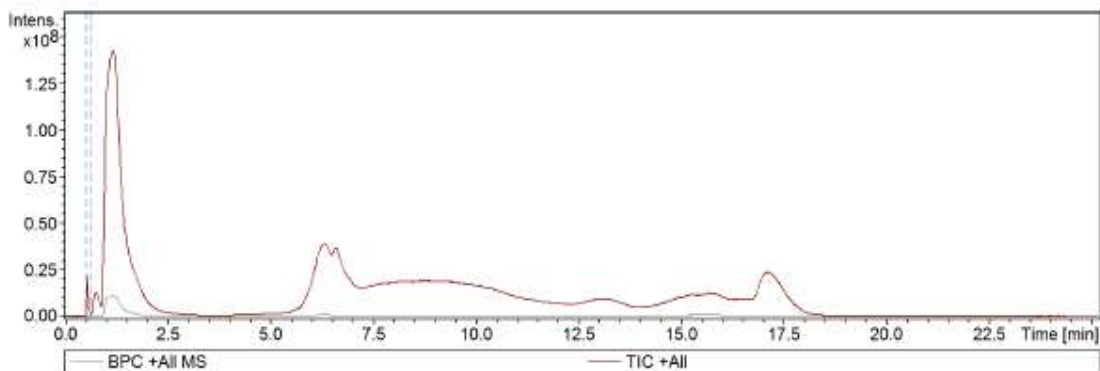
Acquisition Date 2/10/2022 6:13:04 PM

Operator Demo User

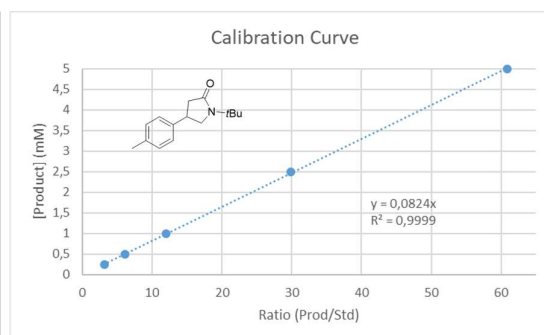
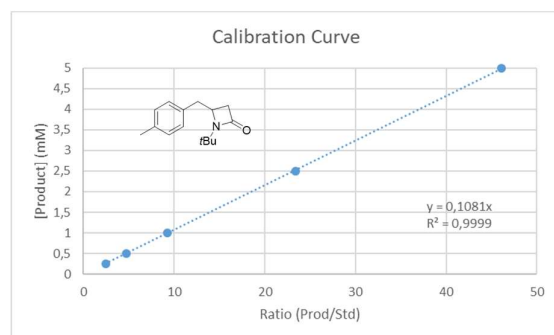
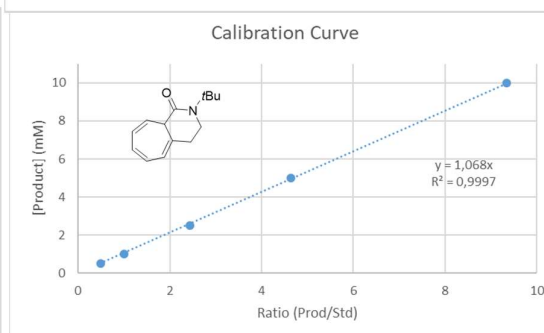
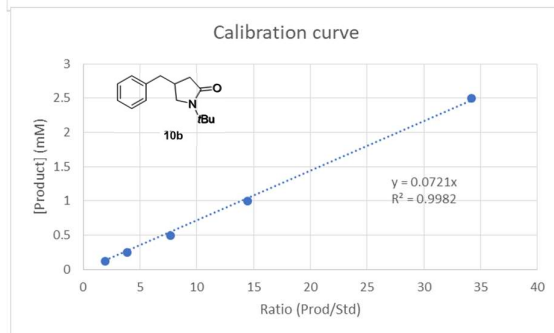
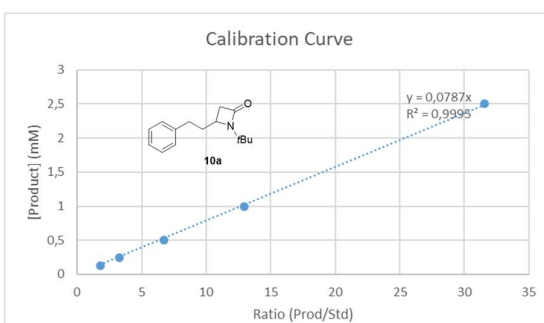
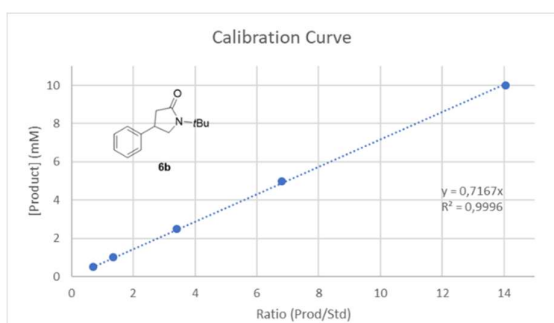
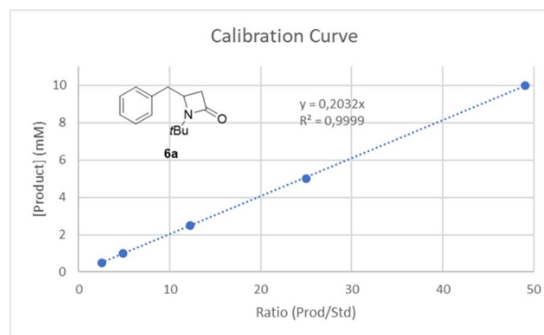
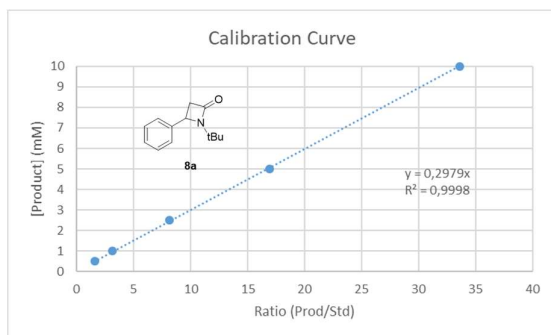
Instrument maXis II

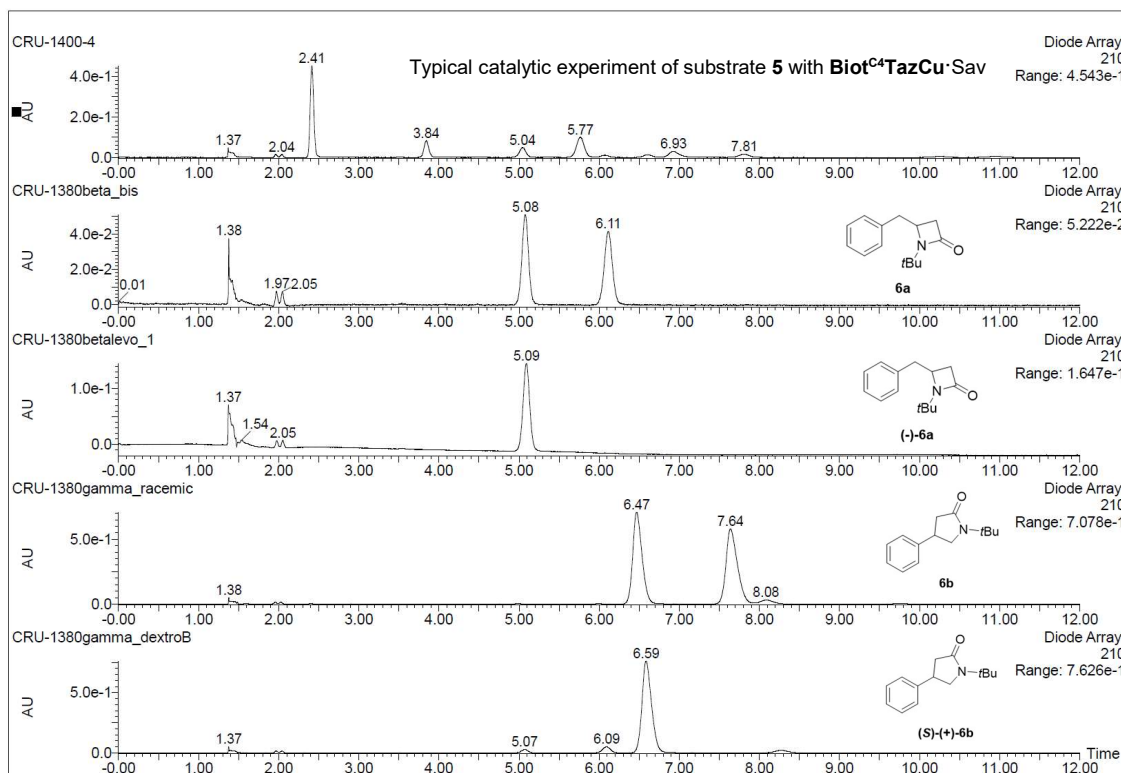
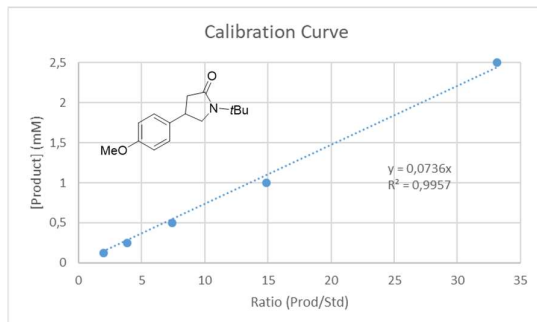
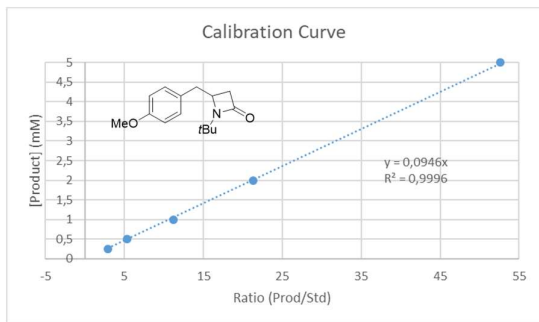
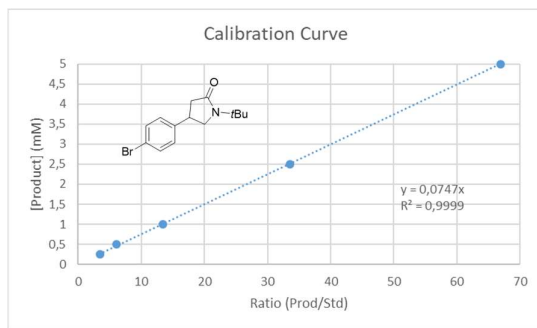
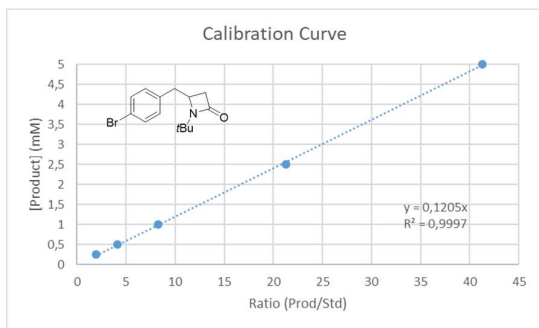
Acquisition Parameter

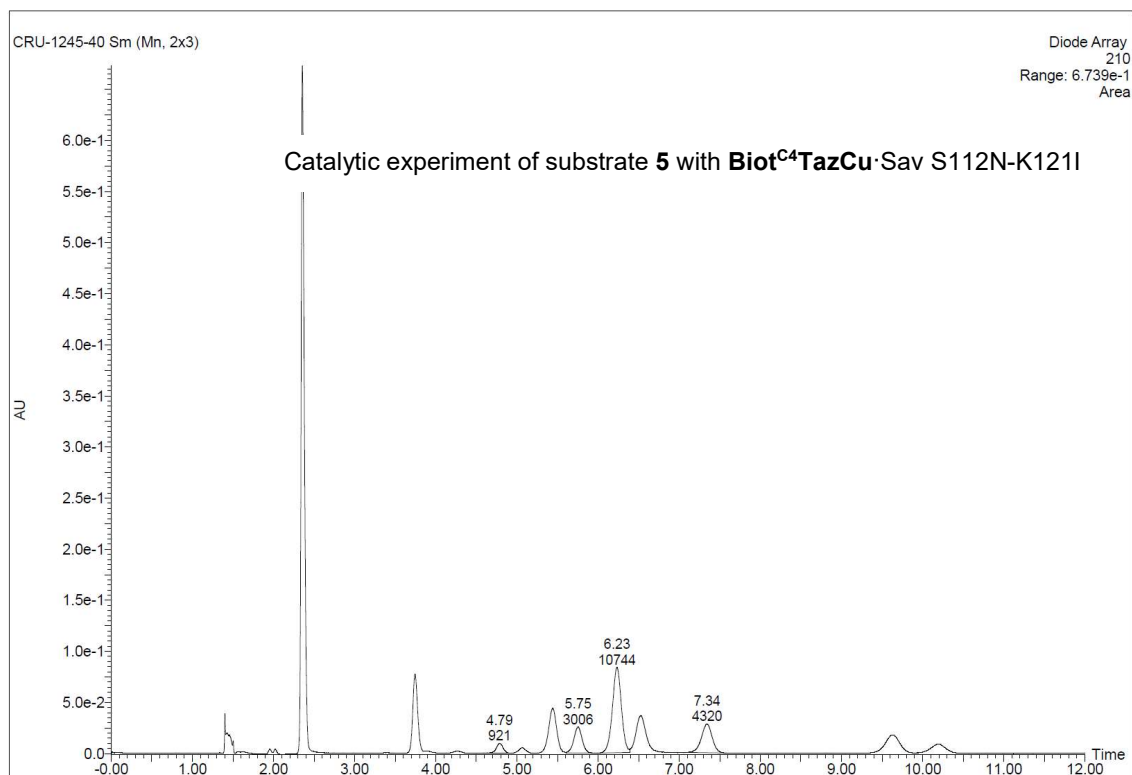
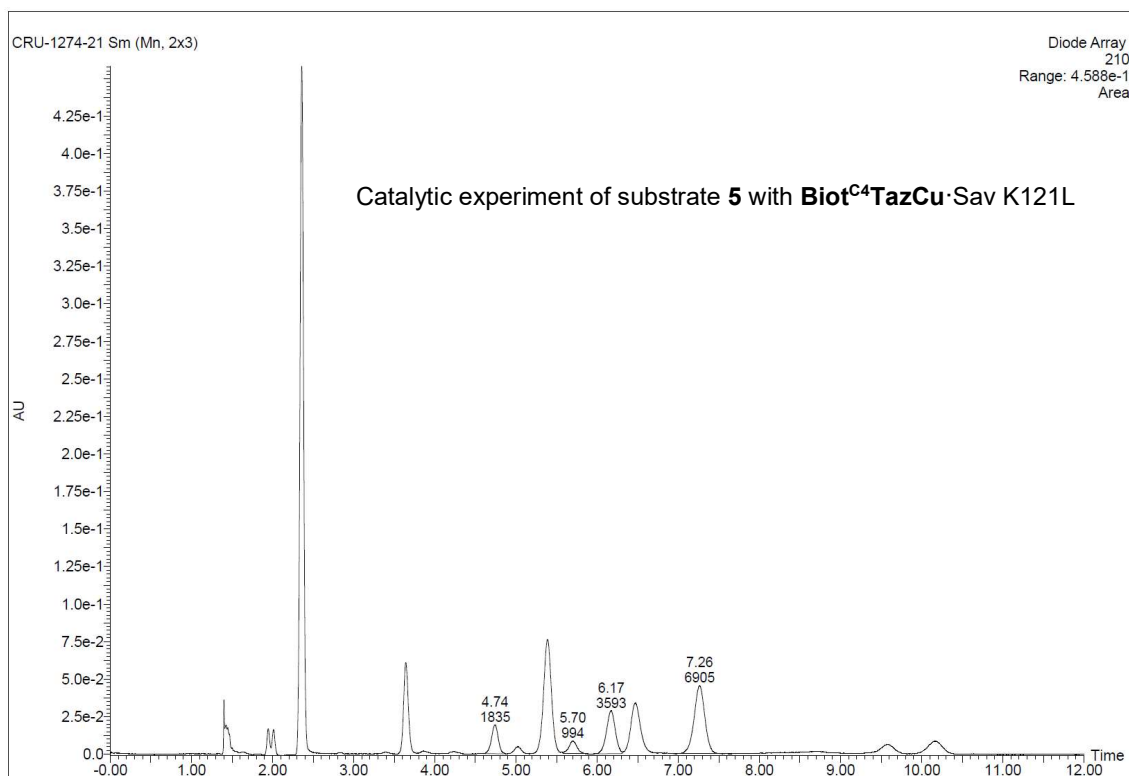
Source Type	ESI	Ion Polarity	Positive	Set Nebulizer	1.8 Bar
Focus	Active	Set Capillary	4500 V	Set Dry Heater	220 °C
Scan Begin	300 m/z	Set End Plate Offset	-500 V	Set Dry Gas	8.0 l/min
Scan End	3000 m/z	Collision Energy	10.0 eV	Set Ion Energy (MS only)	4.0 eV

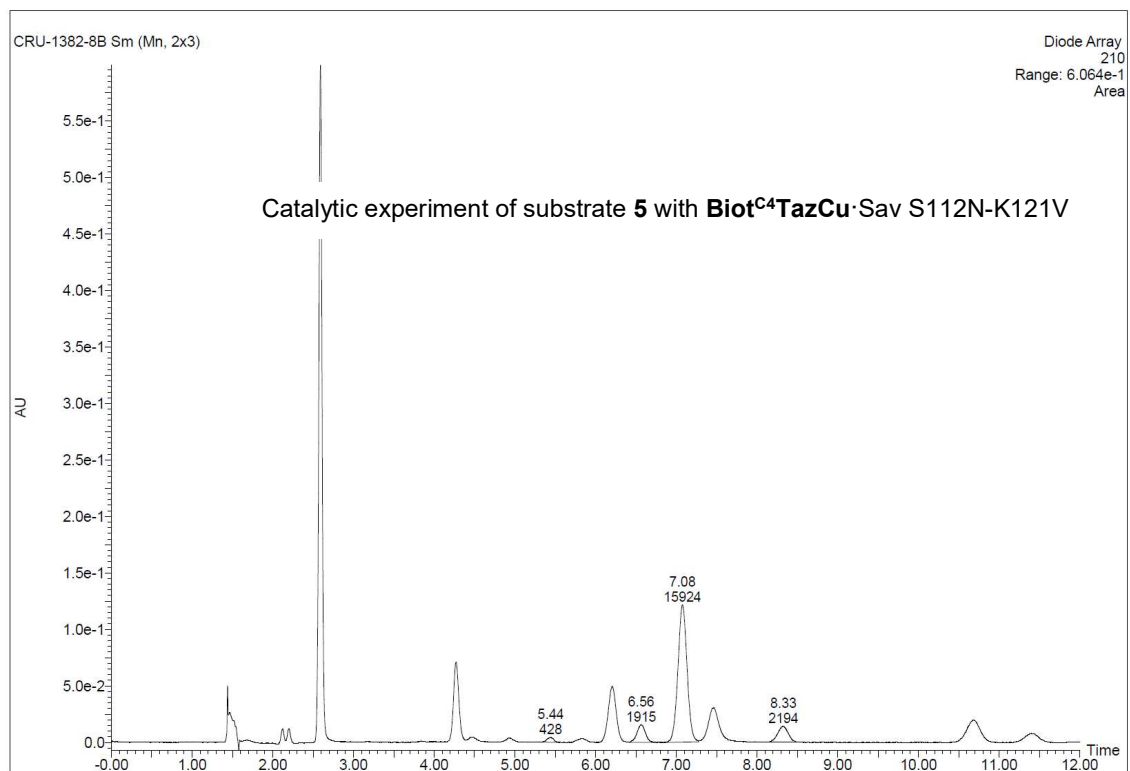
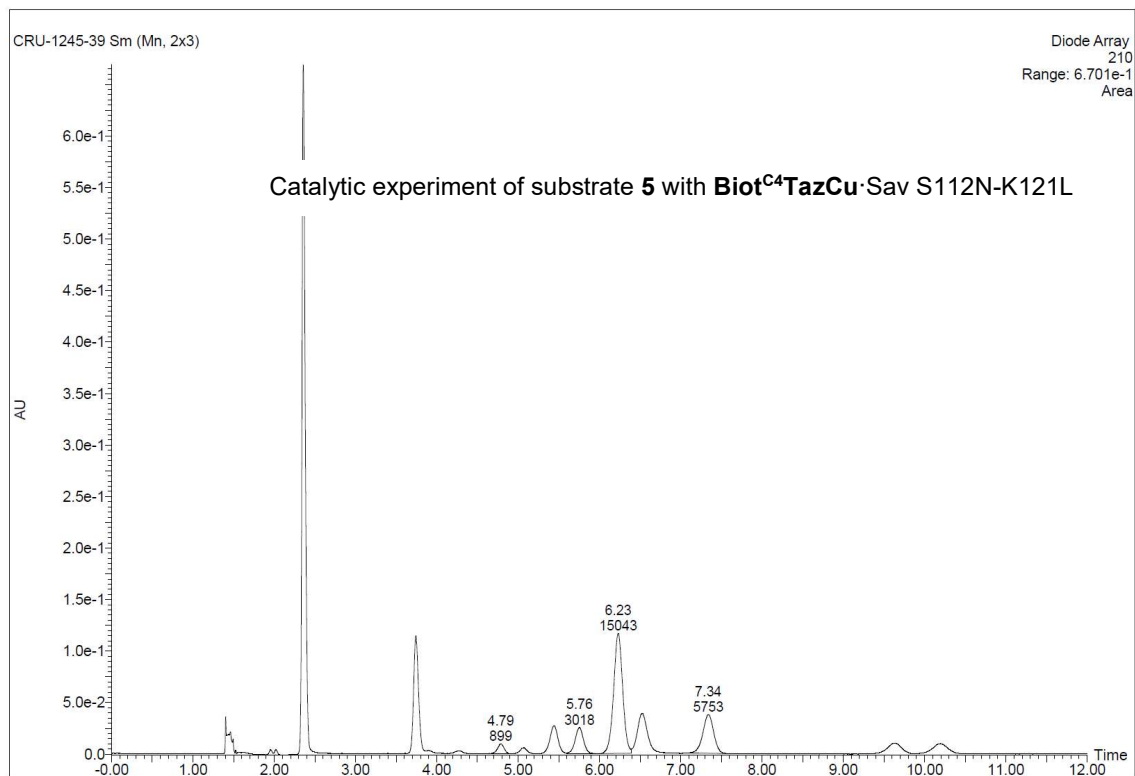


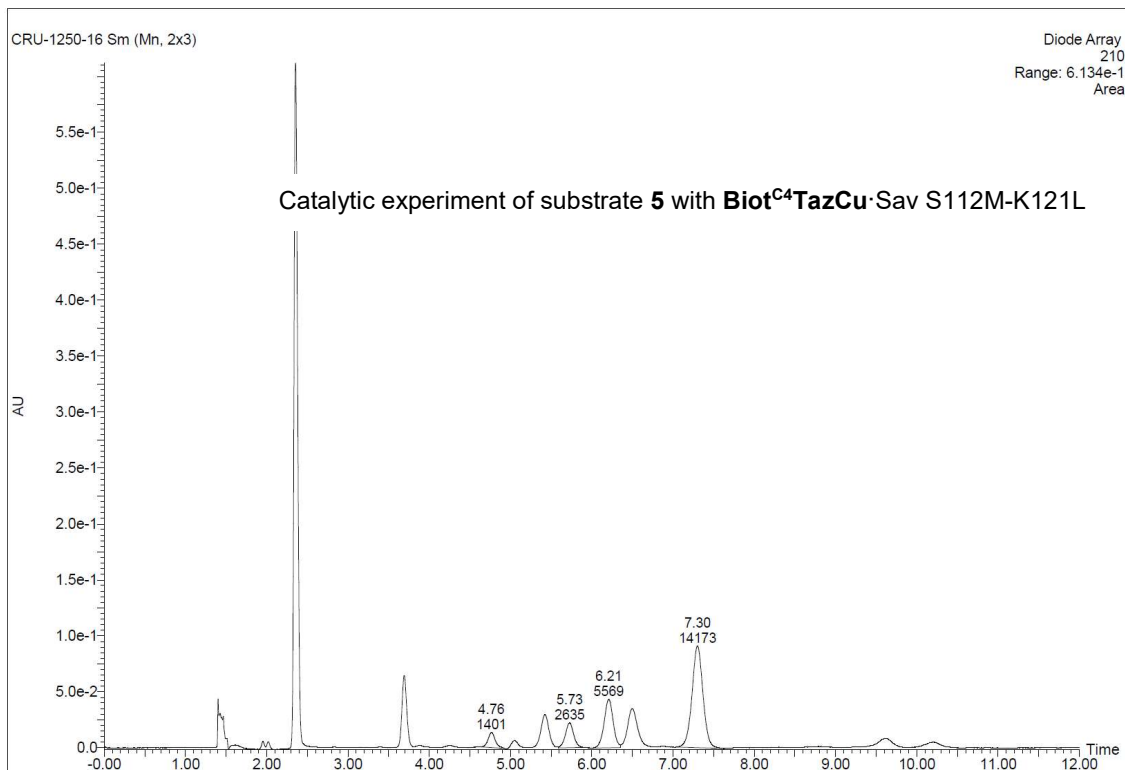
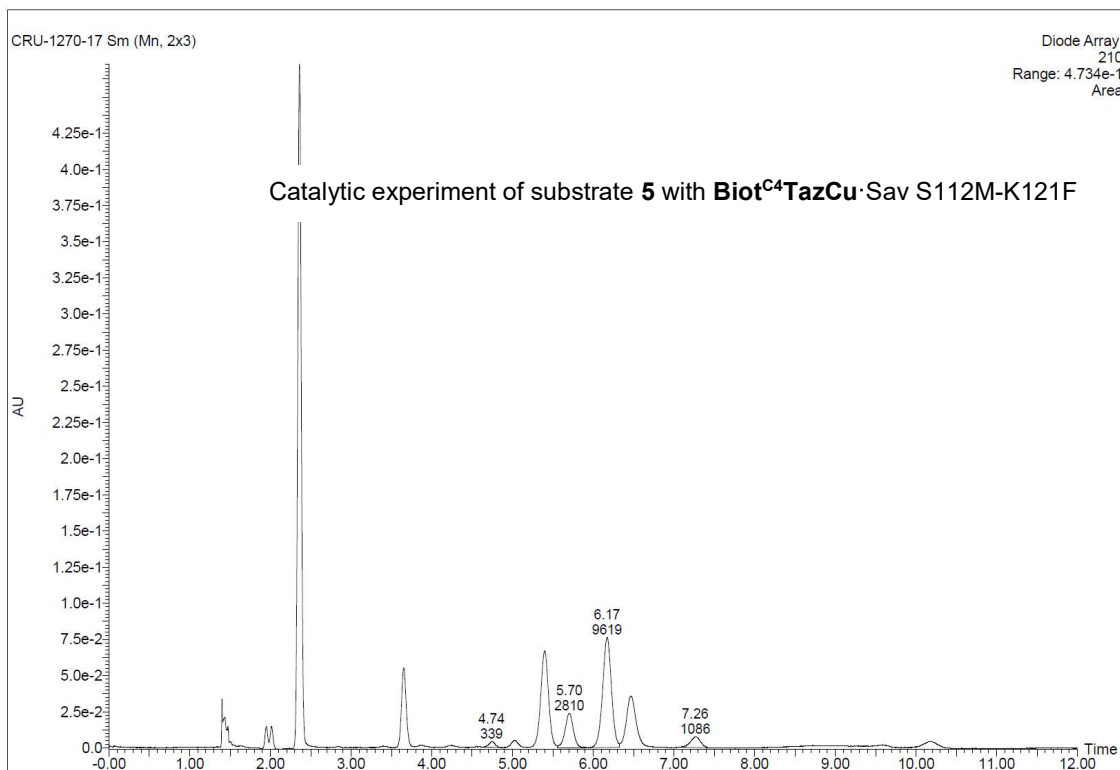
4.5.12 Calibration curves and chromatograms

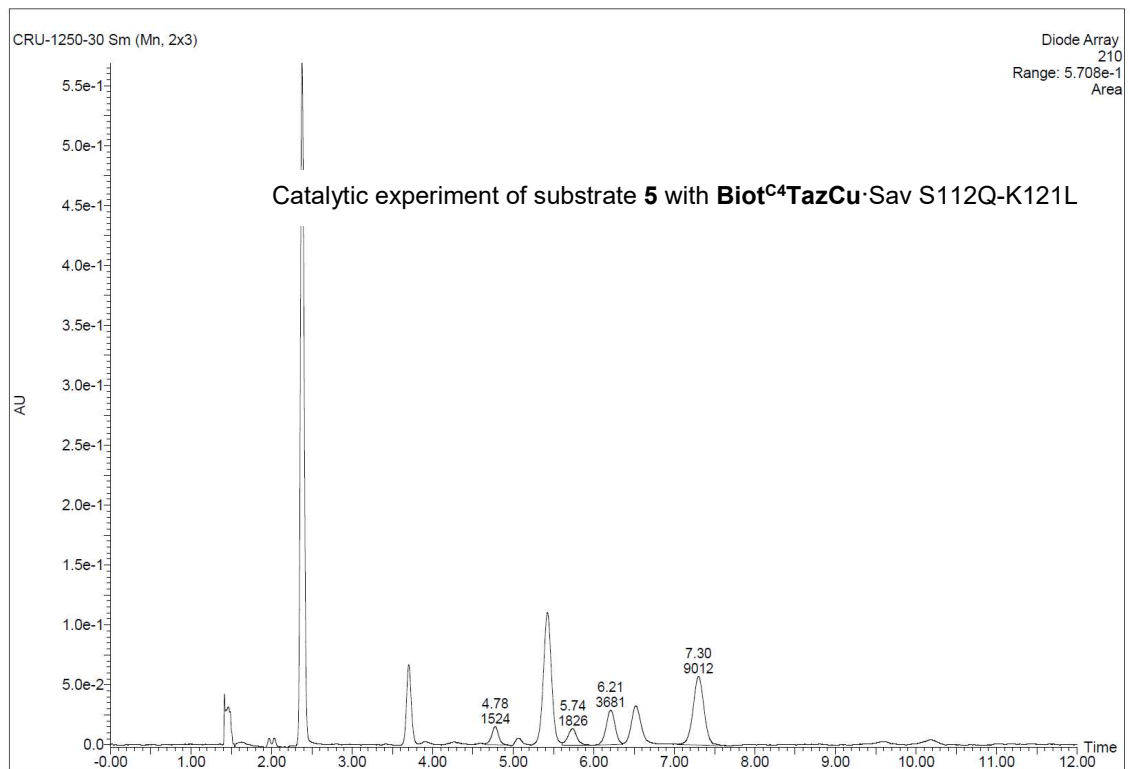
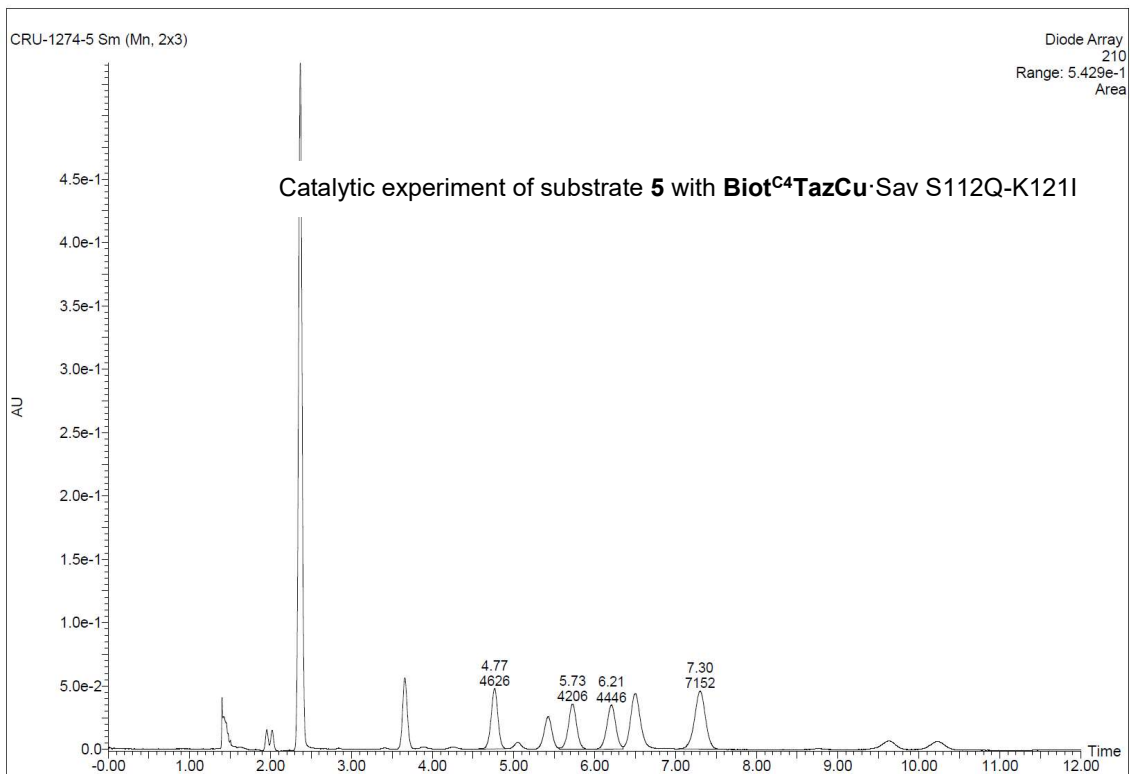


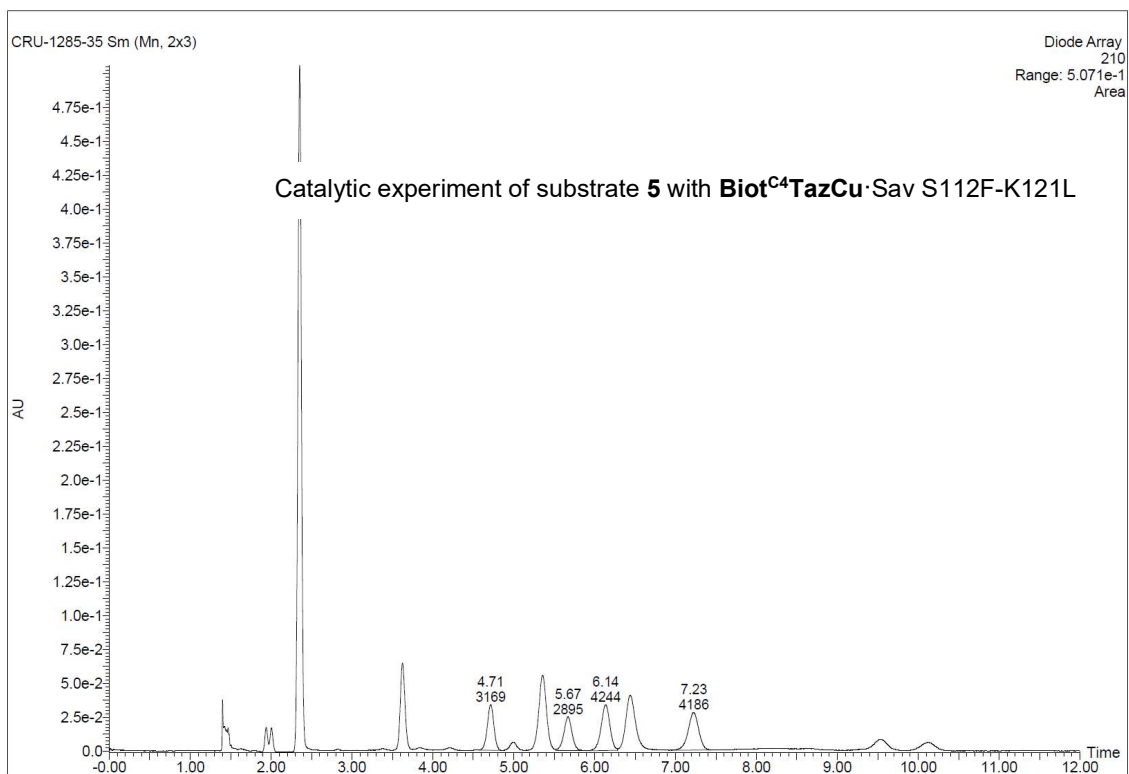
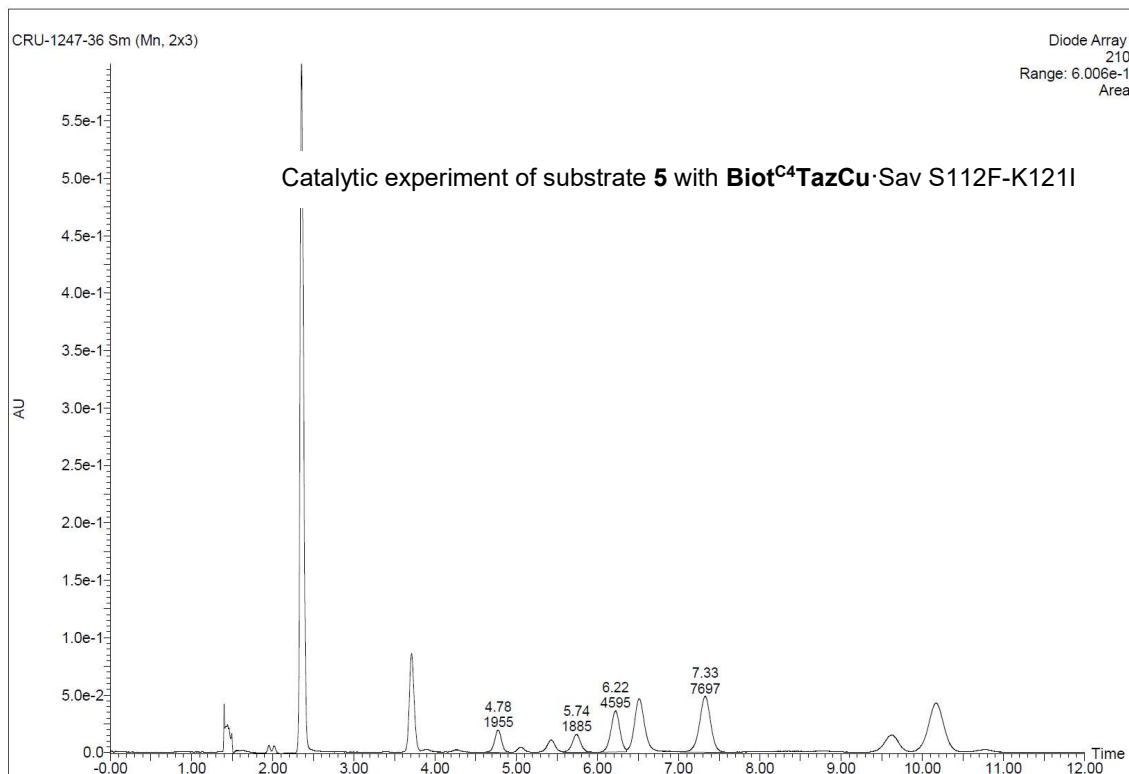


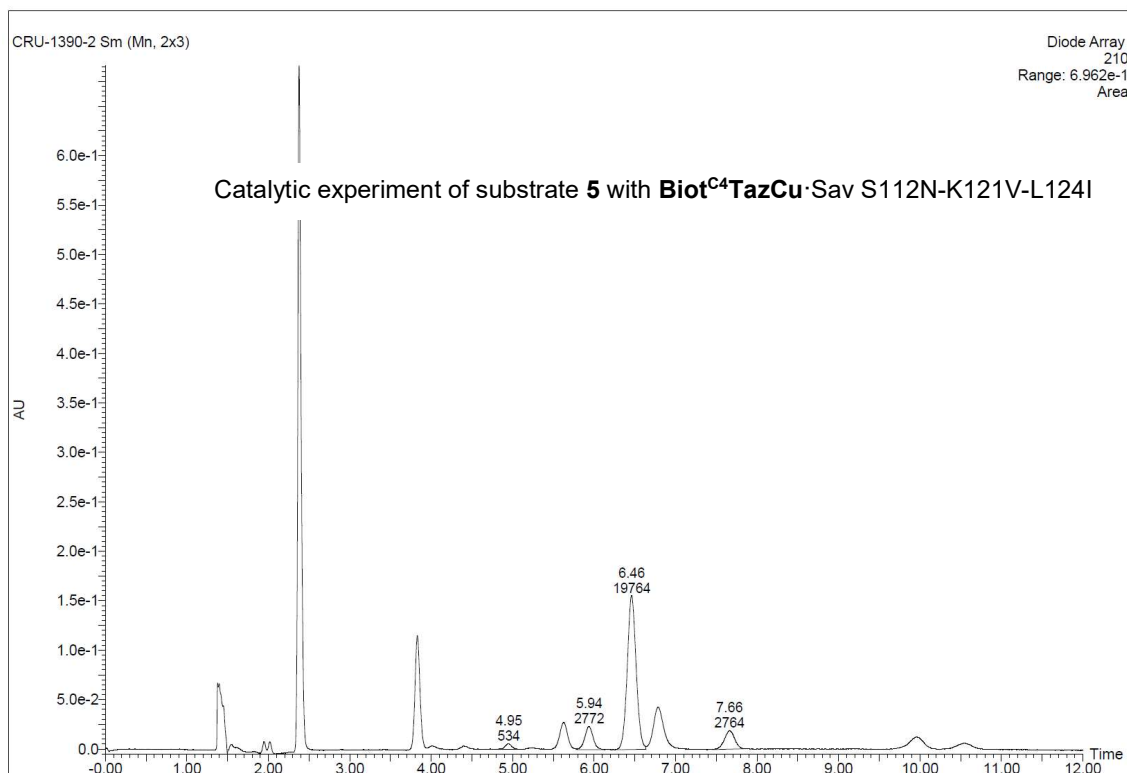
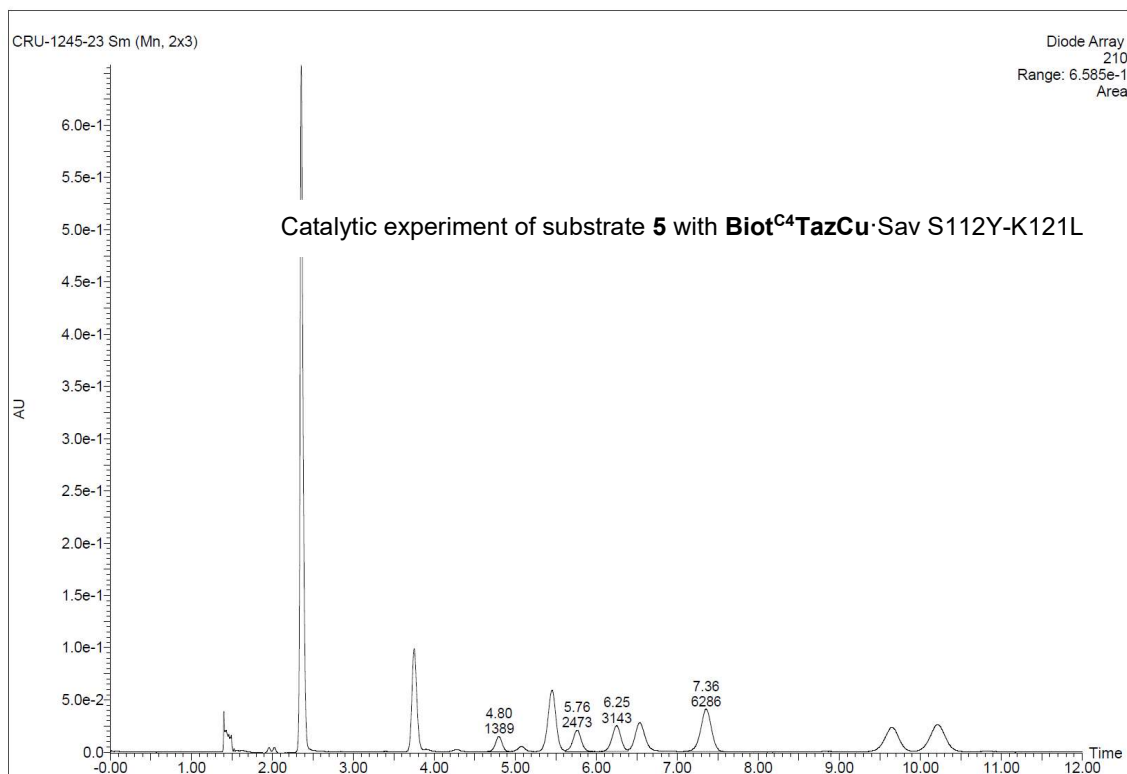


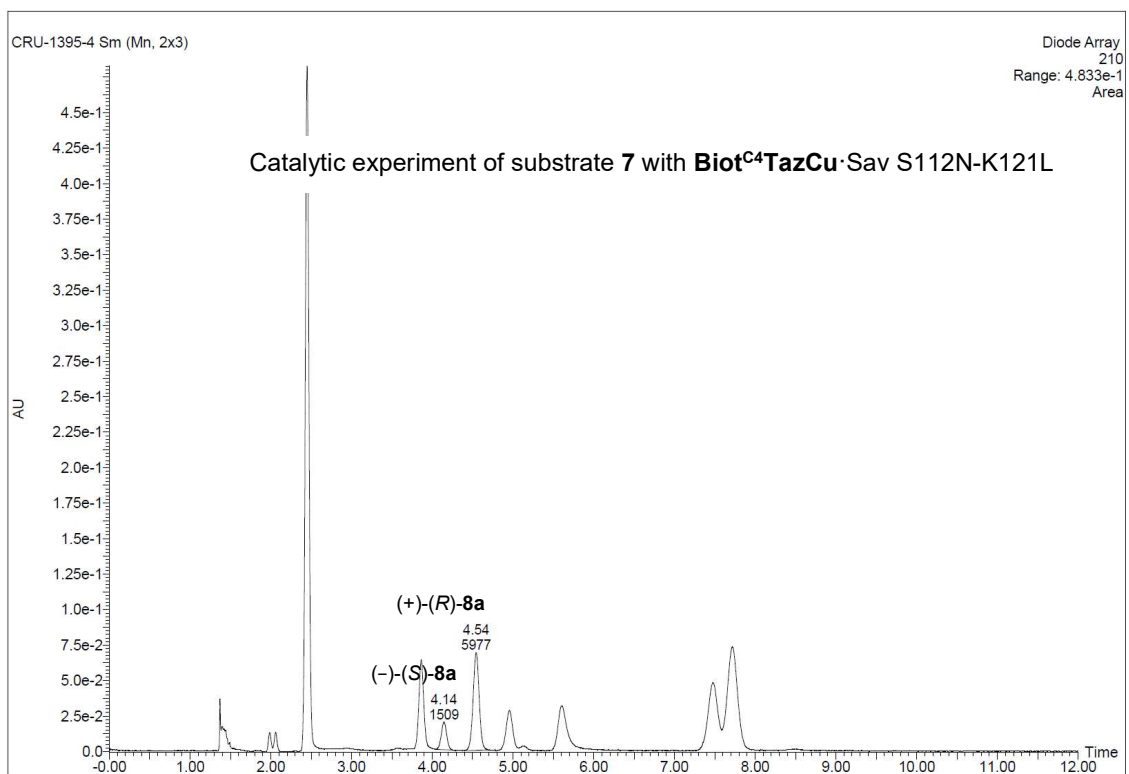
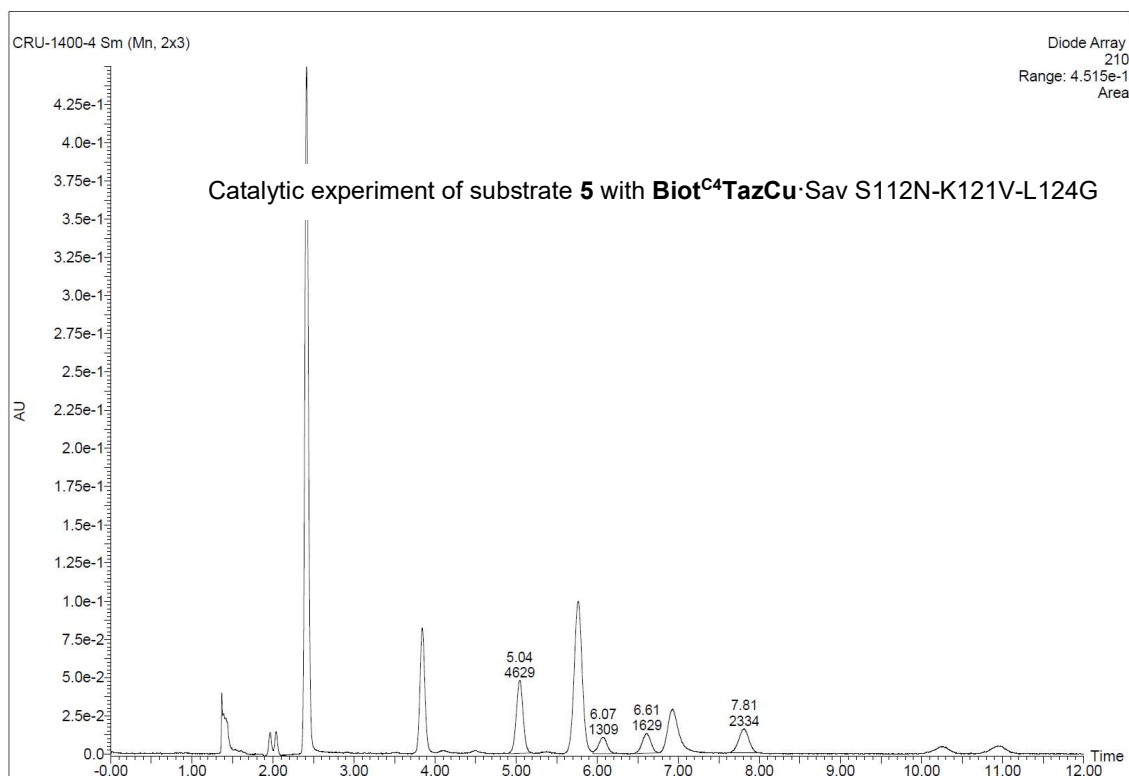


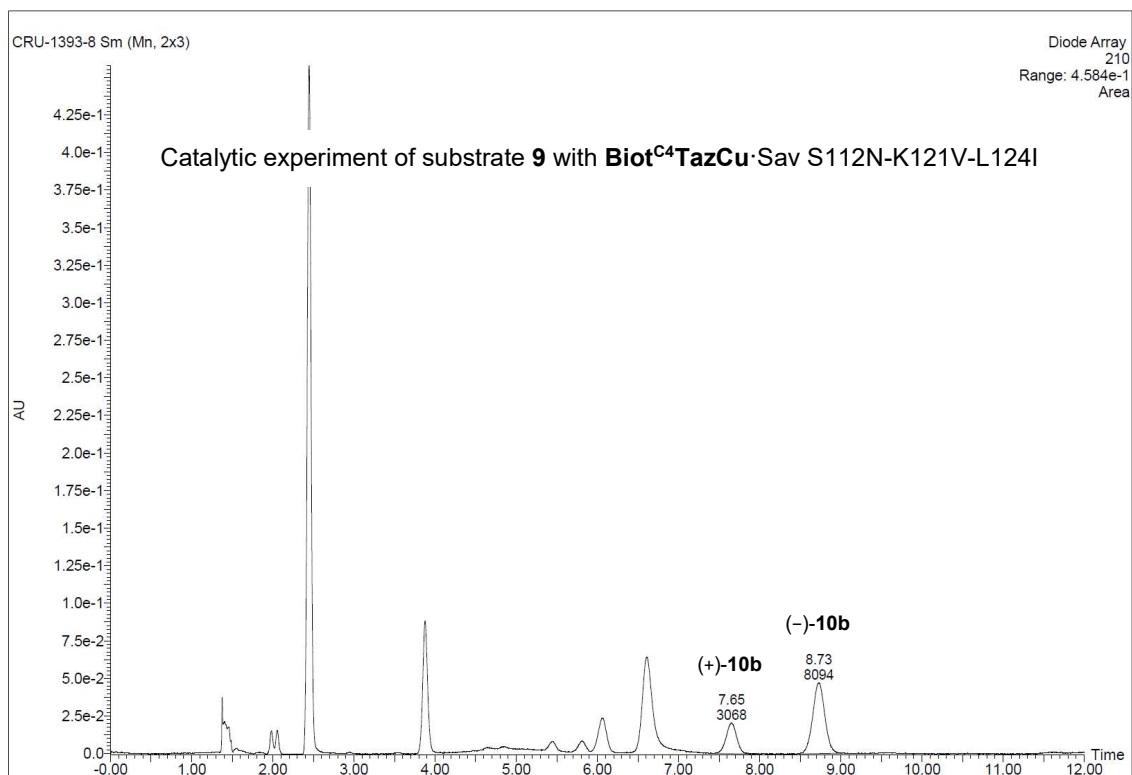
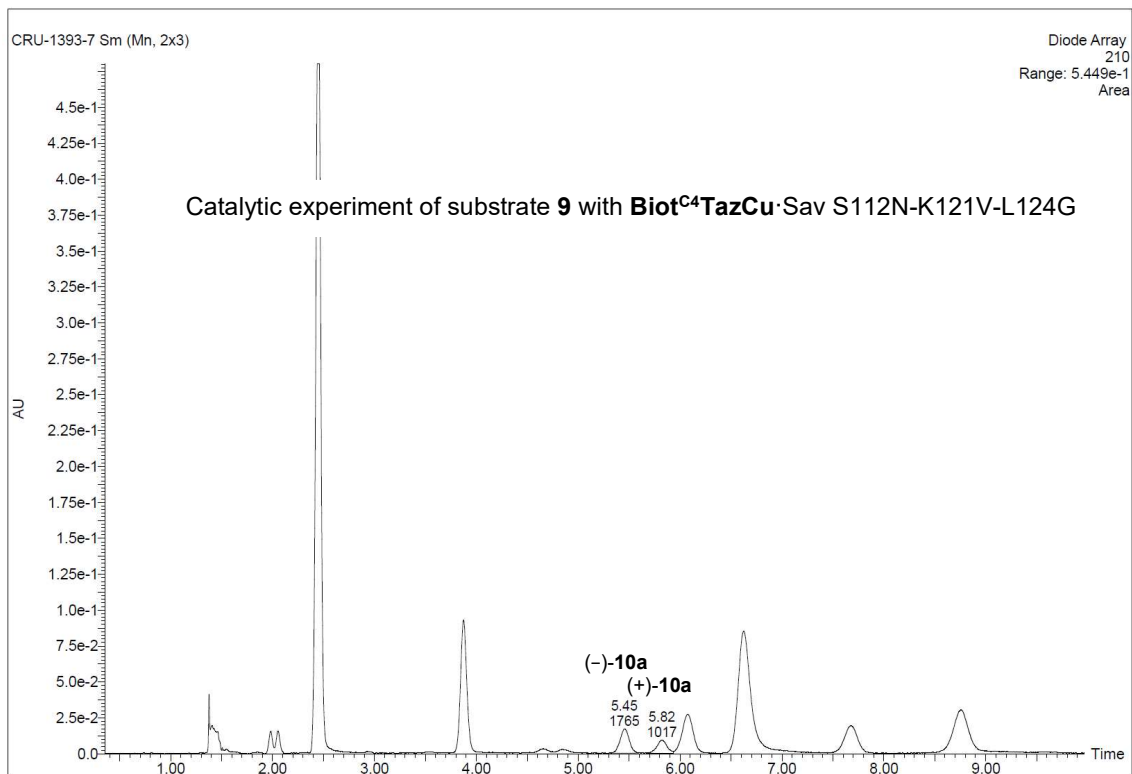


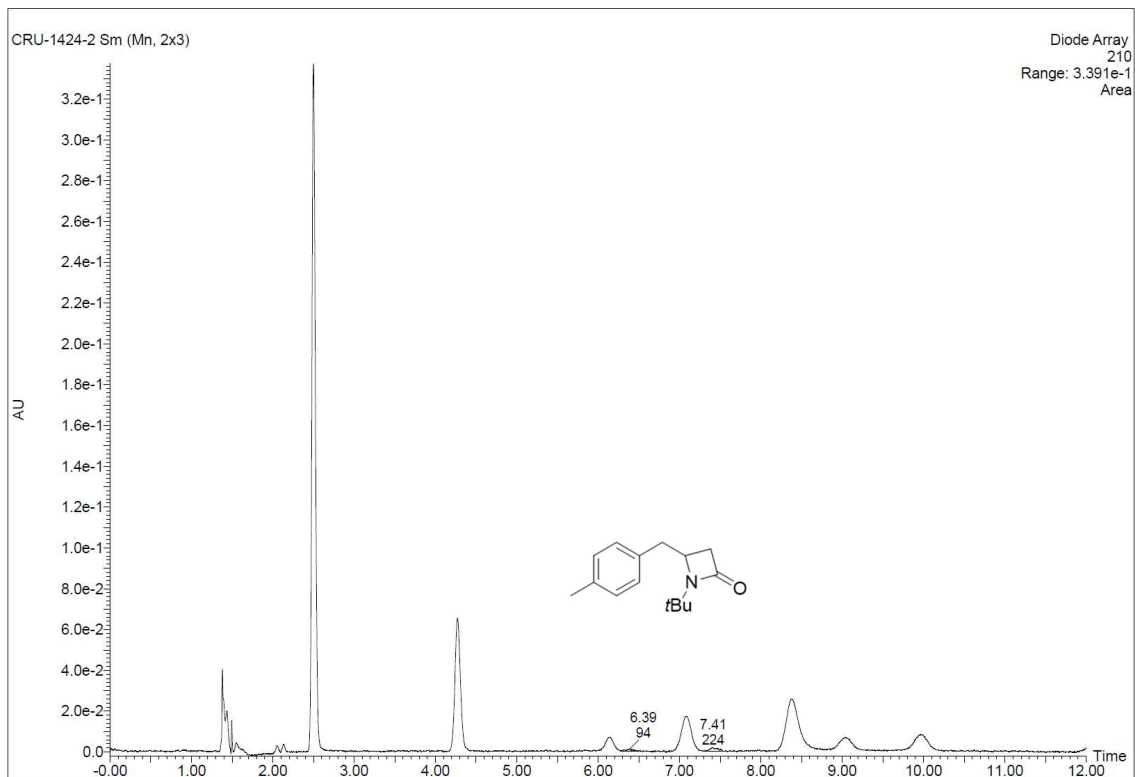
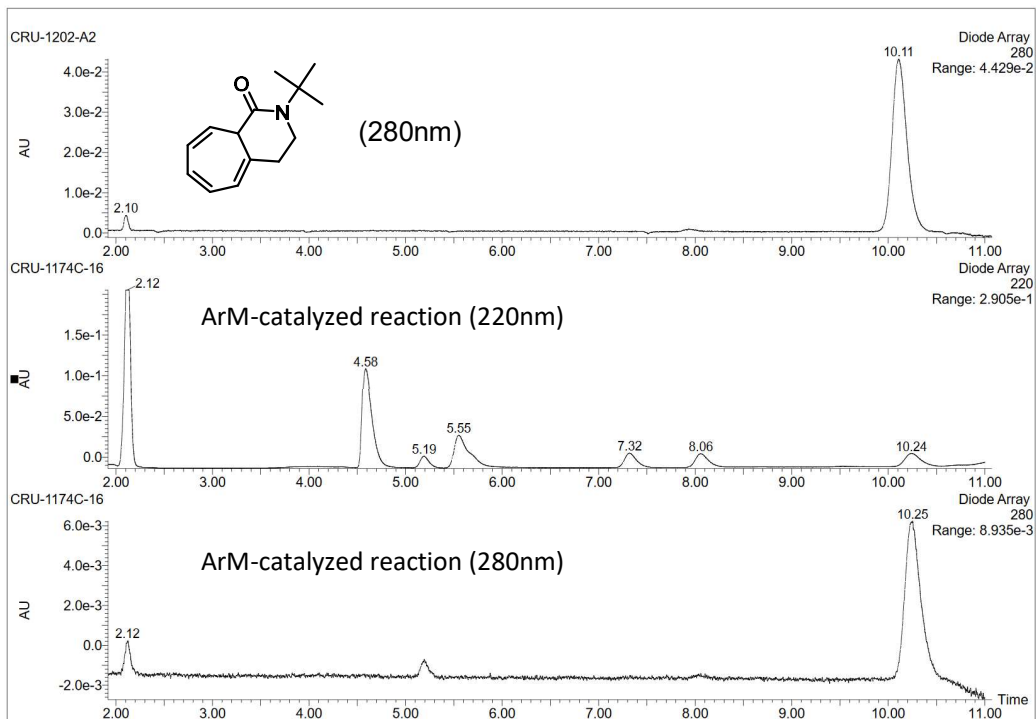


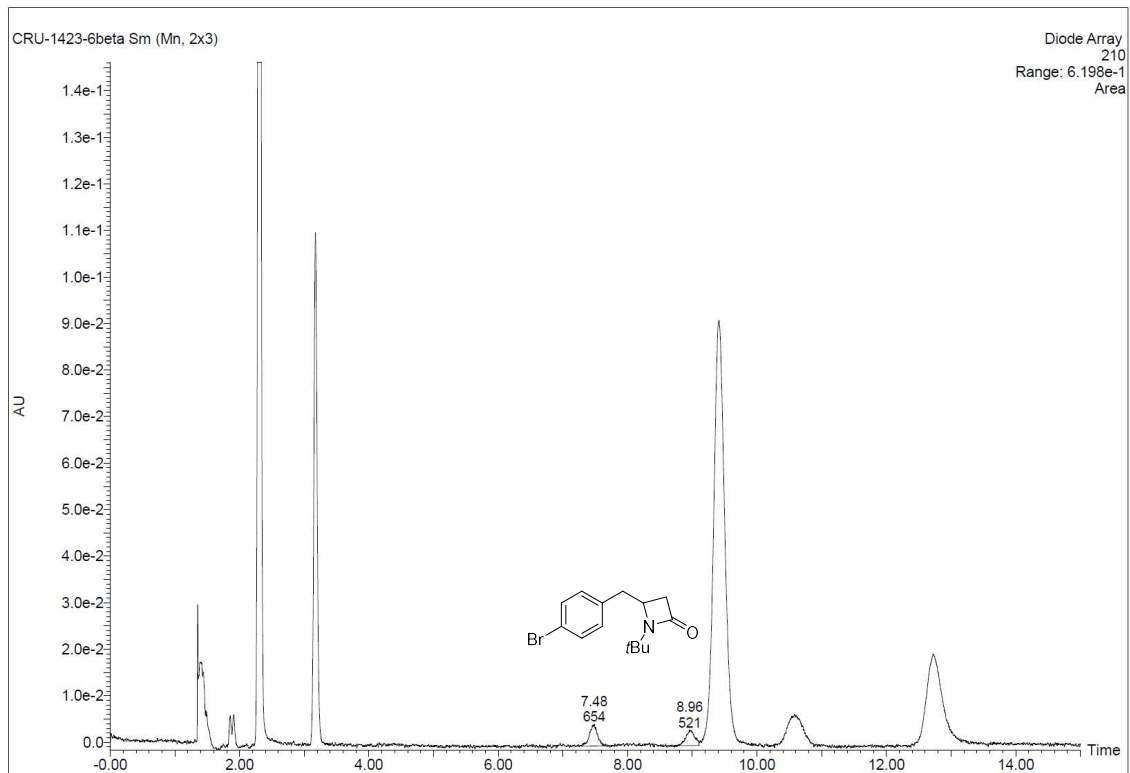
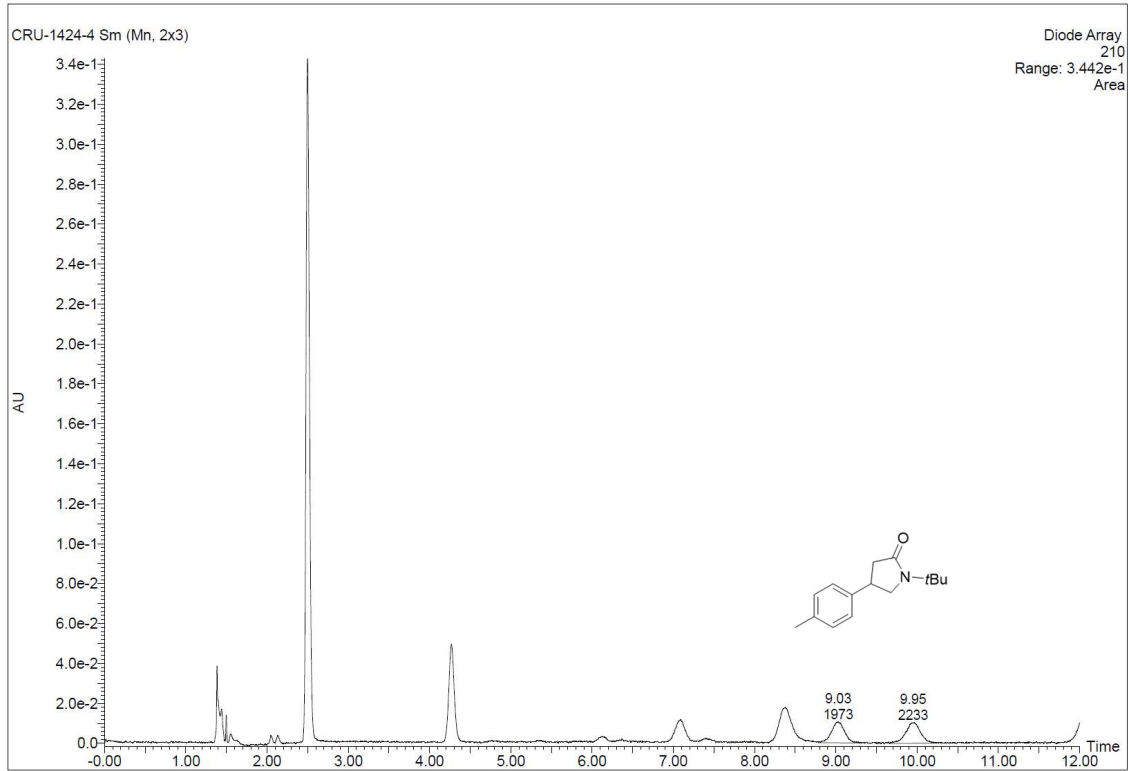


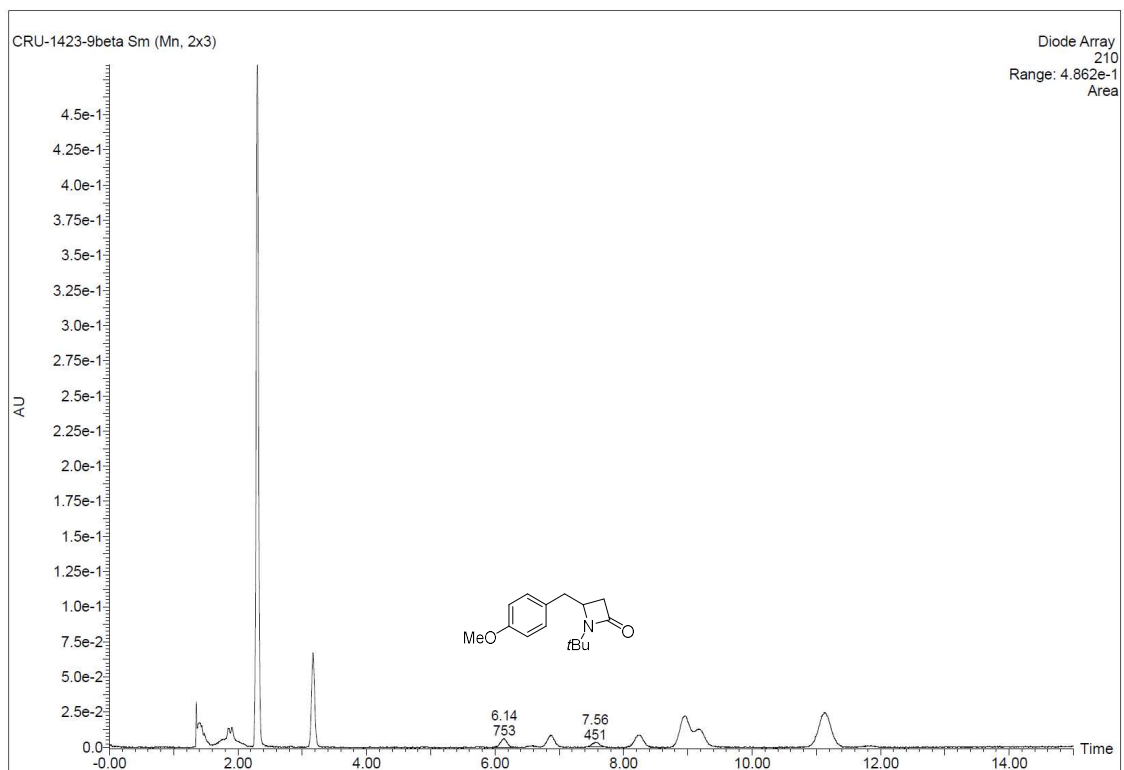
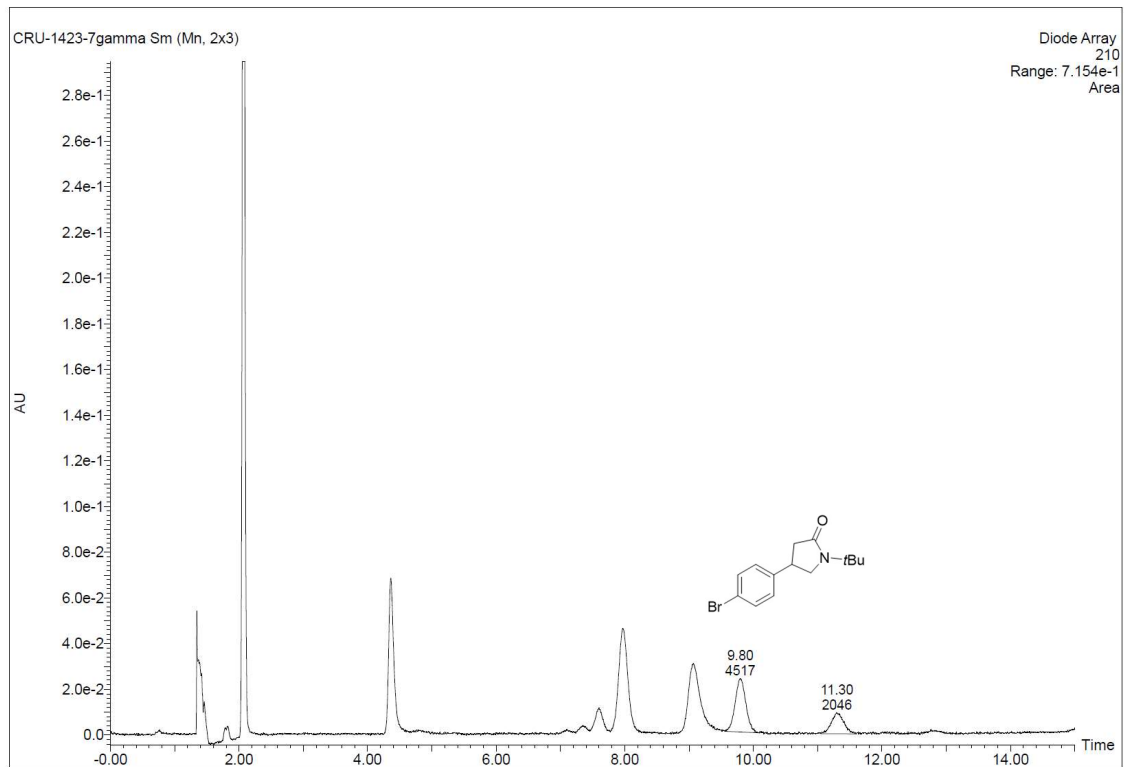


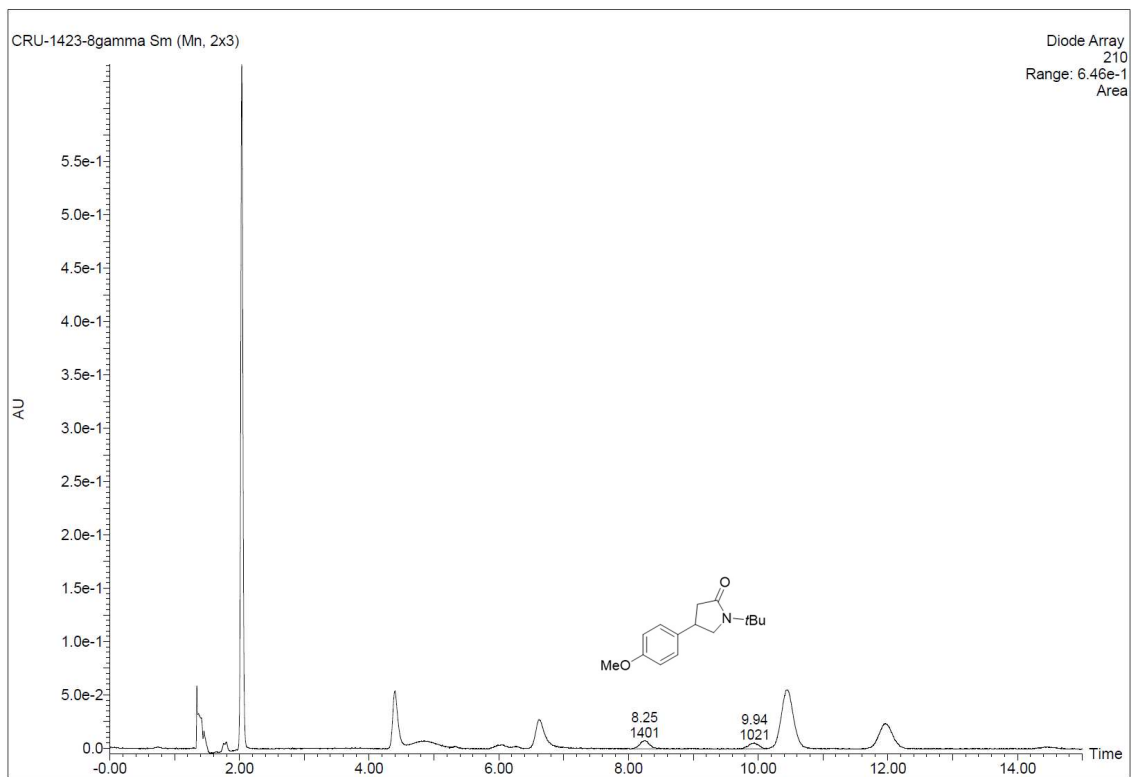






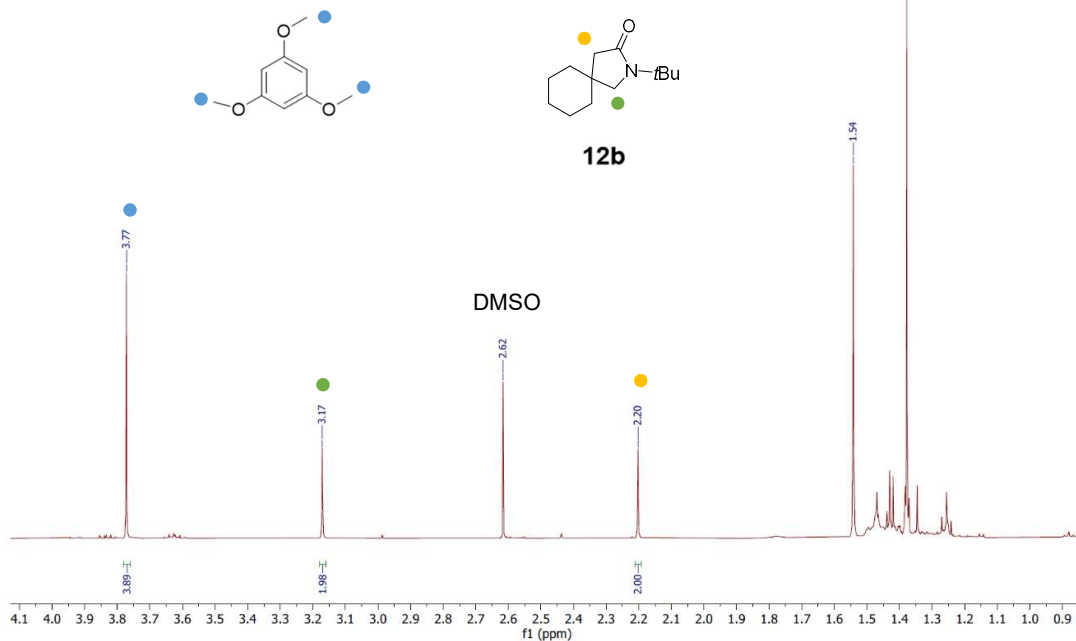






4.5.13 Quantitative NMR

rumocoR-.1222.1.fid
Kuerzel CRU
Gruppe Ward
Nummer 1395-9
group Ward



Quantitative NMR of the catalytic experiment with **Biot^{C4}TazCu**-Sav S112N-K121L. 0,6 μmol of internal standard (1,3,5-trimethoxybenzene) was added at the end of the reaction. The reaction contained 1,5 μmol of substrate.

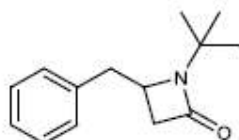
4.5.14 VCD Spectrum

VCD Analysis Report

1. Sample Information

No.	Sample ID	Batch No.
1	CRU-1411 β	CRU-1411 β -P1

Structure:



Chemical Formula: C₁₄H₁₇NO
Molecular Weight: 217.31

2. Analysis Results:

VCD data indicate that the features of experimental spectrum of CRU-1411 β is very similar to the computed VCD spectrum for (R)-configuration model, but opposite to (S)-configuration model.

Spectrum Comparison:

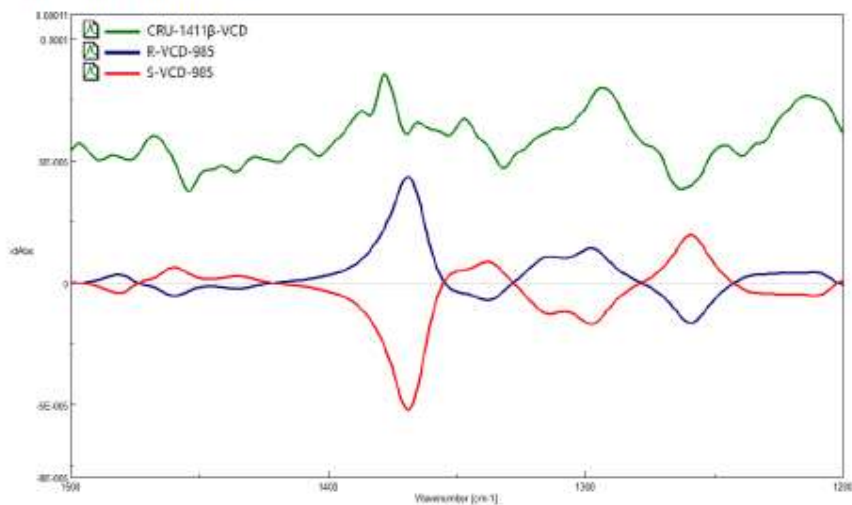


Figure 1. Comparison of experimental VCD spectra of CRU-1411 β to calculated VCD spectrum for the model structure of (R)-configuration and (S)-configuration.

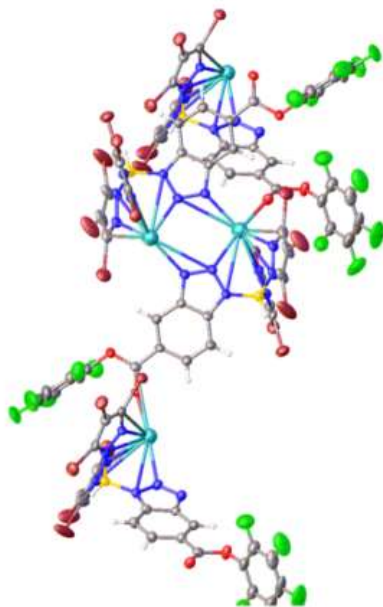
Experimental VCD spectrum of (–)-6a (green curve) overlaid with computed spectra of (R)- and (S)-6a (blue and red curves respectively). Sample preparation: 18 mg of (–)-6a were dissolved in CDCl₃ (50 μ l). The solution was transferred to a BaF₂ cell and the VCD spectrum was acquired on a JASCO FVS-6000 instrument.

4.5.15 X-ray reports

X-Ray Crystallographic Information for 3: CDCC 2151848

Crystal Data and Experimental

0.0715)



Experimental. Single colourless plate crystals of **CRU_{1244_150K}** were used as supplied. A suitable crystal with dimensions $0.21 \times 0.16 \times 0.08 \text{ mm}^3$ was selected and mounted on a mylar loop in perfluoroether oil on a STOE STADIVARI diffractometer. The crystal was kept at a steady $T = 150 \text{ K}$ during data collection. The structure was solved with the ShelXT 2018/2 (Sheldrick, 2018) solution program using dual methods and by using Olex2 (Dolomanov et al., 2009) as the graphical interface. The model was refined with ShelXL 2018/3 (Sheldrick, 2015) using full matrix least squares minimisation on F^2 .

Crystal Data. $\text{C}_{19}\text{H}_4\text{BBr}_6\text{F}_5\text{KN}_7\text{O}_2$, $M_r = 986.66$, monoclinic, $P2_1/c$ (No. 14), $a = 15.2664(3) \text{ \AA}$, $b = 20.1121(4) \text{ \AA}$, $c = 9.4588(2) \text{ \AA}$, $\beta = 105.759(2)^\circ$, $\alpha = \gamma = 90^\circ$, $V = 2795.06(10) \text{ \AA}^3$, $T = 150 \text{ K}$, $Z = 4$, $Z' = 1$, $\mu(\text{GaK}\alpha) = 8.193$, 57237 reflections measured, 5609 unique ($R_{\text{int}} =$

0.0715) which were used in all calculations. The final wR_2 was 0.1753 (all data) and R_1 was 0.0562 ($I \geq 2 \sigma(I)$).

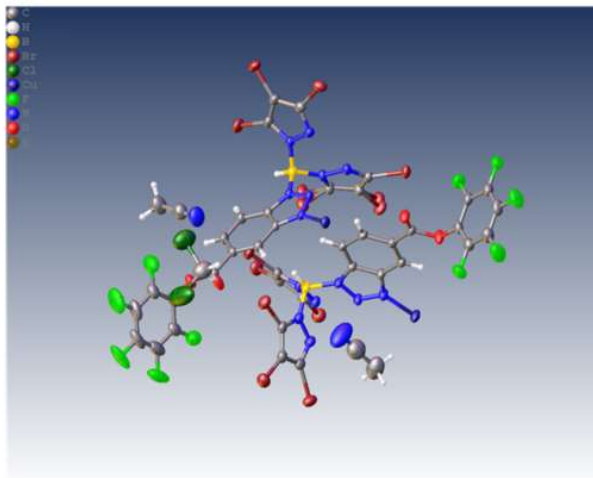
Compound	CRU_{1244_150K}
Formula	$\text{C}_{19}\text{H}_4\text{BBr}_6\text{F}_5\text{KN}_7\text{O}_2$
$D_{\text{calc.}} / \text{g cm}^{-3}$	2.345
μ / mm^{-1}	8.193
Formula Weight	986.66
Colour	colourless
Shape	plate
Size/ mm^3	$0.21 \times 0.16 \times 0.08$
T / K	150
Crystal System	monoclinic
Space Group	$P2_1/c$
$a / \text{ \AA}$	15.2664(3)
$b / \text{ \AA}$	20.1121(4)
$c / \text{ \AA}$	9.4588(2)
$\alpha / ^\circ$	90
$\beta / ^\circ$	105.759(2)
$\gamma / ^\circ$	90
$V / \text{ \AA}^3$	2795.06(10)
Z	4
Z'	1
Wavelength/ \AA	1.34143
Radiation type	GaK α
$\theta_{\text{min}} / ^\circ$	2.616
$\theta_{\text{max}} / ^\circ$	56.641
Measured Refl's.	57237
Indep't Refl's	5609
Refl's $I \geq 2 \sigma(I)$	4243
R_{int}	0.0715
Parameters	370
Restraints	0
Largest Peak	2.043
Deepest Hole	-2.486
GooF	1.097
wR_2 (all data)	0.1753
wR_2	0.1689
R_1 (all data)	0.0702
R_1	0.0562

Bond Lengths of **3** in Å:

Atom	Atom	Length/Å
Br3	C16	1.877(6)
Br2	C15	1.870(6)
Br2	K1 ¹	3.584(3)
Br2	K1 ²	3.764(2)
Br1	C14	1.858(6)
Br6	C19	1.873(7)
Br6	K1	3.875(3)
Br4	C17	1.865(7)
Br5	C18	1.869(7)
O2	C7	1.218(7)
O2	K1 ³	2.319(4)
O1	C7	1.374(7)
O1	C1	1.385(8)
F1	C2	1.310(9)
N1	N2	1.323(7)
N1	C10	1.380(7)
N1	K1 ⁴	2.436(5)
N3	N2	1.349(6)
N3	C11	1.353(7)
N3	B1	1.573(8)
N3	K1	3.348(5)
N5	N4	1.378(7)
N5	C16	1.321(8)
N5	K1	2.399(5)
N2	K1	2.588(5)
N2	K1 ⁴	3.337(5)
N4	C14	1.362(8)
N4	B1	1.540(8)
N4	K1	3.310(5)
F5	C6	1.329(9)
N7	N6	1.366(7)

Atom	Atom	Length/Å
N7	C19	1.341(9)
N7	K1	2.395(6)
N6	C17	1.376(9)
N6	B1	1.536(9)
N6	K1	3.265(6)
F4	C5	1.326(11)
F3	C4	1.357(9)
C11	C10	1.407(8)
C11	C12	1.408(8)
C10	C9	1.398(8)
C10	K1 ⁴	3.472(6)
F2	C3	1.320(10)
C9	C8	1.380(7)
C14	C15	1.360(9)
C15	C16	1.386(8)
C7	C8	1.467(8)
C7	K1 ³	3.446(6)
C12	C13	1.359(9)
C8	C13	1.423(8)
C16	K1	3.458(6)
C19	C18	1.361(10)
C19	K1	3.393(7)
C1	C2	1.394(10)
C1	C6	1.374(11)
C18	C17	1.349(11)
C2	C3	1.371(11)
C6	C5	1.401(11)
C5	C4	1.361(15)
B1	K1	3.463(7)
C4	C3	1.399(16)

Crystal Data and Experimental



Experimental. Single yellow plate crystals of **CRU_TpCu_150K** were used as supplied. A suitable crystal with dimensions $0.25 \times 0.17 \times 0.07 \text{ mm}^3$ was selected and mounted on a mylar loop in perfluoroether oil on a STOE STADIVARI diffractometer. The crystal was kept at a steady $T = 150 \text{ K}$ during data collection. The structure was solved with the ShelXT 2018/2 (Sheldrick, 2018) solution program using dual methods and by using Olex2 (Dolomanov et al., 2009) as the graphical interface. The model was refined with ShelXL 2018/3 (Sheldrick, 2015) using full matrix least squares minimisation on F^2 .

Crystal Data. $\text{C}_{43}\text{H}_{16}\text{B}_2\text{Br}_{12}\text{Cl}_2\text{Cu}_2\text{F}_{10}\text{N}_{16}\text{O}_4$, $M_r = 2189.24$, triclinic, $P-1$ (No. 2), $a = 11.2685(2) \text{ \AA}$, $b = 17.3349(4) \text{ \AA}$, $c = 18.2407(4) \text{ \AA}$, $\alpha = 64.945(2)^\circ$, $\beta = 81.838(2)^\circ$, $\gamma = 74.559(2)^\circ$, $V = 3109.58(13) \text{ \AA}^3$, $T = 150 \text{ K}$, $Z = 2$, $Z' = 1$, $\mu(\text{GaK}\alpha) = 10.725$, 59400 reflections measured, 12346 unique ($R_{\text{int}} = 0.0664$) which were used in all calculations. The final wR_2 was 0.1416 (all data) and R_1 was 0.0532 ($I \geq 2 \sigma(I)$).

Compound	CRU_TpCu_150K
Formula	$\text{C}_{43}\text{H}_{16}\text{B}_2\text{Br}_{12}\text{Cl}_2\text{Cu}_2\text{F}_{10}\text{N}_{16}\text{O}_4$
$D_{\text{calc.}} / \text{g cm}^{-3}$	2.338
μ / mm^{-1}	10.725
Formula Weight	2189.24
Colour	yellow
Shape	plate
Size/ mm^3	$0.25 \times 0.17 \times 0.07$
T / K	150
Crystal System	triclinic
Space Group	$P-1$
$a / \text{Å}$	11.2685(2)
$b / \text{Å}$	17.3349(4)
$c / \text{Å}$	18.2407(4)
$\alpha / ^\circ$	64.945(2)
$\beta / ^\circ$	81.838(2)
$\gamma / ^\circ$	74.559(2)
$V / \text{Å}^3$	3109.58(13)
Z	2
Z'	1
Wavelength/ Å	1.34143
Radiation type	GaK α
$\theta_{\text{min}} / ^\circ$	2.515
$\theta_{\text{max}} / ^\circ$	56.739
Measured Refl's.	59400
Indep't Refl's	12346
Refl's $I \geq 2 \sigma(I)$	11575
R_{int}	0.0664
Parameters	840
Restraints	2
Largest Peak	1.429
Deepest Hole	-1.289
GooF	1.079
wR_2 (all data)	0.1416
wR_2	0.1384
R_1 (all data)	0.0570
R_1	0.0532

Bond Lengths of 4 in Å:

Atom	Atom	Length/Å	Atom	Atom	Length/Å
Br6	C19	1.870(6)	N8	N9	1.313(7)
Br1	C16	1.851(6)	N8	C20	1.373(7)
Br2	C15	1.855(6)	N13	N14	1.385(7)
Br7	C33	1.854(6)	N13	C36	1.359(8)
Br3	C14	1.861(6)	N13	B2	1.551(8)
Br10	C38	1.870(6)	N12	C35	1.323(9)
Br12	C36	1.855(7)	N5	C16	1.339(8)
Br11	C37	1.866(6)	N14	C38	1.323(8)
Br9	C35	1.869(6)	F4	C12	1.343(11)
Br8	C34	1.855(7)	C1	C2	1.394(8)
Br5	C18	1.857(7)	C1	C6	1.384(8)
Cu1	N1	1.917(5)	C2	C3	1.381(8)
Cu1	N2 ¹	2.370(5)	C6	C5	1.422(8)
Cu1	N7 ¹	2.035(5)	F3	C11	1.324(9)
Cu1	N5 ¹	1.990(5)	C26	C22	1.480(8)
Cu2	N8	1.908(5)	F2	C10	1.343(11)
Cu2	N12 ²	2.040(6)	C3	C7	1.493(8)
Cu2	N9 ²	2.167(5)	C3	C4	1.431(8)
Cu2	N14 ²	2.047(5)	C19	C18	1.376(9)
Cl2	C43	1.732(11)	C5	C4	1.377(8)
F10	C28	1.336(8)	C22	C21	1.371(8)
O4	C26	1.190(7)	C22	C23	1.427(8)
O1	C7	1.394(7)	C21	C20	1.392(8)
O1	C8	1.385(7)	C25	C20	1.398(8)
F9	C29	1.330(8)	C25	C24	1.400(8)
Cl1	C43	1.697(12)	C33	C34	1.370(9)
O3	C26	1.371(7)	C14	C15	1.363(9)
O3	C27	1.394(7)	C23	C24	1.379(8)
N1	N2	1.309(7)	C34	C35	1.384(10)
N1	C1	1.370(7)	C15	C16	1.402(9)
F6	C32	1.353(8)	C18	C17	1.387(9)
F5	C13	1.327(10)	C18	Br15	1.905(10)
N4	N5	1.374(7)	C17	Br13	1.848(6)
N4	C14	1.361(7)	C17	Br14	1.908(7)
N4	B1	1.536(8)	C38	C37	1.382(9)
N2	N3	1.354(6)	C36	C37	1.366(9)
F8	C30	1.344(8)	C27	C28	1.384(10)
O2	C7	1.179(8)	C27	C32	1.350(10)
N6	N7	1.374(6)	C8	C9	1.372(11)
N6	C17	1.339(8)	C8	C13	1.386(11)
N6	B1	1.563(8)	C28	C29	1.392(9)
N11	N12	1.382(7)	C29	C30	1.354(11)
N11	C33	1.359(8)	C32	C31	1.383(10)
N11	B2	1.555(9)	C9	C10	1.371(11)
F1	C9	1.322(10)	C31	C30	1.377(11)
N3	C6	1.365(7)	C13	C12	1.384(11)
N3	B1	1.556(8)	C10	C11	1.389(15)
N10	N9	1.342(7)	C41	N15	1.093(11)
N10	C25	1.377(7)	C41	C42	1.450(12)
N10	B2	1.562(8)	C12	C11	1.364(15)
F7	C31	1.338(9)	N16	C39	1.169(17)
N7	C19	1.321(8)	C39	C40	1.463(19)

4.6 References

- (1) Bergman, R. G. C–H Activation. *Nature* **2007**, *446* (7134), 391–393. <https://doi.org/10.1038/446391a>.
- (2) Dalton, T.; Faber, T.; Glorius, F. C–H Activation: Toward Sustainability and Applications. *ACS Cent. Sci.* **2021**, *7* (2), 245–261. <https://doi.org/10.1021/acscentsci.0c01413>.
- (3) Hartwig, J. F.; Larsen, M. A. Undirected, Homogeneous C–H Bond Functionalization: Challenges and Opportunities. *ACS Cent. Sci.* **2016**, *2* (5), 281–292. <https://doi.org/10.1021/acscentsci.6b00032>.
- (4) Sambigiato, C.; Schönbauer, D.; Blicek, R.; Dao-Huy, T.; Pototschnig, G.; Schaaf, P.; Wiesinger, T.; Zia, M. F.; Wencel-Delord, J.; Basset, T.; Maes, B. U. W.; Schnürch, M. A Comprehensive Overview of Directing Groups Applied in Metal-Catalysed C–H Functionalisation Chemistry. *Chem. Soc. Rev.* **2018**, *47* (17), 6603–6743. <https://doi.org/10.1039/C8CS00201K>.
- (5) Hartwig, J. F. Organotransition Metal Chemistry. From Bonding to Catalysis. Edited by John F. Hartwig. *Angew. Chem. Int. Ed.* **2010**, *49* (42), 7622–7622. <https://doi.org/10.1002/anie.201004890>.
- (6) Zheng, C.; You, S.-L. Recent Development of Direct Asymmetric Functionalization of Inert C–H Bonds. *RSC Adv.* **2014**, *4* (12), 6173–6214. <https://doi.org/10.1039/C3RA46996D>.
- (7) Gillingham, D.; Fei, N. Catalytic X–H Insertion Reactions Based on Carbenoids. *Chem. Soc. Rev.* **2013**, *42* (12), 4918–4931. <https://doi.org/10.1039/C3CS35496B>.
- (8) Davies, H. M. L.; Beckwith, R. E. J. Catalytic Enantioselective C–H Activation by Means of Metal–Carbenoid-Induced C–H Insertion. *Chem. Rev.* **2003**, *103* (8), 2861–2904. <https://doi.org/10.1021/cr0200217>.
- (9) Muñoz-Molina, J. M.; Belderrain, T. R.; Pérez, P. J. Trispyrazolylborate Coinage Metals Complexes: Structural Features and Catalytic Transformations. *Coord. Chem. Rev.* **2019**, *390*, 171–189. <https://doi.org/10.1016/j.ccr.2019.03.013>.
- (10) Díaz-Requejo, M. M.; Pérez, P. J. Copper, Silver and Gold-Based Catalysts for Carbene Addition or Insertion Reactions. *J. Organomet. Chem.* **2005**, *690* (24–25), 5441–5450. <https://doi.org/10.1016/j.jorganchem.2005.07.092>.
- (11) Díaz-Requejo, M. M.; Pérez, P. J. The TpxM Core in Csp³–H Bond Functionalization Reactions: Comparing Carbene, Nitrene, and Oxo Insertion Processes (Tpx = Scorpionate Ligand; M = Cu, Ag). *Eur. J. Inorg. Chem.* **2020**, *2020* (11–12), 879–885. <https://doi.org/10.1002/ejic.201901168>.
- (12) Caballero, A.; Despagnet-Ayoub, E.; Díaz-Requejo, M. M.; Díaz-Rodríguez, A.; González-Núñez, M. E.; Mello, R.; Muñoz, B. K.; Ojo, W.-S.; Asensio, G.; Etienne, M.; Pérez, P. J. Silver-Catalyzed C–C Bond Formation Between Methane and Ethyl

- Diazoacetate in Supercritical CO₂. *Science* **2011**, 332 (6031), 835–838. <https://doi.org/10.1126/science.1204131>.
- (13) Gava, R.; Olmos, A.; Noverges, B.; Varea, T.; Álvarez, E.; Belderrain, T. R.; Caballero, A.; Asensio, G.; Pérez, P. J. Discovering Copper for Methane C–H Bond Functionalization. *ACS Catal.* **2015**, 5 (6), 3726–3730. <https://doi.org/10.1021/acscatal.5b00718>.
- (14) Wilson, M. E.; Whitesides, G. M. Conversion of a Protein to a Homogeneous Asymmetric Hydrogenation Catalyst by Site-Specific Modification with a Diphosphinerhodium(I) Moiety. *J. Am. Chem. Soc.* **1978**, 100 (1), 306–307. <https://doi.org/10.1021/ja00469a064>.
- (15) Reetz, M. T. Biocatalysis in Organic Chemistry and Biotechnology: Past, Present, and Future. *J. Am. Chem. Soc.* **2013**, 135 (34), 12480–12496. <https://doi.org/10.1021/ja405051f>.
- (16) Schwizer, F.; Okamoto, Y.; Heinisch, T.; Gu, Y.; Pellizzoni, M. M.; Lebrun, V.; Reuter, R.; Köhler, V.; Lewis, J. C.; Ward, T. R. Artificial Metalloenzymes: Reaction Scope and Optimization Strategies. *Chem. Rev.* **2018**, 118 (1), 142–231. <https://doi.org/10.1021/acs.chemrev.7b00014>.
- (17) Chen, K.; Arnold, F. H. Engineering New Catalytic Activities in Enzymes. *Nat. Catal.* **2020**, 3 (3), 203–213. <https://doi.org/10.1038/s41929-019-0385-5>.
- (18) Hönig, M.; Sondermann, P.; Turner, N. J.; Carreira, E. M. Enantioselective Chemo- and Biocatalysis: Partners in Retrosynthesis. *Angew. Chem. Int. Ed.* **2017**, 56 (31), 8942–8973. <https://doi.org/10.1002/anie.201612462>.
- (19) Jeschek, M.; Panke, S.; Ward, T. R. Artificial Metalloenzymes on the Verge of New-to-Nature Metabolism. *Trends Biotechnol.* **2018**, 36 (1), 60–72. <https://doi.org/10.1016/j.tibtech.2017.10.003>.
- (20) de Souza, R. O. M. A.; Miranda, L. S. M.; Bornscheuer, U. T. A Retrosynthesis Approach for Biocatalysis in Organic Synthesis. *Chem-Eur J.* **2017**, 23 (50), 12040–12063. <https://doi.org/10.1002/chem.201702235>.
- (21) Perez-Rizquez, C.; Rodriguez-Otero, A.; Palomo, J. M. Combining Enzymes and Organometallic Complexes: Novel Artificial Metalloenzymes and Hybrid Systems for C–H Activation Chemistry. *Org. Biomol. Chem.* **2019**, 17 (30), 7114–7123. <https://doi.org/10.1039/C9OB01091B>.
- (22) Bennett, M. R.; Shepherd, S. A.; Cronin, V. A.; Micklefield, J. Recent Advances in Methyltransferase Biocatalysis. *Curr. Opin. Chem. Biol.* **2017**, 37, 97–106. <https://doi.org/10.1016/j.cbpa.2017.01.020>.
- (23) Yokoyama, K.; Lilla, E. A. C–C Bond Forming Radical SAM Enzymes Involved in the Construction of Carbon Skeletons of Cofactors and Natural Products. *Nat. Prod. Rep.* **2018**, 35 (7), 660–694. <https://doi.org/10.1039/C8NP00006A>.

- (24) Lewis, J. C.; Coelho, P. S.; Arnold, F. H. Enzymatic Functionalization of Carbon–Hydrogen Bonds. *Chem. Soc. Rev.* **2011**, *40* (4), 2003–2021. <https://doi.org/10.1039/C0CS00067A>.
- (25) Upp, D. M.; Lewis, J. C. Selective C–H Bond Functionalization Using Repurposed or Artificial Metalloenzymes. *Curr. Opin. Chem. Biol.* **2017**, *37*, 48–55. <https://doi.org/10.1016/j.cbpa.2016.12.027>.
- (26) Zhang, R. K.; Huang, X.; Arnold, F. H. Selective CH Bond Functionalization with Engineered Heme Proteins: New Tools to Generate Complexity. *Curr. Opin. Chem. Biol.* **2019**, *49*, 67–75. <https://doi.org/10.1016/j.cbpa.2018.10.004>.
- (27) Zetsche, L. E.; Narayan, A. R. H. Broadening the Scope of Biocatalytic C–C Bond Formation. *Nat Rev Chem* **2020**, *4* (7), 334–346. <https://doi.org/10.1038/s41570-020-0191-2>.
- (28) Ren, X.; Fasan, R. Engineered and Artificial Metalloenzymes for Selective C–H Functionalization. *Curr. Opin. Green Sustain. Chem.* **2021**, 100494. <https://doi.org/10.1016/j.cogsc.2021.100494>.
- (29) Zhang, R. K.; Chen, K.; Huang, X.; Wohlschlager, L.; Renata, H.; Arnold, F. H. Enzymatic Assembly of Carbon–Carbon Bonds via Iron-Catalysed Sp³ C–H Functionalization. *Nature* **2019**, *565* (7737), 67–72. <https://doi.org/10.1038/s41586-018-0808-5>.
- (30) Zhang, J.; Huang, X.; Zhang, R. K.; Arnold, F. H. Enantiodivergent α -Amino C–H Fluoroalkylation Catalyzed by Engineered Cytochrome P450s. *J. Am. Chem. Soc.* **2019**, *141* (25), 9798–9802. <https://doi.org/10.1021/jacs.9b04344>.
- (31) Dydio, P.; Key, H. M.; Nazarenko, A.; Rha, J. Y.-E.; Seyedkazemi, V.; Clark, D. S.; Hartwig, J. F. An Artificial Metalloenzyme with the Kinetics of Native Enzymes. *Science* **2016**, *354* (6308), 102–106. <https://doi.org/10.1126/science.aah4427>.
- (32) Key, H. M.; Dydio, P.; Clark, D. S.; Hartwig, J. F. Abiological Catalysis by Artificial Haem Proteins Containing Noble Metals in Place of Iron. *Nature* **2016**, *534* (7608), 534–537. <https://doi.org/10.1038/nature17968>.
- (33) Gu, Y.; Natoli, S. N.; Liu, Z.; Clark, D. S.; Hartwig, J. F. Site-Selective Functionalization of (Sp³)C–H Bonds Catalyzed by Artificial Metalloenzymes Containing an Iridium-Porphyrin Cofactor. *Angew. Chem. Int. Ed.* **2019**, *58* (39), 13954–13960. <https://doi.org/10.1002/anie.201907460>.
- (34) Liu, Z.; Huang, J.; Gu, Y.; Clark, D. S.; Mukhopadhyay, A.; Keasling, J. D.; Hartwig, J. F. Assembly and Evolution of Artificial Metalloenzymes within *E. Coli* Nissle 1917 for Enantioselective and Site-Selective Functionalization of C–H and C=C Bonds. *J. Am. Chem. Soc.* **2022**, *144* (2), 883–890. <https://doi.org/10.1021/jacs.1c10975>.

- (35) Sreenilayam, G.; Moore, E. J.; Steck, V.; Fasan, R. Metal Substitution Modulates the Reactivity and Extends the Reaction Scope of Myoglobin Carbene Transfer Catalysts. *Adv. Synth. Catal.* **2017**, *359* (12), 2076–2089. <https://doi.org/10.1002/adsc.201700202>.
- (36) Vargas, D. A.; Tinoco, A.; Tyagi, V.; Fasan, R. Myoglobin-Catalyzed C–H Functionalization of Unprotected Indoles. *Angew. Chem. Int. Ed.* **2018**, *57* (31), 9911–9915. <https://doi.org/10.1002/anie.201804779>.
- (37) Hyster, T. K.; Knörr, L.; Ward, T. R.; Rovis, T. Biotinylated Rh(III) Complexes in Engineered Streptavidin for Accelerated Asymmetric C–H Activation. *Science* **2012**, *338* (6106), 500–503. <https://doi.org/10.1126/science.1226132>.
- (38) Hassan, I. S.; Ta, A. N.; Danneman, M. W.; Semakul, N.; Burns, M.; Basch, C. H.; Dippon, V. N.; McNaughton, B. R.; Rovis, T. Asymmetric δ -Lactam Synthesis with a Monomeric Streptavidin Artificial Metalloenzyme. *J. Am. Chem. Soc.* **2019**, *141* (12), 4815–4819. <https://doi.org/10.1021/jacs.9b01596>.
- (39) Facchetti, G.; Rimoldi, I. 8-Amino-5,6,7,8-Tetrahydroquinoline in Iridium(III) Biotinylated Cp* Complex as Artificial Imine Reductase. *New J. Chem.* **2018**, *42* (23), 18773–18776. <https://doi.org/10.1039/C8NJ04558E>.
- (40) Reetz, M. T. Directed Evolution of Artificial Metalloenzymes: A Universal Means to Tune the Selectivity of Transition Metal Catalysts? *Acc. Chem. Res.* **2019**, *52* (2), 336–344. <https://doi.org/10.1021/acs.accounts.8b00582>.
- (41) Lewis, J. C. Beyond the Second Coordination Sphere: Engineering Dirhodium Artificial Metalloenzymes To Enable Protein Control of Transition Metal Catalysis. *Acc. Chem. Res.* **2019**, *52* (3), 576–584. <https://doi.org/10.1021/acs.accounts.8b00625>.
- (42) Lin, C.-C.; Lin, C.-W.; Chan, A. S. C. Catalytic Hydrogenation of Itaconic Acid in a Biotinylated Pyrphos–Rhodium(I) System in a Protein Cavity. *Tetrahedron: Asymmetry* **1999**, *10* (10), 1887–1893. [https://doi.org/10.1016/S0957-4166\(99\)00193-7](https://doi.org/10.1016/S0957-4166(99)00193-7).
- (43) Liang, A. D.; Serrano-Plana, J.; Peterson, R. L.; Ward, T. R. Artificial Metalloenzymes Based on the Biotin–Streptavidin Technology: Enzymatic Cascades and Directed Evolution. *Acc. Chem. Res.* **2019**, *52* (3), 585–595. <https://doi.org/10.1021/acs.accounts.8b00618>.
- (44) Roy, A.; Vaughn, M. D.; Tomlin, J.; Booher, G. J.; Kodis, G.; Simmons, C. R.; Allen, J. P.; Ghirlanda, G. Enhanced Photocatalytic Hydrogen Production by Hybrid Streptavidin–Diiron Catalysts. *Chem-Eur J.* **2020**, *26* (28), 6240–6246. <https://doi.org/10.1002/chem.202000204>.
- (45) Santi, N.; Morrill, L. C.; Luk, L. Y. P. Streptavidin-Hosted Organocatalytic Aldol Addition. *Molecules* **2020**, *25* (10), 2457. <https://doi.org/10.3390/molecules25102457>.

- (46) Vornholt, T.; Christoffel, F.; Pellizzoni, M. M.; Panke, S.; Ward, T. R.; Jeschek, M. Systematic Engineering of Artificial Metalloenzymes for New-to-Nature Reactions. *Sci. Adv.* **2021**, *7* (4), eabe4208. <https://doi.org/10.1126/sciadv.abe4208>.
- (47) Qin, Y.; Cui, C.; Jäkle, F. Tris(1-Pyrazolyl)Borate (Scorpionate) Functionalized Polymers as Scaffolds for Metallopolymers. *Macromolecules* **2008**, *41* (9), 2972–2974. <https://doi.org/10.1021/ma800310v>.
- (48) Zagermann, J.; Kuchta, M. C.; Merz, K.; Metzler-Nolte, N. Para-Bromophenyl[Tris(Pyrazolyl)]Borate Complexes of Group 1 Metals, Thallium and Magnesium: Synthesis and Characterization of Transfer Agents for “Third-Generation” Tp Ligands. *Eur. J. Inorg. Chem.* **2009**, *2009* (35), 5407–5412. <https://doi.org/10.1002/ejic.200900707>.
- (49) Nakamizu, A.; Kasai, T.; Nakazawa, J.; Hikichi, S. Immobilization of a Boron Center-Functionalized Scorpionate Ligand on Mesoporous Silica Supports for Heterogeneous Tp-Based Catalysts. *ACS Omega* **2017**, *2* (3), 1025–1030. <https://doi.org/10.1021/acsomega.7b00022>.
- (50) Desrochers, P. J.; Besel, B. M.; Corken, A. L.; Evanov, J. R.; Hamilton, A. L.; Nutt, D. L.; Tarkka, R. M. Immobilized Boron-Centered Heteroscorpionates: Heterocycle Metathesis and Coordination Chemistry. *Inorg. Chem.* **2011**, *50* (5), 1931–1941. <https://doi.org/10.1021/ic102392x>.
- (51) Soares da Costa, T. P.; Tieu, W.; Yap, M. Y.; Zvarec, O.; Bell, J. M.; Turnidge, J. D.; Wallace, J. C.; Booker, G. W.; Wilce, M. C. J.; Abell, A. D.; Polyak, S. W. Biotin Analogues with Antibacterial Activity Are Potent Inhibitors of Biotin Protein Ligase. *ACS Med. Chem. Lett.* **2012**, *3* (6), 509–514. <https://doi.org/10.1021/ml300106p>.
- (52) Skander, M.; Humbert, N.; Collot, J.; Gradinaru, J.; Klein, G.; Loosli, A.; Sauser, J.; Zocchi, A.; Gilardoni, F.; Ward, T. R. Artificial Metalloenzymes: (Strept)Avidin as Host for Enantioselective Hydrogenation by Achiral Biotinylated Rhodium–Diphosphine Complexes. *J. Am. Chem. Soc.* **2004**, *126* (44), 14411–14418. <https://doi.org/10.1021/ja0476718>.
- (53) Wang, Z.-X. An Exact Mathematical Expression for Describing Competitive Binding of Two Different Ligands to a Protein Molecule. *FEBS Lett.* **1995**, *360* (2), 111–114. [https://doi.org/10.1016/0014-5793\(95\)00062-E](https://doi.org/10.1016/0014-5793(95)00062-E).
- (54) Martín, C.; Belderraín, T. R.; Pérez, P. J. Rediscovering Copper-Based Catalysts for Intramolecular Carbon–Hydrogen Bond Functionalization by Carbene Insertion. *ACS Catal.* **2009**, *7* (22), 4777. <https://doi.org/10.1039/b911589g>.
- (55) Caruano, J.; Muccioli, G. G.; Robiette, R. Biologically Active γ -Lactams: Synthesis and Natural Sources. *Org. Biomol. Chem.* **2016**, *14* (43), 10134–10156. <https://doi.org/10.1039/C6OB01349J>.

- (56) Singh, G. S. Beta-Lactams in the New Millennium. Part-I: Monobactams and Carbapenems. *Mini Rev Med Chem* **2004**, *4* (1), 69–92. <https://doi.org/10.2174/1389557043487501>.
- (57) Singh, G. S. Beta-Lactams in the New Millennium. Part-II: Cephems, Oxacephems, Penams and Sulbactam. *Mini Rev Med Chem* **2004**, *4* (1), 93–109. <https://doi.org/10.2174/1389557043487547>.
- (58) Ren, X.; Chandgude, A. L.; Fasan, R. Highly Stereoselective Synthesis of Fused Cyclopropane- γ -Lactams via Biocatalytic Iron-Catalyzed Intramolecular Cyclopropanation. *ACS Catal.* **2020**, *10* (3), 2308–2313. <https://doi.org/10.1021/acscatal.9b05383>.
- (59) Mallin, H.; Hesticová, M.; Reuter, R.; Ward, T. R. Library Design and Screening Protocol for Artificial Metalloenzymes Based on the Biotin-Streptavidin Technology. *Nat Protoc* **2016**, *11* (5), 835–852. <https://doi.org/10.1038/nprot.2016.019>.
- (60) Li, H.; Ma, X.; Lei, M. Substituent Effects and Chemoselectivity of the Intramolecular Buchner Reaction of Diazoacetamide Derivatives Catalyzed by the Di-Rh(II)-Complex. *Dalton Trans.* **2016**, *45* (20), 8506–8512. <https://doi.org/10.1039/C6DT00268D>.
- (61) Wee, A. G. H.; Duncan, S. C.; Fan, G. Intramolecular Asymmetric C–H Insertion of N-Arylalkyl, N-Bis(Trimethylsilyl)Methyldiazoamides Mediated by Chiral Rhodium(II) Catalysts. Synthesis of (R)- β -Benzyl- γ -Aminobutyric Acid. *Tetrahedron: Asymmetry* **2006**, *17* (2), 297–307. <https://doi.org/10.1016/j.tetasy.2005.12.020>.
- (62) St. John, P. C.; Guan, Y.; Kim, Y.; Kim, S.; Paton, R. S. Prediction of Organic Homolytic Bond Dissociation Enthalpies at near Chemical Accuracy with Sub-Second Computational Cost. *Nat. Commun.* **2020**, *11* (1), 2328. <https://doi.org/10.1038/s41467-020-16201-z>.
- (63) Pedroni, J.; Boghi, M.; Saget, T.; Cramer, N. Access to β -Lactams by Enantioselective Palladium(0)-Catalyzed C(Sp³)-H Alkylation. *Angew. Chem. Int. Ed.* **2014**, *53* (34), 9064–9067. <https://doi.org/10.1002/anie.201405508>.
- (64) Dowling, C. M.; Leslie, D.; Chisholm, M. H.; Parkin, G. The Synthesis and Structural Characterization of the Sterically Demanding Tris (3,5-Di-*t*-Butylpyrazolyl) Hydroborato Ligand, [Tp Bu₂t]: A Highly Twisted, Propeller-Like, Ligand System. *Main Group Chemistry* **1995**, *1* (1), 29–52. <https://doi.org/10.1080/13583149512331338245>.
- (65) Rheingold, A. L.; Liable-Sands, L. M.; Incarvito, C. L.; Trofimenko, S. Novel Scorpionate Ligands Devoid of C–H Bonds: BpBr₃ and TpBr₃. *Journal of the Chemical Society, Dalton Transactions* **2002**, No. 11, 2297–2301. <https://doi.org/10.1039/b111568p>.
- (66) Caballero, A.; Díaz-Requejo, M. M.; Belderráin, T. R.; Nicasio, M. C.; Trofimenko, S.; Pérez, P. J. Highly Regioselective Functionalization of Aliphatic Carbon–Hydrogen Bonds

- with a Perbromohomoscorpionate Copper(I) Catalyst. *Journal of the American Chemical Society* **2003**, *125* (6), 1446–1447. <https://doi.org/10.1021/ja0291484>.
- (67) Caballero, A.; Díaz-Requejo, M. M.; Fructos, M. R.; Urbano, J.; Pérez, P. J. Modern Applications of Trispyrazolylborate Ligands in Coinage Metal Catalysis. In *Ligand Design in Metal Chemistry: Reactivity and Catalysis*; Stradiotto, M., Lundgren, R. J., Eds.; John Wiley & Sons, Ltd: Chichester, UK, 2016; pp 308–329. <https://doi.org/10.1002/9781118839621.ch11>.
- (68) Biagini, P.; Calderazzo, F.; Marchetti, F.; Romano, A. M.; Spera, S. Synthesis and Structural Characterization of Sterically Crowded Hydridotris(Pyrazolyl)Borato Complexes: Unusual Double 1,2-Borotropic Shift at a Titanium Centre. *Journal of Organometallic Chemistry* **2006**, *691* (20), 4172–4180. <https://doi.org/10.1016/j.jorganchem.2006.06.026>.
- (69) Jurrus, E.; Engel, D.; Star, K.; Monson, K.; Brandi, J.; Felberg, L. E.; Brookes, D. H.; Wilson, L.; Chen, J.; Liles, K.; Chun, M.; Li, P.; Gohara, D. W.; Dolinsky, T.; Konecny, R.; Koes, D. R.; Nielsen, J. E.; Head-Gordon, T.; Geng, W.; Krasny, R.; Wei, G.-W.; Holst, M. J.; McCammon, J. A.; Baker, N. A. Improvements to the APBS Biomolecular Solvation Software Suite. *Protein Science* **2018**, *27* (1), 112–128. <https://doi.org/10.1002/pro.3280>.
- (70) M. J. Frisch, G. W. Trucks, H. B. Schlegel, G. E. Scuseria,; M. A. Robb, J. R. Cheeseman, G. Scalmani, V. Barone, G. A. Petersson, H. Nakatsuji, X. Li, M. Caricato,; A. Marenich, J. Bloino, B. G. Janesko, R. Gomperts, B. Mennucci, H. P. Hratchian, J. V. Ortiz,; A. F. Izmaylov, J. L. Sonnenberg, D. Williams-Young, F. Ding, F. Lipparini, F. Egidi, J. Goings, B. Peng,; A. Petrone, T. Henderson, D. Ranasinghe, V. G. Zakrzewski, J. Gao, N. Rega, G. Zheng, W. Liang,; M. Hada, M. Ehara, K. Toyota, R. Fukuda, J. Hasegawa, M. Ishida, T. Nakajima, Y. Honda,; O. Kitao, H. Nakai, T. Vreven, K. Throssell, J. A. Montgomery, Jr., J. E. Peralta, F. Ogliaro,; M. Bearpark, J. J. Heyd, E. Brothers, K. N. Kudin, V. N. Staroverov, T. Keith, R. Kobayashi,; J. Normand, K. Raghavachari, A. Rendell, J. C. Burant, S. S. Iyengar, J. Tomasi, M. Cossi,; Millam, M. Klene, C. Adamo, R. Cammi, J. W. Ochterski, R. L. Martin, K. Morokuma, O. Farkas, J.; B. Foresman, and D. J. Fox. *Gaussian 09, Revision E.01*; Gaussian, Inc., Wallingford CT, 2016.
- (71) Nakagawa, Y.; Chanthamath, S.; Liang, Y.; Shibatomi, K.; Iwasa, S. Regio- and Enantioselective Intramolecular Amide Carbene Insertion into Primary C–H Bonds Using Ru(II)-Pheox Catalyst. *The Journal of Organic Chemistry* **2019**, *84* (5), 2607–2618. <https://doi.org/10.1021/acs.joc.8b03044>.
- (72) Luo, C.-H.; Wang, P.-L.; Chang, C.-C. Cascade Vinyl Radical Ipso-Cyclization Reactions and the Formation of α,β -Unsaturated- β -Aryl- γ -Lactams from N-Propargyl Benzamides. *J. Org. Chem.* **2021**, *86* (21), 15033–15044. <https://doi.org/10.1021/acs.joc.1c01717>.

- (73) Wee, A. G. H.; Duncan, S. C.; Fan, G. Intramolecular Asymmetric C–H Insertion of N-Arylalkyl, N-Bis(trimethylsilyl)methyl diazoamides Mediated by Chiral Rhodium(II) Catalysts. Synthesis of (R)- β -Benzyl- γ -Aminobutyric Acid. *Tetrahedron: Asymmetry* **2006**, *17* (2), 297–307. <https://doi.org/10.1016/j.tetasy.2005.12.020>.
- (74) Chen, Z.; Chen, Z.; Jiang, Y.; Hu, W. The Synthesis of Baclofen and GABOB via Rh(II) Catalyzed Intramolecular C–H Insertion of α -Diazoacetamides. *Tetrahedron* **2005**, *61* (6), 1579–1586. <https://doi.org/10.1016/j.tet.2004.11.077>.

5. Enantioselective Hydroxylation of Benzylic C(sp³)-H Bonds by an Artificial Iron Hydroxylase Based on the Biotin–Streptavidin Technology

Joan Serrano-Plana, Corentin Rumo, Johannes G. Rebelein, Ryan L. Peterson, Maxime Barnet, and Thomas R. Ward*

This work was published in the *Journal of the American Chemical Society*

J. Am. Chem. Soc. **2020**, *142*, 10617–10623.

5.1 Contributions to this Work

TRW supervised the project. JSP lead the project. CR contributed to the synthesis of the cofactor and the catalytic experiments. JGR solved the crystal structures. RLP contributed to the design of the study. MB contributed to the synthesis of the cofactor and the catalytic experiments.

5.2 Introduction

The selective functionalization of C–H bonds represents one of the frontiers in synthetic methodology.^{1–7} To address this challenge, homogeneous catalysis often relies on directing groups present on the substrate that coordinate to the metal center, thus allowing distinguishing between equally reactive C–H bonds.⁷ Enzymes have been optimized thanks to evolution to differentiate C–H bonds with exquisite selectivity: The active site around the cofactor is tailored to ensure proper orientation of the substrate. For the hydroxylation of inert C–H bonds, iron-containing enzymes and iron-based homogeneous catalysts occupy a place of choice. They are complementary in many respects. While the former operate under physiological conditions, homogeneous catalysts perform best at low temperature in organic solvents. The reactivity of homogeneous catalysts is often tuned via first-coordination sphere modifications, whereas enzymes rely on secondary sphere interactions. Iron metalloenzymes catalyze the C–H oxyfunctionalization of hydrocarbons via iron–oxygen species resulting from activation of O₂.^{8–17} The selective hydroxylation of C–H bonds using homogeneous catalysts has been achieved by designing structurally elaborated ligands that provide a tailored cavity around the metal center.^{18–33} To complement homogeneous catalysts and enzymes, artificial metalloenzymes (ArMs), that result from anchoring an abiotic cofactor within a macromolecular

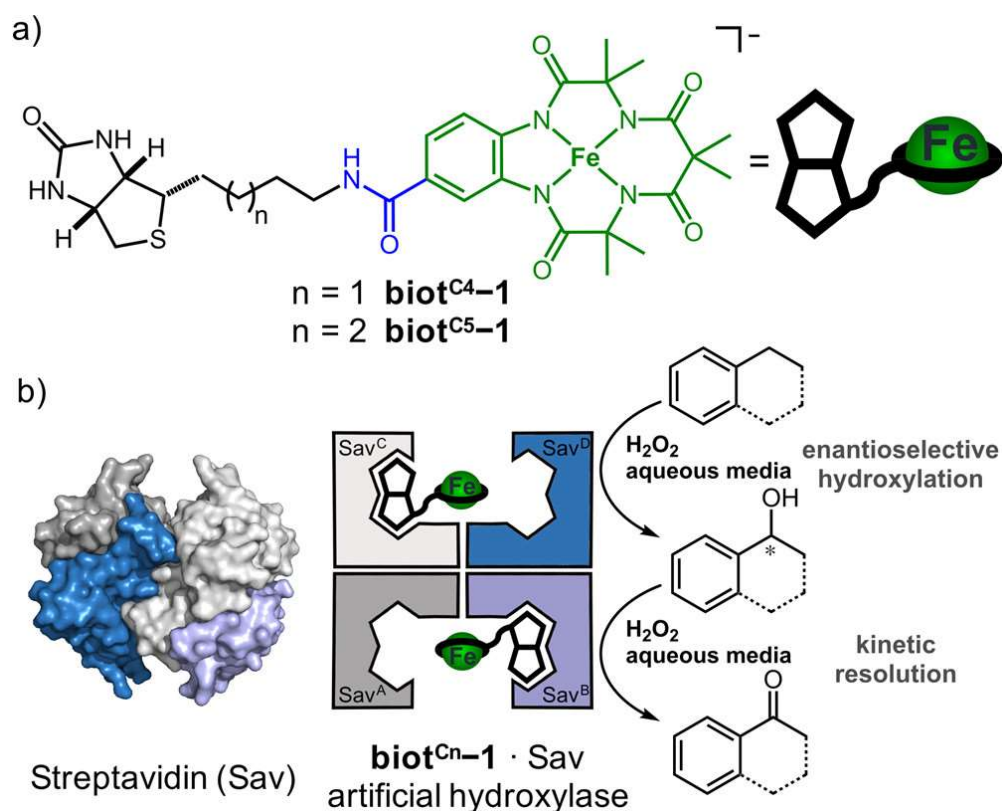
scaffold, have attracted increasing interest in the past years. The well-defined secondary coordination sphere around the cofactor provided by the protein offers fascinating perspectives to optimize both activity and selectivity of the ArMs.^{34–39} In this context several protein scaffolds have proven versatile.³⁴ These include carbonic anhydrase,⁴⁰ hemoproteins,^{41,42} proline oligopeptidase,⁴³ lactococcal multiresistance regulator,⁴⁴ four helix bundles,^{45,46} nitrobindin,⁴⁷ (strept)avidin,^{48–50} etc. In the context of asymmetric C–H hydroxylation, introduction of a Mn-porphycene cofactor within myoglobin afforded promising ArMs⁵¹ that complement evolved cytochrome P450 enzymes.^{52–54} Fe(TAML) complexes are a versatile family of iron complexes that typically contain a ferric center tightly bound to a tetraamido macrocyclic ligand.^{55,56} Their reactivity as peroxidase mimics has been extensively studied.^{55,57,58} Some Fe(TAML) complexes hydroxylate hydrocarbons in aqueous media using oxidants such as *t*BuOOH or *m*-CPBA^{56,59–61} or electrochemically.⁶² Thanks to their stability in water, we surmised that Fe(TAML) complexes may allow assembly of an iron-based artificial hydroxylase using the biotin–streptavidin technology. The secondary coordination sphere provided by streptavidin (Sav) may enable enantioselective hydroxylation and minimize the formation of less reactive diiron dimeric species.

5.3 Results and Discussion

Initial Ligand Design and Reactivity Tests. Sav is a homotetrameric protein that displays exceptional affinity for biotinylated probes (K_d 10–14 M) and maintains its function and quaternary structure in the presence of various chaotropic agents (pH, temperature, cosolvent tolerance, etc.).^{48,50,63} To ensure localization of the TAML cofactor within Sav, we synthesized a complex bearing a biotin anchor, **biot**^{C5}–**1**. The anchor was designed to bind to the Fe-TAML moiety through an “inverted” amide bond to the aromatic ring (Scheme 1a) to increase the electron-withdrawing effect, which has been shown to be beneficial for the reactivity of Fe-TAML complexes.⁶⁴

Initial reactivity tests were performed with ethylbenzene (PhEt, BDE_{C–H} = 87 kcal/mol) using 2 equivalents of H₂O₂ in phosphate buffer (KPB) at pH 8.2 and 40% acetone for 3 h.^{61,65} Under these conditions, **biot**^{C5}–**1**·Sav WT afforded (*rac*)-1-phenylethanol ((*rac*)-PhEtOH) and acetophenone (total turnover number, TTON,⁶⁶ = 23). Both activity and selectivity of **biot**^{C5}–**1**·Sav WT were comparable to the free cofactor **biot**^{C5}–**1** (TTON = 21, (*rac*)-PhEtOH). Next, we screened a Sav library that included mutations at positions Sav S112X and/or Sav K121X (Scheme 2 and Table S4). The TTON and enantioselectivity remained moderate (up to 16% ee (*R*)-PhEtOH and TTON = 29). We hypothesized that the moderate influence of the

Scheme 1. Artificial C–H Hydroxylase Based on Biotin– Streptavidin: (a) Structure of Cofactors **biot**^{C4–1} and **biot**^{C5–1}; (b) Representation of the ArM Resulting from Anchoring **biot**^{Cn–1} in Streptavidin

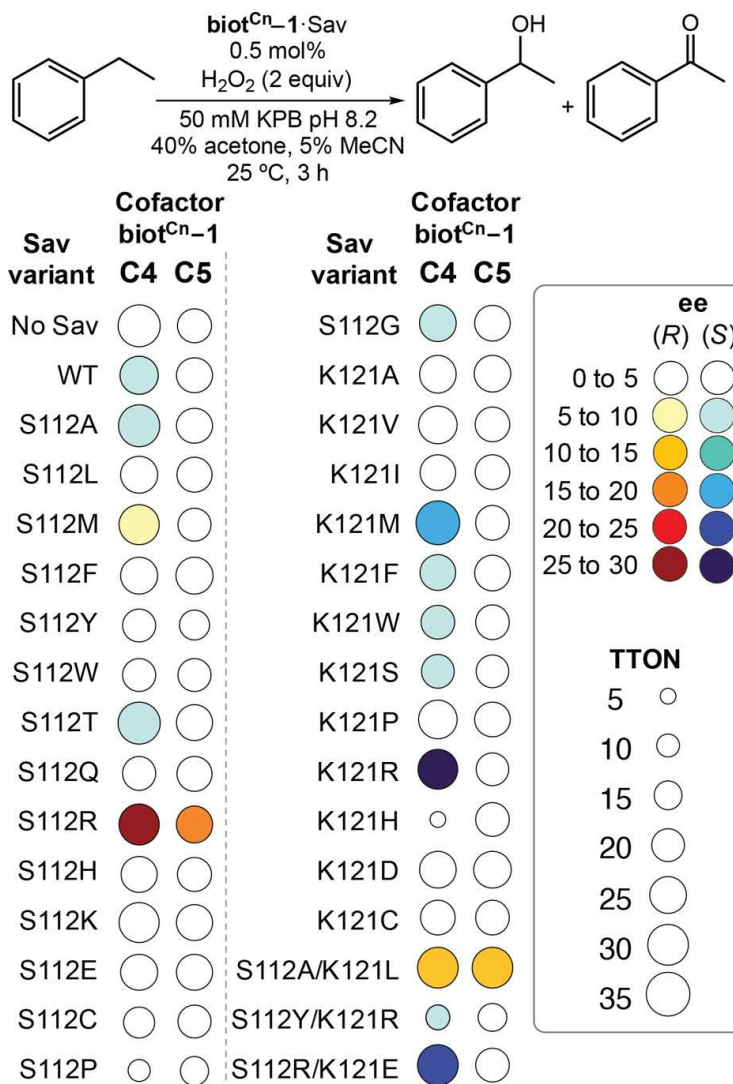


^aTo increase the electron-withdrawing property of the ligand, a biotin amine was coupled to Fe-TAML (green) bearing a carboxylic acid to afford an “inverted” amide (blue).

host protein on the catalytic performance may be due to the poor localization of the FeTAML within the biotin-binding vestibule. We surmised that a shorter biotin Cⁿ-linker may increase the influence of Sav on the catalytic performance by positioning the metal center deeper within the binding pocket. We prepared **biot**^{C4–1} and evaluated its performance (Schemes 1, 2 and Table S4).

Shortening the Cⁿ-linker positively affects the selectivity: **biot**^{C4–1}·Sav WT affords 6% ee (*R*)-PhEtOH. Screening the above Sav library with **biot**^{C4–1} reveals that close-lying amino acids influence the ee: **biot**^{C4–1}·Sav S112R yields 28% ee (*R*)-PhEtOH (TTON = 28), and **biot**^{C4–1}·Sav S112R/K121E affords 24% ee (*S*)-PhEtOH (TTON = 29). Intrigued by these findings, the oxidation of PhEt by **biot**^{C4–1}·Sav S112R was monitored. Two consecutive oxidation steps take place. Initially, hydroxylation of the benzylic position affords (*R*)-PhEtOH with ee >40% after a few TTONs (Figure S8). As the reaction progresses, the formation of acetophenone is observed along with a gradual erosion of the ee. This suggests that the alcohol oxidation is (partially) stereospecific: (*R*)-PhEtOH is oxidized preferentially to

Scheme 2. Fingerprint Summary of the Artificial Hydroxylase Optimization with PhEt



acetophenone. Indeed, kinetic resolution of (*rac*)PhEtOH by **biot^{C4-1}**-Sav S112R affords acetophenone (TTON = 38), leaving enantioenriched (*S*)-PhEt (20% ee after 3 h, $E = k_{(R)}/k_{(S)} = 3.4$, Figure S9).

In contrast, product analysis after PhEt oxidation by **biot^{C4-1}**-Sav (Sav: K121R or S112R/K121E) yielded ee of (*S*)PhEtOH (Scheme 2), the opposite enantiomer than **biot^{C4-1}**-Sav S112R. However, monitoring product formation over time reveals a similar reaction pathway for all three ArMs: The hydroxylation of PhEt yields preferentially (*R*)-PhEtOH, which is then oxidized faster to acetophenone (Figures S10–S11). This mechanistic pathway is reflected in an erosion of ee over time, eventually affording (*S*)-PhEtOH with both Sav K121R and Sav S112R/K121E. Indeed, the ee is highly variable, depending on conversion and mutant.

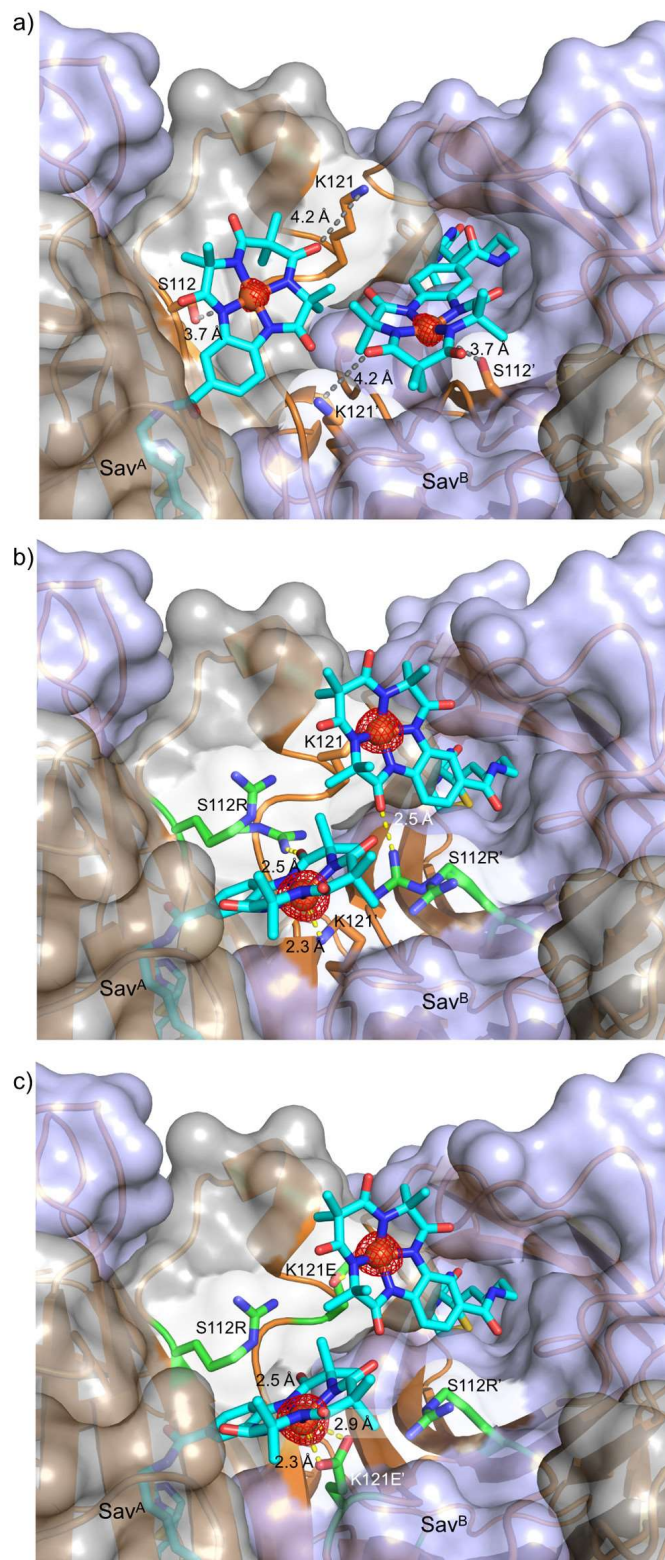


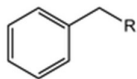
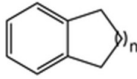
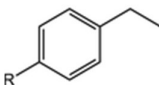
Figure 1. Crystallographic characterization of **biotC4-1-Sav** WT (a, PDB: 6Y2T), **biotC4-1-Sav S112R** (b, PDB: 6Y2M), and **biotC4-1-Sav S112R/K121E** (c, PDB: 6Y25). Sav is depicted as orange cartoon, and its surface representation in gray and mauve (for Sav^A and Sav^B monomers, respectively). The cofactor and relevant amino acids are depicted as sticks. The Fe atoms are depicted as spheres and surrounded by their anomalous electron density (red mesh at 5σ).

The reaction conditions to improve the performance of the hydroxylase were fine-tuned for **biot**^{C4}-1·Sav S112R. A large excess of H₂O₂ favors overoxidation and erosion of ee (Figure S13). The impact of Sav on the activity is also evident at different pH's: **biot**^{C4}-1·Sav S112R displays maximum TTON and enantioselectivity at 8.2 < pH < 8.8. Outside this window, the activity decreases markedly (Figure S14). The free cofactor **biot**^{C4}-1 has maximum activity at 6 < pH < 8 and is quenched at higher pH.

Structural Characterization. To scrutinize the differences in the second coordination sphere that influence the activity of the ArMs, we determined their structure by crystallography. Data sets were obtained for **biot**^{C4}-1·Sav and **biot**^{C5}-1·Sav (Sav = WT, S112R, and S112R/K121E, Tables S1 and S2). The structures reveal the following features: all six structures are nearly superimposable, reflected by a C_α-RMSD varying between 0.038 and 0.256 Å (Table S3). The electron density of the Fe-TAML moiety is defined for **biot**^{C4}-1; the Fe occupancy is 60% for Sav WT and 100% for Sav S112R and S112R/K121E (Figure 1). This contrasts with **biot**^{C5}-1, for which only the electron density of the biotin C5-linker is defined and modeled with 100% occupancy (Figures S5–S7). We tentatively trace this to the higher flexibility of the C5-linker, resulting in delocalization of the Fe-TAML moiety.

The localization of the Fe(TAML) moiety is affected by the residue at position 112 (Figures 1 and S2–S4). For **biot**^{C4}-1·Sav WT, the closest amino acids, are Sav^A S112 (3.7 Å) and Sav^B K121' (4.2 Å). They hardly interact with Fe(TAML), resulting in a reduced occupancy of Fe(TAML). The mutation Sav S112R forces the Fe(TAML) into a fixed conformation with 100%

Table 1. Benzylic C–H Oxidations Catalyzed by **biot**^{C4}-1·Sav S112R^a

Substrate	TTON	ee (%)	$\frac{[\text{alcohol}]}{[\text{ketone}]}$	Conversion (%) (alcohol yield (%)) ^c	
	R = CH ₃	57	32	3.2	11.5 (8.8)
	R = CH ₂ CH ₃	26	45	8.4	5.9 (5.3)
	R = (CH ₂) ₂ CH ₃	19	45	7.5	4.3 (3.8)
	R = C(CH ₃) ₂	0	-	-	-
	n = 2	316	65	5.7	60 (44.3)
	n = 1	205 ^b	>98	1.1	86.8 (34.3)
	n = 1	173 ^b	47	7.4	45.7 (40.2)
	n = 0	0	-	-	55.7 (24.7)
	R = OCH ₃	120	12	5.9	26.3 (22.5)
	R = Cl	20	14	3.8	4.1 (3.3)
	R = Br	9	18	>20	2.3 (2.3)

^aConditions: 25 μM **biot**^{C4}-1·Sav S112R (50 μM Fe), 20 mM substrate, 20 mM H₂O₂, 50 mM KPB pH 8.5, 35% acetone, 2.5% MeCN, 3 h at 25 °C. ^b10 mM substrate, 25 mM H₂O₂, to promote alcohol overoxidation which yields increased ee. ^cSee Table S6 for more details.

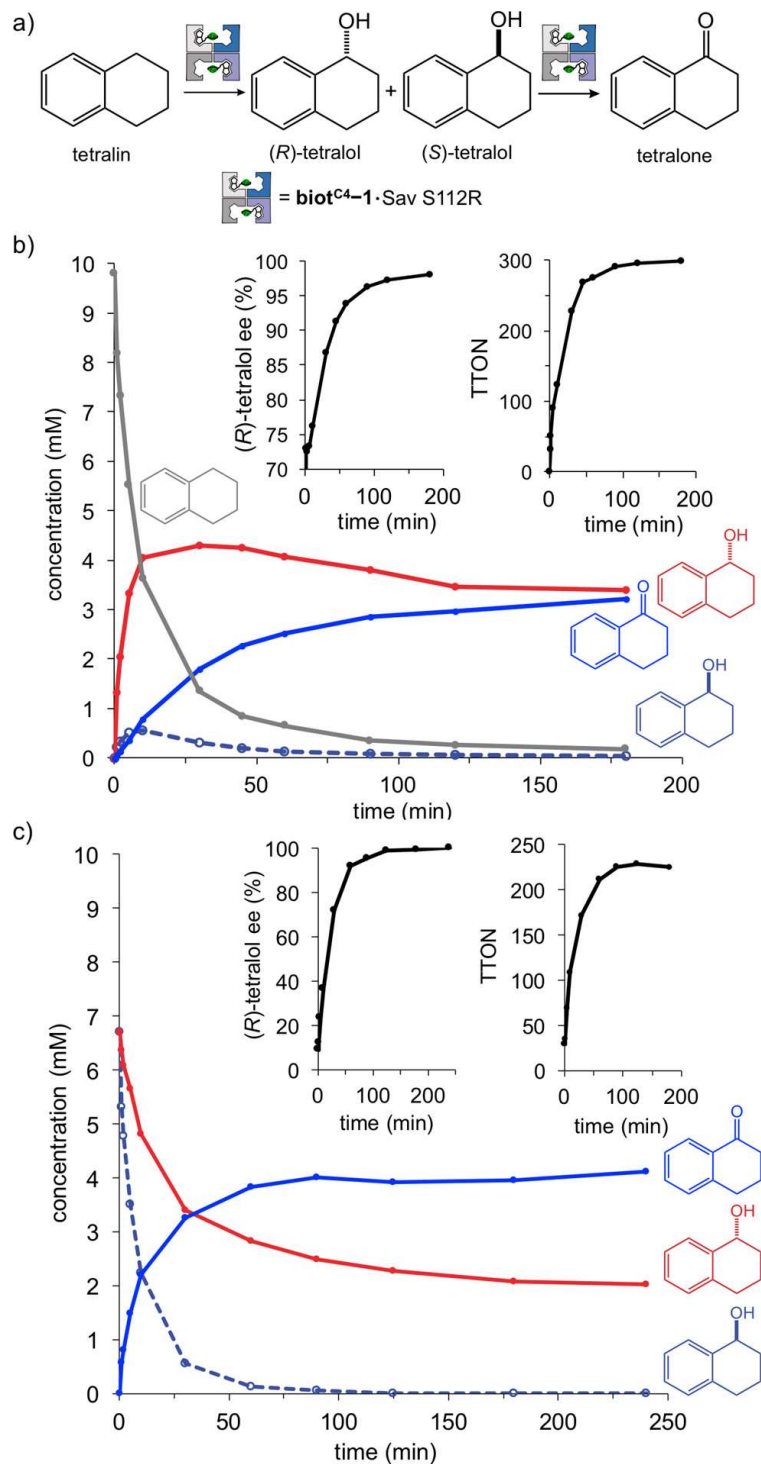
occupancy, placing the arginine within H-bonding distance to the C=O of the Fe(TAML) (2.5 Å, in one of two conformations, Figure 1b). This alternative position of Fe(TAML) allows Sav^B K121' to coordinate to Fe of **biot**^{C4}-1·Sav^A (2.3 Å, Figure 1b). To enable the coordination of Sav^B K121' to the Fe of **biot**^{C4}-1, the lysine side chain adopts a compact conformation with acute dihedral (χ) angles of 54.2°, 106.9°, 80.0°, and 41.2°. We hypothesize that both the precise localization of the Fe(TAML) and its interaction with either K121' or E121' through an η^2 -coordination (in **biot**^{C4}-1·Sav S112R/K121E, Fe···O 2.3 and 2.9 Å, Figure 1c) impact the catalysis outcome (product distribution and ee, Scheme 2).

Substrate Scope. The substrate scope for **biot**^{C4}-1·Sav S112R was expanded to substrates containing benzylic C(sp³)-H bonds (Table 1). Propylbenzene and butylbenzene afforded the corresponding (*R*)-alcohol in 45% ee (TON = 26 and 19, respectively). Electron-rich *p*-substituted ethylbenzenes afforded higher TTONs, highlighting the electrophilic character of the Fe(O) species (Figure S15). A kinetic isotope effect KIE = 9.2 was determined for the oxidation of PhEt/PhEt-*d*₁₀ by **biot**^{C4}-1·Sav S112R at 25 °C (Figure S16). This value compares well with the previously described KIE for Fe-TAML complexes and suggests that the rate-determining step of the reaction is the hydrogen abstraction.^{56,60,67,68}

The oxidation of indane and tetralin (BDE_{C-H} = 87 and 85.7 kcal/mol)⁶⁹ afforded high TTONs (TON = 205 and 316, respectively) and good ee in favor of the (*R*)-alcohol (47% and 65% ee, respectively, Table 1). Prompted by the good TTON and ee for tetralin, its oxidation by **biot**^{C4}-1·Sav S112R was scrutinized. Using 2.5 equivalents of H₂O₂, 73% ee of (*R*)-tetralol was determined at early stages (Scheme 3a). In contrast to PhEt oxidation, the ee increased with conversion, highlighting the preferential (over)oxidation of (*S*)-tetralol. After 3 h, >98% ee (*R*)-tetralol was obtained (TON = 300, Scheme 3b). Minimal overoxidation at the second benzylic position was also detected (Figure S17). Oxidation of (*rac*)-tetralol with **biot**^{C4}-1·Sav S112R yielded tetralone and >99% ee of (*R*)-tetralol (unreacted starting material) after ~120 min (Scheme 3c, $E = k_{(S)}/k_{(R)} = 2.7$, and Figure S18). Similarly, a TTON of 173 was obtained for indane oxidation (80% ee (*R*)-indanol, Figure S19). Thus, (*R*)-benzyl-alcohol derivatives are preferentially overoxidized, while the (*S*)-enantiomers of the cyclic derivatives (tetralol and indanol) are oxidized faster. This phenomenon can be attributed to the 1,3-allylic strain (Scheme S2).^{70,71}

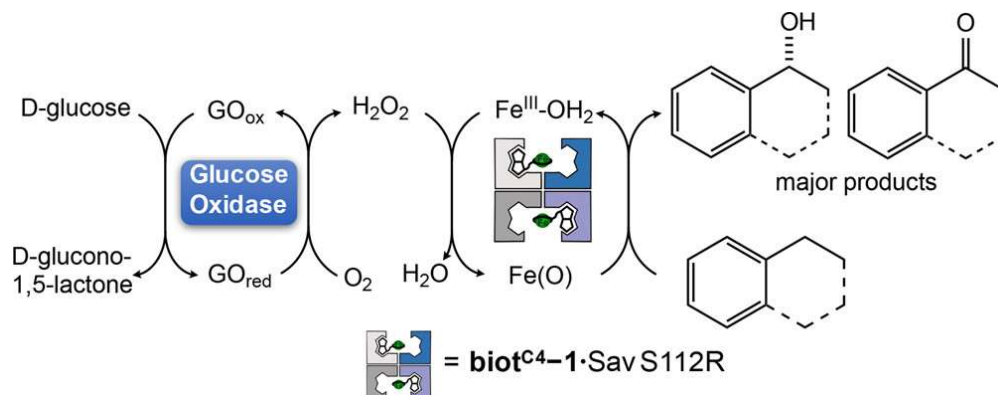
Lastly, we developed an enzymatic cascade with Glucose Oxidase (GO) to enable the in situ production of H₂O₂, using O₂ as oxidant and glucose as reductant (Scheme 4).⁷² To our delight, after combining **biot**^{C4}-1·Sav S112R and GO the oxidation reactions progressed in a similar way compared to the single batch addition of H₂O₂. A TTON of 50 was obtained for PhEt oxidation, with an initial ee of (*R*)-PhEtOH of 47%, which eroded to 37% after kinetic resolution.

Scheme 3. Enantioselective Hydroxylation of Tetralin and Kinetic Resolution of Tetralol by **biot**^{C4}-1-Sav S112R: (a) Consecutive Oxidation Scheme; (b) Time Course of Tetralin Oxidation (Inset: Kinetic Resolution Affords >98% ee (*R*)-Tetralol and TTON = 300); (c) Time Course of the Kinetic Resolution of *rac*-Tetralol by **biot**^{C4}-1-Sav S112R (Inset: Kinetic Resolution Yields >99% ee (*R*)-Tetralol (TTON = 220); See SI for Details)



For tetralin, a TTON of 170 was obtained, again observing the initial formation of (*R*)-tetralol in 64% ee and posterior kinetic resolution that upgraded it to up to 95%.

Scheme 4. Cascade with GO To Generate H₂O₂ *in Situ*, Enabling Hydroxylation Using O₂ as Oxidant.^a



^aSee SI.

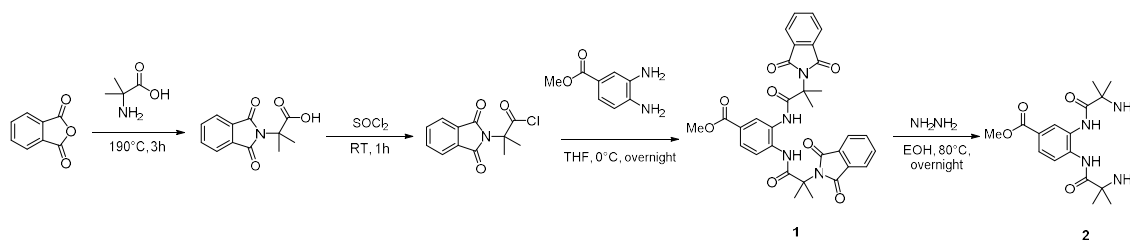
5.4 Conclusion

Catalysts derived from earth-abundant metals are gaining attention in homogeneous catalysis. The inherent lability of most such systems however limits their use in water. In contrast to polypyridinamine-derived catalysts,⁷³ and thanks to its remarkable stability and catalytic activity, the Fe(TAML) system proved amenable to the design and optimization of an artificial hydroxylase based on the biotin–streptavidin technology.

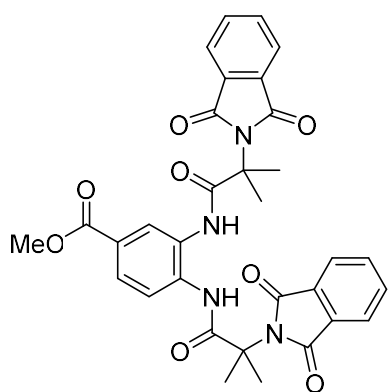
Chemogenetic optimization of the catalytic performance led to the identification of **biot^{C4}-1·Sav S112R** as our best hydroxylase for the oxidation of benzylic C–H bonds. With *in vivo* applications in mind, we have shown that the activity of the artificial hydroxylase is compatible with glucose oxidase, using O₂ as the terminal oxidant. Efforts at modulating the activity of the hydroxylase by finetuning the cofactors' structure, and expanding the substrate scope toward the oxidation of more complex molecules, are currently underway.

5.5 Supporting Information

5.5.1 Synthesis of the ligand

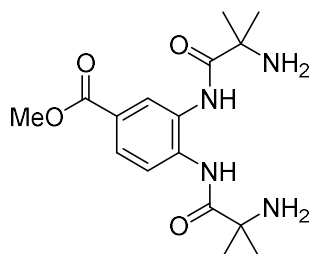


The synthetic steps described above were performed according to reported procedures.^{72,73}



1

^1H NMR (500 MHz, $\text{DMSO}-d_6$, 298 K) δ 9.66 (s, 1H), 9.44 (s, 1H), 8.02 (s, 1H), 7.86 – 7.80 (m, 5H), 7.80 – 7.75 (m, 3H), 7.72 (m, 2H), 3.84 (s, 3H), 1.76 (s, 6H), 1.68 (s, 6H). ^{13}C NMR (125 MHz, $\text{DMSO}-d_6$, 298 K) δ 172.4, 172.2, 168.8, 168.7, 165.9, 135.9, 135.0, 132.1, 132.0, 130.1, 126.8, 126.1, 126.0, 123.9, 123.4, 123.3, 61.6, 61.4, 52.6, 24.7, 24.7.



2

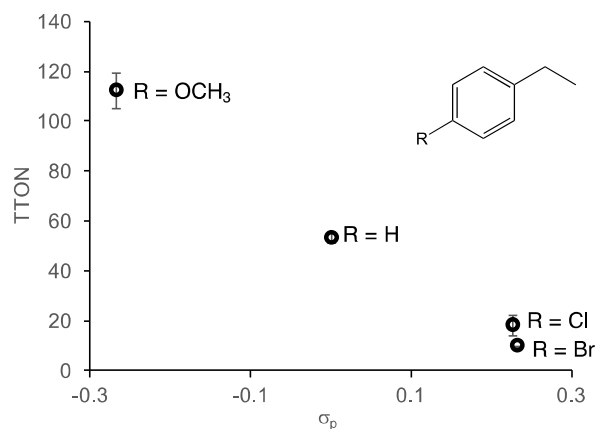
^1H NMR (500 MHz, CDCl_3 , 298 K) δ 10.09 (br, 1H), 9.80 (br, 1H), 8.11 (d, $J = 2.0$ Hz, 1H), 7.98 (d, $J = 8.5$ Hz, 1H), 7.87 (dd, $J = 8.5, 2.0$ Hz, 1H), 3.88 (s, 3H), 1.47 (s, 6H), 1.44 (s, 6H). ^{13}C NMR (125 MHz, CDCl_3 , 298 K) δ 176.9, 176.5, 166.4, 135.8, 128.5, 127.7, 126.5, 126.5, 126.5, 122.7, 55.6, 55.4, 53.4, 52.1, 29.2, 29.1.

5.5.2 Typical catalysis procedure

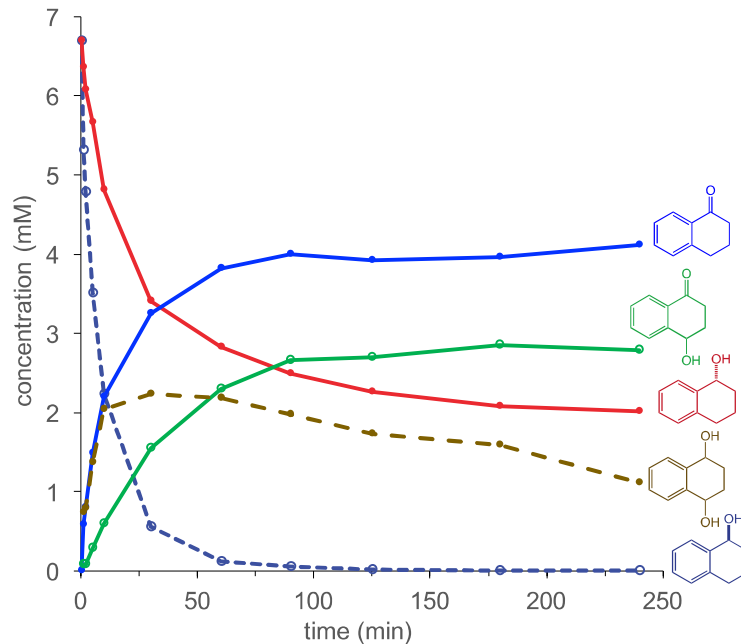
In a typical experiment, a glass vial (2 mL) was loaded with the buffer (potassium phosphate buffer, stock solution 0.2 M), streptavidin (stock solution of 0.4 mM in MQ water), the desired biotinylated cofactor (freshly prepared stock solution 1 M in MQ water), acetone (variable amount 0-50% V/V, final concentration), substrate (stock solution 400 mM in MeCN) and H₂O₂ (stock solution 200 mM in MQ water). MQ water was added to the reaction mixture prior to the H₂O₂ addition to adjust the final volume to 0.2 mL. The vial was sealed and the mixture was stirred in a thermoshaker (800 rpm) at the desired temperature for the given amount of time.

The reaction was quenched by adding HCl (15 μ L, 1 M stock solution). Then, biphenyl was added as internal standard and the products were extracted with EtOAc (2 x 400 μ L). The combined organic phases were dried over MgSO₄, filtered through a short cotton plug and subjected to analysis (typically by GC-FID).

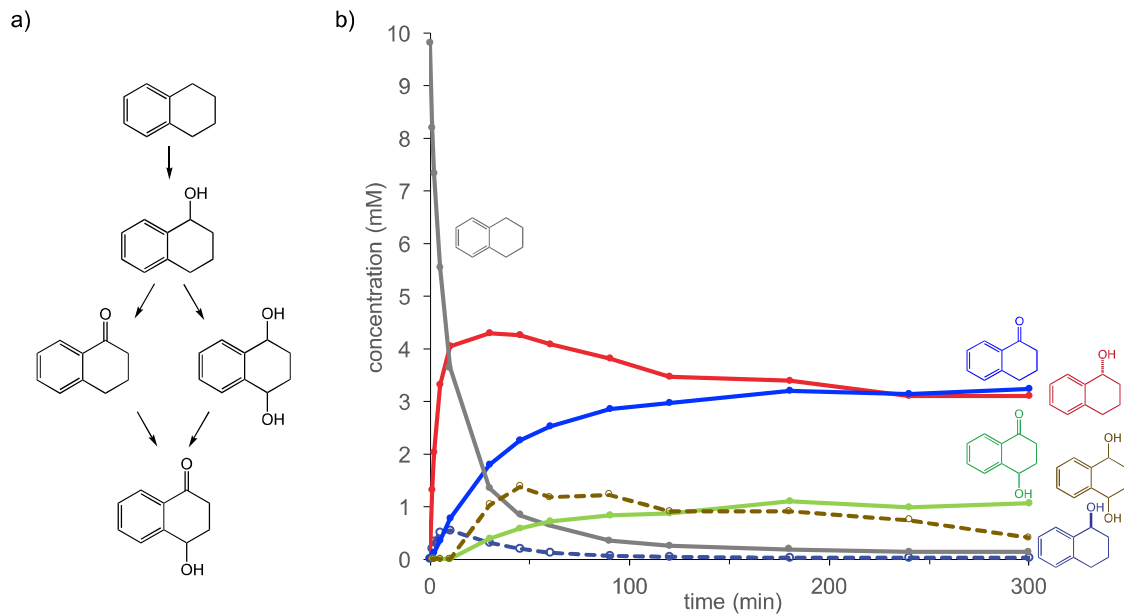
5.5.3 Supplementary plots



Oxidation of *para*-substituted ethylbenzenes by **biot^{C4}-1**-Sav S112R. Conditions: 50 μ M **biot^{C4}-1**, 25 μ M Sav S112R, 20 mM Substrate, 20 mM H₂O₂, 50 mM KPB pH 8.5, 35% acetone, 1.5 h, 25 °C. Figure S15 in the original SI.

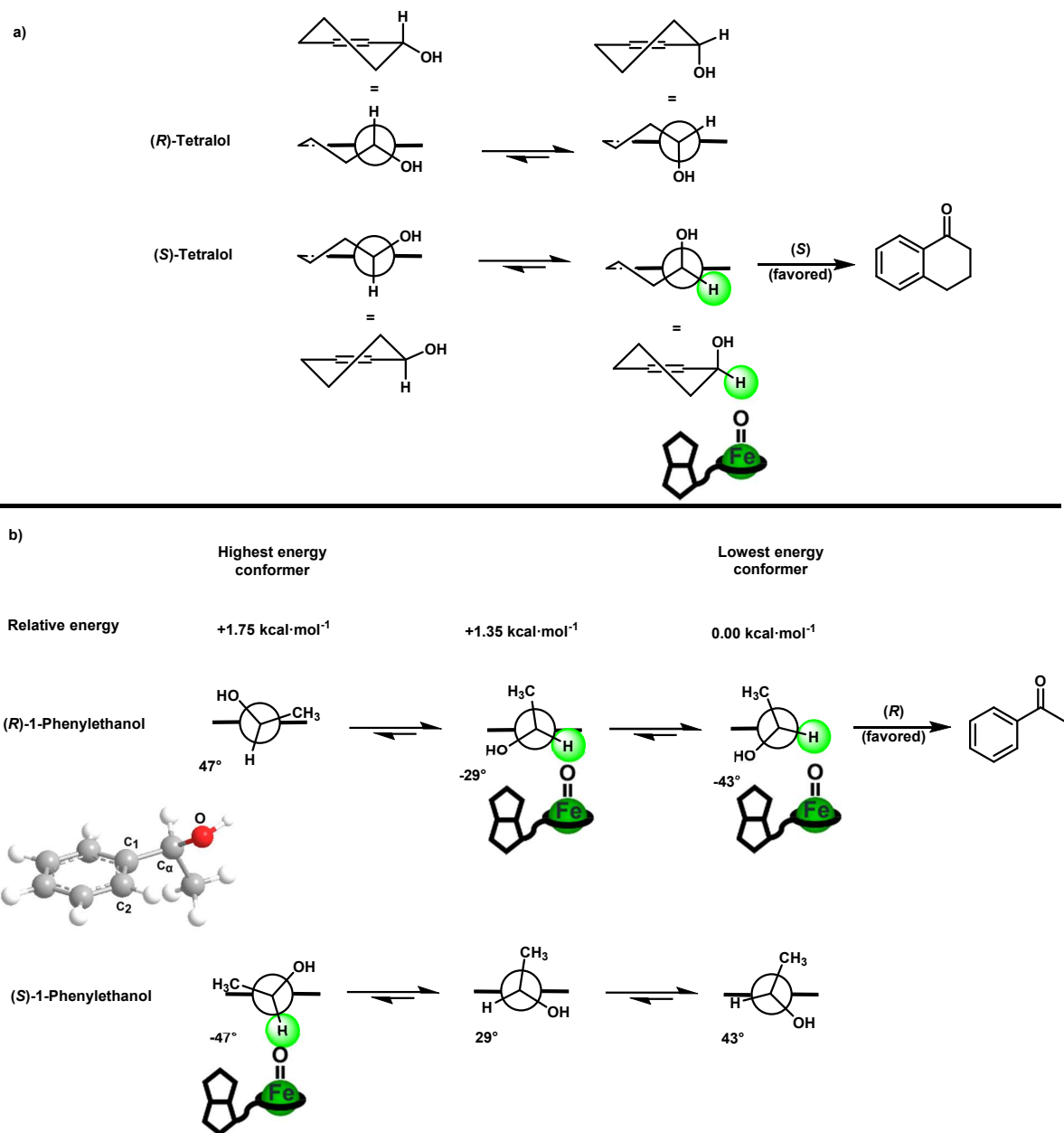


Time course monitoring of the kinetic resolution of (*rac*)-tetralol by **biot**^{C4}-1·Sav S112R. Conditions: 25 μ M **biot**^{C4}-1·Sav S112R, 14 mM (*rac*)-tetralol, 20 mM H₂O₂, 50 mM KPB pH 8.5, 35% acetone, 2.5% MeCN, 25 °C. red, (*R*)-tetralol; dashed dark blue line, (*S*)-tetralol; solid blue line, tetralone; dark green, 4-hydroxy-3,4-dihydronaphthalen-1(2H)-one; gold, 1,2,3,4-tetrahydronaphthalene-1,4-diol. Figure S17 in the original SI.



Monitoring of the tetralin oxidation by **biot**^{C4}-1·Sav S112R . a) Summary of the different oxidation pathways and products b) time course of tetralin oxidation by **biot**^{C4}-1·Sav S112R.

Conditions: 50 μM **biot**^{C4}-1, 25 μM Sav S112R, 10 mM tetralin, 25 mM H₂O₂, 50 mM KPB pH 8.5, 35% acetone, 2.5% MeCN, 25 °C. Figure S18 in the original SI.



Postulated kinetic resolution mechanism for the oxidation of a) tetralol and b) 1-phenylethanol by **biot**^{C4}-1•Sav S112R. For tetralol, the cyclohexene moiety enforces the C_(S)-H in a pseudo-equatorial conformation,^{74,75} which is readily abstracted by the Fe(O) moiety, tightly embedded in Sav S112R. For 1-phenylethanol however, the allylic 1,3-strain disfavors this conformation.⁷⁰ Instead, three minima have been computed on the corresponding potential energy surface for

the rotation along the C₁-C_α bond for 1-phenylethanol: the relative energies and C₂C₁-C_αO dihedral angle are reproduced from Katsumoto and coworkers.⁷¹ Assuming a similar positioning of both tetralol and 1-phenylethanol with respect to the Fe(O) moiety, the two lowest lying conformations of (*R*)-1-phenylethanol project the C_(*R*)-H towards the highly oxidizing Fe(O) moiety. In contrast, only the highest lying minimum of (*S*)-1-phenylethanol, presents its C_(*S*)-H towards the Fe(O) moiety. Accordingly, (*S*)-tetralol and (*R*)-1-phenylethanol are preferentially oxidized by **biot^{C4}-1•Sav S112R**. The green sphere highlights the H subject to abstraction. Scheme S2 in the original SI.

5.5.4 Oxidation of hydrocarbons: enzymatic cascade

In a typical experiment, a 2 mL glass vial was loaded with the buffer (potassium phosphate buffer, stock solution 0.2 M), streptavidin (stock solution of 0.4 mM in MQ water), **biot^{C4}-1** (freshly prepared stock solution 1 M in MQ water), acetone (typically 35% V/V final concentration), substrate (stock solution 400 mM in MeCN) and D-glucose (stock solution 400 mM in MQ water, final concentration 20 mM). MQ water was added to the reaction mixture prior to adjust the final volume to 0.2 mL. Glucose oxidase (GO, 2.45 units/mL or 0.98 units/mL) was added. The vial was sealed and the mixture was stirred in a thermoshaker (800 rpm) at 25 °C for the desired amount of time (typically >20h). The reaction was quenched by adding HCl (15 μL, 1 M stock solution). Then, biphenyl was added as internal standard and the products were extracted with EtOAc (2 x 400μL). The combined organic phases were dried over MgSO₄, filtered through a short cotton plug and submitted to analysis (typically by GC-FID). For ethylbenzene oxidation, 50 TTON were obtained. At early stages of the reaction, an ee of (*R*)-PhEtOH of 47% was obtained ([PhEtOH/acetophenone] = 11.4), and at higher conversions the ee eroded to 37% ([PhEtOH/acetophenone] = 3.2). For tetralin 170 TTON were obtained, again observing the initial formation of (*R*)-tetralol in 64% ee and posterior kinetic resolution that upgraded it to up to 95% ([tetralol]/[tetralone] = 2.8).

5.6 References

- (1) Hartwig, J. F.; Larsen, M. A., Undirected, Homogeneous C–H Bond Functionalization: Challenges and Opportunities. *ACS Cent. Sci.* **2016**, *2*, 281-292.
- (2) Bergman, R. G., C–H activation. *Nature* **2007**, *446*, 391-393.
- (3) Ye, B.; Zhao, J.; Zhao, K.; McKenna, J. M.; Toste, F. D., Chiral Diaryliodonium Phosphate Enables Light Driven Diastereoselective α -C(sp³)–H Acetalization. *J. Am. Chem. Soc.* **2018**, *140*, 8350-8356.
- (4) Hartwig, J. F., Evolution of C–H Bond Functionalization from Methane to Methodology. *J. Am. Chem. Soc.* **2016**, *138*, 2-24.
- (5) Wencel-Delord, J.; Glorius, F., C–H bond activation enables the rapid construction and late-stage diversification of functional molecules. *Nat. Chem.* **2013**, *5*, 369-375.
- (6) Labinger, J. A.; Bercaw, J. E., Understanding and exploiting C–H bond activation. *Nature* **2002**, *417*, 507-514.
- (7) Newton, C. G.; Wang, S.-G.; Oliveira, C. C.; Cramer, N., Catalytic Enantioselective Transformations Involving C–H Bond Cleavage by Transition-Metal Complexes. *Chem. Rev.* **2017**, *117*, 8908-8976.
- (8) Costas, M.; Mehn, M. P.; Jensen, M. P.; Que, L., Dioxygen Activation at Mononuclear Nonheme Iron Active Sites: Enzymes, Models, and Intermediates. *Chem. Rev.* **2004**, *104*, 939-986.
- (9) Lewis, J. C.; Coelho, P. S.; Arnold, F. H., Enzymatic functionalization of carbon–hydrogen bonds. *Chem. Soc. Rev.* **2011**, *40*, 2003-2021.
- (10) Ortiz de Montellano, P. R., Hydrocarbon Hydroxylation by Cytochrome P450 Enzymes. *Chem. Rev.* **2010**, *110*, 932-948.
- (11) Adam, W.; Lukacs, Z.; Harmsen, D.; Saha-Möller, C. R.; Schreier, P., Biocatalytic Asymmetric Hydroxylation of Hydrocarbons with the Topsoil-Microorganism *Bacillus megaterium*. *J. Org. Chem.* **2000**, *65*, 878-882.
- (12) Nam, W., Synthetic Mononuclear Nonheme Iron–Oxygen Intermediates. *Acc. Chem. Res.* **2015**, *48*, 2415-2423.
- (13) Jasniewski, A. J.; Que, L., Dioxygen Activation by Nonheme Diiron Enzymes: Diverse Dioxygen Adducts, High-Valent Intermediates, and Related Model Complexes. *Chem. Rev.* **2018**, *118*, 2554-2592.
- (14) Que, L.; Tolman, W. B., Biologically inspired oxidation catalysis. *Nature* **2008**, *455*, 333-340.
- (15) Bruijninx, P. C. A.; van Koten, G.; Klein Gebbink, R. J. M., Mononuclear non-heme iron enzymes with the 2-His-1-carboxylate facial triad: recent developments in enzymology and modeling studies. *Chem. Soc. Rev.* **2008**, *37*, 2716-2744.

- (16) Battistella, B.; Ray, K., O₂ and H₂O₂ activations at dinuclear Mn and Fe active sites. *Coord. Chem. Rev.* **2020**, *408*, 213176.
- (17) Ray, K.; Pfaff, F. F.; Wang, B.; Nam, W., Status of Reactive Non-Heme Metal–Oxygen Intermediates in Chemical and Enzymatic Reactions. *J. Am. Chem. Soc.* **2014**, *136*, 13942-13958.
- (18) Zheng, C.; You, S.-L., Recent development of direct asymmetric functionalization of inert C–H bonds. *RSC Adv.* **2014**, *4*, 6173-6214.
- (19) Milan, M.; Bietti, M.; Costas, M., Enantioselective aliphatic C–H bond oxidation catalyzed by bioinspired complexes. *Chem. Commun.* **2018**, *54*, 9559-9570.
- (20) Saint-Denis, T. G.; Zhu, R.-Y.; Chen, G.; Wu, Q.-F.; Yu, J.-Q., Enantioselective C(sp³)–H bond activation by chiral transition metal catalysts. *Science* **2018**, *359*, eaao4798.
- (21) White, M. C.; Zhao, J., Aliphatic C–H Oxidations for Late-Stage Functionalization. *J. Am. Chem. Soc.* **2018**, *140*, 13988-14009.
- (22) Shugrue, C. R.; Miller, S. J., Applications of Nonenzymatic Catalysts to the Alteration of Natural Products. *Chem. Rev.* **2017**, *117*, 11894-11951.
- (23) Groves, J. T.; Viski, P., Asymmetric hydroxylation by a chiral iron porphyrin. *J. Am. Chem. Soc.* **1989**, *111*, 8537-8538.
- (24) Frost, J. R.; Huber, S. M.; Breitenlechner, S.; Bannwarth, C.; Bach, T., Enantiotoposelective C-H Oxygenation Catalyzed by a Supramolecular Ruthenium Complex. *Angew. Chem. Int. Ed.* **2015**, *54*, 691-695.
- (25) Burg, F.; Gicquel, M.; Breitenlechner, S.; Pöthig, A.; Bach, T., Site- and Enantioselective C–H Oxygenation Catalyzed by a Chiral Manganese Porphyrin Complex with a Remote Binding Site. *Angew. Chem. Int. Ed.* **2018**, *57*, 2953-2957.
- (26) Murahashi, S.-I.; Noji, S.; Komiya, N., Catalytic Enantioselective Oxidation of Alkanes and Alkenes Using (Salen)Manganese Complexes Bearing a Chiral Binaphthyl Strapping Unit. *Adv. Synth. Catal.* **2004**, *346*, 195-198.
- (27) Srour, H.; Maux, P. L.; Simonneaux, G., Enantioselective Manganese-Porphyrin-Catalyzed Epoxidation and C–H Hydroxylation with Hydrogen Peroxide in Water/Methanol Solutions. *Inorg. Chem.* **2012**, *51*, 5850-5856.
- (28) Komiya, N.; Noji, S.; Murahashi, S.-I., Manganese catalyzed asymmetric oxidation of alkanes to optically active ketones bearing asymmetric center at the α -position. *Tetrahedron Lett.* **1998**, *39*, 7921-7924.
- (29) Milan, M.; Bietti, M.; Costas, M., Highly Enantioselective Oxidation of Nonactivated Aliphatic C–H Bonds with Hydrogen Peroxide Catalyzed by Manganese Complexes. *ACS Cent. Sci.* **2017**, *3*, 196-204.

- (30) Hamada, T.; Irie, R.; Mihara, J.; Hamachi, K.; Katsuki, T., Highly enantioselective benzylic hydroxylation with concave type of (salen)manganese(III) complex. *Tetrahedron* **1998**, *54*, 10017-10028.
- (31) Olivo, G.; Farinelli, G.; Barbieri, A.; Lanzalunga, O.; Di Stefano, S.; Costas, M., Supramolecular Recognition Allows Remote, Site-Selective C–H Oxidation of Methylenic Sites in Linear Amines. *Angew. Chem. Int. Ed.* **2017**, *56*, 16347-16351.
- (32) Gormisky, P. E.; White, M. C., Catalyst-Controlled Aliphatic C–H Oxidations with a Predictive Model for Site-Selectivity. *J. Am. Chem. Soc.* **2013**, *135*, 14052-14055.
- (33) Chen, M. S.; White, M. C., A Predictably Selective Aliphatic C–H Oxidation Reaction for Complex Molecule Synthesis. *Science* **2007**, *318*, 783-787.
- (34) Schwizer, F.; Okamoto, Y.; Heinisch, T.; Gu, Y.; Pellizzoni, M. M.; Lebrun, V.; Reuter, R.; Köhler, V.; Lewis, J. C.; Ward, T. R., Artificial Metalloenzymes: Reaction Scope and Optimization Strategies. *Chem. Rev.* **2018**, *118*, 142-231.
- (35) Pàmies, O.; Diéguez, M.; Bäckvall, J.-E., Artificial Metalloenzymes in Asymmetric Catalysis: Key Developments and Future Directions. *Adv. Synth. Catal.* **2015**, *357*, 1567-1586.
- (36) Upp, D. M.; Lewis, J. C., Selective C–H bond functionalization using repurposed or artificial metalloenzymes. *Curr. Opin. Chem. Biol.* **2017**, *37*, 48-55.
- (37) Perez-Rizquez, C.; Rodriguez-Otero, A.; Palomo, J. M., Combining enzymes and organometallic complexes: novel artificial metalloenzymes and hybrid systems for C–H activation chemistry. *Org. Biomol. Chem.* **2019**, *17*, 7114-7123.
- (38) Davis, H. J.; Ward, T. R., Artificial Metalloenzymes: Challenges and Opportunities. *ACS Cent. Sci.* **2019**, *5*, 1120-1136.
39. Lewis, J. C., Artificial Metalloenzymes and Metallopeptide Catalysts for Organic Synthesis. *ACS Catal.* **2013**, *3*, 2954-2975.
- (40) Monnard, F. W.; Nogueira, E. S.; Heinisch, T.; Schirmer, T.; Ward, T. R., Human carbonic anhydrase II as host protein for the creation of artificial metalloenzymes: the asymmetric transfer hydrogenation of imines. *Chem. Sci.* **2013**, *4*, 3269-3274.
- (41) Oohora, K.; Onoda, A.; Hayashi, T., Hemoproteins Reconstituted with Artificial Metal Complexes as Biohybrid Catalysts. *Acc. Chem. Res.* **2019**, *52*, 945-954.
- (42) Mirts, E. N.; Petrik, I. D.; Hosseinzadeh, P.; Nilges, M. J.; Lu, Y., A designed heme-[4Fe-4S] metalloenzyme catalyzes sulfite reduction like the native enzyme. *Science* **2018**, *361*, 1098-1101.
- (43) Lewis, J. C., Beyond the Second Coordination Sphere: Engineering Dirhodium Artificial Metalloenzymes To Enable Protein Control of Transition Metal Catalysis. *Acc. Chem. Res.* **2019**, *52*, 576-584.
- (44) Roelfes, G., LmrR: A Privileged Scaffold for Artificial Metalloenzymes. *Acc. Chem. Res.* **2019**, *52*, 545-556.

- (45) Chino, M.; Maglio, O.; Nastri, F.; Pavone, V.; DeGrado, W. F.; Lombardi, A., Artificial Diiron Enzymes with a De Novo Designed Four-Helix Bundle Structure. *Eur. J. Inorg. Chem.* **2015**, *2015*, 3371-3390.
- (46) Lombardi, A.; Pirro, F.; Maglio, O.; Chino, M.; DeGrado, W. F., De Novo Design of Four-Helix Bundle Metalloproteins: One Scaffold, Diverse Reactivities. *Acc. Chem. Res.* **2019**, *52*, 1148-1159.
- (47) Grimm, A. R.; Sauer, D. F.; Polen, T.; Zhu, L.; Hayashi, T.; Okuda, J.; Schwaneberg, U., A Whole Cell E. Coli Display Platform for Artificial Metalloenzymes: Poly(phenylacetylene) Production with a Rhodium–Nitrobindin Metalloprotein. *ACS Catal.* **2018**, *8*, 2611-2614.
- (48) Heinisch, T.; Ward, T. R., Artificial Metalloenzymes Based on the Biotin–Streptavidin Technology: Challenges and Opportunities. *Acc. Chem. Res.* **2016**, *49*, 1711-1721.
- (49) Liang, A. D.; Serrano-Plana, J.; Peterson, R. L.; Ward, T. R., Artificial Metalloenzymes Based on the Biotin–Streptavidin Technology: Enzymatic Cascades and Directed Evolution. *Acc. Chem. Res.* **2019**, *52*, 585-595.
- (50) Wilson, M. E.; Whitesides, G. M., Conversion of a protein to a homogeneous asymmetric hydrogenation catalyst by site-specific modification with a diphosphinerhodium(I) moiety. *J. Am. Chem. Soc.* **1978**, *100*, 306-307.
- (51) Oohora, K.; Kihira, Y.; Mizohata, E.; Inoue, T.; Hayashi, T., C(sp³)–H Bond Hydroxylation Catalyzed by Myoglobin Reconstituted with Manganese Porphycene. *J. Am. Chem. Soc.* **2013**, *135*, 17282-17285.
- (52) Kille, S.; Zilly, F. E.; Acevedo, J. P.; Reetz, M. T., Regio- and stereoselectivity of P450-catalysed hydroxylation of steroids controlled by laboratory evolution. *Nat. Chem.* **2011**, *3*, 738-743.
- (53) Zhang, K.; Shafer, B. M.; Demars, M. D.; Stern, H. A.; Fasan, R., Controlled Oxidation of Remote sp³ C–H Bonds in Artemisinin via P450 Catalysts with Fine-Tuned Regio- and Stereoselectivity. *J. Am. Chem. Soc.* **2012**, *134*, 18695-18704.
- (54) Peters, M. W.; Meinhold, P.; Glieder, A.; Arnold, F. H., Regio- and Enantioselective Alkane Hydroxylation with Engineered Cytochromes P450 BM-3. *J. Am. Chem. Soc.* **2003**, *125*, 13442-13450.
- (55) Collins, T. J., TAML Oxidant Activators: A New Approach to the Activation of Hydrogen Peroxide for Environmentally Significant Problems. *Acc. Chem. Res.* **2002**, *35*, 782-790.
- (56) Collins, T. J.; Ryabov, A. D., Targeting of High-Valent Iron-TAML Activators at Hydrocarbons and Beyond. *Chem. Rev.* **2017**, *117*, 9140-9162.
- (57) Chahbane, N.; Popescu, D.-L.; Mitchell, D. A.; Chanda, A.; Lenoir, D.; Ryabov, A. D.; Schramm, K.-W.; Collins, T. J., Fe^{III}–TAML-catalyzed green oxidative degradation of the azo dye Orange II by H₂O₂ and organic peroxides: products, toxicity, kinetics, and mechanisms. *Green Chem.* **2007**, *9*, 49-57.

- (58) Ryabov, A. D.; Collins, T. J., Mechanistic considerations on the reactivity of green Fe^{III}-TAML activators of peroxides. In *Advances in Inorganic Chemistry*; van Eldik, R.; Hubbard, C. D., Eds. *Academic Press*: **2009**; *61*, 471-521.
- (59) Ghosh, M.; Nikhil, Y. L. K.; Dhar, B. B.; Sen Gupta, S., Mechanism of Alcohol Oxidation by Fe^V(O) at Room Temperature. *Inorg. Chem.* **2015**, *54*, 11792-11798.
- (60) Kwon, E.; Cho, K.-B.; Hong, S.; Nam, W., Mechanistic insight into the hydroxylation of alkanes by a nonheme iron(v)-oxo complex. *Chem. Commun.* **2014**, *50*, 5572-5575.
- (61) Napoly, F.; Kieffer, R.; Jean-Gérard, L.; Goux-Henry, C.; Draye, M.; Andrioletti, B., Fe(TAML)Li/tert-butyl hydroperoxide as a new combination for benzylic C–H oxidation. *Tetrahedron Lett.* **2015**, *56*, 2517-2520.
- (62) Das, A.; Nutting, J. E.; Stahl, S. S., Electrochemical C–H oxygenation and alcohol dehydrogenation involving Fe-oxo species using water as the oxygen source. *Chem. Sci.* **2019**, *10*, 7542-7548.
- (63) Dundas, C. M.; Demonte, D.; Park, S., Streptavidin–biotin technology: improvements and innovations in chemical and biological applications. *Appl. Microbiol. Biotechnol.* **2013**, *97*, 9343-9353.
- (64) Ren, Q.; Guo, Y.; Mills, M. R.; Ryabov, A. D.; Collins, T. J., On the Iron(V) Reactivity of an Aggressive Tail-Fluorinated Tetraamido Macrocyclic Ligand (TAML) Activator. *Eur. J. Inorg. Chem.* **2015**, *2015*, 1445-1452.
- (65) acetone was selected as co-solvent to ensure dissolution of the substrates. Its presence influences the product distribution by diminishing alcohol oxidation. See SI for more details.
- (66) TTON refers to total turnover number, and includes the C-H hydroxylation and alcohol oxidation products, quantified by GC-FID
- (67) Ghosh, M.; Singh, K. K.; Panda, C.; Weitz, A.; Hendrich, M. P.; Collins, T. J.; Dhar, B. B.; Sen Gupta, S., Formation of a Room Temperature Stable Fe^V(O) Complex: Reactivity Toward Unactivated C–H Bonds. *J. Am. Chem. Soc.* **2014**, *136*, 9524-9527.
- (68) Kundu, S.; Thompson, J. V. K.; Shen, L. Q.; Mills, M. R.; Bominaar, E. L.; Ryabov, A. D.; Collins, T. J., Activation Parameters as Mechanistic Probes in the TAML Iron(V)–Oxo Oxidations of Hydrocarbons. *Chem. Eur. J.* **2015**, *21*, 1803-1810.
- (69) St. John, P. C.; Guan, Y.; Kim, Y.; Kim, S.; Paton, R. S. Prediction of organic homolytic bond dissociation enthalpies at near chemical accuracy with sub-second computational cost. *Nat. Commun.* **2020**, *11*, 2328.
- (70) Hoffmann, R. W. Allylic 1,3-strain as a controlling factor in stereoselective transformations. *Chem. Rev.* 1989, *89*, 1841–1860.
- (71) Shin-ya, K.; Sugeta, H.; Shin, S.; Hamada, Y.; Katsumoto, Y.; Ohno, K. Absolute Configuration and Conformation Analysis of 1Phenylethanol by Matrix-Isolation Infrared and

Vibrational Circular Dichroism Spectroscopy Combined with Density Functional Theory Calculation. *J. Phys. Chem. A*, **2007**, *111*, 8598–8605.

(72) Miller, J. A.; Alexander, L.; Mori, D. I.; Ryabov, A. D.; Collins, T. J., In situ enzymatic generation of H₂O₂ from O₂ for use in oxidative bleaching and catalysis by TAML activators. *New J. Chem.* **2013**, *37*, 3488-3495.

(73) Doble, M. V.; Jarvis, A. G.; Ward, A. C. C.; Colburn, J. D.; Götze, J. P.; Bühl, M.; Kamer, P. C. J., Artificial Metalloenzymes as Catalysts for Oxidative Lignin Degradation. *ACS Sustain. Chem. Eng.* **2018**, *6*, 15100-15107.

(74) Ghosh, A.; Ramidi, P.; Pulla, S.; Sullivan, S. Z.; Collom, S. L.; Gartia, Y.; Munshi, P.; Biris, A. S.; Noll, B. C.; Berry, B. C., Cycloaddition of CO₂ to Epoxides Using a Highly Active Co(III) Complex of Tetraamidomacrocyclic Ligand. *Catal. Lett.* **2010**, *137*, 1-7.

(75) DeNardo, M. A.; Mills, M. R.; Ryabov, A. D.; Collins, T. J., Unifying Evaluation of the Technical Performances of Iron-Tetra-amido Macrocyclic Ligand Oxidation Catalysts. *J. Am. Chem. Soc.* **2016**, *138*, 2933-2936.

(76) Nobuo, M.; Mitsuo, Y.; Yoshihiro, A.; Yojiro, T., Intramolecular Hydrogen Bonds. XVI. Preferable Conformation of 1-Tetralols. *B. Chem Soc. Jpn.* **1971**, *44*, 1137-1139.

(77) Senda, Y.; Imaizumi, S., Carbon-13 pulse Fourier transform NMR : Conformational preference of the hydroxyl and the acetoxy group in 2-cyclohexenol and its acetate. *Tetrahedron*, **1974**, *30*, 3813-3815.

6. Final Conclusion and Outlook

Artificial metalloenzymes based on earth-abundant transition metals catalyzing C–H functionalization reactions were developed using the biotin-streptavidin technology. Each of the studied systems displayed promising activities for further developments.

In chapter 3, a strategy for the synthesis of bioconjugated Tp complexes was developed. A novel approach based on pyrazole metathesis of a sterically crowded Tp complex enabled the access to biotinylated heteroscorpionates and an unprecedented enantiopure Tp chiral-at-boron. The biotinylated copper(I) Tp complexes were incorporated in Sav for initial reactivity tests. The resulting ArM's displayed promising activity and selectivity for intramolecular C–H insertion reactions.

In chapter 4, an ArM based on a copper heteroscorpionate was designed and studied using CD spectroscopy. Computational modelling highlighted a set of close-lying amino acid residues that were targeted for genetic optimization. A substrate offering regio- and enantioselectivity opportunities was selected for the reactivity studies. Single and double mutant screening at position S112/K121 provided detailed information on individual amino acid contribution for TON and enantioselectivity. Directed evolution at a third position allowed to favor individual regioisomers with up to 88:12 e.r and 4627 TON on selected substrates.

In chapter 5, an artificial C–H hydroxylase based on an Fe(TAML) cofactor was designed. Installation of a modified biotin anchor and genetic optimization permitted the identification of Sav S112R as the most promising variant. X-ray crystallography allowed to obtain structural details of the second coordination sphere of the cofactor. Kinetic studies revealed a kinetic resolution effect in the catalytic pocket and provided >99 % ee of (*R*)-tetralol in 300 TTON. Finally, an enzymatic cascade with glucose oxidase enabled the use of molecular oxygen as terminal oxidant.

Incorporating a first row transition metal complex in a protein scaffold has multiple advantages. It can shield the metal from undesired coordinations, provides a genetically evolvable second coordination sphere and paves the way to *in vivo* applications. Artificial metalloenzymes thus creates excellent prospects to solve the major challenges of C–H functionalization methodologies such as regio- and enantioselectivity.

